A Methodology for the Rapid Identification of Neotectonic Features using Geographical Information Systems and Remote Sensing: A Case Study from Western Crete, Greece.

Athanasios Argyriou

A thesis submitted in partial fulfilment of the requirements for the degree of Doctor of Philosophy.

School of Earth and Environmental Sciences
University of Portsmouth
United Kingdom

April 2012

Abstract

The investigation of neotectonic activity is of high priority when dealing with inaccessible regions where a lack of data and a limited knowledge of the tectonic activity is often typical. There are various individual analyses that investigate features associated with neotectonic activity (for example geoinformatics, geophysical methods and field surveys). However, none of these methods combine low cost techniques based on geospatial and geophysical technologies with field validation of the outcomes. This study offers a methodology that covers all aforementioned approaches for detecting zones of neotectonic activity, linking computer-based observations with actual field observations and geophysical measurements. The combination of satellite imagery and DEM analysis can provide a cost-effective alternative to satellite radar interferometric analysis (InSar) and differential GPS monitoring.

Crete is a complex, tectonically active region: an ideal ñatural laboratoryò to assess the interaction between neotectonic processes and geomorphological processes in landscape evolution and to test the effectiveness of geomorphometric methods for determining zones of neotectonic activity.

Geoinformatic and geomorphometric techniques have been used here to assess landscape evolution in tectonically active zones. The results provide new information about the influence of tectonic and erosional processes on geomorphological evolution, with specific insights into the interactions between neotectonic deformation, faulting and drainage networks.

Geomorphic indices have been used here to evaluate neotectonic behaviour at regional and local scales, identifying uplifted blocks, valley-floor tilting and zones of relatively intense neotectonic activity. Landsat ETM+ imagery and DEMs were used to discriminate lithological boundaries and identify lineaments. Field and VLF geophysical surveys verified that the lineaments coincide with faults. The GIS based multi-criteria decision analysis (MCDA) was considered as a strong approach to integrate the various factors associated with tectonic activity and to highlight, spatially, the potential zones undergoing active tectonic control.

Whilst registered as a candidate for the above degree, I have not been registered for any other research award. The results and conclusions embodied in this thesis are the work of the named candidate and have not been submitted for any other academic award.

CONTENTS

LIST OF FIGURES

Fig. 4.1: Schematic table showing the sequence and contribution of calculated geomorphic indices to evaluate and isolate tectonically active zones, at regional scale of study.

Fig. 4.2: The basin asymmetry factor of Hare and Gardner (1985) (modified by Alastair, 2008). Ar is is the percent of the area in the basin that is found on the right of the main stream. Al is is the percent of the area in the basin that is found on the left of the main stream. Meander belt midline is the long axis of the mainstream if stable settings of a drainage network formation were taking place. Drainage divide is the boundary that defines the limits of the basin.

Fig. 4.3: Sample plots of total stream numbers to order of the streams (Nu-u). The order stream where a deviation is observed in the linear regression indicates a lower number of streams than the higher order which follows. This is not in accordance with Horton's first law, indicating that the deviation observed is a result of variation in relief (that issue implies that exogenous factors such as tectonic might be influencing the drainage network development).

Fig. 4.4: The AF (%) index, with the values indicating the level of tilting. It is notable that drainage basins with westward tilting are surrounded by basins with eastwards tilting (basins 7, 8, 19), indicating zones of high structural control. White arrows show the tilting orientation with regard to the mainstream direction.

Fig. 4.5: Hypsometric integral evaluation. The areas of well defined deep incision and slight erosion in basin as a whole are the drainage basins that are associated with higher tectonic activity (due to erosion not being the underlying, principle factor).

Fig. 4.6: Graphical plot of HI against A. Negative correlation is observed indicating that small basins have a convex hypsometry, whilst larger ones are concave. Presence of few basins is not in accordance with the statement corresponding in the negative correlation (see black circle).

Fig. 4.7: Graphical plot of HI against Dd. Negative correlation is observed indicating that increase in Dd leads to decrease of HI. Presence of few basins is

not in accordance with the statement corresponding in the negative correlation (see black circle).

Fig. 4.8 a, b: Moderate negative correlation observed between relief ratio (Rr) with drainage density (Dd) and drainage frequency (F). The relation is not in accordance with Strahler (1964) and Al-Sulaimi (1997) study, where moderate positive correlation was observed.

Fig. 4.9: Schematic diagram, showing how regional tectonic control of the drainage basins is determined from an initial number of geomorphometric indices, by using factor analysis and AHP procedures.

Fig. 4.10: The scree plot shows that the first four components are those containing most of the information (regarding percentage of variance) and those are expected to be retained in final stage of factor analysis.

Fig. 4.11: The AHP results for Arapi basin.

Fig. 4.12: The AHP results for Pelekaniotis basin.

Fig. 4.13: The AHP results for Samaria Gorge basin.

Fig. 4.14: The AHP procedure applied in this research regarding the determination of regional tectonic control showed that the basins in: i) reddish owe their development in high tectonic activity; ii) yellowish in moderate tectonic activity and; iii) bluish in minimal tectonic activity.

Fig. 5.1: The transverse topographic symmetry method proposed by Cox (1994) (modified from Salvany, 2004; in Tsodoulos, 2008)

Fig. 5.2: The ratio of valley floor width to valley height developed by Bull & McFadden (1977) (modified by Ramirez, 1998).

Fig. 5.3: The mountain front sinuosity calculated parameters (modified by Ramirez, 1998).

Fig. 5.4: The basin asymmetry vectors of the Transverse Topographic Symmetry factor (T) along the main streams of the study area. The vectors highlight the degree of tilting with regard to the basin midline (to left downstream with triangle

or to right downstream with circle). Small circles (-0.1<T<0.1) indicate symmetric drainage networks.

Fig. 5.5: S_L index values along the main streams of the drainage basins. The S_L index clearly varies, with anomalous changes in values, indicating regions with higher tectonic activity.

Fig. 5.6: The SLk anomaly map with a ýxed dl of 200 m. The black arrows indicate the higher tectonically active zones, where the index has major fluctuation anomalies.

Fig. 5.7: The calculated Vf index with values lower than one (red points), indicate high tectonic activity of the mountain fronts, particularly in the western basins where high incised valleys are present. Values larger than 1 (green points) indicate mountain fronts with less tectonic activity (even inactive).

Fig. 5.8: The mountain fronts for which the Smf index was estimated and the Vf index points calculated upstream of the front. The fault- bounded fronts indicate the sinuosity and the degree of mountain front tectonic activity.

Fig. 5.9: a) The Vf-Smf index classification of the mountain front in three classes of tectonic activity (after Verrios, 2004); **b)** The classes represent the relative degree of tectonic activity (with the values in class 1 being most active). Values in the red circle show that the Vf-Smf indices calculated for the study region correspond to class 1, indicating high tectonic activity.

Fig. 5.10: The hypsometric curves extracted for each drainage basin. The upper graph (concave) contains the drainage basins that are transitional from intermediate incision and erosion to severe erosion and low relief. The lower graph (convex) represents the drainage basins that are transitional from deep incision and slight erosion to an intermediate stage of incision and erosion.

Fig. 5.11: Sample of the hypsometric curves (HC) of drainage basins with the fluctuations along the curve, indicating depositional surfaces (alluvial fans) or knickpoints (uplift). Lithology across the basins is depicted to make more meaningful these observed fluctuations.

Fig. 5.12: Slope map of drainage basins. (Region A), flat surfaces to slight gentle slopes, occupying 6.8% of the study region; (Region B), gentle slopes, covering

32.27% of total area; (Region C), moderate slopes covering 55% of the study region and; (Region D), steep to very steep slopes covering 5.8% of the total area.

Fig. 5.13: Amplitude relief. The black rectangles indicate tectonically active zones, with high relative relief observed. Alignment formation zones and high variations in relative relief, with regard the surrounding neighborhood regions, are the highly active zones.

Fig. 5.14: The TWI regions cited in the text. Region A shows high values of TWI; Region B has high values (but lower that region A due to lower stream ordering and water discharge); Region C has intermediate values, revealing steep slopes and major ridges; Region D indicates lower values of TWI characterized by incised V-shaped valleys. The black arrows indicate sample regions of tectonic influence due to the linearity observed between the high and low values of the index.

Fig. 5.15: Left: The drainage density distribution map of the drainage basins, with higher values depicted in blue. Right: The drainage frequency distribution map of the drainage basins, with higher values depicted in red. Lower values of drainage density and frequency mainly to impervious rocks indicate tectonically structural zones (Region A).

Fig. 5.16: Tilting of drainage basins affected by major faults in E-W (Platanos fault) and N-S (Keras Fault) directions. For the broadly N-S aligned basins, green tones indicate eastward tilting while red/yellow tones indicate westward tilting (see black arrows). For the western coastal basins, green tone indicates northward tilting while red/yellow tones show southward tilting (see black arrows).

Fig. 5.17: The shaded relief map reveals the difference of the tilting observed in the south-west basins, due to the tectonically active Keras fault presence.

Fig. 5.18: Site 1: The three individual segments of mountain front sinuosity (with values 1.489; 1.212 and; 1.534) with the central being the most tectonically active (Smf =1.212). The total Smf value of the mountain front is 1.4

Fig. 5.19: Site 2: Map of Smf, Vf and SL indices with mountain front locations referred to in the text.

RGB combination (4*3*2)(7*3*2)(7*3*1), after application of the band multiplication image processing procedure: this discriminates lithology and suppresses vegetation; **c)** overlay of the 1971 geological map on panchromatic Landsat ETM+ imagery of the Tiflos basin.

Fig. 6.13: The digitised faults of the geologic maps.

Fig 6.14: The lineament extraction based on the multispectral image analysis of RGB colour combination (4*3*2)(7*4*1)(7*5*3) Landsat ETM+ images.

Fig. 6.15: Lineaments extracted by Laplacian spatial filtering technique.

Fig. 6.16: The lineaments identified by the shaded reliefs in different azimuth orientations with sun elevation angle 45^0.

Fig. 6.17: Coinciding lineaments from different lineament mapping techniques were discriminated by buffer zones and were considered as singular lineaments.

Fig. 6.18: Final tectonic lineament mapping consisting of fault lines, as a product of coinciding lineaments (within 100m buffer zones) from all techniques.

Fig. 6.19: Lineaments that correspond to previously mapped faults from geological maps that were not detected using satellite imagery and DEM analysis.

Fig. 6.20: Lineaments extracted by satellite imagery and DEM techniques that fit with previously identified faults in geological maps.

Fig. 6.21: Lineaments extracted by satellite imagery and DEM techniques, previously unrecorded by geological maps.

Fig. 6.22: The lineament azimuth classification in four major azimuths. Their statistical analysis indicated which drainage basins are subject to structural control.

Fig. 6.23: Density map of manually digitised lineaments.

Fig. 6.24: Frequency map of manually digitised lineaments.

Fig. 6.25: The rose diagrams of faults with regard to drainage network azimuths for particular drainage basins (as a sample) of the study region, indicating mainly their E-W strike.

Fig. 6.26 a: Offshore faults from various studies indicate the major trench structures. The map was compiled by Ten Veen & Postma (1999) with offshore

data being acquired from Jongsma (1977), Foose (1977), Le Pichon et al. (1979), Angelier et al. (1982), Leite & Mascle (1982), Peters (1985), Peters & Huson (1985), Mascle et al. (1986) and Mascle & Martin (1990).

Fig. 6.26 b: Major fault patterns existing in the surrounding of the study region, with (ï) indicating grabens and (+) indicating horsts (modified by Ten Veen & Postma, 1999). Note the lack of data information in the western Crete study region.

Fig. 6.27: The comparison between the offshore and onshore faults/lineaments indicates their effective association. Offshore N-S striking faults are associated with onshore N-S striking fault lines in the NW of the study area. The offshore NE-SW striking faults on the southern west part of the study area seem to be extended on the mainland by cross-cutting the study region from its southern western part to its north eastern part. Finally, the NW-SE and E-W offshore striking faults seem to play a significant role in the whole study area, particularly in the western and eastern part of study area.

Fig. 7.1: Acquisition of geophysical measurements with the VLF equipment in the field.

Fig. 7.2 (a): The fault/fractured zone, is identified on the ñrealò part as an anomalous curve. In the ñimaginaryò part no anomaly is detected (values close to 0). This is observed in conductive zones, characterized by high resistivity filled material. This plot is typical for representing a fault/fracture zone with a fresh water filled structure.

Fig. 7.2 (b): The fault/fractured zone is identified on the ñrealò part as an anomalous curve. In the ñimaginaryò part there is a symmetrical anomaly detected in the negative values. This is due to the presence of good conductive zones. This plot is typical for representing a fault/fracture zone with a saline water filled structure.

Fig. 7.3: The VLF equipment and the individual components.

Fig. 7.4: The raw data as presented in SECTOR software with the faults determination by filtered real and imaginary part observation (left image) and

vertical cross section from the actual profile with the depth and the dipping direction of the fracture zone being depicted (right image).

Fig. 7.5 a, b: The locations of VLF profile surveys (sites a & b) overlain on the Landat TM8 panchromatic band. Inset map in (a) shows the location of sites with regard to the study region.

Fig. 7.6: Overview of study area landscape where the VLF measurements were acquired.

Fig. 7.7: The overview of the VLF survey profiles with regard to identified lineaments/faults and the identified faults location by the VLF data, using SECTOR software.

Fig. 7.8 (a) to (f): The graph plots of the two magnetic components of VLF data (real and imaginary part) and the interpreted identified faults (black arrows).

Fig. 7.9: Sample of VLF data after 2D inversion modelling (with fracture zones, faults and bedrock depicted). Transition from low-conductivity values to high-conductivity values, indicates the discrimination between fracture zones and bedrock. Longitudinal profiles were extracted utilising DEMs. The plot diagrams depict abrupt breaks of slope and faults indicated with black arrows.

Fig. 7.10: The sites where ground truthing was performed.

Fig. 7.11: Ground-truthing of E-W striking fault plane that offsets young deposits; fault breccia and slickenlines are exposed (Site 1).

Fig. 7.12: Fault plane with an NE-SW strike of 80 ^{0} and a dip of 67 ^{0} to north. Oblique slip is recorded by slickenlines (Site 1).

Fig. 7.13: Slickenlines identified within the fault plane with a strike of 80 ^{0} (Site 1).

Fig. 7.14: a) Fault scarps exposed and linked to each other under the same active fault on an E-W strike (Site 1); **b)** Fault scarp exposed parallel to the fault scarp in (a); **c)** The carbonate of Tripolis nappe superimposed over the Phyllite-quartzite series (Site 1); **d,e)** Folds related to nappe emplacement, exposed in Site 2**; f,g,h)** Fault breccia and slickenlines exposed in Site 2; i) En echelon ENE-WSW fault set, both normal and reverse slip (Site 2).

Fig. 7.15: Fault scarps (red circles) exposed in the south of the study region close to Cape Krios (Site 2).

LIST OF TABLES

LIST OF APPENDICES

APPENDIX II

Fig. 11: Sample site selected to represent the outcomes of compass gradient masks, Laplacian filter and non directional filters (Sobel and Prewitt) applied in Landsat ETM+ TM7 and second principal component of Landsat ETM+ sensors.

Fig. 12: The shaded reliefs of DEMs for various azimuths and sun elevation.

Fig. 13: The graph plots of the two magnetic components of raw VLF data (real and imaginary part) and the interpreted identified faults (black arrows). Vertical cross sections of observed faults also performed.

Fig. 14: The figures of the rest VLF data after 2D inversion modelling with fracture zones, faults and bedrock being depicted on them. Transition from low conductivity values to high conductivity values, indicates the discrimination between fracture zones and bedrock. Longitudinal profiles were extracted utilising DEMs. The plot diagrams depict abrupt breaks of slope and faults indicated with black arrows.

APPENDIX II TABLES

Table 1: The covariance values per each spectrum band of the Landsat ETM+ multispectral imagery.

Table 2: The correlation values per each spectrum band of the Landsat ETM+ multispectral imagery.

Table 3: The eigenvectors of the principal component analysis of the Landsat ETM+ multispectral imagery, with higher values making the bands representative of the principal component.

Table 4: Best OIF false colour composites combination for Landsat ETM+.

LIST OF ACRONYMS

A: Area of drainage basins

AF: Asymmetry Factor

ASTER: Advanced Spaceborne Thermal Emission and Reflection Radiometer

ATHR: Angular difference threshold

C: Constant of channel maintenance

D_d: Drainage density

DEMs: Digital Elevation Models

DN: Digital Numbers

DTHR: Linking distance threshold

DWT: Discrete Wavelet Transform

ERSDAC: Earth Remote Sensing Data Analysis Center

ESRI : Environmental Systems Research Institute

EM: Electro Magnetic

F_u: Stream frequency

FCCs: False Colour Composites

FTHR: Line fitting error threshold

GCPs: Ground Control Points

GGRS '87: Greek geodetic reference system, 1987

GIS: Geographic Information Systems

GPS : Global Positioning System

GTHR: Gradient threshold

HI: Hypsometric Integral

HC: Hypsometric Curve

HMGS: Hellenic Military Geographical Service

HPF: High Pass Filtering

HSZ: Hellenic subduction zone

IDWT: Inverse Discrete Wavelet Transform

IGME: Institute of Geology and Mineral Exploration

IHS: Intensity Hue Saturation

L_b: Basin length

L_g: Length of overland flow

Landsat ETM+: Landsat Enhanced Thematic Mapper Plus

LTHR: Length threshold

MNF: Minimum Noise Fraction transformation

N: Number of streams

NASA: National Aeronautics and Space Administration

OIF: Optimum Index Factor

P: Perimeter of basins

PCA: Principal Component Analysis

PC: Principal Component

R: Basin relief

R_b: Bifurcation ratio

R_c: Basin circularity

R_e: Elongation ratio

R_f: Form factor

R_l: Average stream-length ratio

R_n: Ruggedness number

R_r: Relief ratio

RADI: Filter radius

RGB combination: Red-Green-Blue combination

RSM: Relative Shift in the Mean value

SAR: Synthetic Aperture Radar

SI: stream gradient index

Smf: Mountain front sinuosity

SRTM: Shuttle Radar Topography Mission

STA: Segment Tracing Algorithm

T: Transverse topographic symmetry factor

(T): Texture ratio

TRI: Topographic Ruggedness Index

TWI: Topographic Wetness Index

Vf: Valley floor width to valley height ratio

VLF: Very Low Frequency

ΣL: Total stream length

Acknowledgements

This research would not be possible without the support of specific people that believed on me and filled me with the burning desire to achieve the goal of the study. I am really thankful to them.

Special thanks to my supervisors Derek Rust and Richard Teeuw by the University of Portsmouth (United Kingdom) for their guidance all these years.

Special thanks to Fillipos Vallianatos and Pantelis Soupios by the Technological Educational Institute of Crete (Greece) for inspiring me to start this research project.

Special thanks to George Variemezis by the Aristotle University of Thessaloniki (Greece) and Mehrdad Bastani by the Uppsala University (Sweden) for their crucial help to the acquisition and modelling of VLF geophycical measurements.

Special thanks to the Greek State Scholarships Foundation (I.K.Y.) for the support and the funding of this research.

This thesis is dedicated to my family for their understanding and encouragement all these years. Special dedication to the memory of my grandmother Dafni Kipouridou.

CHAPTER 1 INTRODUCTION

1.1 Introduction

- **Understanding tectonically active zone**
- **What is active tectonics**
- **How can active tectonics be determined**
- **Which regions have priority for active tectonics investigation**
- **Why a robust approach needed for evaluation of active tectonics**

1.2 Aim and objectives of the research

1.3 Case study area

1.4 Thesis structure

1.1 Introduction

- **Understanding tectonically active zone**

In the last decade, more than 780.000 deaths and $960 billion in economic loses have resulted from natural disasters, with earthquakes causing 60% of them (Bartels & VanRooyen, 2011; Guha-Sapir et al., 2011). This shows clearly the devastating socio-economic impact of earthquakes and the need to assess regions of high tectonic activity. Earthquake prediction is at present an unattainable task, due to difficulties such as: i) no access for direct observation of the source, deep in the Earth and; ii) no direct measurement of the state of stress (Wyss, 2001). However, during the last few years tectonically active zones have been investigated with more sophisticated instruments and techniques (such as GPS and digital satellite data) (Zumberge et al., 1997; Lu et al., 2000). In some cases those new systems can be relatively costly (e.g. GPS networks, interferometric synthetic aperture radar (InSAR) etc). A broader usage of cost effective new systems is needed to provide rapid evaluations of poorly known potentially tectonically active regions. Understanding active tectonics and its implications for ground deformation can offer a valuable tool in natural hazard assessment.

- **What is active tectonics**

Active tectonics can be defined as ñ*those tectonic processes that produce deformation of the earth's crust on a time scale of significance to human society*ò (Keller & Pinter, 1996). A tectonic landscape can be developed by fracturing, orogenesis, compression or extension of geological units, revealing the tectonic processes existing and controlling the development of a specific region (Thanassoulas, 2005). Neotectonic activity is defined as recent surface deformation by tectonic processes (Obruchev, 1948; Pavlides, 1989; Koster, 2005); while the current tectonic regime of a region is taken as being the regional stress field, particularly the maximum principal stress direction (ů1) (Masana, 1994; Schindler, 1998; Kokkalas & Doutsos, 2001).

- **How can active tectonics be determined**

Tectonic processes are responsible for the development of relief. However, factors such as erosion, tends to smooth down that relief, making the assessment of tectonic deformation more complex. This research focuses on neotectonic activity that is reflected in the development of drainage basins and mountain fronts. Due to differential erosion, streams can be sensitive to abrupt changes in underlying geology, for example through fractures and different lithologies (Hack, 1957). Tectonic deformation can also influence valley floor morphology and the gradients of rivers, by either uplift or subsidence (Schumm, 1986; Humphrey & Konrad, 2000; Snyder et.al, 2000). In addition, tectonic deformation often results in the deflection of streams, the creation of beheaded drainage networks and knick points (Humphrey & Konrad, 2000). Summerfield (1991) refers to types of stream characteristics that can be associated with the identification of active tectonics such as: i) deformation of valley-floor longitudinal profile; ii) change of channel and valley gradient; iii) change of channel width and depth; iv) variations in channel stability like channel shifting and knickpoint formation etc.. All aforementioned stream characteristics can be investigated for the evaluation of tectonic activity in a region. This study focuses on examining such characteristics with various geomorphic indices, as will be described further in chapters 4 and 5.

In semi-arid tectonically active zones the most characteristic landforms are fault-bounded mountain fronts (Silva et al., 2003). Active mountain fronts - being fault bounded - provide information about the presence of neotectonic activity, such as by their mountain front sinuosity (Mayer, 1986; Keller & Pinter, 2002). Erosional processes influencing the topography can be evaluated by examining such geomorphometric characteristics (e.g. drainage network, mountain fronts etc.) within drainage basins, in order to determine the degree of tectonic activity. For that reason this research examines all those geomorphometric characteristics against the erosional and tectonic processes as they can be particular useful in the assessment of the regional and local tectonic deformation.

- **Which regions have priority for active tectonics investigation**

The assessment of regional tectonic deformation is often hampered by dense vegetation, steep-sided high relief and rugged, poorly-accessible terrain. Especially when dealing with areas away from well-exposed coastal zones. Such landscapes are often mountainous, where walk-over surveys and field mapping are difficult and cannot provide a full perspective on the extent of recent tectonic activity. Moreover such landscapes are not well known and are poorly examined regarding the tectonic history. Ground-based surveys are costly and time consuming relative to geoinformatic techniques, such as mapping based on digital satellite imagery or geomorphometric analysis of Digital Elevation Models (DEMs). Fortunately, that kind of geoinformatic data enables many tectonic and geomorphological features to be identified and assessed. The analysis of geomorphic features, such as lineaments and drainage patterns, can provide insights into the tectonic setting, tectonic history and landscape evolution of a region.

Developed countries associated with tectonically active zones, such as Japan and the USA (California in particular), have sophisticated systems in place for monitoring and assessing current tectonic regimes. However, such monitoring is too expensive for many countries, hence the need for alternative, low-cost techniques to better assess current tectonic regimes that may cause earthquake and earthquake related hazards.

Remote sensing datasets are widely available freely nowadays and this encourages researchers to use these datasets. Such datasets can be used for lithological discrimination or lineament mapping offering an innovative piece of information in the evaluation of tectonic activity (Crosta 1989; Suzen & Toprak, 1998; Won-In & Charusiri, 2003; Masoud & Koike, 2006). This research provides an innovative, low-cost, set of geoinformatic techniques for assessing regional tectonic regimes and zones of neotectonic activity. This approach is particularly useful where the current tectonic regime produces active faults, with related erosion and deposition that obscures the surface expression of those faults. Thus, in many tectonically active regions, outcrops that expose active faults are rare. Active faults may therefore not be depicted on published geological maps, which are typically based mainly on outcrop fault mapping.

- **Why a robust approach needed for evaluation of active tectonics**

Most of current usage of geoinformatics is not focused on the evaluation of a series of techniques for the investigation of tectonics. It is agreed that there are particular individual approaches examining partly the tectonics in specific well known tectonically active regions. Despite that, there is no existence of an ideal overview perspective that makes use of the assemblage of established and new sophisticated techniques to evaluate the tectonic activity of a region and validate the outcomes in the field. Thus this research aims to provide a robust methodology of major parameters to be used in a relatively cost effective methodology. It makes use of the rapidly usage of geoinformatics to assess tectonic deformation, even in tectonically active regions where there is not in depth knowledge of tectonic activity. Moreover, field validation assesses Earth observational results reinforcing the reliability of the techniques.

1.2 Aim and objectives of the research

The overall aim of this study is to establish a robust methodology that uses geoinformatics and geomorphometric factors to identify areas of current tectonic deformation. The study combines both Geographical Information Systems (GIS) and digital satellite data (DEMs and multispectral satellite imagery), with factors such as fracture patterns and drainage basin morphological variations, to provide a low-cost approach for the evaluation of neotectonic activity. This methodology is seen as particularly valuable in regions that are poorly mapped, through inaccessibility or economic constraints, and yet have the potential to produce damaging earthquakes. Development in such regions should take place guided by knowledge of the currently active tectonic framework. Finally, the proposed methodology provides a useful tool for planning ground-truth surveys and the effective management of the associated survey resources. The robust methodology package of this research provides approaches that offer both usage of latest developed sophisticated techniques and robustness testing on the ground.

The test region for this research is the island of Crete, southern Greece, where zones of neotectonic faulting identified by this methodology will be compared with published geological map data and validated in the field using Very Low Frequency (VLF) radiowave responses. A GIS-based multi-criteria decision

analysis (MCDA) will aim to assess the spatial distribution of active tectonics. The research questions and the objectives that will be addressed in this study are as follows (Fig. 1.1):

Research question 1: How is active tectonic deformation of bedrock reflected in the landscape, particularly in drainage basins and along mountain fronts?

Objectives:

Task 1.1) Geomorphometric analysis of the drainage basins, using geomorphometric indices to assess influences of geological variables and geomorphological processes on landscape evolution,

Task 1.2) Morphotectonic analysis of the drainage basins and mountain fronts, using morphotectonic indices to identify tectonically active areas,

Research question 2: What neotectonic features can optical satellite imagery and DEMs detect?

Objectives:

Task 2.1) The processing of satellite remote sensing images to discriminate the lithological units,

Task 2.2) The processing of satellite imagery and DEMs, to identify surface tectonic lineaments,

Task 2.3) Field validation of the lineaments and lithologies identified by the satellite remote sensing and DEMs,

Task 2.4) The acquisition, analysis and modelling of VLF geophysical data for the identification of the active fault zones identified by satellite imagery and DEMs,

Task 2.5) Comparison between lineaments mapped using the geoinformatic datasets (satellite multispectral imagery and DEMs), with faults shown on the 1:50000 geological map (IGME, 1971) and the results of the VLF geophysical surveys.

The evaluation of the itemized aspects of the above two research questions is considered on the basis of a GIS-based multi-criteria decision analysis (MCDA) for performing an objective assessment of neotectonic status.

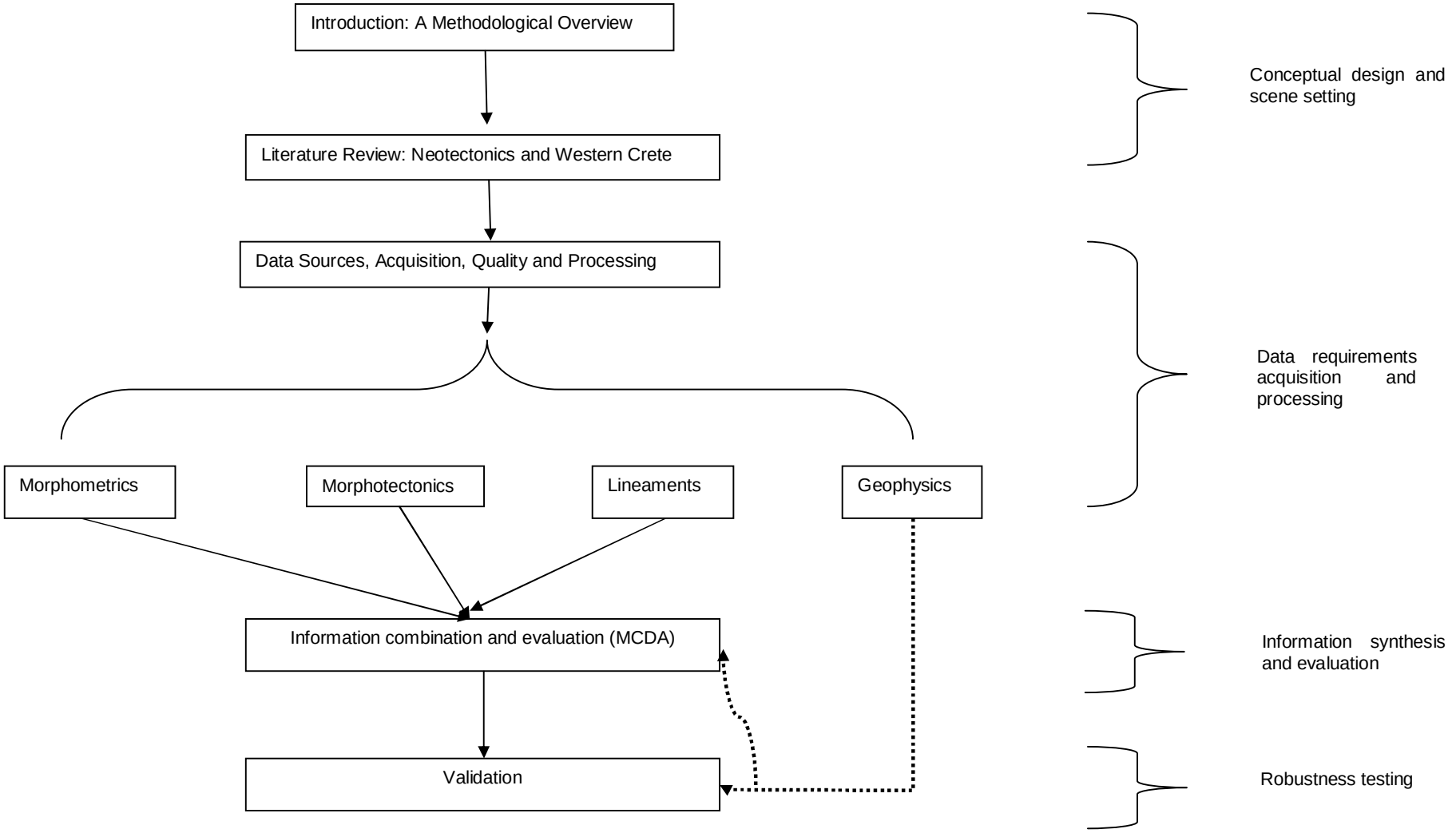

Fig. 1.1: A graphical scheme of the methodological framework of this research and its individual components.

1.3 Case study area

This study considers as a case study the island of Crete in southern Greece (Fig. 1.2b). This is a region that lies within the emergent outer fore-arc of the largest and most active subduction zone in Europe, the Hellenic arc, and is therefore characterized by high rates of tectonic activity and seismicity (Fig. 1.2 a, b) (McKenzie, 1978; Papazachos & Comninakis, 1978; Le Pichon et.al, 1982; Pirazzoli et al., 1992; Kellletat, 1996; Pirazzoli, 2005; Shaw et.al, 2008). The rectilinear outline of the island suggests the importance of tectonic controls in its evolution. Additionally, Crete has low-gradient shores on its northern coast and steep rocky shores on its south coast (Sarris, 2005), possibly suggesting the role of regional tilting. Cenozoic nappe stacking and thrusting are responsible for crustal thickening and isostatic emergence of this outer forearc terrain, now affected by active tectonics in the upper-plate of the Hellenic arc subduction zone (e.g. Dewey et al., 1973; Doutsos et al., 1993).

The geology of the region is complex and is made up of a thrusted sequence of nappes, formed during a Tertiary (~10 Ma) dominantly compressional tectonic regime now inactive associated with the closure of Tethys (Fassoulas, 1999). Limestones and dolomites characterise the south-east part of the study region, while central and south-westerly areas are made up of phyllites and quartzites. Marls, clays, conglomerates, flysch and carbonates are exposed in the north-west part of the study region. The northern coastline is partly made up of Quaternary and Neogene marine deposits (see geological map in Fig. 2.7).

The study area is characterised by mountainous relief (0-2500 m) with N-S trending deeply incised valleys and gorges (Sarris, 2005). The current tectonic regime is producing at least two sets of faults. Most faults are normal and have E-W or NW-SE strikes (Fig. 1.3) (Angelier et al., 1982; Jost et al., 2002). This tectonic framework can be related to slab rollback at the African margin as well as arc parallel extension of the Anatolian micro-plate (Royden, 1993; Wegmann, 2008). However, the complex tectonic evolution of western Crete is not well understood and the location of active fault features are still largely unknown (Papazachos, 1996).

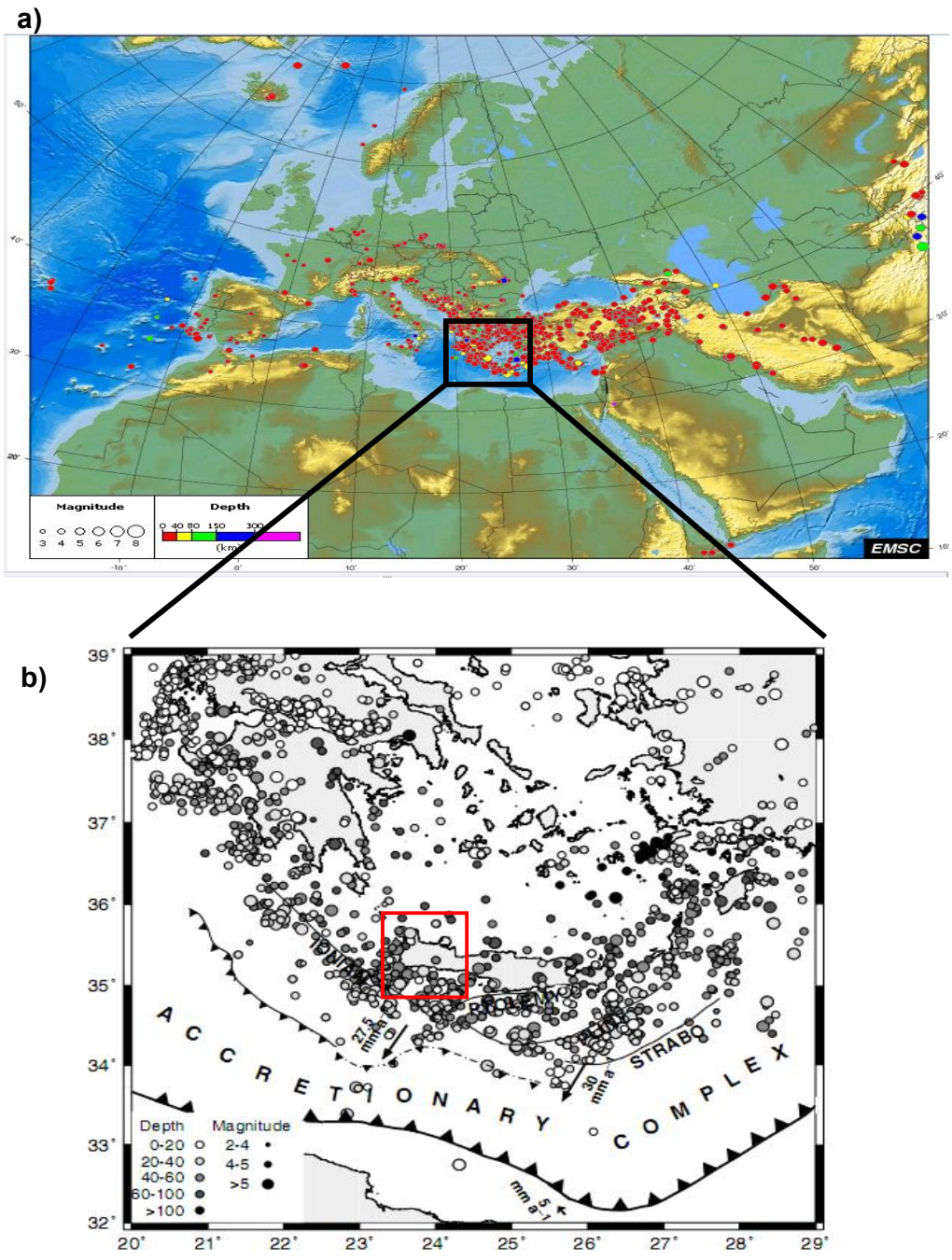

Fig. 1.2: a) Seismicity of events: February 20, 2010 ï March 3, 2010 (source: European-Mediterranean Seismological Centre (EMSC)). This reveals the high density of earthquakes in the study region (black rectangle) with regard to the rest of Europe. **b)** Seismicity of southern Greece, (source: Endrun 2004). The red box indicates the study region.

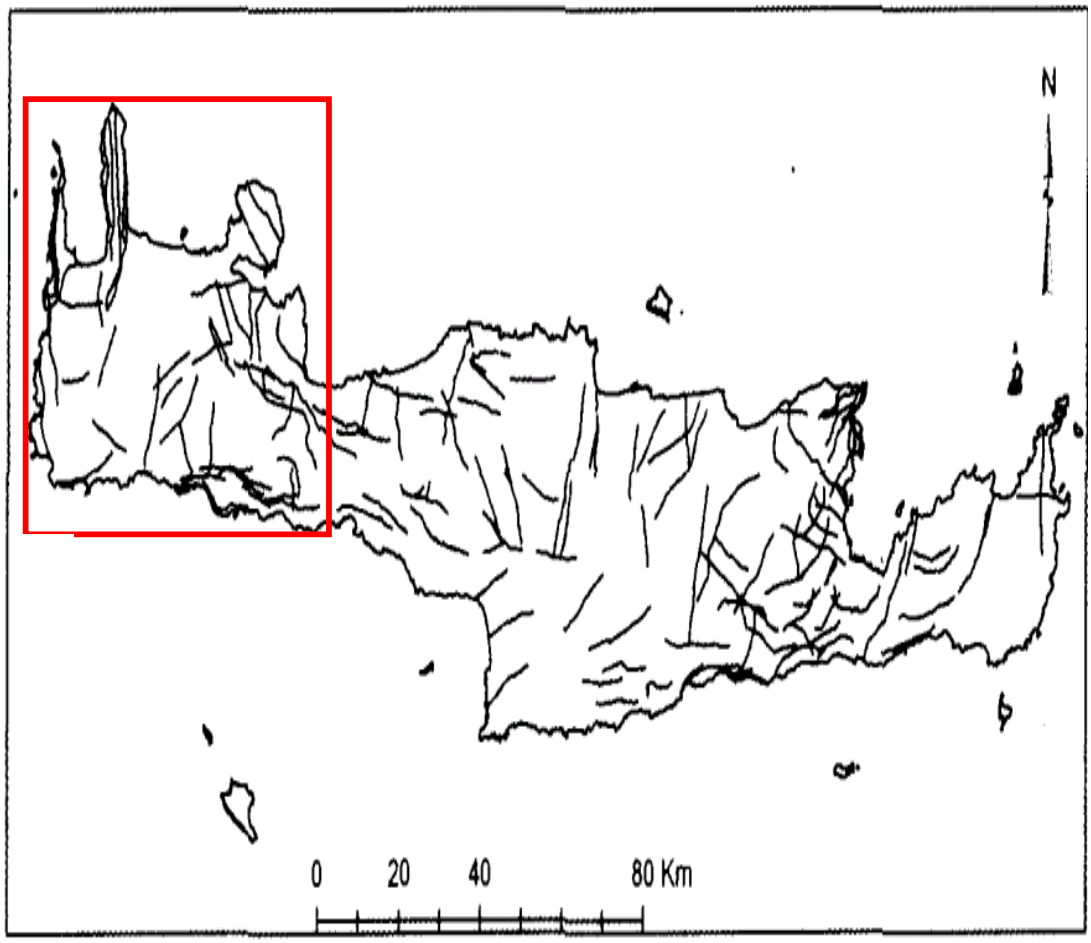

Fig. 1.3: The major faults of the study region (see red box) (modified by Fassoulas, 2005).

Crete has an east to west orientation and is parallel to the Hellenic trench in the south, with the elevation ranging from 0- 2.453 m (Fig. 1.4). The island measures approximately 260 km from east to west, and around 20 to 60 km, from north to south. Total length of coastline is around 1000 km.

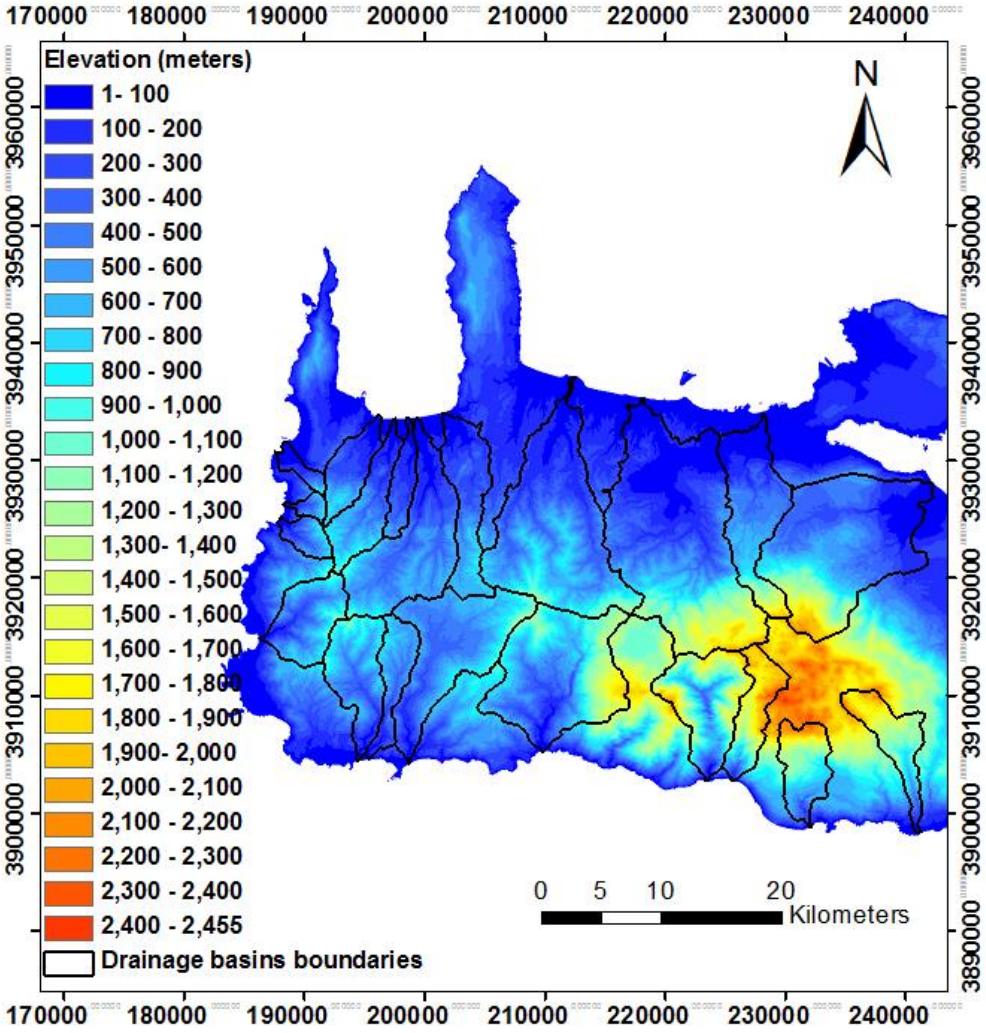

Fig. 1.4: Elevation range and drainage basins of the study region.

1.4 Thesis structure

This thesis offers a methodology that combines geoinformatics with geomorphological and geophysical data, to assess the tectonic setting and activity level of areas with neotectonic landscape deformation.

Chapter 1 introduces the key topics, research questions and objectives.

Chapter 2 describes the geology and tectonic evolution of the study region.

Chapter 3 reviews the fundamental data requirements for the basic methological framework. It outlines the required datasets and the methods used to their creation, while the datasets quality assessment is also reviewed.

Chapter 4 describes the methods used to derive morphometric indices for the identification of regional neotectonic settings. The usefulness of methods and data used in this chapter are evaluated. Various indices, such as bifurcation ratio, elongation ratio, hypsometric integrals, asymmetry factor etc., are examined for the drainage basins of the study region, on the basis of multi-criteria modelling. This evaluation aims to determine the higher regional degree of neotectonic activity influencing drainage basins deformation. The zones with higher degree of neotectonic activity are selected as case studies for the subsequent Chapters 5, 6, 7 and 8.

Chapter 5 describes the methods used to derive morphotectonic indices for the identification of local scale neotectonic settings. The usefulness of methods and data used in this chapter are evaluated. Various indices, such as mountain front sinuosity, amplitude relief, stream length-gradient etc., are examined within the drainage basins of the study region. This evaluation aims to determine the higher local degree of neotectonic activity influencing drainage basin deformation and prepare the datasets to be used in subsequent Chapter 8.

Chapter 6 presents the use of remote sensing to discriminate lithologies and identify lineaments. The extraction methods, such as principal component analysis, spectral band arithmetic operators, directional filtering etc., are described. The comparison of the extracted lineaments with other benchmark data is examined. Key findings and their relation to the current tectonic regime of western Crete are determined. This chapter focuses on identifying lineaments corresponding to fault lines and preparing datasets to be used in subsequent Chapter 8, such as lineament density and lineament frequency.

Chapter 7 presents the geophysical technique to be used in this research, as a validation tool for justifying the identified lineaments determined by Chapter 6, as fault structures. The methods and results are presented, with selected fracture zones sites investigated by ground truthing.

Chapter 8 describes the interrelationship of spatially analyzed maps extracted in earlier Chapters 5 and 6, on the basis of multi-criteria decision analysis (MCDA). Such analysis aims to associate lineaments determined by Chapter 7 with zones of neotectonic activity responsible for the deformation of the drainage basins determined in Chapter 5. A neotectonic activity map is presented, along with the significance for geohazard management.

Chapter 9 contains the conclusions from this research project. Recommendations for future work are also assessed.

CHAPTER 2 GEOLOGICAL SETTING

2.1 Introduction

2.1 Geological and tectonic setting

2.2.1 Evolution of the Aegean region and island of Crete

2.2.2 Evolution of western Crete

2.3 Tectonics of Crete

2.3.1 Western Crete tectonics

2.3 Drainage basins tectonics

2.4 Tectonic factors against other interrelated factors

- **Tectonics factors vs Lithological/structural factors**
- **Tectonic factors vs Climatic factors**
- **Tectonics factors vs human factors**

2.5 Summary

2.1 Introduction

This chapter describes the geological and tectonic setting of the case study area, in western Crete, based on published literature. Through this description it will be clearly understandable that the geological and tectonic setting play a significant role in the development of the landscape in the study area. Developing an understanding of the mechanisms that take place will provide the basis for refining the methodology.

2.2 Geological and tectonic setting

The outer-forearc of the Hellenic subduction zone is a particularly tectonically active region. This is due to convergence between the African and Eurasian tectonic plates, which results in the African plate descending below the Eurasian (Makris, 1977; McKenzie, 1978; Papazachos & Comninakis, 1978; Le Pichon et.al, 1982). The island of Crete, which represents the closest emergent crust to this subduction zone, is located in this tectonically complex area. The geology and the tectonic structure are of high scientific interest, as the region is characterized by major tectonic structures, with active behavior and recent ground deformation. By way of an example, the 21 July, 365 AD earthquake (Mw 8.3-8.5), the ñEarly Byzantine Tectonic Paroxysmò, produced coseismic uplift up to 9 meters on southwestern Crete (Fig. 2.1 & 2.2 a, b) (Thommeret et al., 1981; Pirazzoli et al., 1992; Kellletat, 1996; Stiros, 2001; Peterek, 2004; Pirazzoli, 2005; Shaw et.al, 2008). Considering the extensional basin formation and the Cretan sedimentation, as described by Drooger & Meulenkamp (1973), lead Le Pichon & Angelier (1979) to evaluate the beginning of neotectonics in the region 13 Ma ago. Recent studies have considered neotectonics to start around 11 Ma ago (Van Hindesbergen & Meulenkamp, 2006; Van Hindesbergen, 2010; Zachariasse et al., 2011).

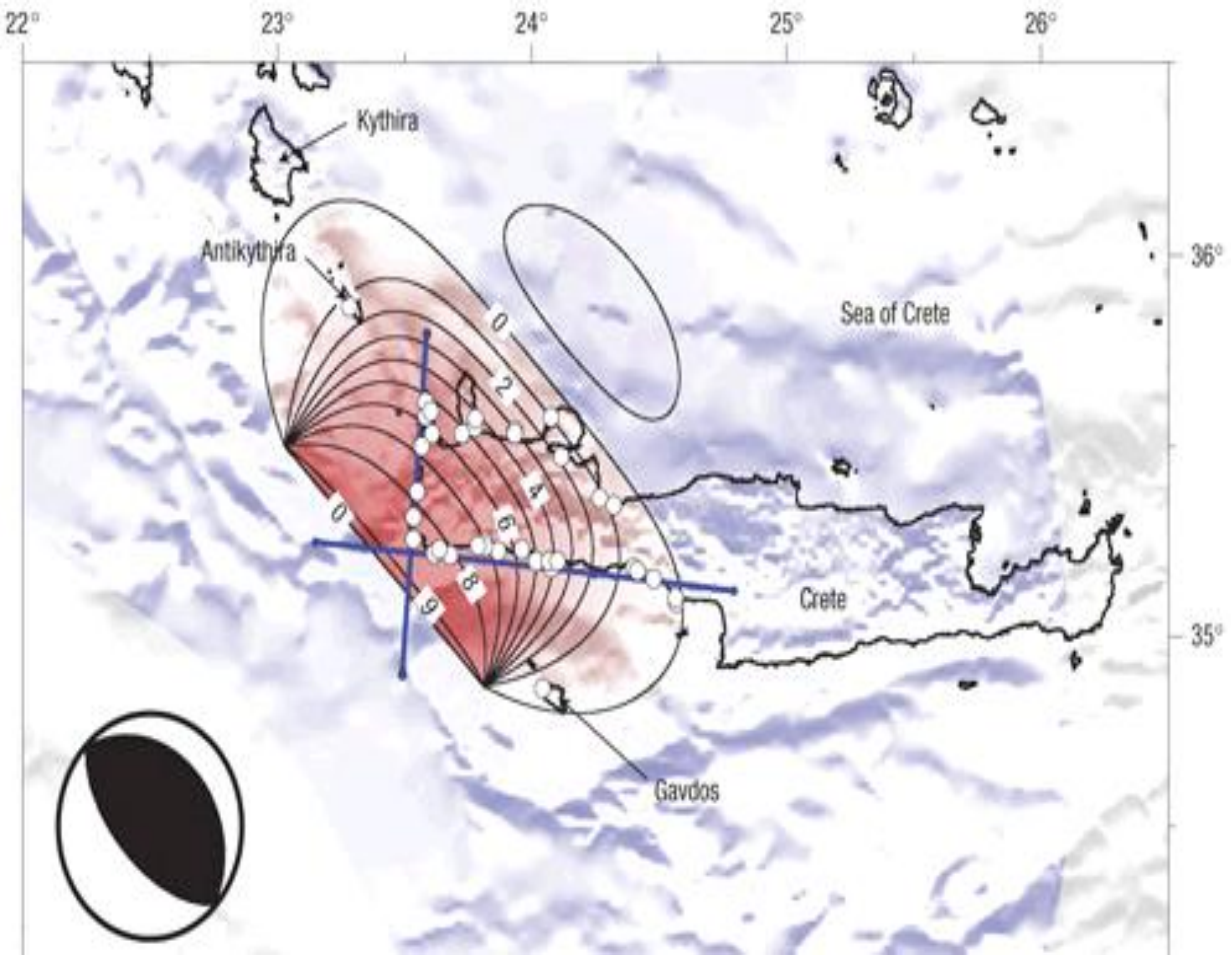

Fig. 2.1: Contours of the calculated uplift sites (white circles) along western Crete coastline during the AD 365 earthquake (modified by Shaw et al., 2008).

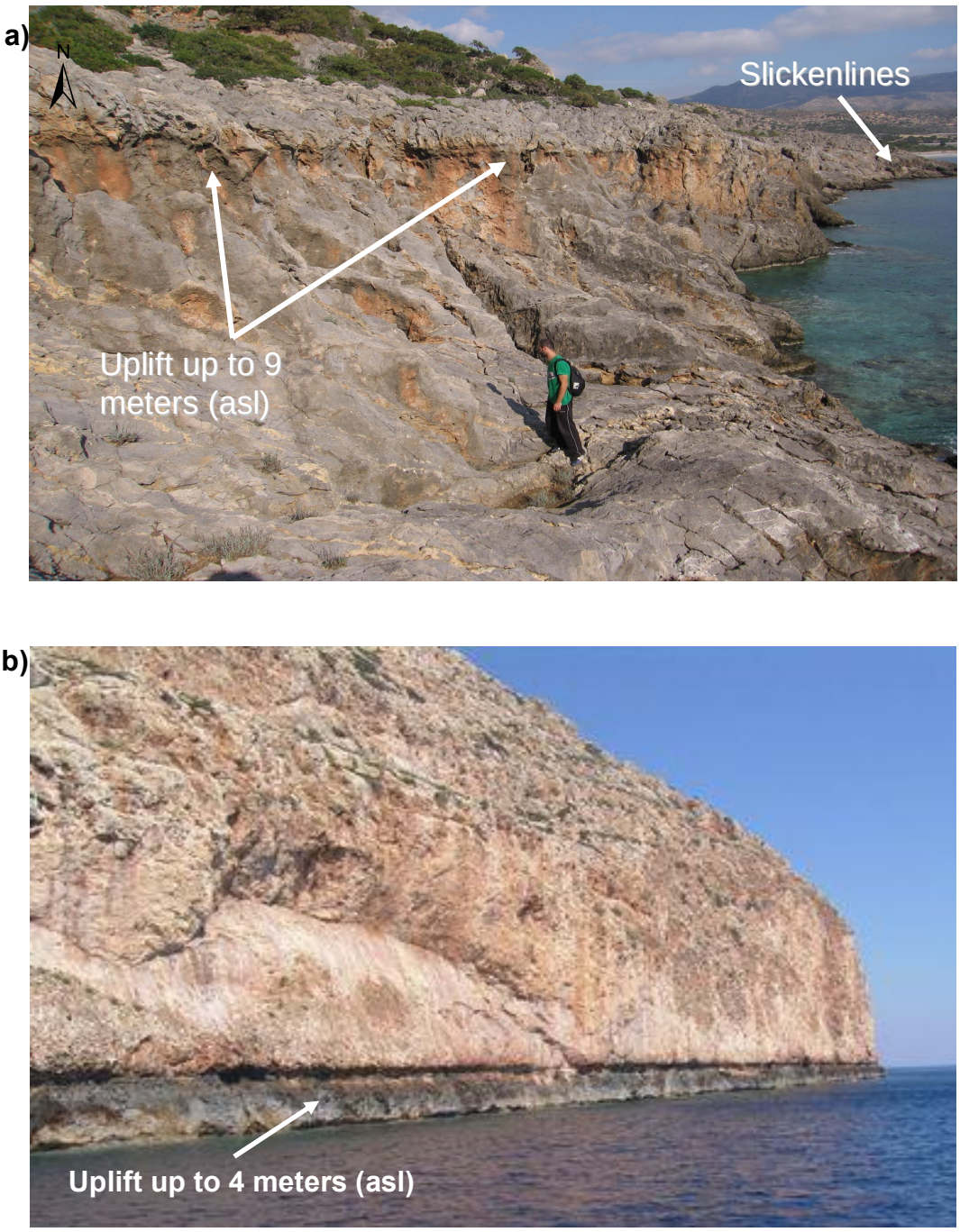

Fig. 2.2: a) Linear feature in Cape Krios, southwestern Crete, with N-S strike, along which the uplifted marine wave-cut bench up to 9 meters can be observed, associated with the 365 AD earthquake. Slickenlines reveal the fault's recent tectonic movement and; **b)** Uplift shoreline in Gramvousa peninsula, northwestern Crete, with uplift up to 4 meters being observed.

2.2.1 Evolution of the Aegean region and island of Crete

During the Tertiary period, convergence of the African and Eurasian plates occurred, with the closure of the Tethyan seaway and the formation of the Alpine chain (Le Pichon & Angelier, 1979; Krahl et.al, 1983; Jackson et al., 1994; Le Pichon et al., 1995). As a result, the E-W Mediterranean Sea basin was formed. The African plate is characterized by an anti-clockwise rotation with respect to the Eurasian plate together with movement in a northerly direction, at a rate of 6 mm/yr (McClusky et.al, 2000). McKenzie (1972) was the first to conclude that the eastern Mediterranean region could be divided into smaller plates, thereby affecting the geodynamic behaviour of the region.

There are three small plates, the Arabian, the Anatolian and the Aegean (Fig. 2.3 a) (Kahle et al, 1998). The movement of all these plates in different directions has resulted in the complicated neotectonic deformation of the region. The Arabian plate moves north-northwest, at a rate of about 18mm/yr, relative to the Eurasian plate, with its eastern part moving faster (Fig. 2.3 a) (Le Pichon & Angelier, 1979; Papazachos & Kirtazi 1996; Kahle et al., 1998; McClusky et.al, 2000). The compression between the Arabian and Eurasian plates was part of the northward movement of the African plate (Molnar & Tapponier, 1975). The Anatolian plate is bounded by the north and east Anatolian faults which define its movement towards the W and SW and results in the rapid movement of the Aegean region towards the SW. The Anatolian microplate is rotating anti-clockwise, relative to Eurasian, with a slip velocity of 24 mm/yr on the North Anatolian Fault (Fig. 2.3 a) (McClusky et al., 2000). The Aegean region has been rotated counter-clockwise as a coherent microplate (Fig. 2.3 a) (Le Pichon & Angelier, 1979, 1981), relative to Eurasia with a higher velocity (~30mm/yr) than the slip velocity of the Anatolian plate (Kahle et al., 1998). Fracturing and brecciation occur in the neotectonic fault zones of Aegean region (Stewart & Hancock, 1994).

The island of Crete is located near the edge of the Hellenic trench (Fig. 2.3b) and as a result is highly affected and deformed by complex movements of the plates. It lies in the Cretan basin with boundaries being determined by the

volcanic arc (Santorini, Nisyros) and the outer forearc of the Hellenic trench. The south boundary of this basin (where the outer forearc of the Hellenic subduction zone is located) is characterised by high uplift. This uplift of Crete is thought to be a result of compressive tectonic movements in that region, resulting in nappe stacking with regard to the rest of the Aegean and under-plating of subducted sediments beneath the island (Angelier & Le Pichon, 1980; Angelier et al., 1982; Barton et al., 1983; Kopp & Richter, 1983; Fortuin & Peters, 1984; Meulenkamp et al., 1988; Taymaz, 1990; Postma et al., 1993 ; Jost, 2002). Generally, this region has evolved under the influence of extensional activity that took place all over the Aegean region (Fig. 2.3 b) (Le Pichon & Angelier, 1979, 1981; Angelier et al., 1982). The rapid seismogenic uplift of the tectonic structures, exposed along the Cretan coastline, in comparison with the extensional forces taking place, could be related to lithospheric processes associated with rollback of the subducting slab (Dewey, 1980; Royden, 1993; Peterek, 2004; Husson, 2006; Wegmann, 2008). The formation of the south-facing Hellenic accretionary wedge, due to plate convergence, could lead to crustal extension with deep under-plating along the subduction zone (Angelier et al., 1982; Platt, 1986). This is also thought to have led to uplift and exhumation of young (~20 Ma) high pressure metamorphic rocks on Crete (Fassoulas et al., 1994; Jolivet et al., 1996; Thomson et al., 1998; 1999; Rahl, 2004; Chatzaras et al., 2006). Crete is characterised by a tilting movement to the NE, indicating uplift in the west and subsidence in the east (Fytrolakis, 1980), although neotectonic studies assume that separate tectonic blocks react independently to provide differential rates of uplift or subsidence in the whole island (Papanikolaou, 1988; Fassoulas, 2005). Studies of crustal thickness and extension of the area indicate the southwards movement of Crete, resulting in its detachment from the rest of the Cyclades islands (McKenzie, 1978; Le Pichon & Angelier, 1979; Angelier et al., 1982).

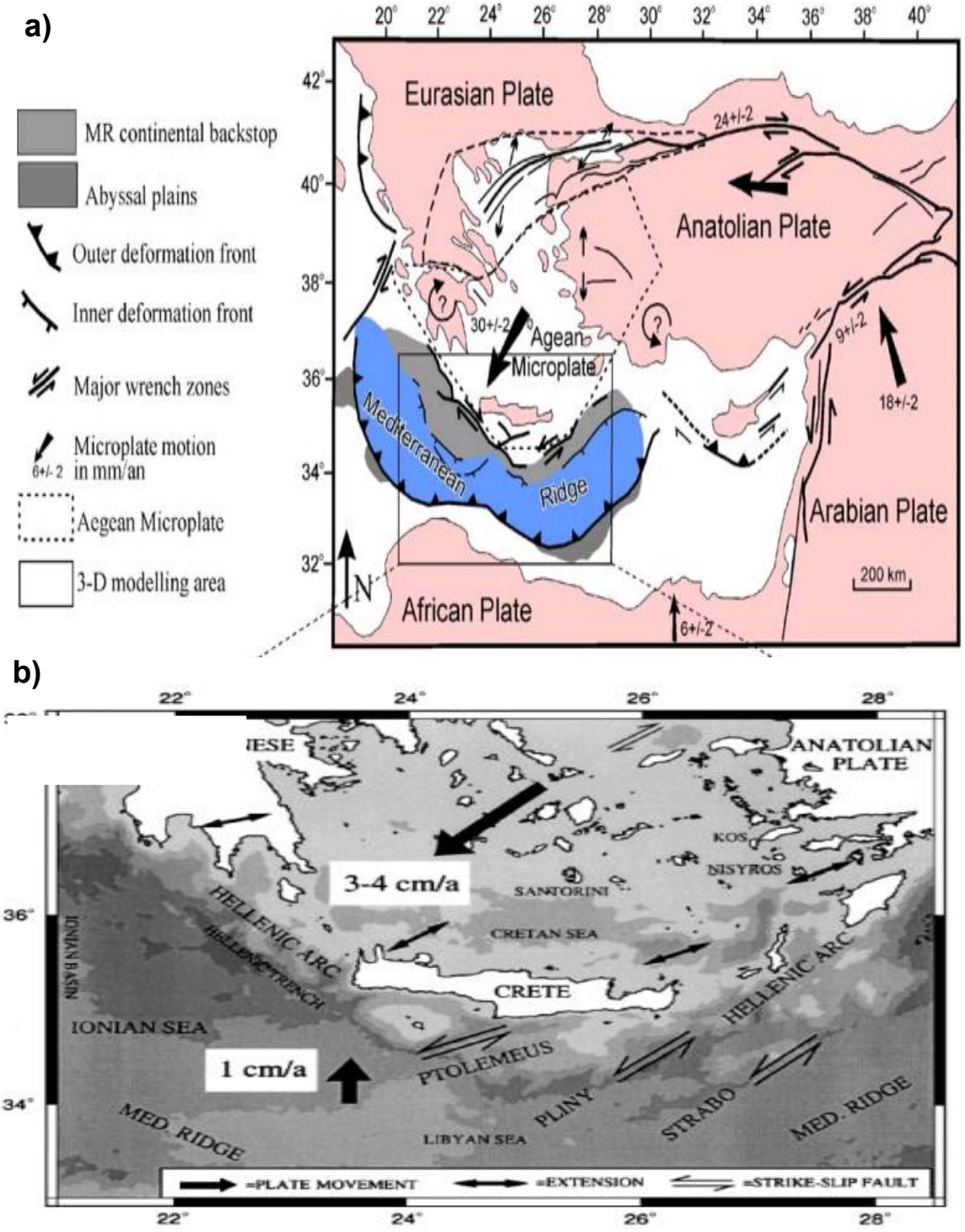

Fig. 2.3: The major tectonic regime characteristics of: **a)** the eastern Medditereanean region (modified from Papazachos and Papazachou, 1997 in Karagianni et. al, 2005) and; **b)** Aegean region (modified from Bohnhoff et al., 2001).

2.2.2 Evolution of western Crete

As described earlier, the island of Crete lies at the convergence of two different plates (Eurasian and African): one of the most active tectonic and seismic regions of Europe, due to the subduction of the African plate beneath the Aegean area. The subduction interface is located beneath the south coast of Crete at a depth of about 35 to 40 km (Gudmundsson & Sambridge, 1998; Snopek et al., 2007; Wegmann, 2008). The geological and tectonic setting of the island was initially investigated in the early 1950s (Papastamatiou & Reichel, 1956; Papastamatiou et al., 1959 a,b). These studies indicated the presence of two major nappes, the Pindos nappe overlying the Tripolis nappe unit. These units belong to the external Hellenides and were deformed after the deposition of flysch formations in the Late Eocene-Oligocene (Renz, 1955; Aubouin et al., 1963, 1976). Further work in the 1970s established a better tectonostratigraphic framework for Crete by indicating the presence of several nappes, either below the Tripolis unit or above the Pindos nappe (Papanikolaou & Vassilakis, 2009).

There are significant differences in the geology between western and eastern regions of Crete. This research is focused on the western region, which lies closer to the outer-forearc of the Hellenic subduction zone. The geological setting of western Crete is characterized: i) by a number of nappes that are part of the Alpine and pre-Alpine rocks (Fig. 2.4, 2.5) (Fassoulas, 1994) and; ii) the presence of Neogene and Quaternary deposits which comprise the post-Alpine rocks (Fig. 2.4) (Fytrolakis 1980; Bonneau 1984; Sarris, 2005).

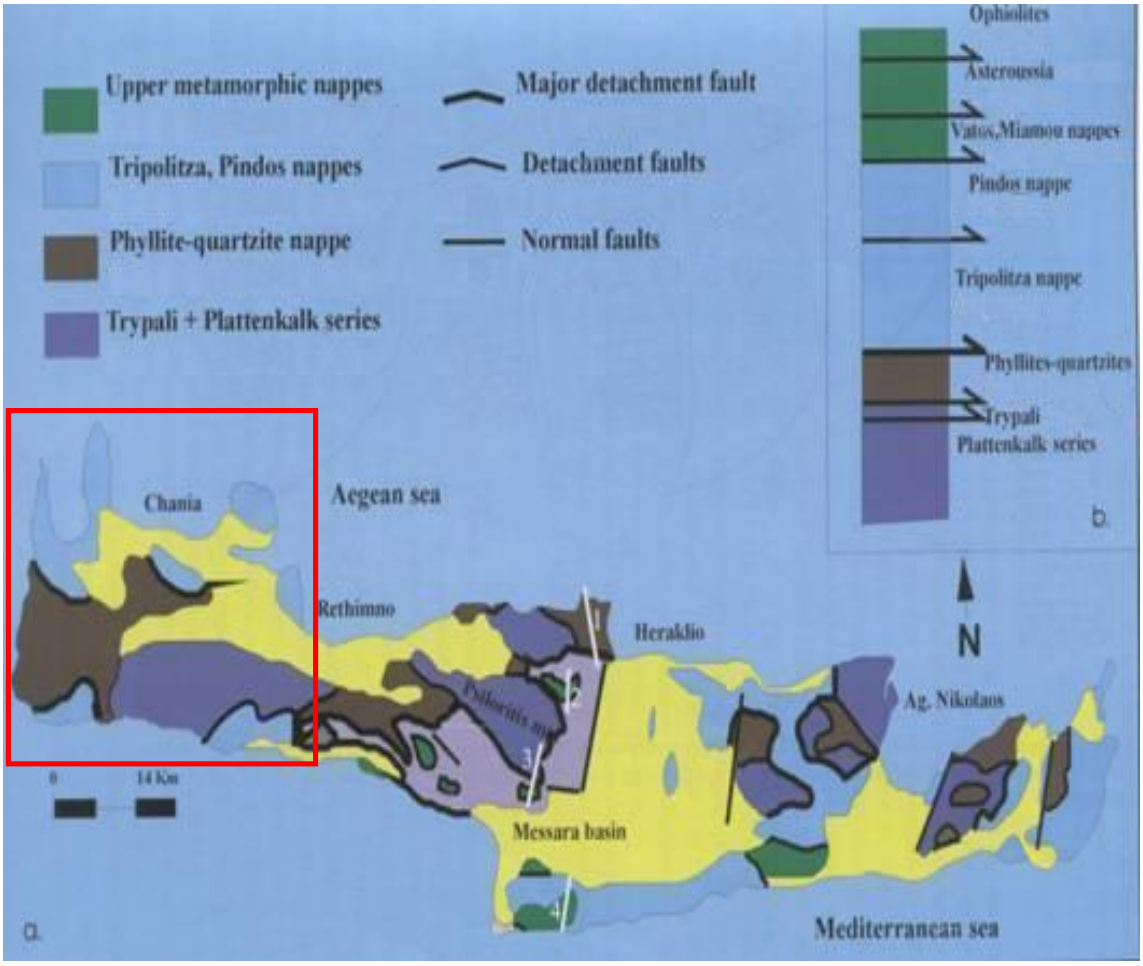

Fig. 2.4: The distribution of the major nappes across Crete (modified from Fassoulas, 1994). Red box indicates the study region.

The nappes can be divided into two groups: the lower nappes and the upper nappes (Table 2.1). Lower nappes are composed of i) Plattenkalk, ii) Tripali and iii) Phyllite- Quartzite nappes. These nappes are separated by thrust faults and characterized by high pressure-low temperature (HP-LT) blueschist facies metamorphism. A major thrust fault divides lower nappes from the upper nappes. Upper nappes are comprised of: i) Tripolis, ii) Pindos and iii) Uppermost nappes, being divided by thrust faults.

<table>
<tr><td rowspan="2">Post Alpine Rocks</td><td colspan="3">Quaternary</td><td rowspan="2">Alluvial and marine deposits
Marls, clays, conglomerates, limestones</td></tr>
<tr><td colspan="3">Neogene</td></tr>
<tr><td rowspan="10">Alpine and Pre-Alpine Rocks</td><td rowspan="5">Upper nappes</td><td>LP-HT metamorphosed</td><td>Uppermost nappes</td><td>Schists, oceanic pillow basalts</td></tr>
<tr><td colspan="3">Thrust fault</td></tr>
<tr><td>unmetamorphosed</td><td>Pindos nappe</td><td>Limestones, shales and calc-breccias</td></tr>
<tr><td colspan="3">Thrust fault</td></tr>
<tr><td>LP-LT metamorphosed</td><td>Tripoli nappe</td><td>Carbonates, dolomites and flysch</td></tr>
<tr><td colspan="4">Major thrust fault</td></tr>
<tr><td rowspan="5">Lower nappes</td><td rowspan="5">HP-LT metamorphosed</td><td>Phyllite-Quartzite nappe</td><td>Phyllites and quartzites</td></tr>
<tr><td colspan="2">Thrust fault</td></tr>
<tr><td>Tripali nappe</td><td>Limestones, mudstones, recrystallized conglomerates</td></tr>
<tr><td colspan="2">Thrust fault</td></tr>
<tr><td>Plattenkalk nappe</td><td>Dolomites, dolomitic limestones,</td></tr>
</table>

Table 2.1: The discrimination of the nappe pile formation of Crete (modified from Chatzaras, 2006).

The detailed tectono-stratigraphy and composition of Alpine and pre-Alpine rocks present in the region follows (Fig. 2.5, 2.7 and Table 2.2):

The *Plattenkalk* nappe is the oldest exposed nappe. It mainly consists of carbonate breccia with Permian schists and clastic sediments (conglomerate, phyllites, quartzites) in the lower level covered by stromatolitic dolomites, cherts and limestones (Epting et al., 1972; Seidel et al., 1982; Hall and Audley-Charles, 1983; Krahl et al., 1988; Rahl, 2004).

In western Crete, limestones, mudstones, recrystallized conglomerates, detrital carbonates and dolomites of Triassic to Lower Jurassic age constitute the *Tripali* formation, which overlies the Plattenkalk nappe (Creutzburg and Seidel, 1975; Fytrolakis, 1980). This sequence formed during the upper Triassic or lower Jurassic (Karakitsios, 1987). Subaerial karst weathering during the late Quaternary is probably responsible for the recent formation of the carbonate breccias and karst of the Trypali (Pomoni-Papaioannou and Karakitsios, 2002). The Trypali has highly brecciated horizons, resulting from solution-collapse, forming after the removal of evaporite beds, (Pomoni-Papaioannou and Karakitsios, 2002), or formed as fault scarp breccias. The fault scarp breccias were formed either from the Plattenkalk carbonate platform collapse during the Early Jurassic (Hall et al., 1984; Rahl, 2004) or just before subduction of the Plattenkalk rocks in the Eocene to Oligocene from bending of the foreland (Thomson et al., 1999; Rahl, 2004).

The *Phyllite-Quartzite* nappe, consisting of relatively hard metamorphic rocks, forms the next highest nappe and extends over much of Crete. It consists of dolomitic limestones, gypsum, volcanic rocks, dolomites, argillaceous schists covered by quartzites, phyllites and thin foliated marble (Krahl et al., 1983; Katsikatsos, 1992). A similar Phyllite-Quartzite nappe is also found in southern Peloponnesus (Katsikatsos, 1992; Theye and Seidel, 1991; Rahl, 2004).

The next nappe in the sequence is the *Tripolis* (or Gavrovo) nappe. It consists of Middleï Upper Triassic dolomites, dolomitic limestones and carbonates, with the carbonates deposited between the Late Triassic and the middle Eocene. Flysch sediments are also exposed, from the overriding Eurasian

plate, deposited between the Upper Eocene and Middle Oligocene (Katsikatsos, 1992; Rahl, 2004).

Next in the sequence is the thrust contact between the Tripolitsa nappe and the overlying *Pindos* nappe. Deep water sediments are a characteristic feature of this sequence, with limestones, calciturbidites and calc-breccias comprising the nappe formations during the late Triassic. Paleocene to Eocene turbidite sandstones and shales also cover this sequence, which is similar to the Plattenkalk and Tripolitsa nappes (Rahl, 2004).

The rocks appearing in the *uppermost* nappe are pre-Jurassic (Seidel et al., 1976; Rahl, 2004). This nappe consists of oceanic pillow basalts, amphibolites, gabbros, schists, deep water sediments and an ophiolitic cap of mainly serpentinite (Seidel et al., 1976; Thomson et al., 1998; Rahl, 2004). Its subunits are considered as individual mappable thrusted nappes (Creutzburg and Seidel, 1975; Bonneau, 1984; Rahl, 2004), with others supposing that an olistostrome in the upper part of the Pindos units formed massive blocks in a ñBlocky Flyschò(Hall et al., 1984; Rahl, 2004).

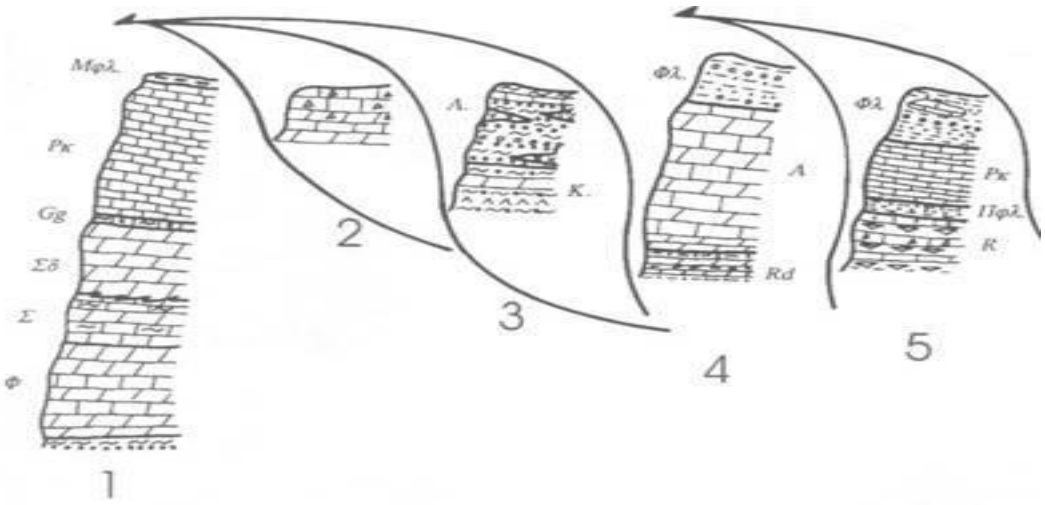

Fig. 2.5: Schematic representation of the sequence of thrusted nappe stacking in western Crete (modified from Fassoulas, 1994). The nappe pattern and their overlying internal units (e.g. limestone, sandstone, clays) are represented as: 1) Plattenkalk carbonate platform; 2) Tripali nappe; 3) Phyllite-quartzite nappe; 4) Tripoli nappe and; 5) Pindos nappe.

The post-Alpine sedimentary basins, with Quaternary and Neogene deposits, were created by normal faulting in the nappe pile since the Middle Miocene and are exposed mainly in the north of western Crete (Meulenkamp et al., 1979; Fytrolakis, 1980; Angelier et al., 1982; ten Veen and Postma, 1999; Papanikolaou & Vassilakis, 2009). Quaternary formations are characterized by alluvial fan deposits, while marine terraces exposed along the coastline are composed of conglomerates, marls and gravels. Beach rock consisting of cemented gravels and conglomerates is also found along the coastline. Neogene formations are composed of Pliocene and Miocene deposits, with the presence of marls, limestones and conglomerates (IGME, 1971).

2.3 Tectonics of Crete

The tectonic framework of Crete is extremely complex. This has ensured that widely diverging points of view exist in the literature. The most dominant of these views are discussed briefly below.

One opinion suggests that during the Lower Miocene the contact of high pressure rocks with overlying thrusts was an extensional detachment with a shallow dip. This was completed in three extensional periods providing EW, NS, NE-SW and NW-SE normal strike faults (Fig. 2.6) (Kilias et al., 1994; Fassoulas et al., 1994; Jolivet et al., 1996; Fassoulas, 2000; Ring & Reischmann, 2002). On the other hand, it is suggested that the exhumation of high pressure rocks results from a series of compressional phases. Identification of two compression phases is a result of initially: i) low angle thrusting leading to the nappe stacking and; ii) thrust related folding and the formation of a Middle Miocene basin. A third extensional phase, which characterizes the ongoing subduction zone, is a result of high-angle normal faulting, generating WNW-ESE and NNE-NNW strike faults (Xypolias & Doutsos, 2000; Chatzaras, 2006).

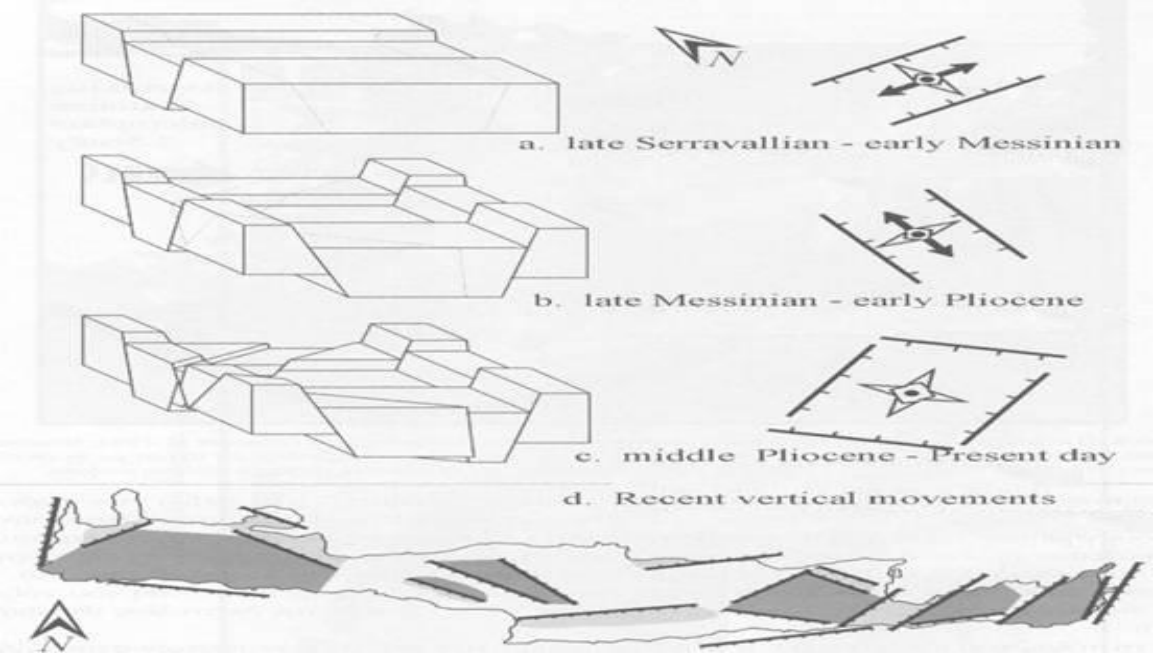

Fig. 2.6: Geotectonic evolution of Crete with the blocks diagram indicating the three extensional periods (modified from Fassoulas, 1994).

2.3.1 Western Crete tectonics

One reason why Crete is of particular interest is that the Hellenic arc borders the whole island length, and the upper plate displays differential tectonic behavior. This emergent outer-forearc is affected by NW-SE extension as indicated in western Crete, E-W extension in central and SW-NE extension in eastern Crete (Hatzfeld et al., 1993; Papazachos, 1996) (see Fig. 2.6).

This research focuses on western Crete. This region coincides with the rupture of the 365 AD earthquake which is the largest known earthquake in the eastern Mediterranean, creating the largest tsunami to be recorded in this region (Guidoboni et.al, 1994).

High angle normal faults and low angle extensional faults are exposed at the surface in the study region (Fassoulas et al., 1994; Bohnhoff et al., 2005). A series of active normal faults with an E-W to NW-SE and SW-NE strike, formed during the Pliocene and Quaternary period, dominate the neotectonic structure of western Crete (Angelier et al., 1982; Hatzfeld et.al, 1993; Fassoulas, 2001; Jost et al., 2002; Wegmann, 2008). The most recent faults (NW-SE, SW-NE) were

developed on a diagonal axis relative to the older fault structures (N-S, E-W). In general, the majority of the faults follow an E-W strike with N-S faults being less observed (Angelier et al., 1982). Most of the faults observed in western Crete are E-W extensional faults that cut Miocene sediments and basement rocks. There are also several larger-scale N-S striking faults, which cross-cut the E-W faults. Transtentional faults with major NE-SW extension and lesser NW-SE extension are the most recent faults (Le Pichon and Angelier, 1979; Ten Veen and Meijer, 1998; Ten Veen and Postma, 1999; Fassoulas, 2001). In western Crete, recent micro-earthquakes have fault plane solutions with near horizontal T-axes with an E-W orientation in the upper crust. P-axes obtained suggested varied horizontal and near vertical fault planes, indicating strike-slip and normal faulting (Jost et al., 2002).

2.3.2 Drainage basin tectonics

In chapter 1 it was reported that neotectonic activity can be reflected in the drainage patterns and as a consequence in the formation of the drainage basins in a region (i.e. Hack, 1957; Schumm, 1986; Humphrey & Konrad, 2000). Tectonic control affects drainage basin shape and the variety of geological structures observed. Investigation of drainage basin morphologies can reveal important information about the tectonic regime influencing the region. There are only a few studies existing in the literature regarding the investigation of drainage basins in western Crete that can be associated with factors influencing the landscape development (i.e. Kouli et al., 2007; Kouli et. al., 2008). One of these studies reveals that geomorphological and lithological factors are the dominant influence on the drainage network of Tauronitis and Keritis drainage basins within the study region of this research (Kouli et al., 2007).

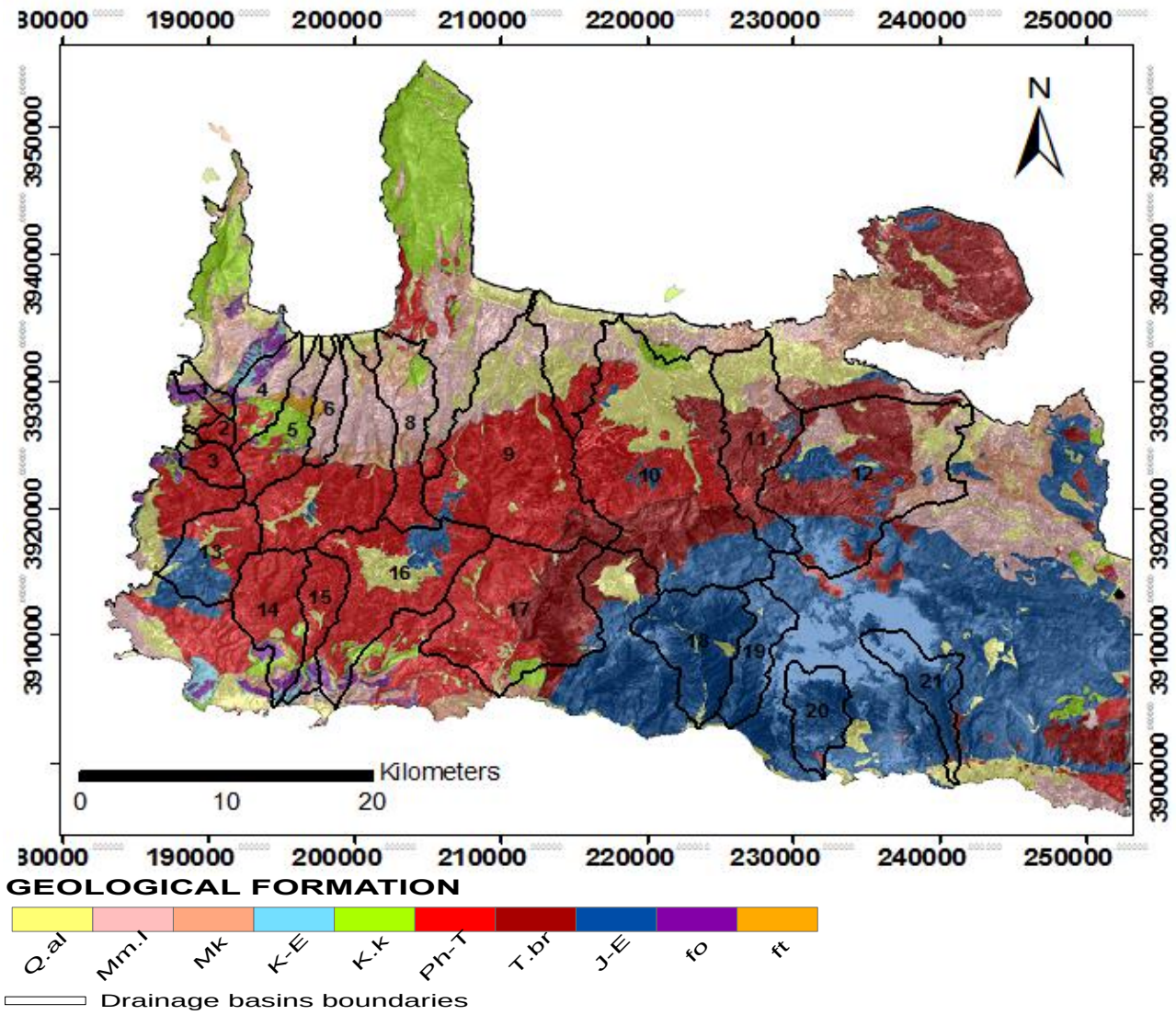

1. Metoxi Platanos
2. Balsamakia
3. Mesa Rema
4. Magagistra
5. Kastelli
6. Milias
7. Tiflos
8. Arapi
9. Tauronitis
10. Keritis
11. Therisiano Gorge
12. Kalami
13. Xsiropotamos
14. Pelekaniotis
15. Sarakiniotis
16. Kakodikianos
17. Agia Eirini
18. Samaria Gorge
19. Potamos
20. Aradaina Gorge
21. Sfakiano Gorge

Fig. 2.7: Digitized geological map of the study area (IGME, 1971) and the drainage basins boundaries.

Symbol	Geological formation	Rock Type	Rock strength
Q.al	Quaternary	Sedimentary rocks (alluvial deposits)	Weak
Mm.l	Neogene	Sedimentary rocks	Weak
Mk	Neogene		Weak
K-E	Carbonate Pindos zone tectonic nappe	A class of sedimentary rocks composed primarily of carbonate minerals	Extremely strong
K.k	Carbonate Tripolis zone tectonic nappe		Extremely strong
Ph-T	Phyllite-Quartzite series	Hard metamorphic rocks	Medium strong
T.br	Carbonate Tripali zone tectonic nappe	A class of sedimentary rocks composed primarily of carbonate minerals	Extremely strong
J-E	Plattenkalk nappe		Medium strong
fo	Flysch Pindos zone tectonic nappe	A sequence of sedimentary rocks that is deposited in a deep marine facies in the foreland basin of a developing orogen.	Weak
ft	Flysch Tripolis zone tectonic nappe		Weak

Table 2.2: Geological formation of the study area (IGME, 1971).

2.4 Tectonic factors in comparison to other interrelated factors

- **Tectonics factors vs Lithological/structural factors**

Lithological controls are a significant factor in the landscape evolution of an examined region. This research takes into account the lithological/structural influence, even where the dominant strong tectonic signal occurs within the study area. As described in subsequent chapters, this thesis evaluates in its main context the drainage patterns with regard to their reflection of neotectonic activity. Drainage patterns are influenced by factors such as climate but lithological and geological structure is the most important of the non tectonic influences. Several types of drainage network characteristics (i.e. valley-floor longitudinal profile, channel width and depth, drainage basin elongation etc.) can be used as indicators for their association with active tectonics (Summerfield, 2001). This is

the main focus of this research and further details are to be presented in following Chapters 4, 5, 6, 7 & 8. As presented in those chapters, the majority of the lineaments, where local neotectonic activity was indicated, were located in homogeneous lithologies (i.e. the lineaments were not due to lithological boundaries). In some cases various geomorphic indices were applied to mountain fronts or eroded escarpments cutting across different lithologies. Presence of unconsolidated Cenozoic sediments crop out along these mountain fronts and yet the evidence of active tectonic deformation is still clearly recognizable, regardless of the lithologies (see Chapter 5 & 7). This indicates that the neotectonic activity is pervasive enough to dominate all rock types, both weak and strong, along the mountain fronts and eroded escarpments.

- **Tectonic factors vs Climatic factors**

The interrelationship of tectonic and erosional processes can be straightforwardly associated with climate. In this research this parameter is not believed to be playing a major role due to the nature of the selected study area, as described below (see section ñ*1.3 Case study area"*). So this research focuses mainly on the strongest signals of tectonic or erosional processes taking place. The reason for not taking into account the climate factor is that the presence of Late Pleistocene depositional and erosional marine terraces in western Crete (study area) can provide good geomorphic indicators to check whether climate changes, during glacial and interglacial periods, affected the landform development of the study region. Marine Isotope Stages (MIS) identify the alternating warm and cool periods that took place in the recent past. In many Mediterranean coastal regions the identification of the last interglacial sea level highstand, known as the Thyrrenian shoreline, took place around ~125 ka ago with regard to MIS. The presence of the warm-water index fossil *Strombus bubonius* characterizes that period (e.g. Ferranti et al, 2006). The absence of that fossil from the terraces of western and southwestern Crete makes clear that the period characterizing the last interglacial sea level highstand cannot be identified (Lambeck et al., 2004). The ages of western Crete marine terrace deposits have

instead an age range between 40 and 50 ka (Shaw et al., 2008; Wegmann, 2008). This indicates that the study region is undergoing rapid uplift and deformation, with Thyrrenian terraces being rapidly uplifted and destroyed by erosion, suggesting that tectonic activity is the major factor in landform development.

As described above, the neotectonic signal in the region of Crete is stronger than that from climate. This is indicated by uplifted marine terraces of late Pleistocene age around the south-west coast of western Crete (Lambeck et al., 2004; Wegmann, 2008). Other authors identify terraces with algal reef deposits at altitudes of between 22 and 24 m, with (^{14}C) ages of 40-50 ka (Ferranti et al., 2006; Shaw et al., 2008). These terraces indicate rapid tectonic uplift and they are consistent with the major coseismic uplift that accompanied the 365 AD earthquake, which involved up to 9 m of uplift (Fig. 2.1) (Thommeret et al., 1981; Pirazzoli et al., 1992; Kellletat, 1996; Stiros, 2001; Peterek, 2004; Pirazzoli 2005; Shaw et.al, 2008).

As far as the present day climate of Crete is concerned, it has a semi-arid seasonal climate with short humid winters (November-February) and long dry summers (March-October). The average annual precipitation is low, with a high percentage lost due to evapotranspiration (~65%): Chartzoulakis et al., 2001). The highest annual precipitation takes place in the mountainous Leuka Ori region, which consists of the permeable Plattenkalk limestone (see southeast region in Fig. 2.7). In contrast, impermeable Phyllite-quartzites form regions of low relief and have significantly lower annual precipitation. As a result, the landscape is in general subject to limited amounts of surface runoff, with correspondingly limited amounts of both slope/soil erosion and fluvial erosion. The low rainfall over most of western Crete also results in very limited chemical weathering and thin soils with sparse vegetation cover. The procedure that was applied to extract the drainage network, revealed that dense vegetation is mainly limited to the valley floors (see Chapter 3). Therefore, relative to neotectonic activity, climatic controls play only a minor role in the landscape evolution of the study areas.

- **Tectonics factors vs human factors**

Another factor to consider is the impact of agricultural activity on landscape evolution in the study area, with small-scale arable farming mainly in the large northern basins, and sheep and goat grazing in the southern basins. The relatively low intensity of land use and the general inaccessibility of the study area, indicates a relatively low impact on landscape evolution from agriculture, in comparison with neotectonic activity and the size of the landscape features that have been investigated in this research.

2.5 Summary

This chapter reviewed the geological and tectonic setting of the study area. The complex tectonic setting of this region, in the outer-forearc of the Hellenic subduction zone, determines the increased tectonic activity, making it an ideal study region for testing neotectonic deformation. Sequences of thrusted nappes make up the bedrock setting, while the current tectonic regime is governed by N-S and by E-W striking faults. The most recent significant seismic event in the present regime is the 365 AD earthquake (Mw 8.3-8.5), which produced coseismic uplift up to 9 meters in southwestern Crete. This region is one of the most seismically active worldwide and provides an appropriate test area to investigate neotectonic activity.

CHAPTER 3 DATA: SOURCES, ACQUISITION, QUALITY & PROCESSING

3.1 Introduction

3.2 Sources and acquisition

3.3 Pre-processing procedure of data sources

- **Registration of dataset maps**
- **Registration of satellite imagery**
- **Land-sea Mask for satellite images**
- **Contrast stretching**
- **Pan-sharpening of satellite images**
  - **i) Comparison of pan-sharpening methods**
  - **ii) Image fusion evaluation**
- **Filling of depression and hole sinks in DEMs and data fusion of SRTM and ASTER DEM data**

3.4 Accuracy and quality assessment of data sources for extraction of tectonic characteristics

i) Digital maps accuracy assessment

ii) Aerial photography accuracy assessment

iii) Satellite image data accuracy assessment

iv) SRTM DEM accuracy assessment

v) ASTER DEM accuracy assessment

vi) VLF method accuracy assessment

3.5 Summary of the expected final datasets

3.1 Introduction

As outlined in chapter 1, this thesis will be presenting a geoinformatic methodology for the characterization of neotectonic features in semi-arid regions (see Fig. 3.1). Brief description of the methodological framework stages will follow in order to make more meaningful the use of the fundamental data to be used in this research. Initially, zones of potential neotectonic activity will be investigated by drainage basin analysis (see Chapters 4 & 5). Drainage basin analysis will consist of various geomorphometric factors to be used for the evaluation of landscape development and specification of areas of tectonic activity. The extracted geomorphometric and tectonic information from drainage basin analysis will then be compared and validated by: i) scanned digitised geological maps; ii) lithological and lineament maps derived from multispectral satellite data and DEM; iii) ground truth surveys, including geological mapping; iv) VLF geophysical measurements of fault zones and; v) a GIS based multi-criteria decision analysis (MCDA) procedure. The reason of the comparison and validation is to offer a full perspective overview of the tectonic activity taking place in the study region by using an assemblage of both Earth observational data and ground truthing survey.

In brief, the methodology initially consists of drainage basin analysis to identify any regionally and locally tectonically active zones (see Chapters 4 & 5). As a later stage, acquisition of lithological information from satellite image processing and tectonic information from both drainage basin and lineament analysis of satellite imagery, will offer information for the characterization of neotectonic features. Further detailed information of the necessary methods to construct the appropriate satellite image data that will highlight tectonic and lithological features are presented in following chapter (see Chapter 6). As it will be presented in that subsequent chapter, image processing of multispectral satellite data discriminates the main lithological units and recognizes the lineaments of the study region. This acquired information in comparison with the drainage basin analysis is utilized to highlight tectonically active regions. The next section of the applied methodology in this research, as presented in a subsequent chapter (see Chapter 7), covers verification of tectonic structures by geological

fieldwork and VLF geophysical measurements. Lastly, selective outcome datasets from earlier chapters will provide the basis of a GIS-based multi-criteria decision analysis (MCDA) procedure.

The fundamental data requirements to be used for completion of the aforementioned stages are documented in this chapter. This chapter consists of three parts: i) the initial data sources; ii) the pre-processing procedures from those initial data sources and; iii) the quality assessment of these datasets. These stages aim to provide datasets to be used in the main body of the methodology to determine the research project aims and objectives. A brief description of the expected final datasets is included at the end of this chapter.

3.2 Sources and acquisition

The initial datasets to be acquired for this study were the digital scanned maps (600dpi): topographical, geological and hydrological. These datasets were acquired by the Hellenic Military Geographical Service, the Institute of Geology and Mineral Exploration and the Ministry of Agriculture respectively and were imported into ArcGIS to create the necessary vector data. These digital scanned maps were useful for the digitization of the major drainage network, lithologies, faults and drainage basin boundaries as vector data. The georeferencing of these aforementioned digital maps in the Greek Geodetic Reference System (GGRS'87), was based on triangulation points information acquired by the Hellenic Military Geographical Service, that were imported into ArcGIS environment and used as ground control points (GCPs). Acquisition of aerial photos in digital format, with 1m spatial resolution, by the Hellenic Military Geographical Service (georeferenced in the GGRS87 based on the triangulation points), were imported into ArcGIS and used as reference maps for:

i) improving positional accuracy of the drainage network and updating the drainage network map with stream segments not recorded on published maps;

ii) ground truth surveys;

iii) calculation of geomorphic indices;

iv) justification of extracted results with aerial photos as reference map.

Satellite imagery datasets of Landsat ETM+ (30m spatial resolution) with acquisition date 30/06/2000 and ASTER (15m spatial resolution) with acquisition date (06/04/2002) were imported into ArcGIS environment and used for: i) updating the drainage network map with stream segments not recorded on published maps and; ii) updating the lithology discrimination and lineament mapping with regard to published geological maps. The processing procedure is described further in the methodology in Chapter 6.

Throughout the study there is a usage of one DEM provided after the pre-processing and data fusion of both SRTM and ASTER DEM as it will be described below. The digital elevation models of SRTM (acquisition date, 2000), with 90m spatial resolution and ASTER (acquisition date, 2002), with 30m spatial resolution, were imported into ArcGIS in order to help with the calculation and extraction of the geomorphic indices, as well as the lineament mapping.

Geophysical measurements were accomplished in order to justify fault presence with regard to the lineaments identified by the lineament mapping analysis of satellite imagery and faults recorded by the geological map (IGME, 1971). The geophysical measurements were taken during June-July of 2008. The Very Low Frequency (VLF) equipment to be used was a portable geophysical tool developed by the ABEM-WADI company and the VLF signal could be acquired from the antenna transmitters across Europe. The dataset sources of this study are summarised in Table 3.1.

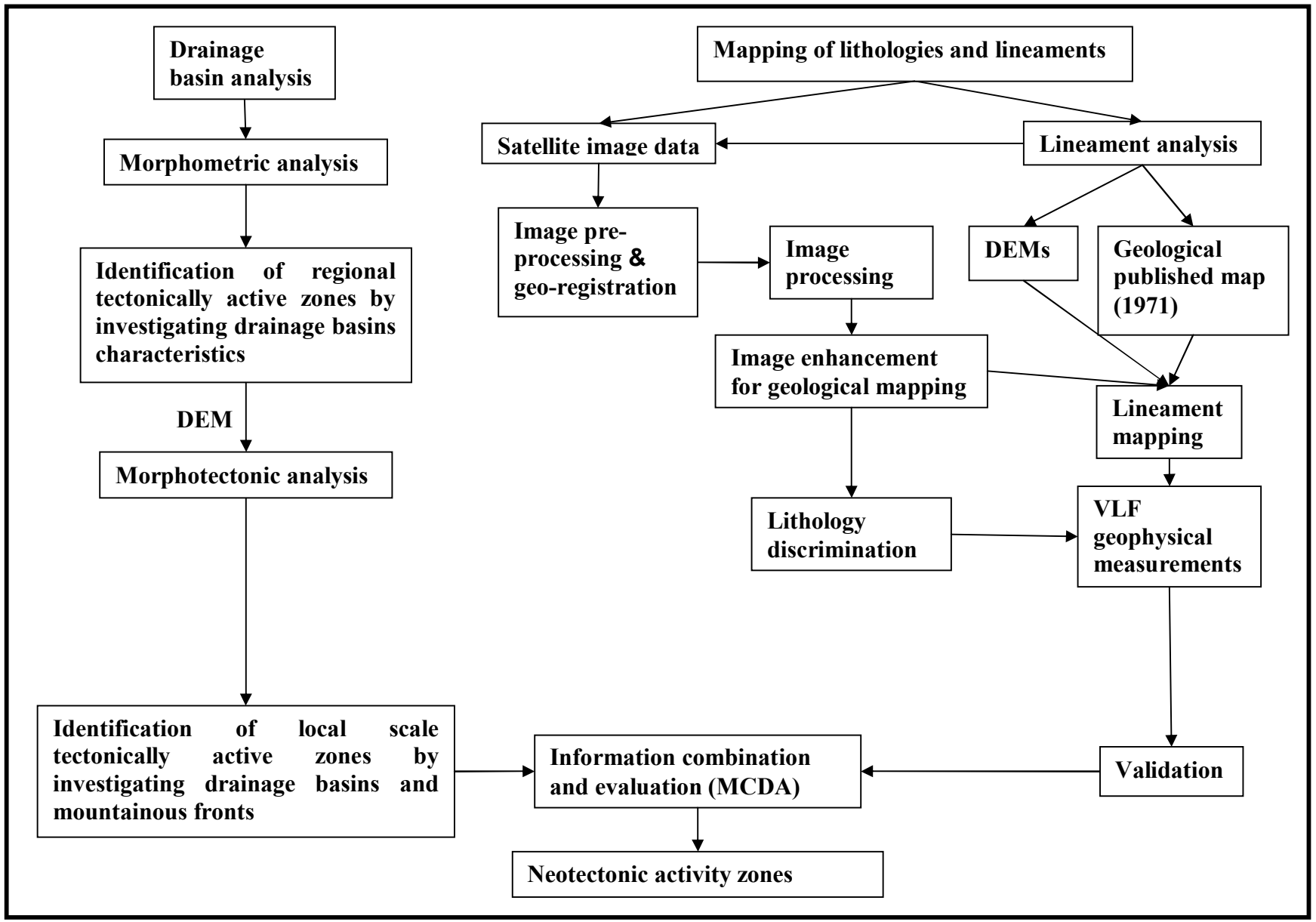

3.4

Fig. 3.1: The flow diagram of the methodology to be applied.

Datasets	Source	Application	Data resolution
Topographical maps (1:50000)	Hellenic Military Geographical Service (1994)	- Digitizing: stream network and 20 m contour intervals - Usage of contours to improve positional accuracy of drainage basins boundaries	Scanned at 600dpi. Nomimal pixel size is 6 meters
Geological map (1:50000)	Institute of Geology and Mineral Exploration (1971)	Use of a digitized geological map, digitization of the recorded faults and soft/hard rocks.	Scanned at 600dpi. Nomimal pixel size is 6 meters
Hydrological maps (1:50000)	Ministry of Agriculture (2002)	Delineation and digitizing of drainage basins	Scanned at 600dpi. Nomimal pixel size is 6 meters
Triangulation points	Hellenic Military Geographical Service (HMGS) (1987)	Georeferencing of all the images of the study area to the Greek geodetic system (GGRS'87)	T2 wild theodolite Error of few millimeters (mm).
Aerial photos (1:15000)	Aerial photos (1960)	- Usage of aerial photos as reference map: i) to improve positional accuracy of drainage network, ii) to establish ground truth surveys; - Updating the drainage network map with stream segments not recorded on published maps; - Calculation of geomorphometric indices - Justification of results with aerial photos as reference map	Aerial photos spatial resolution is 1m.
Landsat ETM+, ASTER	Landsat acquisition date (30/06/2000), ASTER acquisition date (06/04/2002)	- Updating the drainage network map with stream segments not recorded on published maps; - Lithology discrimination; - Lineament mapping	Landsat ETM+ spatial resolution is 30m, ASTER spatial resolution is 15m
SRTM DEM, ASTER DEM	SRTM DEM acquisition date (2000)	- Extracting geomorphometric indices; - Lineament mapping	ASTER DEM spatial resolution is 30m, SRTM DEM spatial resolution is 90m

Table 3.1: Summary of datasets used in this study.

3.3 Pre-processing procedure of data sources

In the case of some datasets the need of basic pre-processing procedures was essential for the datasets to become usable further on by the methodological approaches of this study. The basic pre-processing stages that were applied were: i) registration of the scanned maps; ii) registration of the satellite images; iii) creation of masks for the satellite images; iv) contrast stretching of the satellite images; v) pan-sharpening of satellite images; vi) filling of depression and hole sinks of the SRTM and ASTER DEMs and; vii) data fusion of SRTM and ASTER DEMs in order to overcome the artefacts occurrence provided due to cloud coverage in ASTER DEM data.

- **Registration of dataset maps**

The digital format of the dataset maps needed to be georeferenced for their further utilization. The georeference was achieved by using the Greek Geodetic Survey triangulation points as Ground Control Points (GCPs). The RMSE produced after the geocorrection was 0,06 based on 30 GCPs.

- **Registration of satellite imagery**

Despite having the same coordinate system (GRSG87), a slight displacement was observed when ASTER and Landsat ETM+ images were overlain, even after the pan-sharpening of Landsat ETM+ to 15m spatial resolution (see below for pan-sharpening procedure). The geocorrection was based on 30 GCPs (pixel by pixel basis) where clearly depicted features (such as cross roads, buildings etc.) were observed in both images as reference points. The registered satellite images were co-registered with the geocorrected scanned dataset maps to further reduce the RMSE and improve registration accuracy (see section 3.4 below). The minimization of spectral information loss, due to disruption of pixels by co-registration, was obtained by the nearest neighbour resampling method (Wenbo, 2008).

- **Land-sea Mask for satellite images**

The initial satellite image scenes used in this study had a high percentage of sea coverage. As a result, the image histograms were influenced by the low reflectance of the sea surface. Land-sea masks were therefore used to isolate the sea from the land. On-screen digitising of the coastline was accomplished using near infra-red imagery (band 4 for Landsat ETM+ imagery and band 3N for ASTER imagery, discriminated more accurately the land and sea boundaries) (Fig. 3.2).

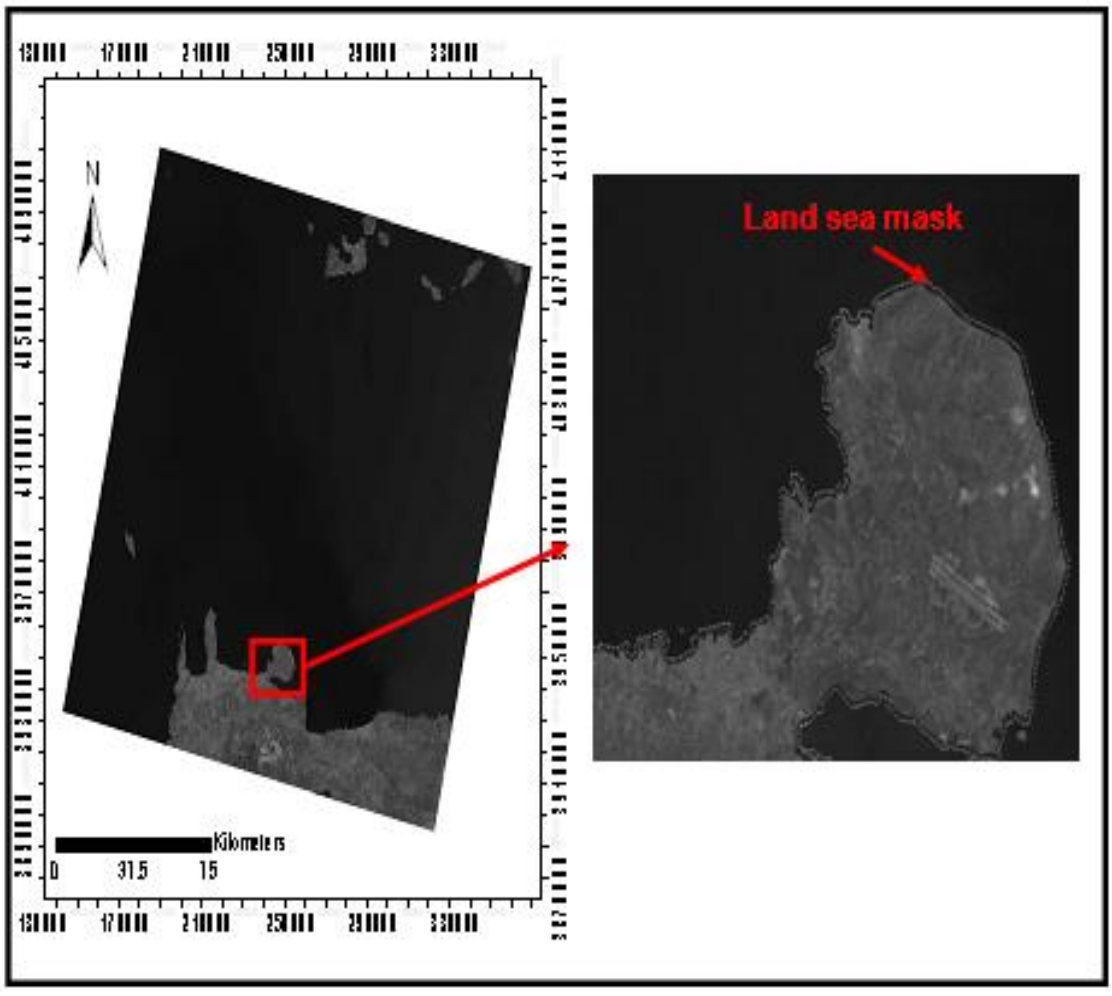

Fig. 3.2: The Landsat ETM+ scene (north part), reveals the large coverage from sea (left image). The land-sea mask was created to isolate the sea from the land, in band TM4 (right image, white dashed line).

- **Contrast stretching**

Linear contrast stretching was used to enhance the contrast of the images by adjusting the values of brightness in the 0-255 grey level range of satellite imagery bands. The initial DN values of each band (both Landsat ETM+ and ASTER) before and after the contrast stretching are presented in Table 3.2. The thermal bands of each sensor were not included due to the significantly larger spatial resolution of these bands. An example of an initial image before and after the stretching is given in figure 3.3.

Bands	***Landsat ETM+***	***Landsat ETM+ after contrast stretching***	***ASTER***	***ASTER after contrast stretching***
Band 1	33-196	44-150	55-175	55-150
Band 2	16-198	17-167	27-157	27-139
Band 3	24-209	24-183	22-143	52-130
Band 4	26-217	30-202	16-113	29-108
Band 5	39-229	83-195	19-89	24-87
Band 6	-	-	16-100	24-98
Band 7	36-220	56-204	17-90	21-90
Band 8	-	-	15-90	17-90
Band 9	-	-	14-88	16-82

Table 3.2: DN values of the Landsat ETM+ and ASTER images, before and after the contrast stretching.

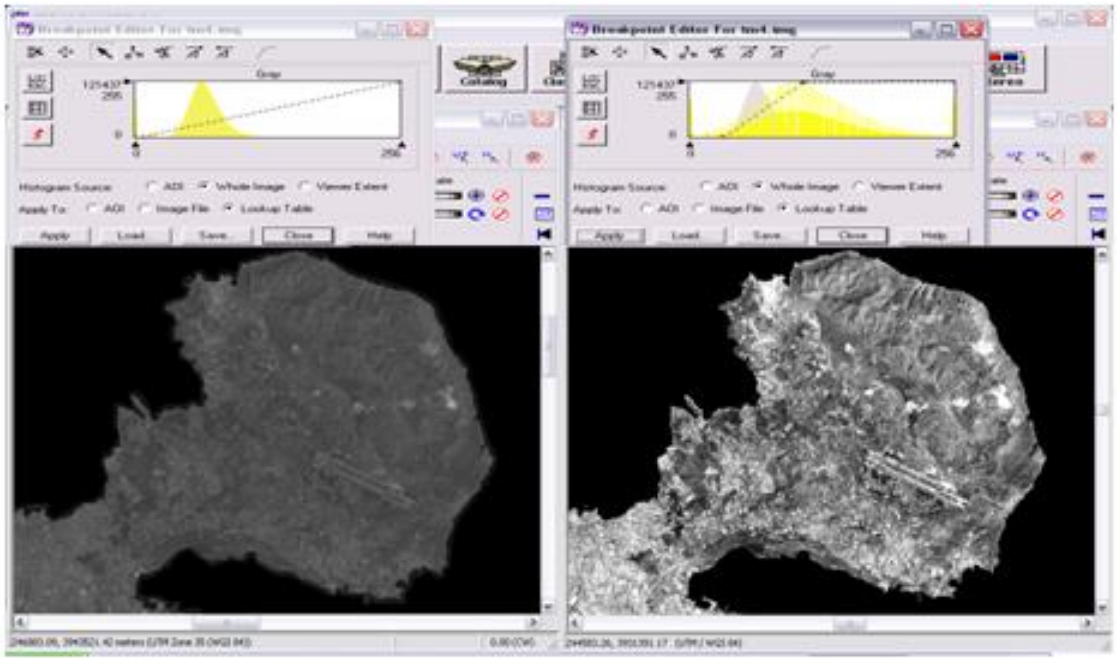

Fig. 3.3: On the left, sample area of original TM 4 band of the Landsat ETM+ after its subset with territorial mask and without any stretching. On the right, the image after the stretching to the full range of the 256 intensity levels of grey.

- **Pan-sharpening of satellite images**

The positional accuracy provided by the satellite images has a straightforward connection with their spatial resolution. Many remote sensing and mapping application studies need high spatial and high spectral information (Song et al., 2007). Fused images combine the characteristics of various data to offer increased interpretation capabilities and reliable results (Soulakelis et al., 2006). Better spatial resolution leads to improvement of the accuracy of the lineament identification and image quality (Ricchetti & Orabona, 1999). Pixel size is improved with the fusion of the images, providing more detailed discrimination of lineaments or feature boundaries (tonal contrast) as well as making spectral band arithmetic operations more effective. These are characteristics that will be evaluated in Chapter 6, so pan-sharpening is essential in this part of the study. In our study Landsat ETM+ images with 30m spatial resolution are converted to 15m spatial resolution using the panchromatic band of Landsat ETM+ for the pan-sharpening techniques.

i) Comparison of pan-sharpening methods

Pan-sharpening is an image fusion technique that is applied in multispectral images to increase their spatial resolution. The panchromatic band (TM8) of Landsat ETM+ is used to improve the spatial resolution of multispectral Landsat images from 30 m pixels to 15 m pixels. Various algorithms are used for pan-sharpening, notably:

i) *Multiplicative transform*, where multiplication of the panchromatic with the low resolution spectral bands emphasizes the intensity component and provides a fused image (Goforth, 1998).

ii) *Principal Component Analysis (PCA) transform*, where PCA substitutes the first principal component with the panchromatic band. The product is then transformed back to RGB space, in order to provide an image with high-spatial and spectral resolution (Shah, 2008; Wenbo, 2008).

iii) *High pass filtering fusion*, which emphasizes the high-frequency information of the panchromatic band and overlays it onto each band of the low resolution multispectral image (Goforth, 1998).

iv) *Intensity-Hue-Saturation (IHS) transform*, which is limited by the fact that only three bands can be used during pan-sharpening (Jensen, 2005). The intensity of the image is substituted by the panchromatic band of 15 m spatial resolution and the image is transformed back to an RGB (Tu et al., 2001; Kalpoma, 2007).

v) *Brovey transform*, which is based on the chromaticity transform (Gillespie et al., 1987). It is an appropriate pansharpening transform for change detection applications. However, it affects the spectral characteristics of the image scene (Jensen, 2005).

vi) *Wavelet transform*, which is similar to Fourier transform analysis. The difference is that instead of long continuous waves (Fourier analysis), the wavelet transform uses short, discrete wavelets (Erdas field guide, 2003). It is a more complicated algorithm where the multispectral bands can be: transformed into the PCA domain, or the panchromatic detail information added to the intensity information of the IHS transformed multispectral bands, or both multispectral and

panchromatic bands can be decomposed in the wavelet domain (Vijayaraj, 2004; Zhang, 2005).

Although some studies recognize that multiplicative and brovey transform are the weakest, among other pan-sharpening techniques, as low spectral fidelity is produced (Crippen, 1989; Goforth, 1998), these techniques are not excluded from the study. The reason is that a comparative analysis between various pan-sharpening techniques was carried out for this study. So the higher the sample range of pansharpening techniques to be used the more effective comparative analysis to be determined. Initially, the most effective pan-sharpening technique for each band was recognised and then used prior to creating RGB composite images (see Table 3.3 & 3.4). The interpretation and identification of features not previously seen might be revealed after the fusion of satellite imagery. Apart from providing a õgood lookingö image, a quantitative evaluation of the fused images was carried out in order to find which pan-sharpened bands had no loss of spectral information. For that purpose, consideration of all pan-sharpened techniques as a sample, provide a widely and reliable quantitative evaluation.

ii) Image fusion evaluation

The image fusion evaluation parameters are based on the evaluation of means, standard deviations and correlation coefficients. The selection of the pan-sharpened bands for further interpretation takes into account those quantitative parameters.

The central value of the pixel distribution in that band is defined by the calculation of the pixel mean value in a band (Vijayaraj, 2004). The changes occurring in the histogram (due to processing) are evaluated by the relative shift in the mean value (Parcharidis, 2000), which reveals the degree of spectral information kept by original multispectral image, defined as:

$$RSM = \frac{\text{Mean(output)} - \text{Mean (Original)}}{\text{Mean (Original)}} \%$$

The standard deviation gives information about the stretch of the histogram and in combination with the relative shift at the mean values, the changes of the histogram for each band are evaluated. Comparison of correlation coefficient outputs between the original and pan-sharpened images shows which pan-sharpened bands have kept the spectral information of the original bands. The best pan-sharpened bands were extracted after quantitative analysis of the pan-sharpening algorithms. Those bands are used to create the final pan-sharpened multispectral image for further processing (see below for details).

As described earlier, the Landsat ETM+ imagery has 30 m spatial resolution. However, the 15 m panchromatic band (TM8) can be used for the pan-sharpening of the image and increase the spatial resolution of the original multispectral bands. This provides a visually enhanced image of the study area, allowing easier identification of lithologic and tectonic features. A sample of an original and a pan-sharpened image is presented for a regional region in figure 3.4. In the next section a detailed sample (local) region is presented, where all the pan-sharpening techniques results are compared to each other (Fig. 3.5). The aforementioned pan-sharpening techniques were performed in order to obtain images that were most visually enhanced to the human eye. The choice depends on the level of discrimination of edges and linear features, so ensuring the selection of the optimum images in the lineament analysis. Image fusion evaluation was also considered for the final selection of the most appropriate pan-sharpened bands to be used further. A site selection of the study region was taken as a sample in order to present the satellite image outcomes of Landsat ETM+ RGB combination 732 (both before and after the pan-sharpening techniques outlined in Figure 3.5).

The histogram metrics, relative shift in the mean and standard deviation were calculated to assess image fusion quality (Tables 3.3 and 3.4). A percentage shift to the mean of the histogram is determined by the relative shift in the mean. A shift towards white is revealed by a positive value, while a shift towards grey by a negative value. The mean values of the Brovey transformation sharpened images are shifted by almost 80% for each of the bands. This indicates

considerable distortion in the pixel DN values. The shift in the mean values (Table 3.3) shows that the histogram of the Brovey pan-sharpened image is relatively distorted. This implies that the pan-sharpened image contains more spectral information from the panchromatic band than from the multispectral image (Van de Meer, 1997; Vijayaraj, 2004). In contrast, the techniques of Wavelet and PCA seem to be the least affected. The standard deviation values indicate that Wavelet and IHS methods have similar histograms in terms of original multispectral image, while the histogram range in Brovey is reduced (Table 3.4). A new multispectral image for further processing is created and used by this point and beyond by using: i) bands 1, 2 and 3 from Wavelet transformation and; ii) bands 4, 5 and 7 from PCA transformation. The selection was based prior to the mean values that reveal those bands to be keeping most spectral information of original multispectral image after pansharpening (Table 3.3). The standard deviation values of Wavelet are selected as ideal for bands 1, 2 and 3 but bands 4, 5 and 7 for PCA reveal a low related histogram with regard to original multispectral image. For that reason histogram matching was applied for those bands between PCA and pansharpening technique offering closer related histogram with original multispectral image which is IHS transformation.

Method	Band 1	Band 2	Band 3	Band 4	Band 5	Band 7	ID Final
	Mean	Mean	Mean	Mean	Mean	Mean	Mean
HPF	-38.378	-42.413	-44.641	-37.360	-41.645	-43.554	4
Multiplicative	-40.631	-43.526	-45.472	-39.271	-43.123	-44.746	5
IHS	19.311	11.577	7.693	21.031	13.202	9.987	3
PCA	-32.751	-42.997	-30.463	-14.196	7.721	-2.250	2
Wavelet	17.147	9.463	5.220	19.170	10.939	7.299	1
Brovey	-80.343	-81.434	-82.212	-77.691	-80.956	-81.754	6

Table 3.3: The mean values of the pan-sharpened methods with regard to the original multispectral image.

Method	Band 1	Band 2	Band 3	Band 4	Band 5	Band 7	ID final
	Stdev	Stdev	Stdev	Stdev	Stdev	Stdev	Stdev
Original MS	53.463	51.096	50.833	43.525	48.024	48.957	
HPF	70.454	66.355	64.509	68.554	65.982	64.905	5
Multiplicative	47.399	46.329	45.279	39.991	41.778	42.464	3
IHS	54.689	52.104	51.313	41.245	48.966	49.800	2
PCA	36.788	38.072	38.240	34.834	38.554	37.000	4
Wavelet	53.080	50.853	50.407	49.281	49.004	50.202	1
Brovey	8.679	8.296	8.178	11.573	7.629	7.580	6

Table 3.4: The standard deviation values of pan-sharpened methods in comparison with the original multispectral values. Those closer to original multispectral image values imply the most related histogram.

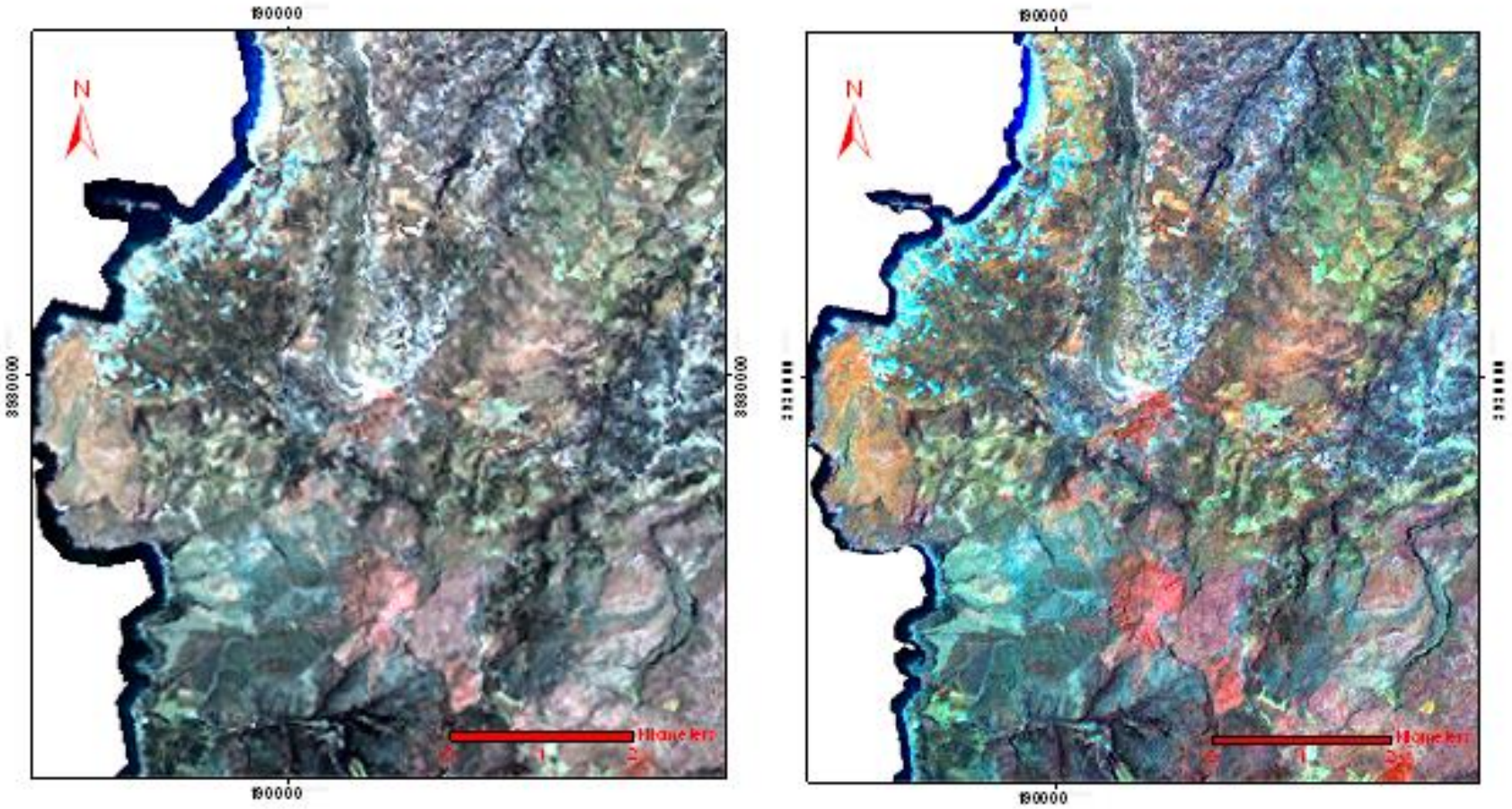

Fig. 3.4: Landsat ETM+ RGB combination 732 before (left image) and after (right image) the data fusion with the panchromatic band using the pan-sharpening technique of PCA transform.

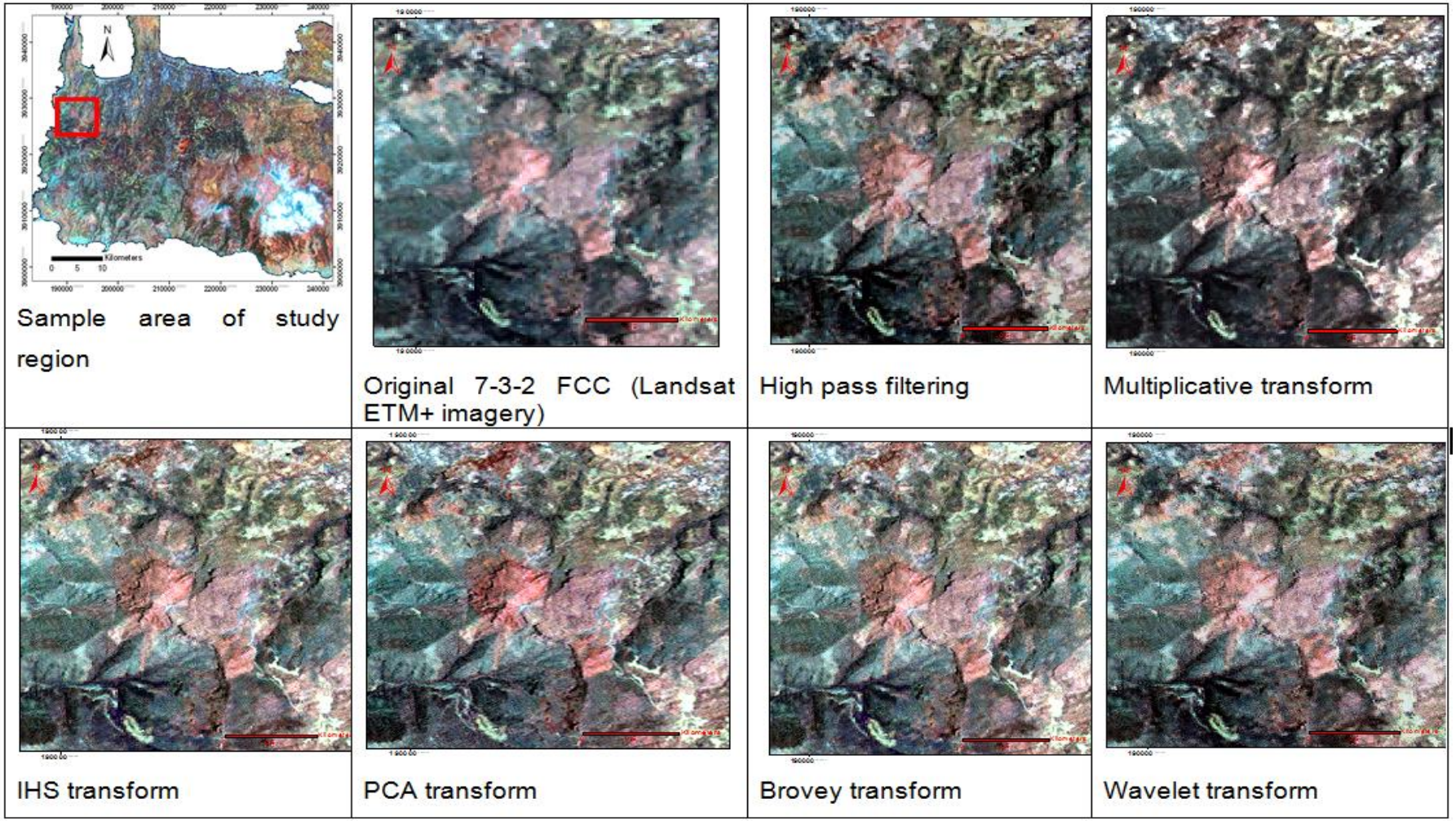

Fig. 3.5: The difference between the original and pan-sharpened imagery of Landsat ETM+ RGB combination 732.

- **Filling of depression and hole sinks in DEMs and data fusion of SRTM and ASTER DEM data**

The SRTM and ASTER DEMs were pre-processed to fill the depressions and hole sinks using algorithms (Jenson & Dominique, 1988), which can be found in various GIS software (eg. GRASS, PCI Geomatica, ArcGIS). In this study the Hawthôs analysis tool for ArcGIS is used to carry out the filling of depressions and hole sinks that can be found in the DEMs. This procedure can be particular useful within the stream valleys by providing a more homogeneous dataset without depression and hole sinks. Relief is a spatial interpolation of elevation data, which until recently was extracted by topographic maps by tracing the contour lines. Geometric inaccuracies involved in the final interpolated DEM result in imprecise measurements. Recent developments in computer software allow direct measurements of elevation from satellite images and digital photographs (Al-Rusan, 1998; Gooch, 2001; Toutin, 2002). The ASTER DEM, extracted by ASTER satellite imagery, is used in this study providing a spatial resolution that is adequate for geological, geomorphological and tectonic studies (Abrams & Hook 1995; Welch et al. 1998; Cheng, 2002; Fu et al., 2004; Komolafe, 2010). In order to overcome gaps caused by cloud cover, the ASTER DEM was merged with the SRTM DEM to combine the higher spatial resolution of the former with the better absolute vertical height accuracy (~16 m) of the latter (Koch & Lohmann, 2000; Muller, 2005; Austin, 2007) (see Appendix I, Theory formulas (ii)).

The processing stages required to merge ASTER and SRTM DEMs are described in the Appendix I (Theory formulas (ii)). A sample area selected to highlight the missing ASTER DEM data due to cloud coverage, depicted with red circles, is shown in Figure 3.6 a. Due to the fact that the missing data regions where voids that contained values from the surrounding ñtrueò values the clouds were masked (using original ASTER multispectral imagery) in order to convert these regions to an no data values (zero). The reason is that the threshold value in the formula (see Appendix I) needed to be 0, as a higher threshold value will fill in

areas of ASTER DEM with SRTM data values (such as valleys) (Figure 3.6 b). Filled data elevation values were in accordance with the SRTM elevation values.

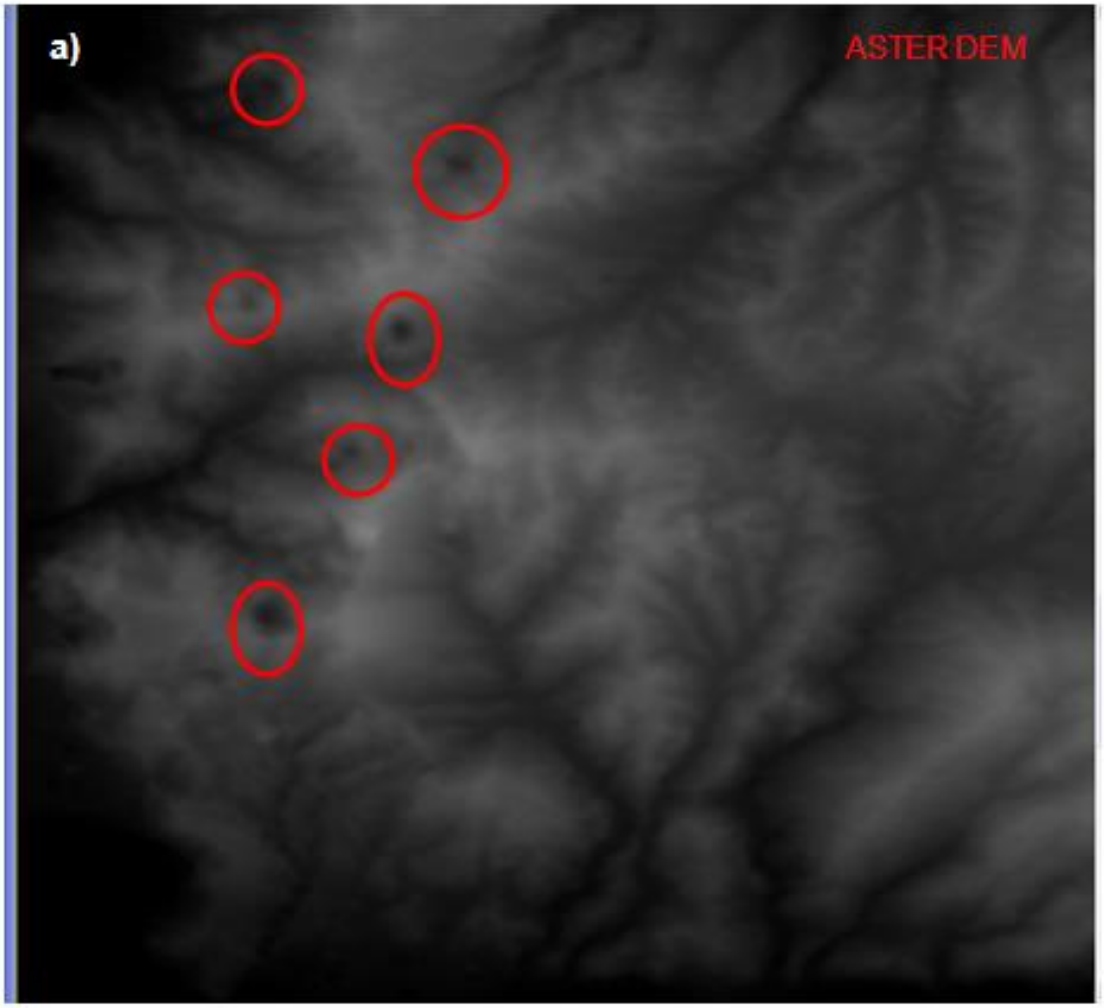

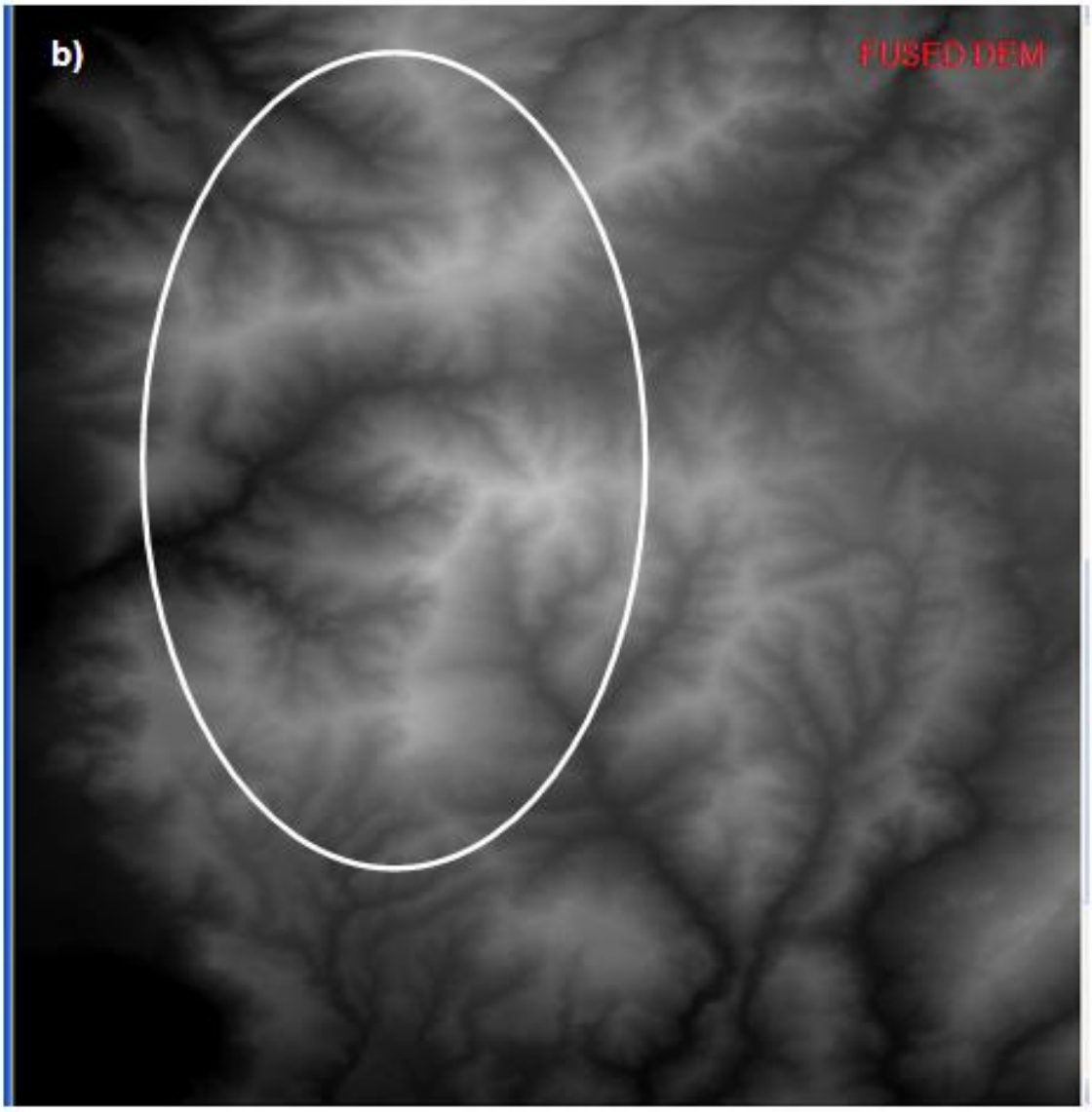

Fig. 3.6: a) The gaps caused by cloud cover in the ASTER DEM data (upper image), in red circle and; **b)** the fused DEM (lower image) after the fusion with SRTM data. No gaps caused by cloud cover can be observed in the fused SRTM/ASTER DEM (see within white circle).

3.4 Accuracy and quality assessment of data sources for extraction of tectonic characteristics

The accuracy assessment of the data plays an important role in the accuracy and reliability of the results. Therefore it is important to know the positional and vertical accuracy errors and their influence on the outcome products. The database used in this study includes satellite imagery, DEMs, aerial photos and dataset maps. In order to make use of this inter-related data it is important to check the error limits that are provided by the results. As can be observed below, the root mean square error (RMSE) value is not high so no significant influence is expected in the final datasets to occur. Aerial photos (with 1 m spatial resolution) are also utilized. These act as reference maps and perform better positional accuracy of other data. This improves the reliability of the results, and subsequently ensures that the data can be utilised in further study without any significant deviations.

i) Digital maps accuracy assessment

The topographical, geological and hydrological dataset maps were scanned at 600 dpi. Dataset maps of 6 m pixel size were then generated. These maps were georeferenced by using triangulation points from the Hellenic Military Geographic Service (HMGS) as GCPs for minimizing the RMSE to 0.06, based on 30 GCPs (see Fig. 3.8). Triangulation points with an error of 2 cm (Apostolakis, 1991) provided highly georeferenced data with regard to the extracted RMSE (0.06). Digital format of aerial photo images (georeferenced by HMGS), with 1 m spatial resolution, were utilized as a reference data to reinforce the accuracy of the georeferenced datasets (Fig. 3.7).

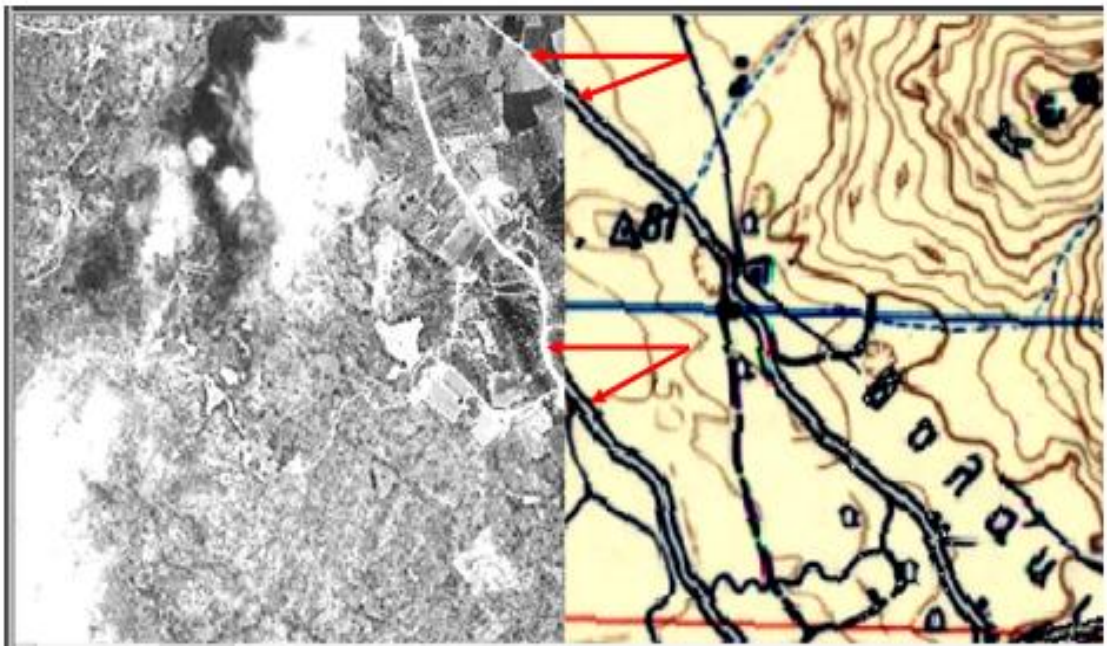

Fig. 3.7: View of an image where the swipe change among the aerial photo (left) and topographical map (right) shows that the road (red arrow) is overlaid accurately.

The scanned digital dataset maps were used to identify important features in this study that need consideration regarding positional accuracy: i) the drainage network; ii) drainage basin boundaries and; iii) lineaments. The drainage pattern was determined using scanned topographical maps and overlaid aerial photos. The usage of aerial photos increased the positional accuracy of mapped streams, in particular considering the small RMSE of 1m aerial photos pixel size (RMSE= 1.05).

The drainage network was initially digitised by the scanned topographical maps. Then the drainage network was extended by identifying new stream segments on the aerial photos and on the ASTER satellite imagery (band 3N-band 1) (Papadaki, 2005). The stream segments identification methodology was based on the detection of abundant vegetation along valley floors (vegetation corridor) (Fig. 3.10). Positional accuracy of drainage network was increased by using aerial photos as a reference map (Fig. 3.9). Drainage basin boundaries were extracted by way of a scanned hydrological map with 6 m pixel size. The

georeferenced topographic map contour lines were also taken into account (in order to recognize the peaks of ridges and to improve positional accuracy).

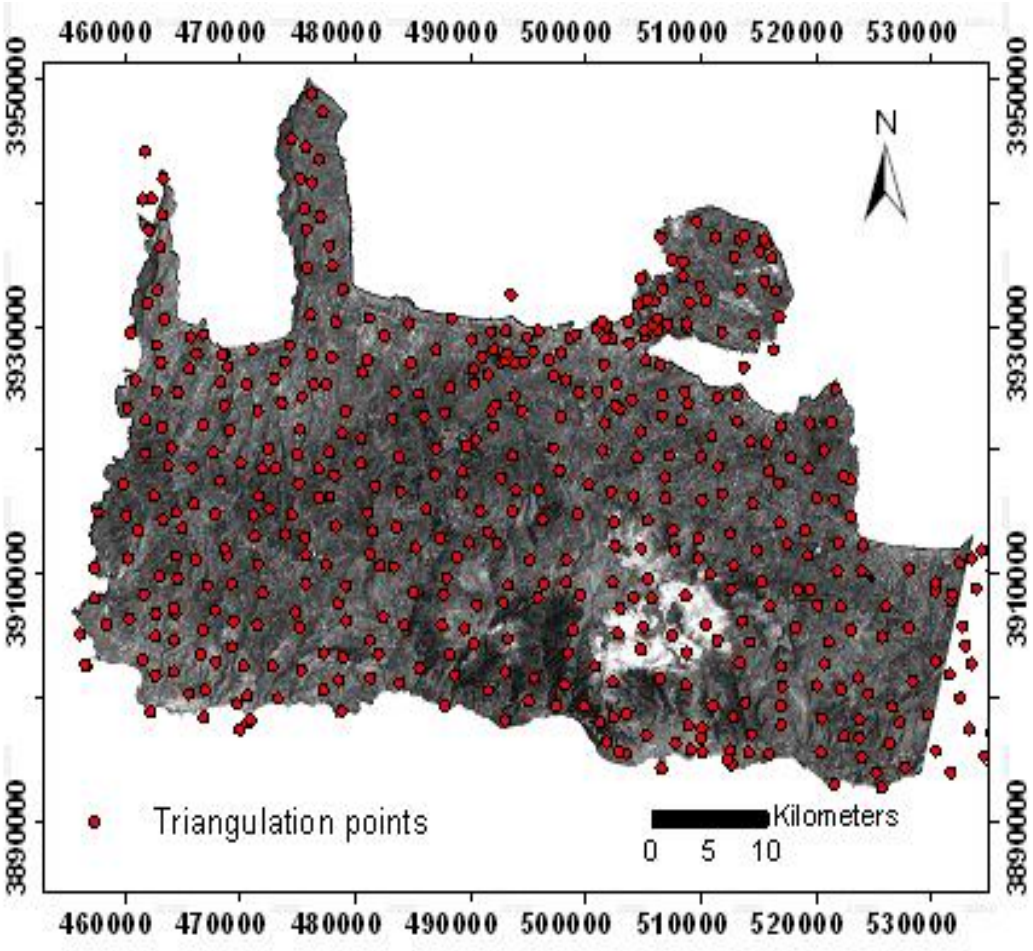

Fig. 3.8: Triangulation points used to georeference the dataset maps.

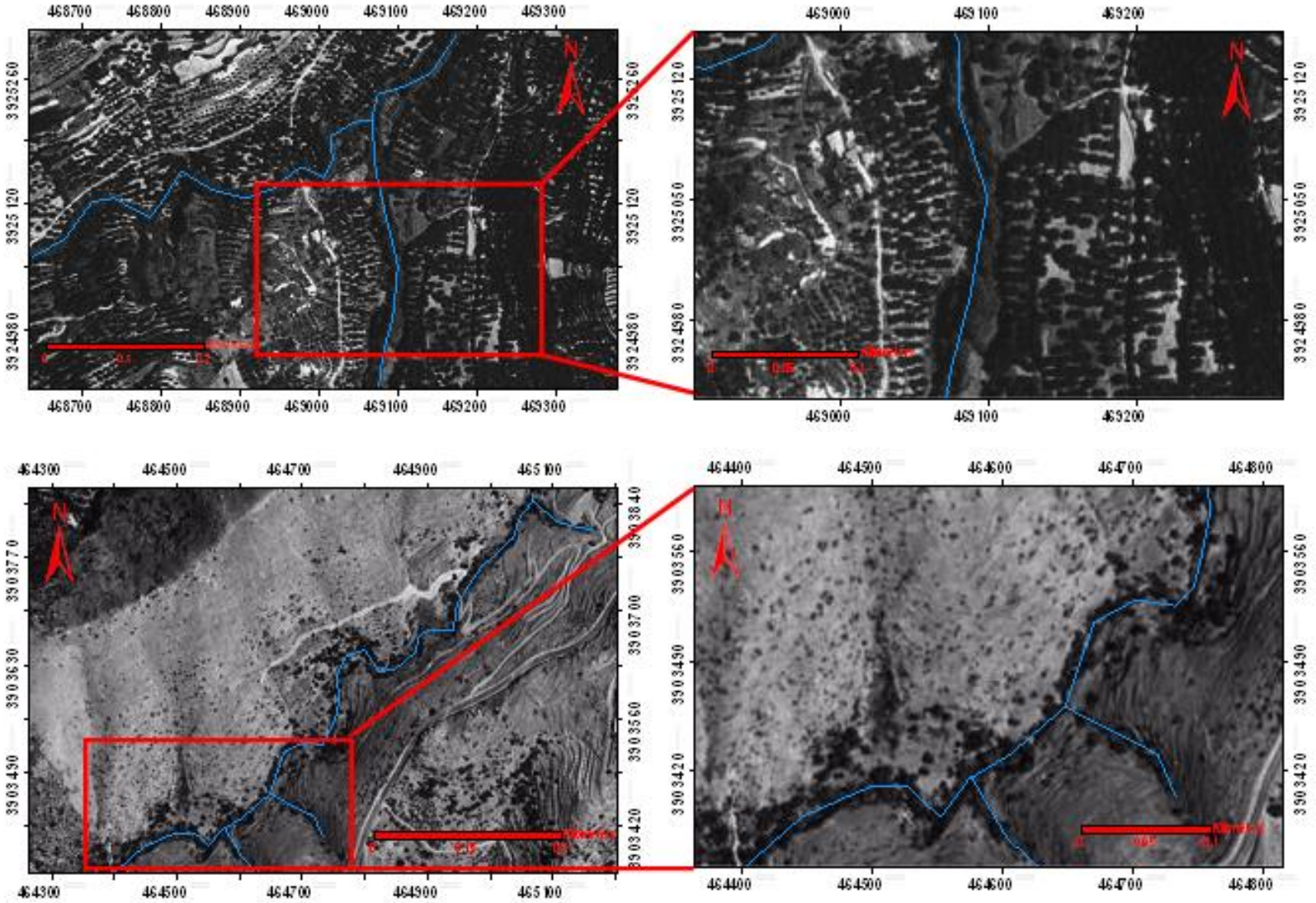

Fig. 3.9: Retail of the drainage networks lines, overlain on aerial photos, for two locations in the study region.

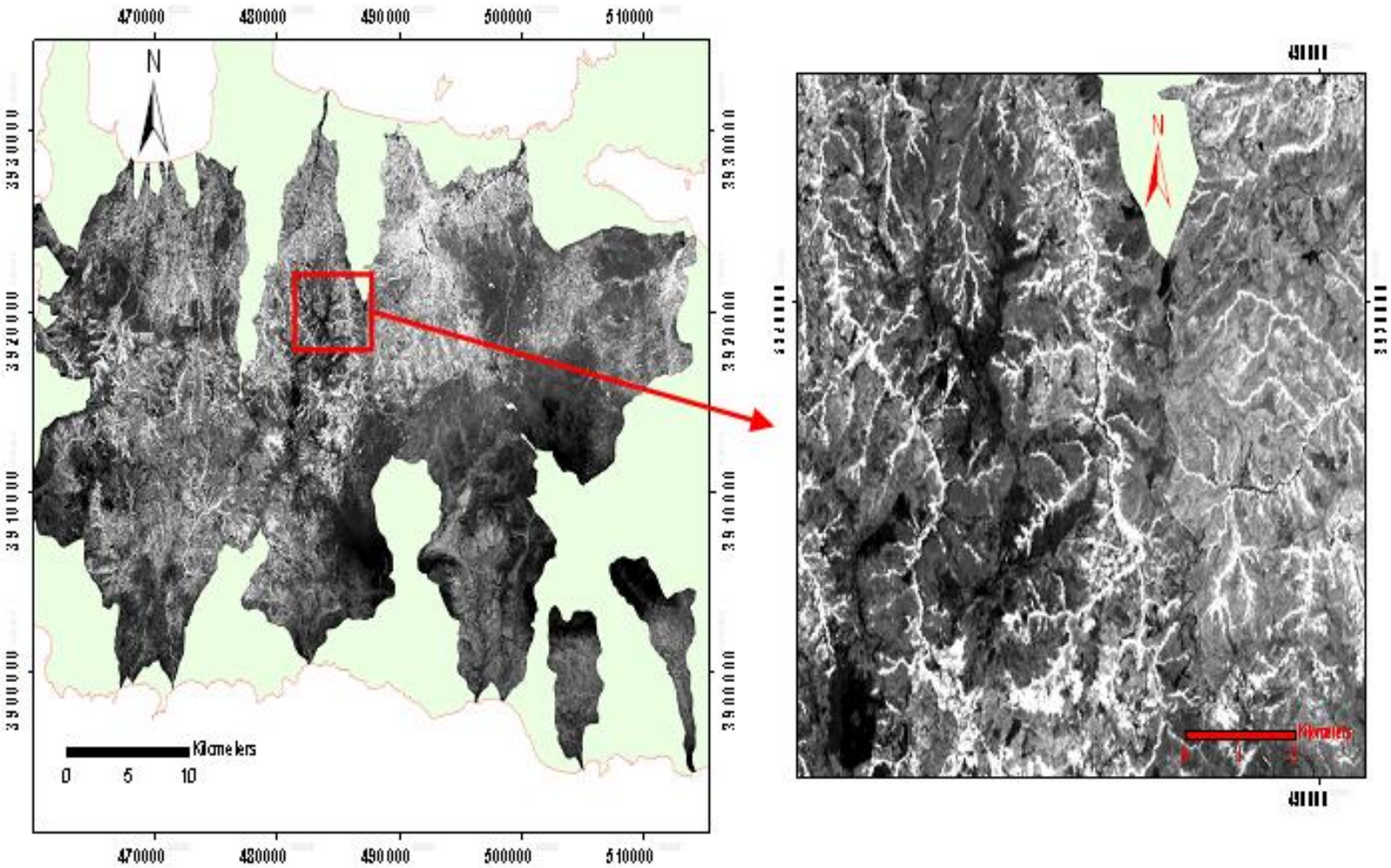

Fig. 3.10: Stream networks of the basins were extracted from ASTER satellite imagery after the subtraction of band 3N from band 1 (band 3N-band 1).

ii) Aerial photography accuracy assessment

Aerial photography with 1 m spatial resolution in this study is used as a high quality reference map. This map is useful because the precise identification of the drainage pattern is determined. Aerial photos also allow to remotely analyse vegetation, land use and stream channel morphology. This enables an evaluation of the importance of any further data extracted in this study (such as geomorphic indices calculation) to be made. The level of aerial photography spatial accuracy can be crucial if evaluation of the changes in small scale parameters, such as localised channel changes is of higher priority (Mount et al., 2003). The geomorphic indices to be evaluated in the subsequent chapters of this study mainly refer to quantifying the changes of parameters at medium to large scale. Aerial photography, apart from providing a high quality reference map, is not the main dataset used in this study: its precise spatial accuracy is therefore not of crucial importance.

The georeferencing of aerial photos was based on triangulation points with 30 GCPs being used to test the RMSE. Resampling throughout the whole image (using cubic convolution) was achieved to equalise pixel size (Hughes et al., 2006). The RMSE calculation was 1.05m, indicating the high positional accuracy of the features recognised with aerial photos and other datasets (Table 3.5).

iii) Satellite image data accuracy assessment

The absolute location accuracy of the satellite imagery is RMSE(xy)= 0.03, as calculated by the residuals of the GCPs used for the geocorrection of the images (provided in the metadata file) (Table 3.5). As previously mentioned, Landsat ETM+ multispectral bands have a spatial resolution of 30 m, while the ASTER VNIR bands have a 15 m spatial resolution. This issue and the different type of the sensors results in a slight displacement among the images when they are overlain. Once images are re-registered, a large RMS (due to differing pixel size) is the result. Therefore, this study uses co-registration of the two different sensor images following the pan-sharpening of Landsat ETM+ imagery to 15 m spatial resolution. This method was adopted to fit pixel location during

georeferencing (due to same pixel size to 15m) and also to reduce the RMS below the pixel size. As mentioned above the RMSE produced by the geocorrection was 7.9m. This is acceptable for the purposes of this research as it does not exceed the minimal spatial resolution of the imagery which is 15m. The better spatial resolution (6m) of the digital scanned maps provided a very low RMSE due to the use of the homogeneous spatial distribution of the triangulation points. This was particular useful, bearing in mind that the digital scanned maps were further geo-corrected with 1m spatial resolution aerial photos, in order to minimize through co-registration the satellite imagery scenes even more with decreasing the RMSE from 7.9m to 3.9m.

The satellite image data, as it will be described in chapter 6, is used for the discrimination of the lithologies in the study area. In order to evaluate the reliability of the outcome discriminated lithologies -whether they fit with the geological map (IGME, 1971) -an accuracy assessment procedure was used. Comparison of satellite image data (provided by Chapter 6) with the geological map (IGME, 1971), by using kappa coefficient statistics, can determine the quality of the satellite image data. Kappa coefficient compares the error matrixes of computer and user's inputs by using multivariate analysis on the discrete values of the classified values (Congalton et al., 1983). It is calculated by:

$$\hat{K} = \frac{N \sum_{i=1}^{r} X_{ii} - \sum_{i=1}^{r} X_{i+} X_{+i}}{N^2 - \sum_{i=1}^{r} X_{i+} X_{+i}}$$

Kappa statistics equation

where N is the total number of sites in the matrix, r is the number of rows and columns in error matrix, N is the total number of observations, Xii is the observation in row i and column i, X_{i+} is the marginal total of row i and X_{+i} is the marginal total of column i (Bishop et al., 1975; Jensen, 1996). It indicates the percentage of the misclassification error that was avoided compared to that which

is generated from a completely random classification (Congalton, 1991). In this study the overall accuracy was estimated for the final processed image that was depicting the lithologies (see Chapter 6) compared to the geological map (IGME, 1971). After the calculation of kappa coefficient statistics for 55 random points, the overall accuracy was 87.76%, which is more than the suggested target of 85% accuracy (Foody, 2002).

iv) SRTM DEM accuracy assessment

The accuracy of a DEM can be represented by its spatial resolution and height accuracy. In mountainous terrain the accuracy of DEMs is generally lower, relative to low relief, low gradient terrain (Hirano et al., 2003; Bhang et al., 2007). Vegetation can also be an important issue as it was estimated to penetrate a quarter or a third of the canopy height (Carabajal, 2005). However, other studies have indicated that the absolute vertical error was smaller (approximately ±5 m) (Rosen et al., 2001; Sun et al., 2003). Kelldorfer (2004) found absolute and relative vertical accuracies of 16 m and 10 m respectively (Table 3.5) (with SRTM 90m-pixel DEM data). The absolute location accuracy of the SRTM DEM is RMSE(xy)= 0.03, based on its co-registration with regard to the georeferenced ASTER DEM (15 m spatial resolution) (Table 3.5).

v) ASTER DEM accuracy assessment

The automated stereo correlation procedures for ASTER DEM creation provide a root-mean-square-error (RMSE) in elevation of between ±7m and ±15m (Hirano et al., 2003), depending on the base-to-height (B/H) ratio (Welch, 1990). ASTER DEM is generated as a stereopair, using bands 3N (nadir viewing) and 3B (backward viewing) of ASTER sensor multispectral bands (Fujisada et al., 1998). In general, the ASTER DEM data products have been created with the following specifications: i) the relative DEMs with no GPCs have an accuracy of ±10-30 m (Fujisada et al., 2001) and; ii) the absolute DEMs have an accuracy of ±7-50 m, depending on the number of GCPs provided (Table 3.5) (O'Neill & Dowman, 1993; Tokunaga et al., 1996). Studies from the United States Geological Survey (USGS)

and Eros Data Centre (EDC) for ASTER DEM, evaluated an RMSE of ±8.6 m (EDC DAAC, 2001). An RMSE of ±8.6 m was also yielded through the utilization of extracted GPS and 1:24000 topographical map ground control points. This indicates that vertical accuracy meets evaluations of earlier studies (Hirano et al., 2003). Although spatial resolution is 30 m, vertical accuracy error seems to be greater than the 90 m SRTM DEM (as mentioned above).

The inaccuracies of ASTER DEMs are limited to their instrumentation. For example, the characteristics of the sensors and processing problems of algorithm during calculation of elevation. In addition, small areas of ASTER DEM data might be presented as elevation anomalies due to cloud coverage in the original multispectral image (ASTER, 2009). The problem of the cloud gaps in the ASTER DEM was solved by replacing the effective areas with the data from the SRTM DEM (Dowman & Balan, 2007). The SRTM DEM has no cloud coverage artefacts due to the radar sensor usage and provides better vertical accuracy (Kelldorfer et al., 2004). The vertical relative error of both DEMs (SRTM and ASTER) is evaluated by using elevation knowledge from triangulation points (as a reference data, using GIS), with the resultant RMSE for both DEMs to be similar (~26m) (Table 3.5). Nikolakopoulos (2006) compared these two types of DEM (both ASTER and SRTM) for regions in Crete having similar complicated physiography with the regions considered in this study. The co-registration of the two DEMs and their comparison revealed a strong correlation for estimated elevation. That is a good indicator for the validity of the DEMs fusion used in this study.

Data		RMSEz (literature) (meters)	RMSEz (study area) (meters)	RMSExy (study area) (meters)
Aerial photos (1:15000 scanned,1m pixel size)		-	-	1.05m
Digital maps (1:150000 scanned,6m pixel size)				0.36m
Landsat ETM+ (30m pixel size)		-	-	0.9m
ASTER (15m pixel size)		-	-	0.45m
ASTER DEM (30m pixel size)	*Absolute*	±7- ±50 m (Tokunaga, 1996) ±8.6 m (Hirano, 2003) ±8.6 m (EDC DAAC,2001)	-	-
	Relative	±10- 30 m (Fujisada, 2001)	0.9m	27m
SRTM DEM (90m pixel size)	*Absolute*	16 m (Kelldorfer, 2004) ±5 m (Rosen, 2001)	-	-
	Relative	10 m (Kelldorfer, 2004)	2.7m	26m

Table 3.5: The root mean square error (RMSE) for the satellite imagery, DEM and aerial photos datasets used in this study.

With regard to lineament analysis, there was an initial, preliminary phase of lineament mapping through the use of the digitizing of the faults from geological maps (IGME, 1971). The identification of the faults present on the 1971 map was based mainly on fieldwork and aerial photo interpretation in the 1960s. However, many mountainous regions have been insufficiently investigated.

The digitized faults from the 1971 geological map provided useful preliminary lineament data for assessing the tectonic status in the study region.

The semi-automated method for lineament analysis was then applied to the ASTER DEM and to Landsat ETM+ multispectral satellite imagery:

i) ASTER DEM shaded relief and various illumination angles aided the identification of fault scarps, particularly in rugged inaccessible mountainous regions. The spatial resolution of the ASTER DEM is of sufficient quality to highlight lineaments, with minimal dimensions of 300 m in length and 30 m in width (Cortes, 1998). Usage of ASTER DEM can lead to small positional inaccuracies of the lineaments. This is due to the width of each shadow zone (as different illumination angles result in a shadowed effect).

ii) Multispectral satellite imagery (Landsat ETM+) was processed (stages described below) in order to enhance tectonic features. As will be presented in the Chapter 6, the lineaments identified via the DEM are fewer than those that can be detected via the multispectral satellite imagery, although similar lineament dimensions criteria were selected in both cases. This is a result of better spatial resolution of the multispectral satellite imagery (relative to the DEM) which can enhance linear features, discriminate better their depiction on the image and provide more accurate location of lineaments. Additionally, lower average lineament lengths are provided on satellite imagery, as more coherent lineaments identified on DEM increases their average length. Lineament mapping using different satellite and aircraft sensors has been shown to highlight different sizes of lineaments (Shuman, 1991) (Fig. 3.11). Spatial filtering and the creation of RGB combinations were utilized in the lineament analysis of the satellite imagery data in order to create a lineament map with a positional accuracy error not exceeding the pixel size of the satellite imagery.

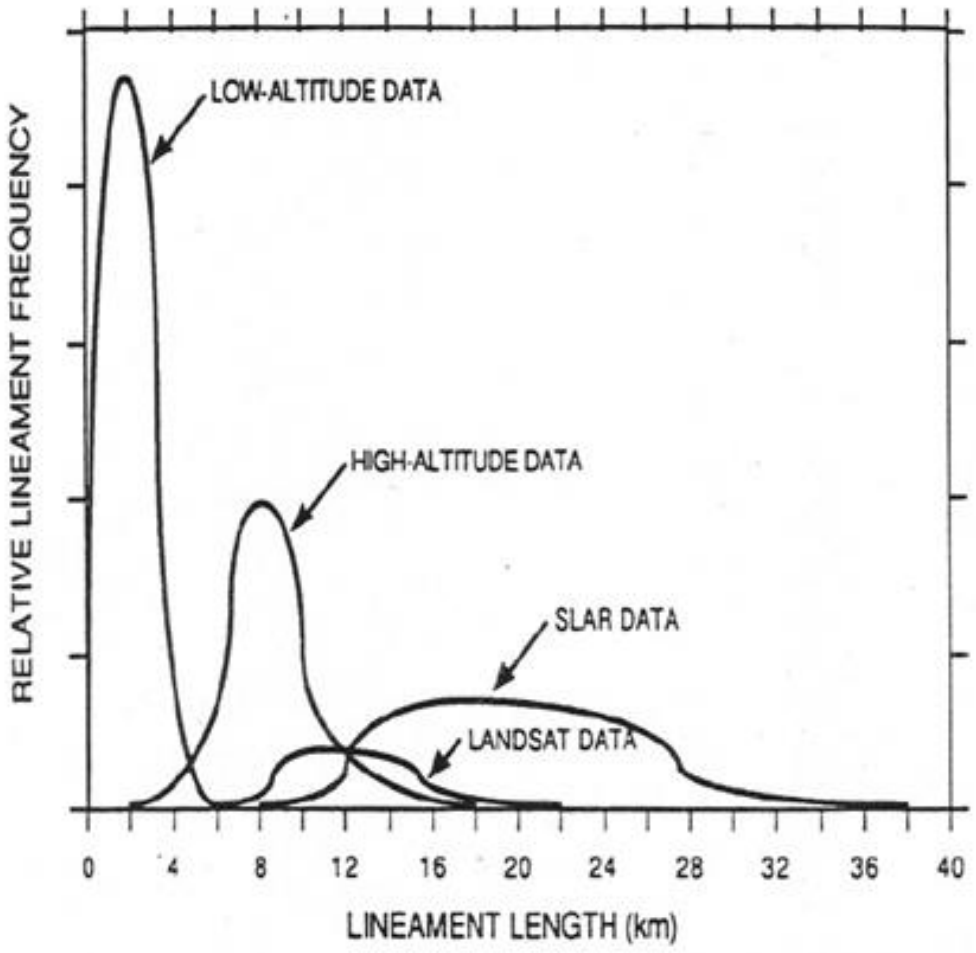

Fig. 3.11: Lineament length distribution is dependant on the scale of the imagery dataset to be applied (see text for detail) (from Shuman, 1991 in Gustafsson, 1993).

vi) VLF method accuracy assessment

The VLF survey profiles positional accuracy yields to the Garmin GPS unit positional accuracy that was used. The Garmin GPS unit positional accuracy is within 10-15 meters (WDNR, 2001) and so does any of the fault location being identified by the use of the geophysical VLF method (see Chapter 7).

3.5 Summary of the expected final datasets

Detailed description of the expected datasets will be provided in the subsequent chapters. This section consists of a summary of the final datasets to be extracted regarding all the initial data sources presented earlier in this chapter. The digital scanned maps provided the initial data sources of this study. These digital maps are used for the digitization of the major drainage network, lithologies, faults and drainage basin boundaries as vector data. The extracted vector data shapefiles of drainage network and drainage basins are used for the calculation of the geomorphic indices, which were added as extra attribute tables of the ArcGIS vector data shapefiles (see Chapters 4 & 5). Those indices are: basin length (Lb), area (A), perimeter (P), basin relative relief (R), relief ratio (R_r), stream frequency (F_u), stream total number (N), total stream length (ΣL), form factor (R_f), elongation ratio (R_e), basin circularity (R_c), drainage basin shape index (Bs), hypsometric integrals (HI), asymmetry factor (AF), stream length gradient (SI) and transverse topographic symmetry factor (T). The indices were based on mathematical equations extracted by using drainage network or drainage basin shapefiles as input datasets (see Chapters 4 & 5).

The fused DEM was used for the extraction of thematic maps based on morphotectonic analysis. ArcGIS extension applications (e.g. spatial analyst, geostatistical analyst), using fused DEM and drainage network vector data as input files, were used to calculate indices such as: slope gradient, slope aspect, topographic wetness index (TWI), amplitude relief (A_r), drainage density (D_d), stream frequency (F_u), ratio of the width of valley floor to valley height (V_f), mountain front sinuosity (S_{mf}), hypsometric curves (HC) and the updated normalized stream-length gradient (SLk) (see Chapter 5).

The satellite imagery data of Landsat ETM+ was used for the lithological discrimination and lineament identification. Image processing stages of Landsat ETM+ image data as input file (using applications of Erdas Imagine, ENVI etc.), were used for lithological and lineament mapping. The vector data of the lithologies and recorded faults extracted by the digital scanned geological map were used as reference map to evaluate lithological and lineament mapping

quality (see section above 3.4 (iii) and Chapter 6). The lineament mapping extracted by DEM and Landsat ETM+ satellite images provided the basis of using buffer zones for coinciding lineaments to determine the final lineament map (see Chapter 6).

CHAPTER 4 DRAINAGE BASIN ANALYSIS AT REGIONAL SCALE

4.1 Introduction

This chapter examines the geomorphological factors developing the drainage basins of the study region, at a regional scale. The relationships between geomorphic indices are examined at the end of this chapter, to determine the control of drainage basins regional tectonic activity in their development. This issue will be further investigated to Chapter 5, focusing on local sites of tectonic activity.

The overall aim of this chapter is to identify which drainage basins are under a high degree of tectonic control. Such basins are the ones that fit the following criteria: i) elongated shape of basin; ii) high or low relief (depending on dominant processes, either tectonic control or ongoing uplift) and; iii) hillslope processes and geological structures dominant in basin development, relative to fluvial processes (Burbank & Anderson, 2000; Molin et al., 2004; Manu & Anirudhan, 2008; Delcaillau et al., 2010; Sougnez & Vanacher, 2011).

Various types of drainage basin analysis have been carried out in this study to examine hydro-geomorphological responses to tectonic deformation at a regional scale. The drainage network investigation consists of a quantitative analysis, using geomorphic indices for the characterization of the drainage basins, regarding the dominance of erosional or tectonic processes. Such processes are evaluated in this chapter, at the regional scale of the drainage basins. That evaluation will highlight the basins to be examined in Chapter 5 for detecting morphotectonic anomalies associated with local tectonic activity.

The drainage basin analysis is based on characteristics, such as stream network or drainage basins, as these are sensitive factors that can be associated with the current tectonic regime. For that reason the major datasets to be used in the methodology of this chapter are: i) the stream network; ii) the drainage basin boundaries and; iii) the DEM. The types of drainage patterns were determined and geomorphic indices were calculated for the stream network and the drainage basins in the study region.

The lithology, the development of the drainage patterns and drainage basins are compared as their interrelationship can provide useful information referring to the potential influence of tectonic activity in the study region. Drainage basin analysis generally provides geomorphic ñsignaturesò (such as drainage

pattern, relief, uplift, tilting etc) that can be associated with tectonic activity and its impact in landscape development (Doornkamp & Cuchlaine, 1971; Abrahams, 1984; Reddy et al., 2004; Ozdemir & Bird, 2008). The stages which constitute the drainage basin analysis at a regional scale, such as the scale of a drainage basin, are described below to make clear their actual contribution to the neotectonic signal.

4.2 Background

The processes that take place in landscape deformation are difficult to recognize and quantify. That is especially so, for regions that are poorly mapped, due to inaccessibility, limited geological survey resources and lack of available datasets. Drainage basin geomorphometry can be quantitatively evaluated by the examination of the drainage network aspects (Onosemuode, 2010). This can determine the relative importance of processes such as tectonic deformation or erosion in the development of drainage network and by extension to landscape evolution (Segura et al., 2007). Analysis of geomorphometric indices concerning stream network, drainage basin and relief aspects can be useful in the characterization of basin geomorphometry and its influence on the development of landforms, at a regional scale (Abrahams, 1984; Reddy et al., 2004). Such analyses can provide a first order of geomorphological and hydrological processes taking place on the landform and evaluate whether their impact is a result of regional tectonic control (Segura et al., 2007). Determination of morphological characteristics is first needed for comprehension of drainage basin scale, while information regarding the stream network or the drainage basin relief and shape can then focus on a quantitative evaluation of drainage basin development against regional tectonic control (Ribolini, 2008).

Several studies have focused on drainage basin characteristics to quantitatively describe their geometry, shape, relief, pattern and texture of drainage network (i.e. Abrahams, 1984; Lykoudi, 2004; Mesa, 2006; Ozdemir & Bird, 2008; Sreedevi, 2009; Malik et al., 2011). Such characteristics can assess landform development, through the type and magnitude of the processes taking place (Al-Sulaimi, 1997). Tectonic activity can be assessed by acquiring valuable information about drainage basins, regarding the aforementioned characteristics

(e.g. geometry, shape, relief etc) (Segura et al., 2007; Ribolini, 2008). In some studies, the characteristics of basin morphometry have been used to predict or describe geomorphic processes such as: i) prediction of þood peaks, basin morphometry and stream þooding relationships, assessment of sediment yields and estimation of erosion rates (e.g. Patton and Baker 1976; Baumgardner 1987; Patton 1988; Gardiner 1990; Cardoso et al., 2005; Ozdemir & Bird, 2008); ii) assessment of groundwater potential zones (e.g. Krishnamurthy & Srinivas, 1995; Al-Sulaimi et al., 1997; Sreedevi et al., 2005; Mesa, 2006; Sreedevi et al., 2009) and; iii) characterization of drainage basin tilting and their degree of erosional/incision process, within the basin, as a whole (e.g. Strahler, 1952; Miller, 1953; Schumm, 1956; Gardner et al., 1987; Weissel and Pratson, 1994; Luo, 1998; Keller & Pinter, 1996; Cuong & Zuchiewicz, 2001; Salvany, 2004; Virdi, 2005; Tsimi, 2007; Segura et al., 2007; Alastair, 2008; Hamdouni et.al, 2008; Tsodoulos, 2008). Despite the characteristics of basin morphometry being mainly linked with such studies, their evaluation can provide information to be interpreted as indicators of tectonic processes (Segura et al., 2007; Ribolini, 2008).

In order to examine and determine a better understanding of drainage basins development, it is necessary to understand the topography, the erosion status and the drainage pattern developed in the region. Detailed geomorphometric analysis can be determined by use of conventional methods (e.g. Horton, 1945; Smith, 1950; Leopold & Miller 1956; Strahler, 1957; Morisawa 1959; Krishnamurthy et al., 1996) or new Earth observational data and GIS (e.g. Srivastava & Mitra, 1995; Biswas et al., 1999; Grohmann, 2004; Cardoso et al., 2005; Mesa, 2006; Narendra & Nageswara Rao, 2006; Ozdemir & Bird, 2008; Sreedevi, 2009; Khavari, 2009; Onosemuode et al., 2010; Nageswara Rao et al., 2010; Javed et al., 2011; Malik et al., 2011).

In the evaluation of geomorphic indices concerning analysis of stream networks, drainage basin and relief, the use of GIS is particularly helpful. Using DEM data and GIS techniques is relatively rapid and can provide an accurate and inexpensive approach to geomorphometric analysis (e.g. Farr and Kobrick, 2000; Smith and Sandwell, 2003; Grohmann, 2004; Grohmann et al. 2007; Segura et al., 2007; Ozdemir & Bird, 2008; Sreedevi, 2009). The relationships between the geomorphic indices can be easily managed through the interpretative techniques

of GIS and easier decisions can be made by analysts, evaluating the tectonic activity in a region.

The width of valleys increases in the downstream direction (Ollier, 1981). When this is not sustained the valley might be influenced by structural or geomorphic factors. In this study various geomorphic indices are quantified, using Earth observational data, and indications of tectonic activity are determined. The comparison between the various geomorphic indices can specify the degree of regional structural control, taking place in the development of each drainage basin (Segura et al., 2007). The calculation of the indices aims to elucidate information on drainage basin geomorphometry which can be used to describe the basin as a landform. The implication of drainage basin geomorphometry for structural control processes, on regional scale, is examined by indices that can assess influences of geological processes on landscape development.

This study focuses on making use of geomorphic indices that will provide meaningful information in evaluating the tectonic activity of a drainage basin. Horton (1945) pioneered studies of drainage morphology along with others following him (Strahler 1952, 1964; Schumm, 1956; Leopold and Miller, 1956; Hack, 1957; Morisawa, 1958; Scheidegger, 1965; Shreve, 1967; Gregory 1966, 1968; Selby, 1968; Smart 1967, 1969; Gregory and Walling, 1973). Based on these, recent studies have developed and highlighted new insights into drainage morphology, regarding the influence of geomorphological or tectonic factors (e.g. Al-Sulaimi, 1997; Krishnamurthy et al., 1996; Cheng et.al., 2001; Pakhmode, 2003; Salvany, 2004; Sreedevi, 2005; Grohmann, 2004; Reddy et al., 2004; Sarangi, 2005; Virdi, 2005; Mesa, 2006; Alastair, 2008; Garcia-Tortosa, 2008; Manu & Anirudhan, 2008). The information extracted through the geomorphometric analysis of drainage systems is valuable in quantitative geomorphologic studies. Mesa (2006) studied the Andean basin in Argentina using an assemblage of morphometric indices (e.g. A, P, Lb, Nu, Lu, Rb, Fu, Dd, R, Re, Rc, Rf (see below for indices details)) that revealed the development of stream segments to be influenced by slope and local relief. In south India Sreedevi (2009) applied a morphometric analysis in the semi-arid Wailapalli basin, using indices such as Nu, ∉L, Rb, Dd, Fu, Re, Rc and Rf, that showed the basin development to be mainly guided by the effect of faulting and thrusting. A similar

study of Sreedevi (2005) took place for the semi-arid Pageru basin in India in order to extract groundwater potential zones. The interpretation of the morphometric indices revealed the structurally controlled development of the basin shape by faulting and thrusting. In Turkey, Ozdemir & Bird (2008) evaluated morphometric indices (e.g. Nu, ΣL, Dd, Fu, R, Rb) for potential flooding effect of Havran basin. The flooding of the main river of Havran basin varies as the sub-basins infiltration capacity, peak discharge, surface runoff conditions are affected by structural complexity, high relief and bedrock permeability.

Geomorphic indices are helpful in the investigation of basin deformation conditions, hydrological characteristics and erosion status on regional scale, such as the scale of a drainage basin. They can also indicate geological processes that have taken place over time, assist with the selection of groundwater recharge sites, and aid the identification of areas prone to erosion and tectonic activity (e.g. Al-Sulaimi, 1997; Wang, 1998; Awasthi, 2002; Pakhmode, 2003; Mesa, 2006; Kouli et al., 2007; Manu & Anirudhan, 2008). In the Manu & Anirudhan (2008) study, geomorphic indices were applied (such as Rb, Dd, Fu, Re, Rf, Rc and Rr) with the outcomes being suggestive of geologically younger tectonic activity controlling the drainage pattern of the Achankovil basin, India. Awasthi (2002) applied geomorphic indices to determine the high degree of erosional conditions presence in drainage basins in Nepal. A quantitative index in order to evaluate the asymmetry of a drainage basin is the asymmetry factor (AF). That index can determine the overall regional tectonic tilting of a drainage basin (Tsodoulos, 2008). Tsodoulos (2008) evaluated the general trend of uniform tilting of basins scale ranging from 80-700km^2 in the Gulf of Corinth, Greece. The AF can be applied in large drainage systems and areas of sustained uplift, obtaining interesting tilting results (Hare & Gardner, 1985; Garrote et.al, 2006). In a study of the Nicoya Peninsula, Costa Rica, the AF index revealed tilting associated with subduction of the Cocos plate (Hare & Gardner, 1985; Alastair, 2008). Ramirez (1998) investigated the active tectonics of Acambay graben, Mexico, via geomorphic assessment of that volcanic belt with one of the indices used being drainage basin shape (Bs). That index was useful to determine the typical elongated shape of a basin, within a tectonically active mountain range (Ramirez, 1998). Useful information about the relationship that exists between the drainage

basin area and the distribution of elevations are obtained by the calculation of the hypsometric integrals (HI), determining whether factors such as tectonics play a role (Strahler, 1952; Miller, 1953; Schumm, 1956; Weissel and Pratson, 1994; Dowling et al., 1998). In rapidly uplifted regions, such as Siwalik Hills in Nepal and Western Foothills of Taiwan, hypsometric integral (HI) proved to be highly correlated with the uplift rate and recently uplifting anticline respectively (Chen, 1999; Hurtrez et al., 1999). The calculation of HI reveals the volume of the drainage basin remaining unweathered and the stages of erosion and incision degree within the regional scale of a basin (Hamdouni et.al, 2008).

The indices that were determined in this study in order to quantitatively analyze the drainage system at a regional scale can be separated into:

i) the ones that determine the stream network characteristics (total number of streams (N), total stream length (ΣL), drainage density (Dd), drainage frequency (Fu) and bifurcation ratio (R_b)). In order to determine the extent of the stream network, its complexity, texture and whether drainage pattern is distorted by geological structures.

ii) relief related indices characterizing drainage basins relief characteristics (relative relief (R) and relief ratio (Rr)), in order to determine the relief structure of the drainage basin and whether it has an impact to the drainage network pattern.

iii) the ones that determine the drainage basin characteristics, such as geometry, shape, asymmetry, erosional and incision degree status in basins at a broader scale (elongation ratio (R_e), form factor (R_f), basin circularity (R_c) asymmetry factor (AF), hypsometric integral (HI) and drainage basin shape (Bs)).

Some basic morphological characteristics have also been calculated, such as the perimeter of basins (P), the basin length (L_b) and the area of drainage basins (A), to better understand the scale of the drainage basins and their extent. These basic morphological characteristics also provide inputs for the calculation of other indices used in this study (see below).

4.3 Methodology

The stages of the methodology for this chapter consist of the quantitative analysis of drainage network and drainage basins. This analysis provides indications about the development of the stream networks and as a consequence the drainage basins. The extent of the basins development due to tectonic activity is evaluated.

4.3.1 Quantitative analysis of drainage network and drainage basins

This section evaluates the drainage network and drainage basins through a quantitative analysis of characteristics derived by various geomorphic indices (see Fig. 4.1). Interpretation of the resulting geomorphic indices reveals information that is needed for the final evaluation of potential regional tectonic deformation within the drainage basins.

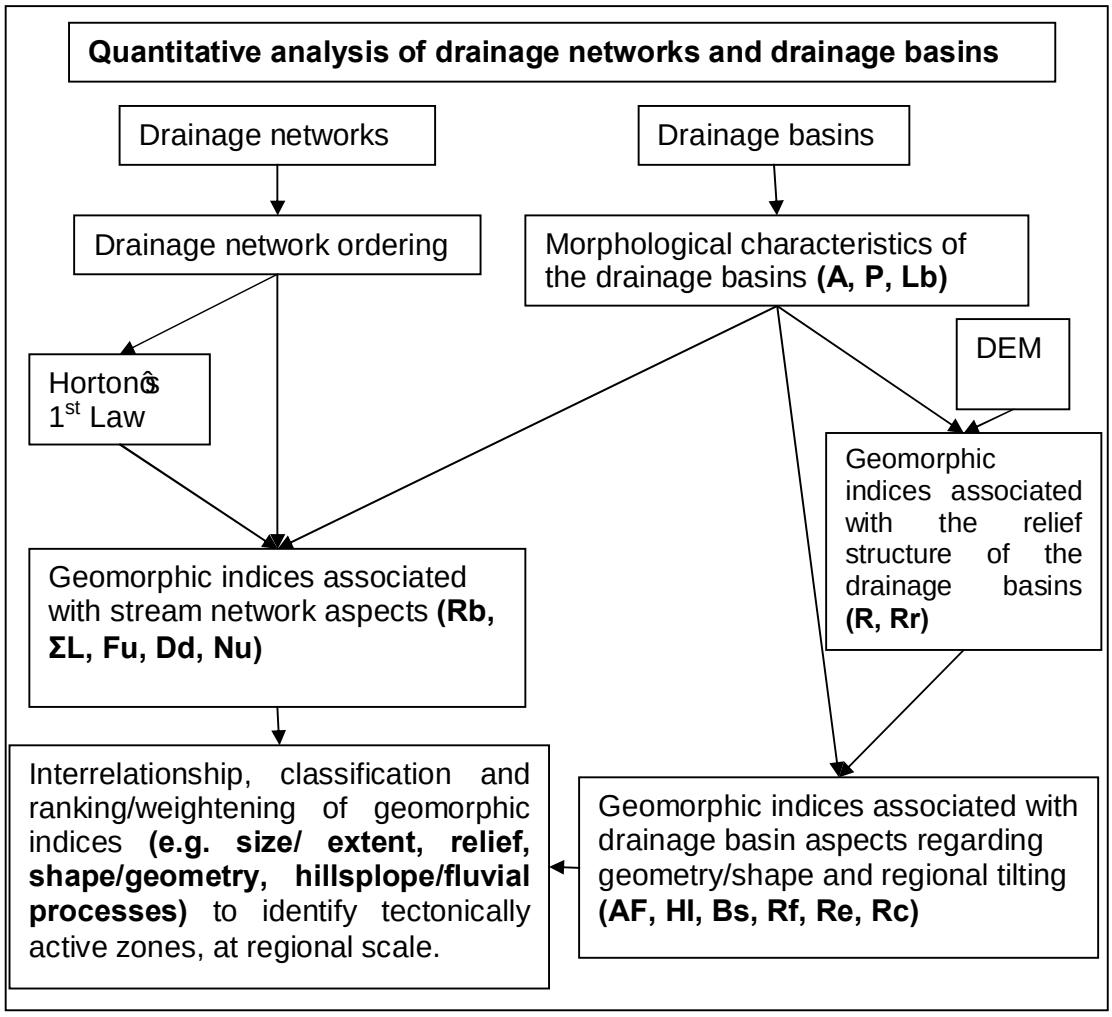

Fig. 4.1: Schematic table showing the sequence and contribution of calculated geomorphic indices to evaluate and isolate tectonically active zones, at regional scale of study.

i) Drainage network ordering

Drainage network ordering can provide information regarding the development and the extent of the drainage network within a drainage basin. A few methods have been proposed for the ordering of drainage networks by examining the relation of stream segments (e.g. Horton, 1945; Strahler, 1952). In this study, the drainage network was extracted (see section 3.4 (i) in Chapter 3) and the classification was based on Strahler's system of stream ordering (Strahler, 1952). During the ordering, dependent streams were characterized as first order, the junction of two first order streams initiated a second order, two second order created a third order channel; any junction of streams of the same order increased the order by one. All the stream orders are counted and presented in Table 4.6 (see *"4.5 Results"* section), with the number of streams, stream length and mean stream length for each order (providing stream analysis). The number of streams regarding the ordering follows a descending sequence. So the higher the order the lower number of streams is expected. Any disruptions in this descending sequence (raise in number of streams for high ordering) can indicate structural control and regional uplift within the basin as examined below by Horton's first law (Chopra et al., 2005).

ii) Morphological characteristics of the drainage basins

The morphological characteristics imply information regarding the overall scale of the drainage basins and their spatial size extent (Table 4.1). These characteristics were calculated within ArcGIS and provide main inputs of the following indices calculations.

Area (A), the area within the drainage basin boundary;

Perimeter (P), the total length of the drainage basin boundary;

Basin length (L_b), the length of the main stream segment, plus the length of the extension between the end of the main stream segment until the longest point of the basin, parallel to the main stream segment (Gregory and Walling, 1973).

Basin Length, L_b(km)	L_b	The length of the main stream order, plus the length of the extension between the end of the main stream order until the longer point of the basin, parallel to the main stream order
Area, A(km^2)	A	The entire area that is comprised by the drainage basin boundary
Perimeter , P(km)	P	The total length of the drainage basin boundary

Table 4.1: Morphological characteristics of the drainage basins.

iii) Geomorphic indices associated with the relief structure of the drainage basins.

After the evaluation of the broader scale of drainage basins size, an overall evaluation of the relief within the basins can be helpful for understanding better their physiographic nature. The following indices are a first sight evaluation of drainage basin relief structure and whether it has an impact to the drainage network pattern (Table 4.2). These indices were calculated by the mathematical equations of Table 4.2, using the DEM data within ArcGIS to calculate the essential parameters.

Basin relative relief (R), the difference between the maximum and the minimum elevation points of the basin (Al-Sulaimi, 1997; Sreedevi, 2005). This is a helpful index to understand drainage formation and its relation to the surface. High values indicate low infiltration, high runoff conditions and high physiographic mountainous structure and vice versa (Reddy et al., 2004; Mesa, 2006).

Relief ratio (R_r), the dimensionless height-length ratio of the basin relief (R) to the basin length (Lb) (Schumm, 1963; Al-Sulaimi, 1997; Jamieson et al., 2003; Mesa, 2006), the values of which may reveal the degree of the rock resistance (Sreedevi, 2005). High values are characteristic of hilly regions and resistant rocks, while low values are characteristic of flat regions and valleys with less resistant rocks (Sudheer 1986; Sreedevi 1999; Mesa, 2006).

Basin relative relief, R(m)	$R= h_{max}-h_{min}$	The difference between the maximum and the minimum elevation points of the basin
Relief ratio, R_r(km/km)	$R_r= R/L_b$	The ratio of the basin relief to the basin length

Table 4.2: Geomorphic indices associated with the relief structure of the drainage basins.

iv) Geomorphic indices associated with stream network aspects

The acquisition of the aforementioned indices provides a general overview of the drainage basins nature regarding morphology and relief. So the next step to start isolating the tectonic signal is to check how the drainage network is developed within such a landscape. The calculated indices presented below concern only stream network aspects and indicate its complexity, texture and distortion by any tectonic disturbances (Table 4.3). These indices were calculated with ArcGIS applications and mathematical equations in Table 4.3.

Total number of streams (N), is the total number of streams in each order inside the drainage basin (Al-Sulaimi, 1997). The plot of the number of streams for each order against the number of order, can examine whether Hortonôs first law observation is confirmed (see below). If it is not confirmed then tectonic control is a factor influencing the drainage network disturbance (Chopra et al., 2005; Paraschou, 2005).

Total stream length (ΣL), the sum of all stream lengths in the basin (Al-Sulaimi, 1997). Stream length can be useful to check Hortonôs second law, which describes the relation of the average stream length to the stream orders (Horton, 1945). The basin stream length is supposed to decrease as the order increases, but any deviation observed implies to variation in relief (Sreedevi, 2005)

Stream frequency (F_u), is the ratio of the total number of the stream segments to the area of the basin (Al-Sulaimi, 1997; Jamieson et al., 2003). The values of stream frequency indicate the degree of slope steepness, rock permeability and surface runoff. High Fu values range (>5) are associated with impermeable subsurface material, high relief and low infiltration capacity, while low values imply high permeability geology, low relief and high infiltration capacity (Reddy et al. 2004; Shaban et al.2005; Ozdemir & Bird, 2008; Bagyaraj & Gurugnanam, 2011).

Drainage density (D_d), is the ratio of the total stream length to the area of the basin (Al-Sulaimi, 1997; Awasthi, 2002; Jamieson et al., 2003). The drainage density reveals information regarding surface runoff potential, ground surface steepness, the degree of landscape dissection, rock permeability and resistance to erosion (Verstappen, 1983; Tucker & Bras, 1998; Awasthi, 2002; Reddy et al., 2004; Mesa, 2006). Drainage density values less than 5 are associated with a coarse drainage network and subsurface material being permeable (Sreedevi, 2005). Drainage density is controlled by factors such as slope gradient and relative relief (Sreedevi, 2009). A low value of Dd is associated with low relief within the basin and permeable materials, while a high Dd value provides a high relief and impermeable rocks (Strahler, 1964; Gardiner, 1995; Sreedevi, 2009).

The drainage network of each basin was analyzed based on Horton's first law (1945). In his first law, Horton observed that the number of streams gets smaller as the stream order increases. The graphic logarithmic plots of the stream order against the number of streams were used in order to estimate the values of **R_b** (***ratio of bifurcation***). This was achieved by calculating the anti-log of the slopes of the linear fit (Maxwell, 1955). The R_b index is useful to determine the degree of the structural complexity of the basin and the influence of geological structure on the drainage network development (Horton, 1945; Strahler, 1957; Wang, 1998; Jamieson et al., 2003). The bifurcation ratio when ranges from 3 to 5 indicate natural drainage system characteristics and minimum influence of geological structures in drainage networks (Chow, 1964; Verstappen, 1983; Kale and Gupta, 2001; Ozdemir et al., 2008). Within that range (3-5), lower values can be considered to refer to less structural disturbances without drainage pattern distortion, while higher values can be indicative of high structural complexity and low permeability (Reddy et al., 2004). Abnormal values of Rb either less than 3 or more than 5 are encountered in areas where geological control is dominant (Mekel, 1970; Raghavan et al., 1983; Reddy et al., 2004; Javed et al., 2011)

The relation between Horton's law is presented in Appendix II (see Fig.1). The equation of the law is as follows:

a) $Nu = R_b^{K-u}$, where Nu= the number of streams of order u;

Rb= the ratio of bifurcation;

K= the maximum order of stream;

u= the order of streams

and as the R_b remains constant for hydrographic drainage, the following equation is applied: R_b=Nu/Nu+1;

The number of streams and the drainage ordering are the inputs needed for applying Horton's first law.

Bifurcation Ratio, R_b	R_b= N_u/ N(u+1)	The ratio of the number of streams of any order to the number of streams with an increased by one order
Stream Frequency, F_u(km^{-2})	F_u= N/A	The ratio of the total number of stream segments to the area of the basin
Drainage Density, D_d(km^{-1})	D_d= ΣL/A	The ratio of the total stream length to the area of the basin
Stream Total Number, N	N_u	The number of streams in each order
Total Stream Length,ΣL(km)	ΣL	The sum of all stream lengths of the basin

Table 4.3: Geomorphic indices associated with stream network aspects.

v) Geomorphic indices associated with drainage basin aspects regarding geometry/shape and regional tilting.

The previous step investigated the stream network using geomorphic indices that can provide information regarding stream network development by potential neotectonic deformation. The next step to follow is to evaluate the drainage basin as a whole. Several indices were used to express the basin geometry, shape, tilting and erosional/incision status (Table 4.4). The calculation of these indices was based in mathematical equations of Table 4.4, use of digitised drainage basins boundaries and DEM data within ArcGIS.

Elongation ratio (R_e), is the ratio of the diameter of the circle of the area of the basin to the basin length (Schumm, 1956; Al-Sulaimi, 1997; Jamieson et al., 2003; Mesa, 2006). This ratio gives the proportion of the basin that has been elongated mainly by tectonic activity control and slightly by lithology (Lykoudi, 2004), while more circular basins indicate less active tectonic processes (Bull & McFadden, 1977; Hamdouni et al., 2008). Low relief can be revealed by values of the index

being higher than 0.8, while steep relief is characterised by values lower than 0.8 (Fairbridge 1968). Low index values imply elongated basins which, due to their primarily downcutting status and the effect of thrusting or faulting within the basin, are representative of areas with continuing rapid uplift and tectonically disturbed rivers (Sreedevi, 2005; Kale & Shejwalkar, 2008). It is a proxy indicator of recent tectonic activity (Cuong & Zuchiewicz, 2001; Bhatt et al., 2007). Values of the Re index less than 0.5 indicate tectonically active regions, values between 0.5 to 0.75 moderate active regions and values larger than 0.75 inactive ones (Bhatt et al.,2007; Kale & Shejwalkar 2008).

Form factor (R_f), the ratio of the basin area to the square of the basin length (Horton, 1945; Mesa, 2006). This index is related to the peak discharge (Gregory and Walling, 1973; Sreedevi, 2005) and flow intensity (Mesa, 2006) of the drainage network. It also indicates that for lower values, the presence of elongated basins with less side flow for shorter duration and high main flow for longer duration takes place, resulting in low peak flows for longer duration. That can imply to exogenous procedures taking place within the basin, preventing the proper development of a homogeneous drainage network (e.g. dendritic). On the other hand, high Rf exists in circular basins with high side þow for longer duration and low main þow for shorter duration, causing high peak þows in a shorter duration (Reddy et al., 2004; Kouli et al, 2007; Javed et al., 2011).

Basin circularity (R_c), indicates the ratio of the basin area to the area of a circle with the same perimeter as the basin, the values of which characterize the current stage of maturity of the basin segments and the degree of circularity (Miller, 1953; Strahler, 1964; Al-Sulaimi, 1997; Sreedevi, 2005; Mesa, 2006). Strongly elongated basins have basin circularity ratios between 0.40 and 0.50 (Miller, 1953; Chow, 1964), with quadrangular basins having values close to 0.8 (Lykoudi 2004).

Drainage basin shape index (Bs), the ratio of the length of the basin measured from the mouth to the most distant drainage divide, to the width of the basin at its widest point (Cannon, 1976; Ramirez-Herrera, 1998; Hamdouni et.al, 2008). This index characterizes drainage basins whose shape was developed and controlled under relatively active tectonics regarding the planimetric shape evaluation of a basin (Ramirez, 1998). Elongated basin shapes indicate high tectonic processes while more circular basins less active tectonic processes (Bull & McFadden, 1977;

Hamdouni et al., 2008). High index values imply elongated basins; Low values are associated with more circular basins. The elongated basins are representative of areas of continuing rapid uplift and tectonic activity presence, in order to recognize the streams primarily downcutting status (Ramirez-Herrera, 1998). Uplifted mountain fronts imply elongated basins while upstream of the mountain front widening of the basins occurs due to lower tectonic activity indication (Ramirez-Herrera, 1998; Khavari, 2009).

Hypsometric integrals (HI)**,** is a powerful technique that reveals the degree of disequilibrium in the balance of erosive and tectonic forces (Strahler, 1952, 1958; Weissel and Pratson, 1994; Luo, 1998; Keller & Pinter, 2002). The values depend on various factors, such as rock resistance, and cannot be related directly to active tectonics (Hamdouni et.al, 2008). Despite that, hypsometric integral (HI) found to be highly correlated with uplift rate and recently uplifted anticlines in tectonically active regions (Chen, 1999; Hurtrez et al., 1999).

The hypsometric integral is the area beneath the hypsometric curve and can be defined as:

$$HI = \frac{\text{mean elevation - minimum elevation}}{\text{maximum elevation - minimum elevation}}$$

High values indicate zones characterized by high relief and deeply incised valleys with minimal upland (plateau) erosion. Conversely, lower values reveal more dissected drainage basins, being highly eroded with less impact from recent active tectonics. The results of HI reveal the characteristics of a drainage basinôs three stages of erosion: i) areas representing basins with deep incision and slight erosion (HI>0.5); ii) areas with approximate equilibrium and an intermediate stage of incision and erosion (0.4<HI<0.5) and; iii) basins characterized by low relief and severe erosion (HI<0.4) (Keller & Pinter, 2002; Hamdouni et.al, 2008). In general, when the HI exceeds 0,5 values then high rates of tectonic activity provide high relief (Tsimi, 2007).

A quantitative geomorphic method to characterize the asymmetry of a drainage network and ground tilting relative to the long axis of a drainage basin is the Asymmetry Factor (AF). The ***asymmetry factor (AF),*** is the percent of the area in the basin that is found on the right of the main stream to the whole area of

the basin (AF = 100*(A_r\A_t)) (Fig. 4.2) (Hare and Gardner, 1985; Keller & Pinter & Pinter, 1996; Cuong & Zuchiewicz, 2001; Salvany, 2004; Virdi, 2005). The AF index proved unreliable in areas with subtle topography and young anticlines (~0.5 Ma in age), making tilting trends imperceptible (Alastair, 2008). This indicates that a region should be undergoing tectonic tilting for a long time, to be recognised by that drainage basin asymmetry index. Such a region is the study area, which is one of the most tectonically active regions in the world. Asymmetry factor (AF) index is applied over a relatively large area or at the scale of a drainage basin (Hare & Gardner, 1985). This index identifies tectonic tilting of a drainage basin and characterizes its asymmetry or symmetry, as it is sensitive to rotations vertical to the axis of the main stream (Tsodoulos, 2008). Under stable settings of a drainage network formation, the index will be equal 50%. In any other case, calculation of the AF index will reveal either AF> 50% (tilting left downstream) or Af< 50% (tilting right downstream). Such tilting is a result of active tectonics rather than lithological factors (e.g. dipping sedimentary layers) (Gardner et al., 1987). The absolute difference (AF-50) is significant in order to evaluate the tectonic activity of the drainage basins (Hamdouni, 2008). Values of absolute difference (AF-50) close to 0 indicate low tectonic activity while values away from 0 indicate higher tectonic activity.

Fig. 4.2: The basin asymmetry factor of Hare and Gardner (1985) (modified by Alastair, 2008). Ar is is the percent of the area in the basin that is found on the right of the main stream. Al is is the percent of the area in the basin that is found on the left of the main stream. Meander belt midline is the long axis of the mainstream if stable settings of a drainage network formation were taking place. Drainage divide is the boundary that defines the limits of the basin.

Asymmetry Factor, AF	$AF = 100*(A_r / A_t)$	The ratio of the area, in the basin, on the right of the main stream (downstream) to the area of the basin multiplied with the percentage.
Drainage basin shape index, Bs	$Bs = Bl / Bw$	The ratio of the length of the basin measured from the mouth to the most distant drainage divide, to the width of the basin at its widest point.
Hypsometric Integrals, HI	$HI = \frac{\text{mean} - \text{minimum}}{\text{maximum} - \text{minimum}}$	The ratio of the difference between mean elevation and minimum elevation, to the difference of maximum elevation minimum elevation.
Form Factor, R_f	$R_f = A/(L_b)^2$	The ratio of the basin area to the square of the basin length
Elongation Ratio, R_e	$R_e = D/L_b = 2A´ /L_b = 1.128*A^{1/2}/L_b$	The ratio of the diameter of the circle of the area of the basin to the basin length
Basin Circularity, R_c	$R_c = 4´ A/ P^2$	The ratio of the basin area to the area of a circle with the same perimeter as the basin

Table 4.4: Geomorphic indices associated with regional drainage basin aspects for the basins as a whole, in order to determine regional tectonic control.

4.4 Multi-criteria modelling of regional neotectonic control

This section examines the classification, ranking and multi-criteria decision analysis (MCDA) of the geomorphic indices relationships, in order to determine the higher regional neotectonic control of the basins. Each one of the geomorphic indices described above offers some particular information such as basin geometry, relief, hillslope or fluvial processes. The large number of those indices can lead to misleading decisions regarding their correlations, so a classification of the indices is needed for coherent data analysis. The necessity to classify these geomorphic indices and make their correlations easier discriminated can be achieved by a multivariate method (Al-Sulaimi, 1997; Lu et al., 2004; Sougnez & Vanacker, 2011). Al-Sulaimi (1997) successfully used a multivariate method to group geomorphic indices of drainage systems in Kuwait. Sougnez & Vanacker

(2011) applied a multivariate method to identify the geomorphic indices that are most likely to represent the observed spatial variability in slope and channel morphology in the Ardennes massif, Western Europe. The type of multivariate analysis to be applied in this study is Factor Analysis, as described by Goddard, & Kirby (1976). Factor Analysis uses correlation coefficient and covariance-variance matrices, to recognize variables within a set of observed variables that discriminate the pattern of correlations. Usually it is used in data reduction to highlight a small number of factors that reveal most of the variance observed in a much larger number of manifest variables (Goddard, & Kirby, 1976). In its final stage, this analysis uses Kaiser's Varimax technique to rotate the factor axes (Davis, 1973). Common applications of factor analysis are: i) identification and exploration of patterns in variables and; ii) testing of hypotheses about the structuring of the variables (Jae-On Kim, 1970).

As soon as the new components of the factor analysis are discriminated the next step is to check the interrelationship of these components. Within each component more than one index will probably be found, so it is necessary to rank the indices found in each component. This procedure aims to maintain priority ranking values for the indices which can be used to acquire one final ranked index for each component. The ranking of the geomorphic indices in this study was based on the same procedure adopted by Chaudhary & Sharma (1998) and Biswas et al. (1999). In these studies the index having the highest value was given a rating of 1, the next lowest value was given a rating of 2, and so on. The lowest value was rated last in the series of numbers. With shape indices (Re, Rf, Rc), the lowest value was given a rating of 1; the next highest value was given a rating of 2, and so forth. In the aforementioned studies after the rating of the indices was completed, the rating values for every drainage basin were averaged in order to calculate a mean compound value. Based on the average value of these indices, the drainage basin having the lowest rating value was assigned the highest priority number of 1; the next highest value was assigned a priority number of 2, and so on. The drainage basin that got the highest value was assigned the last priority number (Chaudhary & Sharma, 1998; Biswas et al., 1999; Biswas et al., 2002; Javed et al., 2011). That kind of ranking is common when dealing with a large number of geomorphic indices. Delineation and priorization of the drainage basins

can be beneficial for planning and development of drainage basins, offering a useful tool to planners and decision makers (Biswas et al., 2002; Singh et al., 2005; Javed et al., 2011; Rekha et al., 2011). For example, in Biswas et al. (2002) study, priorization of microwatersheds was inferred to be essential for suitable soil conservation measures to be suggested. Similarly, in Singh et al. (2005) study, prioritization of sub-watersheds based on estimated soil loss and morphometric indices was considered to suggestion of suitable soil conservation measures of the Maskara Rao watershed, India. Biswas (1999) showed that morphometric analysis could be used for prioritisation of subwatersheds even without the availability of reliable soil maps of the area under study.

In this research study, instead of computing the arithmetic mean compound value of the indices, an Analytic Hierarchy Process (AHP) was used for discriminating basins with higher degree of tectonic control. An appropriate separation can be achieved for determining the degree of very high, high, moderate and low levels of regional tectonic control. The Analytical Hierarchy Process (AHP) was introduced by Saaty (1977) and is today still the most widely spread and used theory for decision making (Kremljak & Buchmeister, 2006). It is a method of analyzing complex problems with multiple criteria. The relative importance of evaluation criteria is determined without considering the scales on which the criteria are measured (Sener, 2004). It can calculate the needed weighing factors by using a preference matrix which compares all relevant factors against each other in a pair-wise comparison matrix, to find the relative preference among the factors (Saaty, 1980). The comparison consists of a range of values from 1 to 9 to describe the intensity of importance (preference/dominance) (Saaty, 1980; Alipoor et al., 2011) (Table 4.5).

Intensity of importance	Definition
1	Equal importance
2	Equal to moderate importance
3	Moderate importance
4	Moderate to strong importance
5	Strong importance
6	Strong to very strong importance
7	Very strong importance
8	Very to extremely strong importance
9	Extreme importance

Table 4.5: Scale for pair-wise comparison matrix (modified after Saaty, 1980)

The classification of the geomorphic indices by factor analysis is beneficial in the AHP procedure as indices with ñequal importanceò can easily be determined in each of the components. The values of the pair-wise comparison matrix have to be thoroughly considered and not set arbitrarily. So there is need to determine if the comparisons are consistent or not. In order to ensure that, a single numerical index to check for consistency of the pair-wise comparison matrix, called consistency ratio Cr, was developed by Saaty (1977). If the ratio has values less than 0.1 (Cr<0.1) then there is a reasonable level of consistency in the pair-wise comparison matrix. A recommended revision of the preference values should be followed if the consistency ratio Cr exceeds a value of 0.1 (CrÓ 0.1) (Saaty & Vargas, 1991). The values of the pair-wise comparison matrix are determined with regard the lithological and permeability formations of the study region. That implies that geological conditions are considered thoroughly for extracting those basins that owe their development in high degree of tectonic control. The map of geological formations can be found in figure 2.7, while the permeability map in the Appendix II (see Fig. 2)

The standard method used to calculate the values for the weights from an AHP matrix, is to take the eigenvector corresponding to the largest eigenvalues of the matrix and then to normalize the sum of the components to one. That provides a way for assigning priority and for making appropriate decisions. The beneficial

point of this approach is that it organizes identifiable and indefinite factors in a systematic way. It is useful in sectors where rationality and irrationality in association with risk and uncertainty can be found (Palcic & Lalic, 2009). Generally AHP consists of: i) make a hierarchy process; ii) calculate weightings and; iii) check system compatibility (Alipoor et al, 2011). Four methods can be used to calculate the coefficients of the factors: logarithmic squares minimum, squares minimum, approximation methods and special vector data, with the latter being used in this study (Alipoor et al, 2011). Further details on AHP procedure and its applicability are discussed in subsequent Chapter 8.

4.5 Results

4.5.1 Quantitative analysis of drainage network

i) Drainage network ordering and analysis of Horton's law

The drainage network ordering was based on Strahler's system (Strahler, 1952), with the drainage basins being characterized by stream segments reaching between 3rd order (the lowest) and 6th order (the highest) (Appendix II, Fig. 3 and 4).

The quantitative analysis of drainage networks was initiated using Horton's first law. The evaluation of the number of the drainage basins stream segments revealed some basic characteristics for the stream analysis, as summarized in Table 4.6. The application of the 1st Horton law was performed with the Nu-u plots created to reveal the relationship between the number of the stream segments with the ordering of the drainage network. Useful information can be extracted by the plots of stream order against the number of streams; for example drainage networks generally follow a linear relationship with regard to Horton's law and the number of streams gets smaller as the stream order increases. However, in some cases (notably basins 3, 5, 7, 13 and 21) a deviation is observed (while stream order increases there is an increase in number of streams during higher ordering); this is a consequence of variation in relief (that issue implies that exogenous factors such as tectonics might be influencing the drainage network development) that influences the development of the particular stream order (Chopra et al., 2005; Paraschou, 2005) (Fig. 4.3 and Appendix II, Fig. 1).

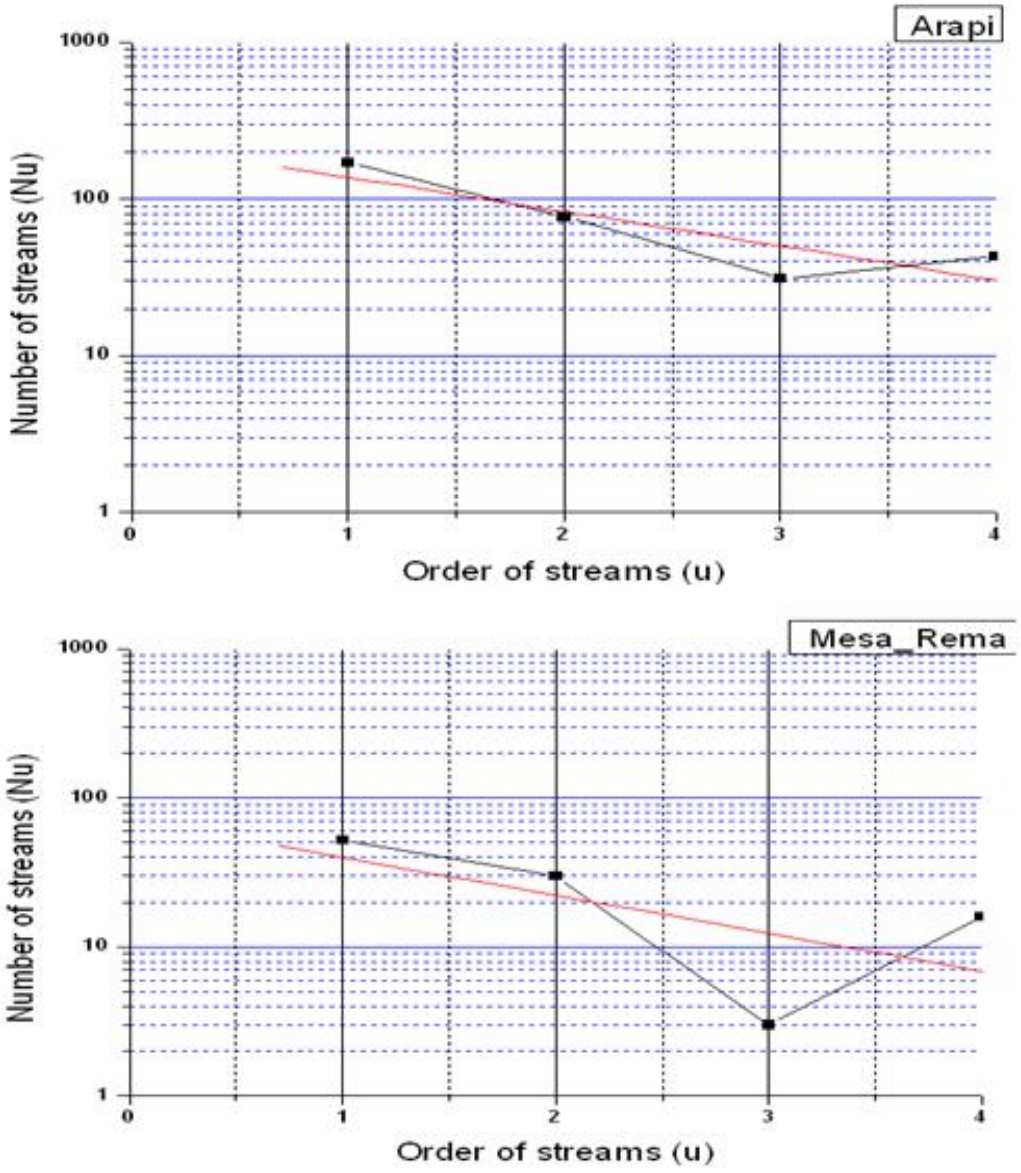

Fig. 4.3: Sample plots of total stream numbers to order of the streams (Nu-u). The order stream where a deviation is observed in the linear regression indicates a lower number of streams than the higher order which follows. This is not in accordance with Hortonôs first law, indicating that the deviation observed is a result of variation in relief (that issue implies that exogenous factors such as tectonic might be influencing the drainage network development).

		Stream Order					
Basins Name	Parameters	1st	2nd	3rd	4th	5th	6th
Ag.Eirini	a)Number of streams	567	279	126	87	39	6
	b)Stream length (km)	142.85	77.617	37.441	23.654	10.682	1.823
	c)Mean stream length (km)	0.251	0.278	0.297	0.271	0.273	0.303
Kakodikianos	a)Number of streams	344	165	57	45	17	29
	b)Stream length (km)	109.37	56.86	17.264	14.099	5.3	11.664
	c)Mean stream length (km)	0.317	0.344	0.302	0.313	0.311	0.402
Kalami	a)Number of streams	736	319	171	127	68	6
	b)Stream length (km)	175.61	86.254	50.374	30.369	21.167	3.405
	c)Mean stream length (km)	0.238	0.27	0.294	0.239	0.311	0.567
Keritis	a)Number of streams	900	438	287	114	33	1
	b)Stream length (km)	227.69	111.06	81.53	34.67	11.43	12.87
	c)Mean stream length (km)	0.252	0.253	0.284	0.304	0.346	1.17
Tauronitis	a)Number of streams	1176	608	232	97	175	24
	b)Stream length (km)	277.45	121.97	51.458	18.588	31.2	10.697
	c)Mean stream length (km)	0.235	0.2	0.221	0.191	0.178	0.445
Tiflos	a)Number of streams	355	153	71	44	53	11
	b)Stream length (km)	101.89	50.087	24.712	10.903	15.572	6.068
	c)Mean stream length (km)	0.287	0.327	0.348	0.247	0.293	0.551
Therisiano Gorge	a)Number of streams	350	171	86	51	21	1
	b)Stream length (km)	77.475	39.302	23.429	17.536	13.188	1.308
	c)Mean stream length (km)	0.221	0.229	0.272	0.343	0.628	1.308
Kasteli	a)Number of streams	137	68	26	18	22	
	b)Stream length (km)	39.755	19.763	11.109	7.434	9.113	
	c)Mean stream length (km)	0.29	0.29	0.427	0.413	0.414	
Pelekaniotis	a) Number of streams	166	68	34	22	26	
	b)Stream length (km)	46.774	22.145	12.458	6.06	9.919	
	c)Mean stream length (km)	0.281	0.325	0.366	0.275	0.381	
Samaria Gorge	a) Number of streams	191	96	36	15	29	
	b)Stream length (km)	63.91	32.112	12.021	5.149	8.095	
	c)Mean stream length (km)	0.334	0.334	0.333	0.343	0.279	
Xsiropotamos	a) Number of streams	139	59	26	37	15	
	b)Stream length (km)	49.405	16.445	8.523	9.783	4.06	
	c)Mean stream length (km)	0.355	0.278	0.327	0.264	0.27	

Aradaina	a) Number of streams	34	19	11	5		
	b)Stream length (km)	15.661	13.449	6.556	6.743		
	c)Mean stream length (km)	0.46	0.707	0.596	1.348		
Arapi	a) Number of streams	170	77	31	43		
	b)Stream length (km)	53.803	24.105	11.841	17.473		
	c)Mean stream length (km)	0.316	0.313	0.381	0.406		
Magagistra	a) Number of streams	91	38	32	16		
	b)Stream length (km)	29.07	12.339	12.375	5.66		
	c)Mean stream length (km)	0.319	0.324	0.386	0.353		
Mesa Rema	a) Number of streams	52	30	3	16		
	b)Stream length (km)	15.636	9.7	1.021	4.153		
	c)Mean stream length (km)	0.3	0.323	0.34	0.259		
Metoxi-Platanos	a) Number of streams	20	10	6	1		
	b)Stream length (km)	7.161	4.988	2.073	1.234		
	c)Mean stream length (km)	0.358	0.498	0.345	1.234		
Milias	a) Number of streams	70	33	19	10		
	b)Stream length (km)	22.242	8.521	6.365	5.781		
	c)Mean stream length (km)	0.317	0.258	0.335	0.578		
Potamos	a) Number of streams	97	35	14	35		
	b)Stream length (km)	30.02	12.964	3.728	10.791		
	c)Mean stream length (km)	0.309	0.37	0.266	0.308		
Sarakiniotis	a) Number of streams	144	59	34	45		
	b)Stream length (km)	31.737	15	7.113	13.782		
	c)Mean stream length (km)	0.22	0.254	0.209	0.306		
Sfakiano Gorge	a) Number of streams	50	21	5	20		
	b)Stream length (km)	21.741	12.039	2.188	7.153		
	c)Mean stream length (km)	0.434	0.573	0.437	0.357		
Balsamakia	a) Number of streams	22	11	7			
	b)Stream length (km)	8.639	2.17	2.454			
	c)Mean stream length (km)	0.392	0.197	0.35			

Table 4.6: The stream analysis for the study area drainage basins.

4.5.2 Quantitative analysis of drainage basins

The various aspects concerning the stream network, relief of drainage basin and drainage basin characteristics at regional scale were determined and summarized in the following tables. Then their classification and relationships are determined to evaluate the drainage basins regarding their development by tectonic factors. A multi-criteria modeling approach identifies the drainage basins undergoing regional neotectonic control.

i) Morphological characteristics of the drainage basins.

The morphological characteristics are a first sight into the scale and extent of the drainage basins even in the case there is not a visual representation of them (Table 4.7). The largest basins are 9, 10, 12 and 17 with the smallest ones being 2, 1, 3 and 6. The highest Lb values are observed in basins 10, 9, 8, 12 and 16, with the shorter in basins 2, 1, 3 and 13. An interesting point is that the range of Lb for most of the basins is around 11-19 km regardless the basins area size. This is a first sight that might some basins have an elongated shape, representing a possible tectonically active mountain range (Ramirez, 1998), which will be confirmed with the calculation of following indices.

Basin ID	Basin names	Area (km^2)	Perimeter (km)	L_b (km)
1	Metoxi	6.86	14.48	5.37
2	Balsamakia	4.77	11.17	3.67
3	Mesa Rema	10.68	14.44	5.78
4	Magagistra	22.52	24.07	10.94
5	Kastelli	31.7	32.86	14.81
6	Milias	15.34	23.94	11.35
7	Tiflos	76.06	48.36	19.48
8	Arapi	41.51	42.04	20.25
9	Tauronitis	128.47	62.78	23.7
10	Keritis	177.9	72.98	24.87
11	Therisiano Gorge	57.46	47.69	19.49
12	Kalami	129.61	52.44	19.98
13	Xsiropotamos	35.36	25.8	8.65

14	Pelekaniotis	40.42	32.82	14.53
15	Sarakiniotis	23.31	30.86	15.05
16	Kakodikianos	77.43	51.59	19.55
17	Agia Eirini	98.33	45.92	14.99
18	Samaria Gorge	51.56	33.92	11.84
19	Potamos	27.82	30.96	12.76
20	Aradaina Gorge	27.79	25.86	11.88
21	Sfakiano Gorge	28.5	34.56	13.4

Table 4.7: Morphological characteristics of the drainage basins.

ii) Geomorphic indices associated with the relief structure of the drainage basins.

The relief aspects of a drainage basin provide an overview of its morphology and relief. The basins have a variable basin relative relief, with the majority having a mountainous landscape (Table 4.8). High basin relative relief values are characteristic of hilly regions and resistant rocks, such as basins 2, 18, 19 and 20, while low values are characteristic of flat regions and valleys with less resistant rocks, such as basins 8, 9 and 7.

Basin ID	Basin names	Basin relative relief (h_{max}-h_{min}) (m)	Basin relief ratio (km)
1	Metoxi	830	0.154
2	Balsamakia	908	0.247
3	Mesa Rema	912	0.157
4	Magagistra	903	0.082
5	Kastelli	1041	0.070
6	Milias	794	0.069
7	Tiflos	1143	0.058
8	Arapi	923	0.046
9	Tauronitis	1294	0.052
10	Keritis	2106	0.089
11	Therisiano Gorge	2067	0.106

12	Kalami	2187	0.109
13	Xsiropotamos	1199	0.139
14	Pelekaniotis	1152	0.139
15	Sarakiniotis	922	0.061
16	Kakodikianos	1458	0.075
17	Agia Eirini	1981	0.132
18	Samaria Gorge	2130	0.180
19	Potamos	2398	0.188
20	Aradaina Gorge	2342	0.197
21	Sfakiano Gorge	2183	0.163

Table 4.8: Geomorphic indices associated with the relief structure of the drainage basins.

iii) Geomorphic indices associated with stream network aspects.

The stream network aspects are presented in Table 4.9 and provide information about the extent of the stream network, its complexity, texture and whether drainage pattern is influenced by tectonic structures. The number of streams (Nu) was considered for each order in stream analysis (see above), to evaluate Hortonôs law. The number of streams (Nu) analysis showed that some of the basins are not in accordance with Hortonôs first law (see above section 4.5.1). An increase of stream length is observed in some stream orders with regard the next highest order, implying variation in relief to be significant. Such basins with significant variation are basins 7, 8, 15 and 19, with others following such as 5, 4, 16 and 21. Low Dd shows a high coarse drainage texture (e.g. basins 1, 19, 20 and 21), while high Dd a fine drainage texture (less coarse) (e.g. basins 9, 11 and 15) (Strahler, 1964). High Fu values range (>5) are observed in almost all basins, associated with impermeable subsurface material, high relief and low infiltration capacity. Low values (<5) are preserved only in basins 20 and 21, implying high permeability geology and high infiltration capacity which is confirmed by the presence of permeable karst formation of Plattenkalk nappe (see permeability map). The bifurcation ratio (Rb) index has values less than 3 for all the basins, indicating that geological structures are disturbing the drainage pattern within all the basins. This issue is in accordance with Mekel (1970) who first showed that

abnormal values of Rb less than 3 are indicative of dominant geological control. The range of values being less that 3 is in accordance also with Kouli et al (2007) study, who calculated Rb for two of the basins within the study area revealing similar low Rb values.

Basin ID	Basin names	Nu	SLu	Dd	Fu	Rb
1	Metoxi	37	15.45	2.25	5.39	2.59
2	Balsamakia	40	13.26	2.78	8.38	1.77
3	Mesa Rema	101	30.51	2.85	9.45	1.79
4	Magagistra	177	59.44	2.64	7.86	1.71
5	Kastelli	271	87.25	2.75	8.54	1.65
6	Milias	132	42.91	2.8	8.60	1.89
7	Tiflos	687	209.24	2.75	9.03	1.82
8	Arapi	321	107.22	2.58	7.73	1.65
9	Tauronitis	2312	511.38	3.91	17.67	1.99
10	Keritis	1783	479.27	2.65	9.87	2.40
11	Therisiano Gorge	680	172.24	2.99	11.83	2.81
12	Kalami	1427	367.18	2.83	11.00	2.29
13	Xsiropotamos	276	86.43	2.44	7.80	1.64
14	Pelekaniotis	316	96.03	2.37	7.81	1.62
15	Sarakiniotis	282	67.63	2.9	12.09	1.50
16	Kakodikianos	656	213.42	2.75	8.47	1.74
17	Agia Eirini	1104	294.07	2.99	11.23	2.29
18	Samaria Gorge	367	124.29	2.41	7.12	1.76
19	Potamos	181	57.5	2.06	6.50	1.49
20	Aradaina Gorge	69	42.46	1.52	2.48	1.88
21	Sfakiano Gorge	96	43.12	1.51	3.37	1.52

Table 4.9: Geomorphic indices associated with stream network aspects.

iv) Geomorphic indices associated with drainage basin aspects regarding geometry/shape and regional tilting.

The geomorphic indices in Table 4.10 are the ones to characterize the geometry and shape of drainage basins, as elongated basins are indicative of tectonic control influencing their development. In addition, acquisition of information considering the tilting of the drainage basin, erosional status and incision degree of a basin as a whole can be determined either. A quantitatively evaluation of the asymmetry of a drainage basin can be examined against the rest of the indices to determine basins where tectonic control has a higher degree impact in their development and deformation.

The calculation of the indices that reveal information regarding the geometry and shape of a basin can be useful in determining regions of higher potential tectonic control. Lower values of elongation ratio (Re) characterize basins 8, 15, 6, 5 and 11, implying elongated basins and high tectonic activity, while circular basins 12, 13 and 17 inactive ones. The basin circularity (Rc) low values characterized basins 6, 8, 11, 15 and 21, revealing their strongly elongated shape, with more quadrangular basins indicated by higher values of the index, such as basins 13, 3, 12 and 17. The form factor (Rf) lower values were observed in basins 5, 6, 8, 11 and 15, indicating elongated basins with less side flow for shorter duration and high main flow for longer duration takes place, resulting in low peak flows for longer duration. On the other hand high values of Rf index were determined for basins 2, 12, 13, 17 and 18, characterizing circular basins with high side þow for longer duration and low main þow for shorter duration, causing high peak þows in a shorter duration. The drainage basin index (Bs) showed that basins such as 9, 12, 13 and 17 had low index values, associated with more circular basins. The high Bs values were observed in basins 6, 8, 15 and 19, indicating high elongation, continuing rapid uplift and tectonic activity presence

Drainage basin asymmetry was revealed by the asymmetry factor (AF). The results indicate the tilting direction of the drainage basins (Fig. 4.4). With AF>50%, there is tilting to the left downstream, while with AF<50%, there is tilting to the right towards the downstream. In the figure 4.4 the relative degree of tilting is presented, with white arrows show the tilting orientation with regard to the

mainstream direction. Based upon the AF index outcomes, it is observed that AF results indicate the tilting direction of the drainage basins (Fig. 4.4). With AF>50%, there is tilting to the left downstream, while with AF<50%, there is tilting to the right towards the downstream. White arrows show the tilting orientation with regard to the mainstream direction (Fig. 4.4). The absolute difference (AF-50) and its classification (used to evaluate the highest tectonic tilting of the drainage basins) is presented in Table 4.10, regarding observed threshold values. The values range from 1 to 35 and 3 classes are discriminated indicating relative high (Class 1), moderate (Class 2) and low (Class 3) active tectonics (Table 4.10). As described in methodology, higher deviation value (no close to 0) explains higher tectonic activity processes present within the basin.

The calculation and classification of hypsometric integrals (HI) for the drainage basins of the study area is presented in figure 4.5. The green areas represent basins with deep incision and slight soil erosion; yellow basins are in the intermediate stage, with moderate incision and erosion (maximum threshold 50%), while the red basins are in the severe stage of erosion, with low relief (maximum threshold 35%) (Fig. 4.5). The HI implies to high rates of tectonic activity and provides high relief when the index exceeds 0,5 values, such as basins 2, 14, 15, 18, 19 and 21. Lower values of HI (<0.35) characterise basins 1, 6, 9, 10, 11 and 12, indicating their mature stage with low relief and undergoing severe erosion (Fig. 4.5).

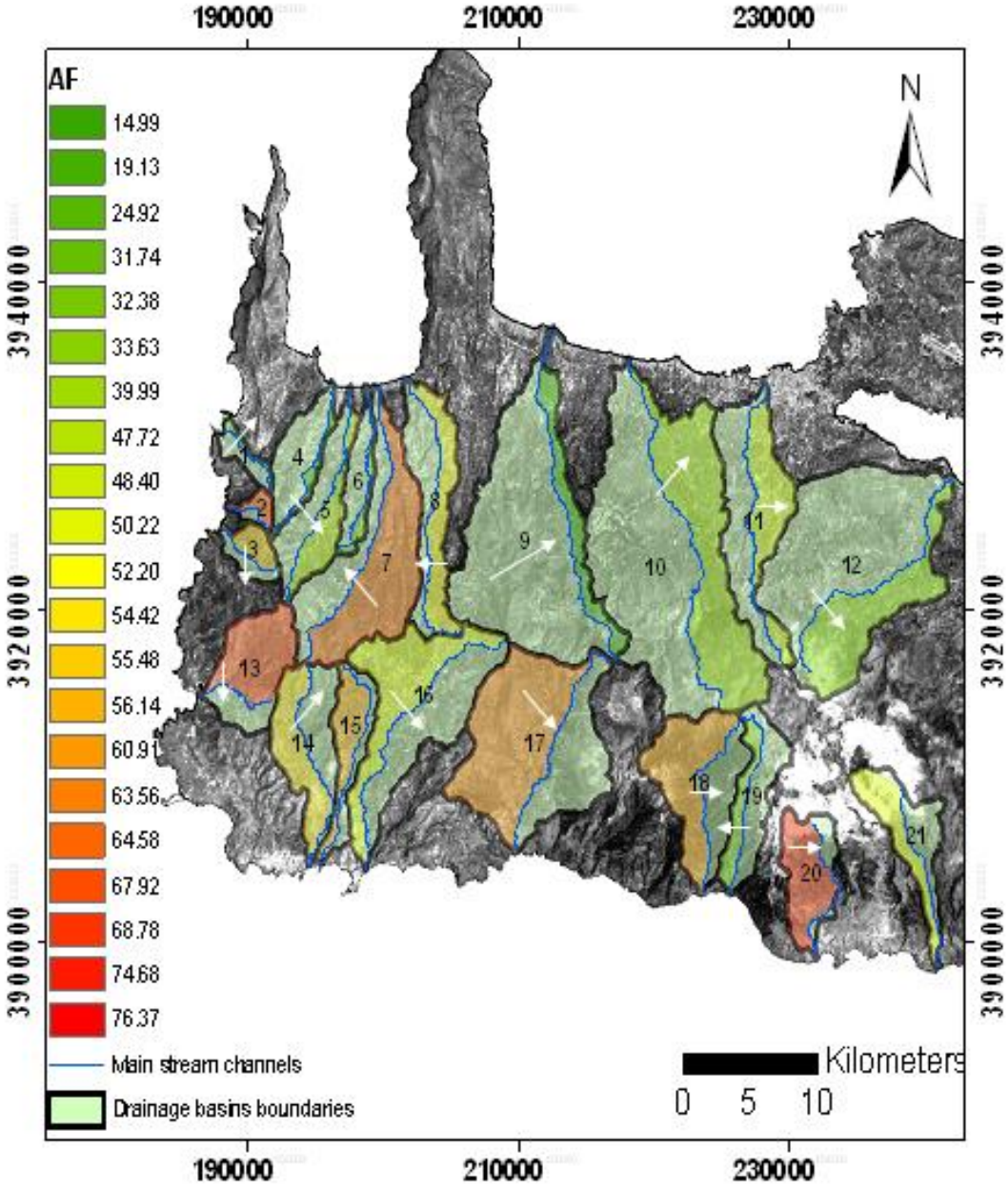

Fig. 4.4: The AF (%) index, with the values indicating the level of tilting. It is notable that drainage basins with westward tilting are surrounded by basins with eastwards tilting (basins 7, 8, 19), indicating zones of high structural control. White arrows show the tilting orientation with regard to the mainstream direction.

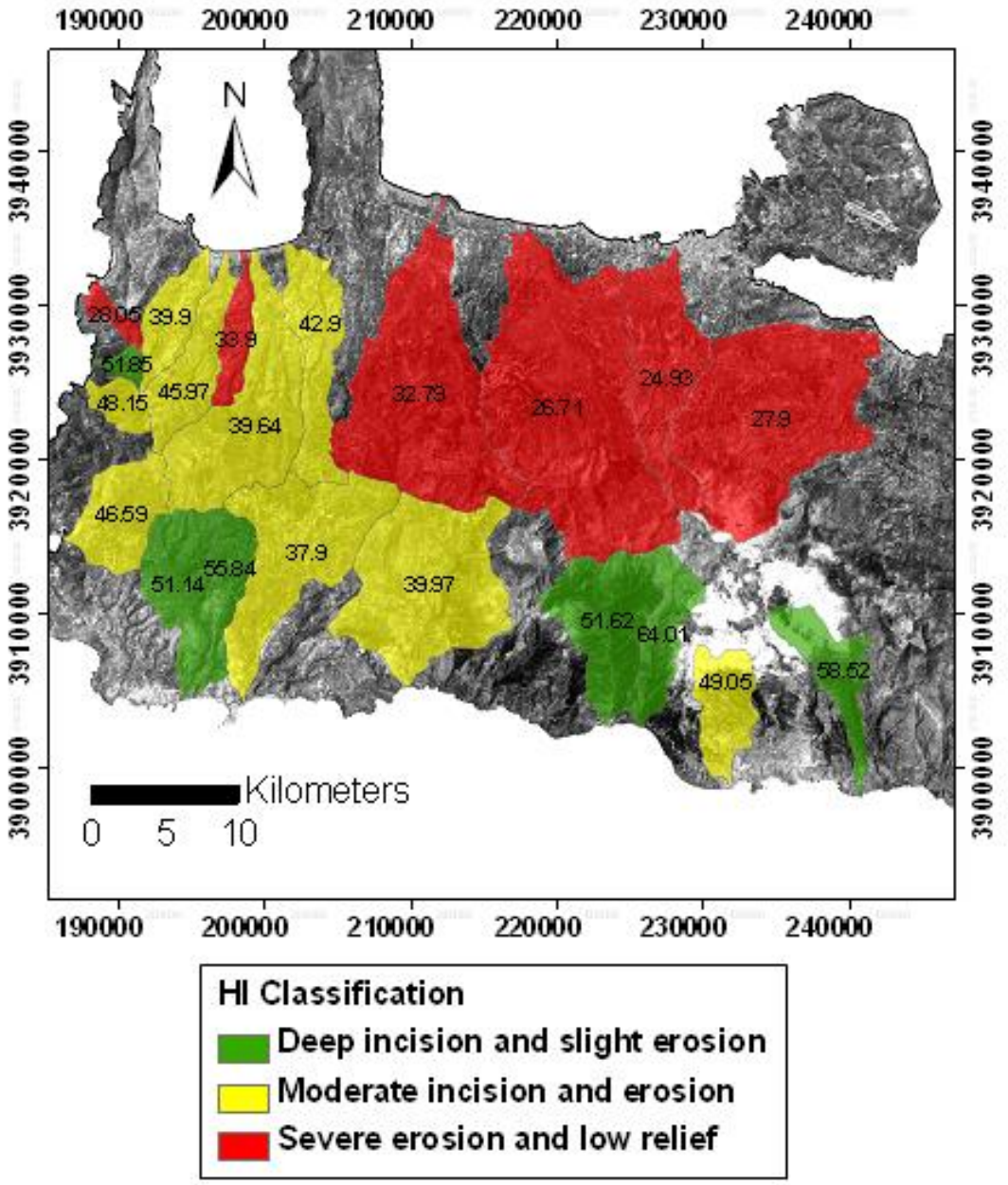

Fig. 4.5: Hypsometric integral evaluation. The areas of well defined deep incision and slight erosion in basin as a whole are the drainage basins that are associated with higher tectonic activity (due to erosion not being the underlying, principle factor).

Basin ID	Re	Rc	Rf	Bs	HI %	AF				Class
						Ar (km^2)	At (km^2)	AF (km^2)	AF-50	
1	0.55	0.41	0.23	2.17	28.0	1.71	6.86	24.92	-25.07	1
2	0.67	0.48	0.35	1.58	51.8	3.281	4.77	68.78	18.78	2
3	0.63	0.64	0.32	1.51	48.1	5.996	10.68	56.14	6.14	3
4	0.49	0.49	0.19	2.75	39.9	4.31	22.52	19.14	-30.86	1
5	0.43	0.37	0.14	2.42	45.9	15.13	31.7	47.72	-2.27	3
6	0.39	0.33	0.12	4.64	33.9	4.87	15.34	31.74	-18.25	2
7	0.51	0.41	0.21	1.83	39.6	51.66	76.06	67.92	17.92	2
8	0.36	0.29	0.11	3.85	42.9	22.59	41.51	54.42	4.42	3
9	0.54	0.41	0.23	1.47	32.8	19.62	130.87	14.99	-35.01	1
10	0.61	0.43	0.29	2	26.7	72.24	180.62	39.99	-10	2
11	0.43	0.31	0.15	2.78	24.9	27.81	57.46	48.40	-1.592	3
12	0.64	0.59	0.32	1.3	27.9	43.59	129.61	33.63	-16.36	2
13	0.77	0.66	0.47	0.96	46.6	26.40	35.36	74.68	24.68	1
14	0.49	0.47	0.19	2.39	51.14	22.43	40.42	55.49	5.49	3
15	0.36	0.3	0.1	3.53	55.8	14.2	23.31	60.91	10.918	2
16	0.5	0.36	0.2	1.59	37.9	38.89	77.43	50.22	0.226	3
17	0.74	0.58	0.43	1	39.9	63.51	98.33	64.59	14.59	2
18	0.68	0.56	0.36	1.31	51.6	32.77	51.56	63.56	13.567	2
19	0.46	0.36	0.17	2.91	64.0	9.01	27.82	32.38	-17.61	2
20	0.51	0.52	0.19	1.95	49.0	21.22	27.79	76.37	26.376	1
21	0.45	0.3	0.16	2.84	58.5	14.88	28.5	52.20	2.207	3

Table 4.10: Geomorphic indices associated with regional drainage basin aspects for the basins as a whole, in order to determine regional tectonic control.

v) Interrelationships of geomorphic indices that are not in accordance with published studies

Among the various interrelationships that were examined for the geomorphic indices in this study, a few of them were not in accordance with related published studies. Their interpretation can offer new insights about the examined basins.

The hypsometric integral (HI) against the area (A) was tested to check whether their relationship accorded with conclusions drawn by Willgoose and Hancock (1998) and Hurtrez et al. (1999). These authors suggested that in small basins the hypsometric curve is convex and the value of the hypsometric integral (HI) approaches unity, indicating a predominance of hillslope processes, whereas in larger basins the curves are concave, the integral approaches zero and þuvial processes predominate. In this study, in all cases, a negative correlation is observed, indicating that small basins have a convex hypsometry, whilst larger ones are concave. This statistically relation is observed for the complete set of the basins (Fig. 4.6). Despite that however, some of the basins in this study do not follow this interpretation as it is not in accordance with the dominant processes (Fig. 4.6). There are small basins, such as Metoxi, where low hypsometric integrals (<0.5) are observed, while on the other hand there are quite large basins such as Sarakiniotis, where high hypsometric integrals (HI) are preserved (see Fig. 4.5). Below this fact is related with drainage densities (Dd) observations, to determine whether fluvial processes or other exogenous factors such as tectonics are the predominant processes.

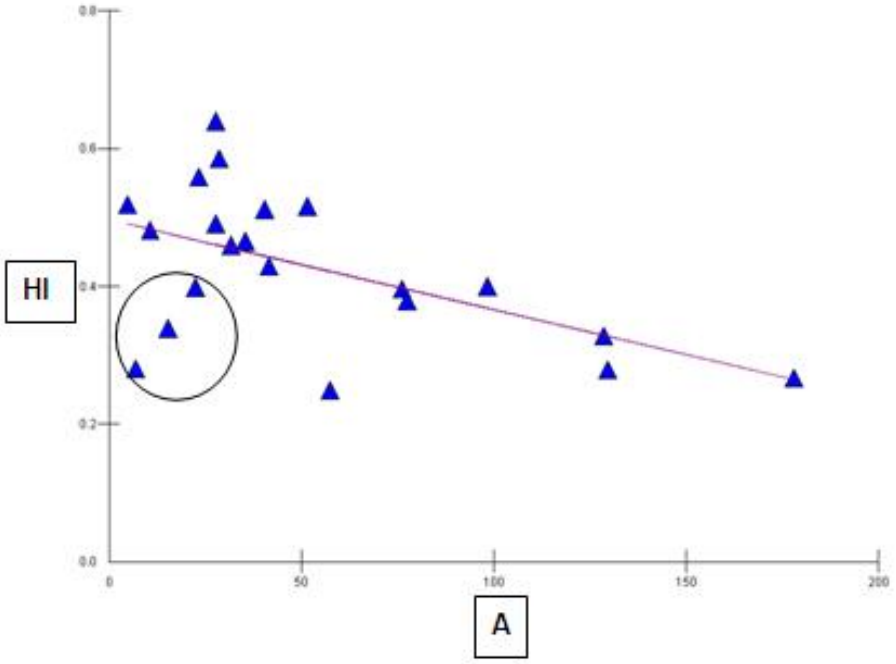

Fig. 4.6: Graphical plot of HI against A. Negative correlation is observed indicating that small basins have a convex hypsometry, whilst larger ones are concave. Presence of few basins is not in accordance with the statement corresponding in the negative correlation (see black circle).

Segura et al. (2007) studied basins in South Menorca, Spain by using hypsometric integrals and came across basins that were not in accordance with the dominant processes, as proposed by Willgoose and Hancock (1998) and Hurtrez et al. (1999). Some basins had low values for hypsometric integral (HI) and drainage density (Dd) indicating that fluvial processes were not responsible for the low relief, while other basins revealed high values of HI and Dd. Despite that, the relation between Dd and HI in Segura (2007) study was in fact zero, as the p-value of this relation was 0.88, indicating that the relation was not statistically signiýcant. This issue in his study suggested that the hypsometric integral of these basins was not fundamentally dependant on þuvial processes, but likewise not dependant on hillslope processes either (Segura, 2007). The graphical plot of HI-Dd in our case is not in accordance with the dominant processes, as proposed by Willgoose and Hancock (1998) and Hurtrez et al. (1999), but itûs not in accordance with Segura (2007) remarks either, as the p-

value of this relation is 0.023, following a negative correlation and indicating that the relation is statistically significant (see Fig. 4.7). That suggests that for the study area, in this research, the HI values are dependent on Dd values. A closer view of the graphical plot clearly reveals some outliers, where for high drainage densities (Dd) there are some basins with high hypsometric integrals (HI) (see Fig. 4.7). This can imply that in these basins, such as Sarakiniotis, fluvial processes are dominated by hillslope processes. Similarly, there are basins with low HI values (<0.5) and low Dd values (<2.5) (such as the Metoxi-Platanos small basin), indicating that no fluvial processes are responsible for the low relief. Especially the fact that the basins overly on impermeable rock formations indicate that exogenous factors such as hillslope processes/ tectonics are the predominant processes to develop the basin. The basins with above observations are of higher interest for investigating the potential tectonic processes taking place, with regard to other basins that follow the dominant processes, as proposed by Willgoose and Hancock (1998) and Hurtrez et al. (1999). Such basins are Tauronitis where low HI values and high Dd values are observed and which overly in impermeable rock formation indicating that fluvial processes are predominant. In addition, basins with high HI values and low Dd values, such as Sfakiano Gorge and Aradaina, owe their high relief due to the absence of streams development. These basins overly on permeable rock formations and as a result incised gorges are predominantly developed. It is clearly discriminated, that the first two cases do not follow the negative correlation of HI-Dd probable due to tectonic signal dominating the fluvial processes, while the latter two cases do follow the negative correlation of HI-Dd graphical plot (see Fig. 4.7).

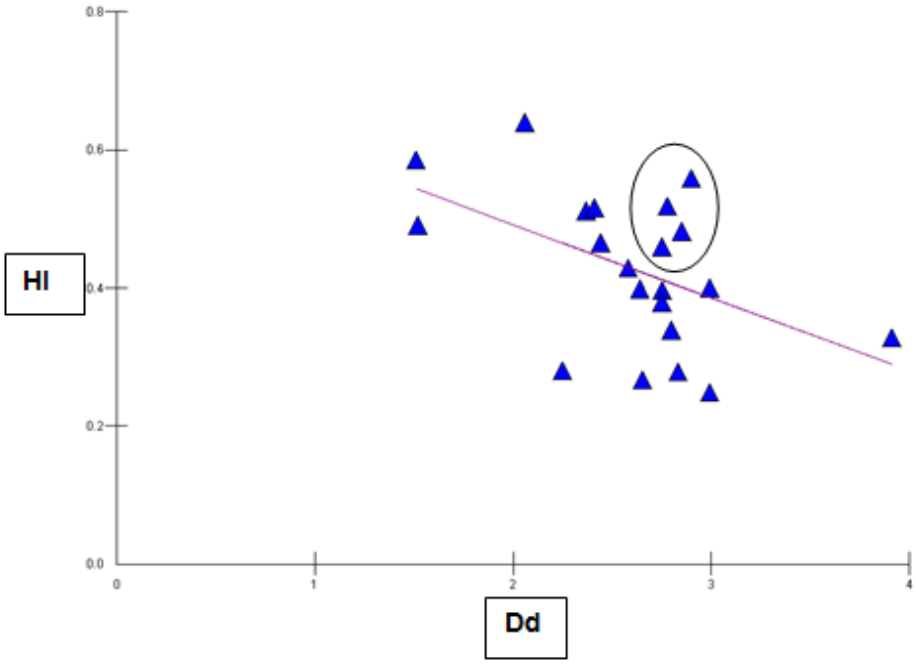

Fig. 4.7: Graphical plot of HI against Dd. Negative correlation is observed indicating that increase in Dd leads to decrease of HI. Presence of few basins is not in accordance with the statement corresponding in the negative correlation (see black circle).

Regarding the Al-Sulaimi (1997) study, low negative correlation is observed between relief ratio and area, perimeter, basin length, number of streams and total stream length, with a moderate positive correlation observed regarding relief ratio with drainage density and drainage frequency. The latter correlation indicates that any increase of Dd or Fu factors lead to relief increase. Relative relief (as a consequence relief ratio either) is one of the main morphological factors controlling drainage density (Strahler, 1964). Strahler (1964) noted that low Dd is favored where basin relief is low, while high Dd is favored where basin relief is high. In this study the relief ratio (Rr) is not in accordance with either Strahler (1964) or Al-Sulaimi (1997) studies regarding its relation with drainage density (Dd) or drainage frequency (Fu) (see Fig. 4.8 a, b). Relief ratio (Rr) in this study follows a negative correlation with these indices, indicating that the higher the drainage density is; then the lower the relief ratio occurs. Few of the basins

characterized by high drainage densities are associated with either high relief or low relief (see Fig. 4.8 a). The basins characterized by high values of drainage density and relief, can imply to basins associated with possible regional uplift.

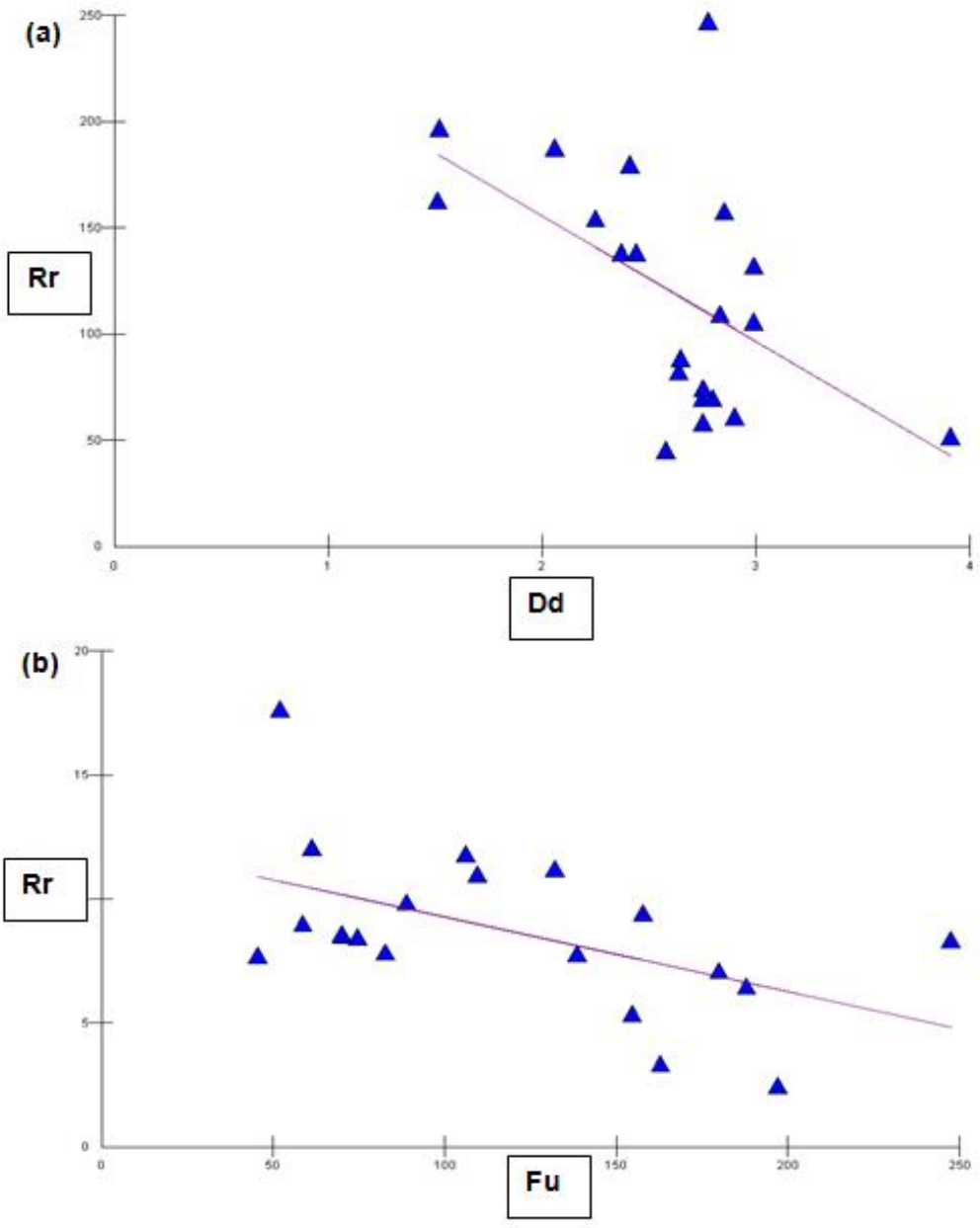

Fig. 4.8 a, b: Moderate negative correlation observed between relief ratio (Rr) with drainage density (Dd) and drainage frequency (F). The relation is not in accordance with Strahler (1964) and Al-Sulaimi (1997) study, where moderate positive correlation was observed.

4.6 Multicriteria modeling of regional neotectonic control

This section aims to discriminate and interpret the relations among the various geomorphic indices used in this chapter. This procedure will provide the manageable stages to isolate and detect which basins owe their development to tectonic control factors. Interrelationships and statistical analysis of the indices are examined to extract meaningful information.

Initially, the correlation coefficient matrix was composed for all the geomorphic indices (Table 4.11). At first sight, the correlation coefficient matrix is in accordance with observations made by Al-Sulaimi (1997) regarding interrelationships of geomorphic indices. The indices of area, basin length, perimeter of basins, total length of streams and total number of streams have a high positive correlation (Ó0.8) (Table 4.11). The stream frequency (Fu) is highly correlated with drainage density, number of streams and total stream length. The drainage density has a strong correlation with stream frequency and number of streams. The strong positive relationship that exists between area, perimeter, basin length, total stream number and total stream length, provides a means of grouping the different basins into distinct groups, based on the identifiable ranges for the different indices, as suggested by Al-Sulaimi (1997). In order to investigate the possibility of grouping the basins and eliminating statistically irrelevant data, this study uses Factor Analysis to reduce data and identify components that will provide easier interpretation of the relations of the various geomorphic indices. All geomorphic indices were used as variables in the factor analysis and the outcomes provided the distinguishing components (Table 4.12).

The Factor Analysis (FA) was carried out using the SPSS statistical analysis software. It is mainly applied to reduce the number of indices, so those selected for retention in the future can be more meaningful (Yevjevich et.al, 1972). Goddard & Kirby (1976) and Dyhr-Nielson (1971) recommend that components with eigenvalues more than 1 should be used. In this study four components are recognized with greater eigenvalues than 1, characterized by almost 87% of variance (see Fig. 4.10). The scree plot in figure 4.10 shows that the first four components are those containing most of the information (regarding percentage of variance and eigenvalues) and those have been retained for the factor analysis.

Within factor analysis, the Kaiser-Meyer-Olkin function measures the sampling adequacy: it should be greater than 0.5 for a satisfactory factor analysis to proceed and in this study it is 0.557. The final stage of factor analysis consists of data rotation to reduce the number factors on which the variables under examination have high loadings and identify distinctive clusters of variables (Goddard, & Kirby, 1976). Rotation of the data makes the interpretation of the analytical results easier.

The Factor Analysis, results show that the first 4 components explain 87% of the variance while the first 8 components explain 98% of the variance (see Figure 4.10). After the rotation of data, only the first 4 components are of important significance (see Table 4.12 - only coefficients greater than 0.5 are shown). The rest of the components (5-16) mainly include a single index for each component (Table 4.12). Such single individual components do not offer any significant grouping of factors. That aspect coincides with the studies of Goddard & Kirby (1976) and Dyhr-Nielson (1971), as their eigenvalues less than 1 are excluded from further interpretation (Yevjevich et.al, 1972). Each of the final 4 components is associated with characteristic information that is provided by the contained indices (see details above) (Table 4.12). These reveal overall that:

i) Component 1: contains information regarding basin size and extent

ii) Component 2: contains information regarding basin shape and geometry

iii) Component 3: contains information regarding basin relief

iv) Component 4: contains information regarding hillslope or fluvial processes and tilting.

Given that the aim of this chapter is to identify which drainage basins are under a high degree of tectonic control, the selected criteria were:

i) elongated shape of basin;

ii) high or low relief (depending on dominant processes, either tectonic control or ongoing uplift) and;

iii) hillslope processes and geological structures dominant in basin development, relative to fluvial processes (Burbank & Anderson, 2000; Molin et al., 2004; Sougnez & Vanacher, 2011).

Those criteria can be explained and associated only by the extracted components of Factor Analysis 2, 3 and 4 (see Table 4.12). Those components provide more

meaningful information regarding the tectonic control of the drainage basins. Component 1 was excluded from the subsequent AHP analysis (described below) because it only contained general information regarding the basin size and extent (i.e. minimal information about tectonic control). Although component 1 gives a high percentage of variance (41%), this is mainly because the calculation of the rest of the indices is dependent on the indices consisting of that particular component (see Table 4.1 to 4.4). Such dependency leads to high correlation among the indices (see Table 4.11), which explains the high percentage of variance.

The factor analysis used the geomorphic indices as input variables to distinguish the indices in four final components (see Table 4.12). The indices within each selected component (2, 3 & 4), were ranked, as described in the ñMulticriteria modeling of regional neotectonic controlò section (page 4.17). Ranking was based on Tables 4.7-4.10, in order that prior values indicate highest elongation, highest relief and highest hillslope/tectonic processes attribute information respectively (see Table 4.13). As referred to the methodology section (see page 4.17-4.18), that kind of ranking is common when dealing with a large number of geomorphic indices, offering a useful tool for planning and development of drainage basins (Biswas et al., 2002; Singh et al., 2005; Rekha et al., 2011). In this study, instead of computing the arithmetic mean compound value of the indices, as shown in Table 4.13, an Analytic Hierarchy Process (AHP) was used for discriminating basins with higher degrees of neotectonic control. This part of the methodology is summarised on a step by step basis in Figure 4.9.

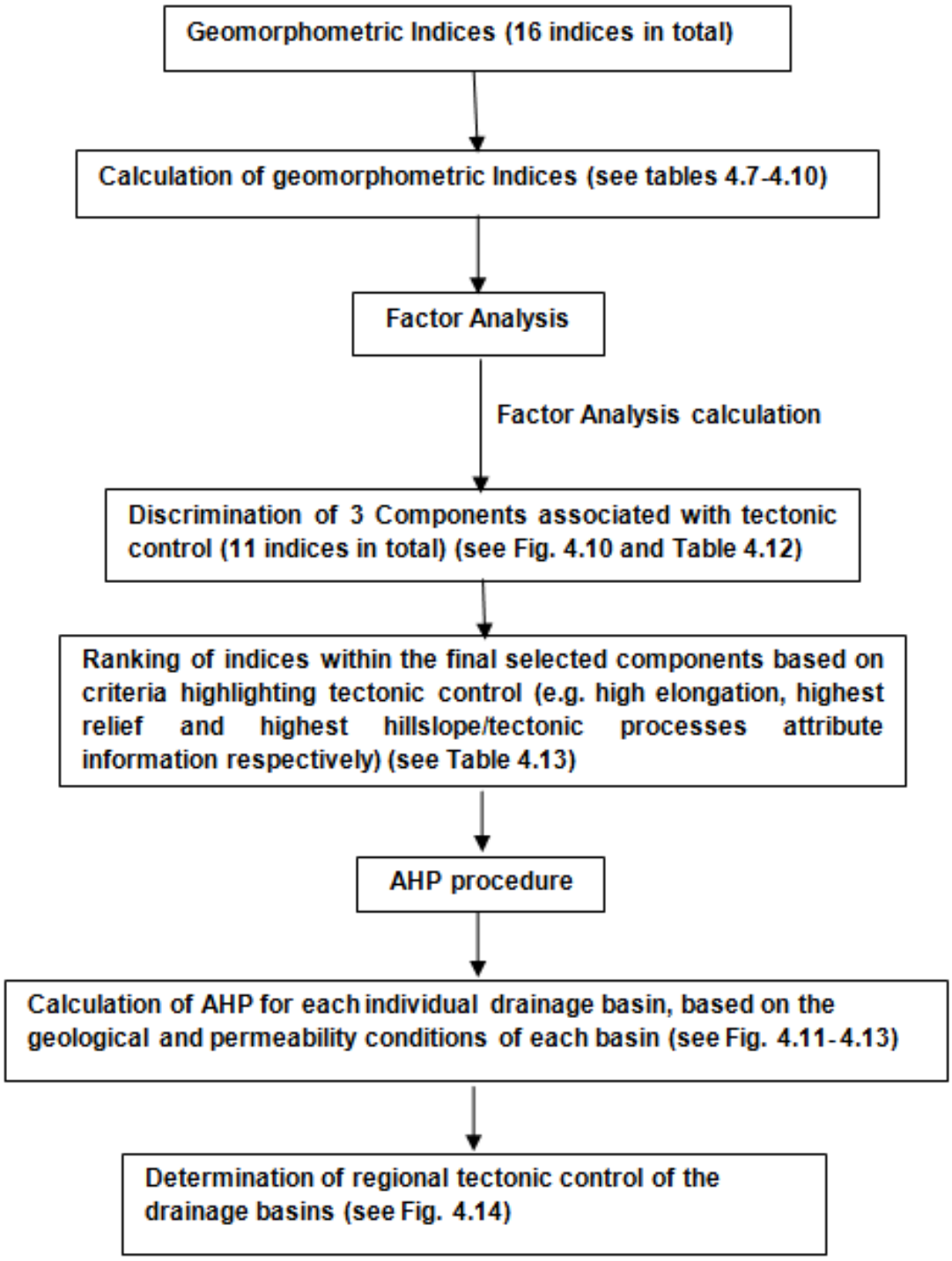

Fig. 4.9: Schematic diagram, showing how regional tectonic control of the drainage basins is determined from an initial number of geomorphometric indices, by using factor analysis and AHP procedures.

These ranked indices were used to the analytical hierarchy process (AHP) procedure in order to discriminate the basins into four groups: very high, high, moderate and low priority, with regard to tectonic control on basin development.

With the AHP method, the judgements can be trustworthy if they are not too close for comfort to randomness. This can be ensured if the consistency ratio is less than 0.1. In this study all extracted preference matrices are acceptable (Cr< 0.1) and no revision of preference values is needed. In the following paragraphs the different geological and permeability conditions of few basins are discussed. These conditions are considered in the AHP for the representative criteria of weights to be determined by the preference matrix. As soon as the preference matrix is completed for each basin and the criteria of weights are determined, then a final value for each basin is extracted. The lower this value is, the higher the degree of tectonic activity within each basin. This is due to the fact that the initial ranking took place regarding the highest basin elongation, highest relief and highest degree of hillslope processes. This indicates that basins with the highest final ranked value will represent those associated with neotectonic control.

The western basins of the study region (i.e. 4, 5, 6, 8, 14 and 15), are the ones characterized by regional neotectonic control (see Fig. 4.14), investigated in Chapter 5. The selected basins fit the criteria documented at the beginning of this chapter which imply neotectonic control. More details are provided below about the completion of the preference matrix for the more representative drainage basins.

Correlation Matrix	P	Area	Rb	Fu	Dd	Re	Rf	Rc	R	Rr	Lb	SLu	Nu	HI	Bs	AF
P (km)	**1.000**	.929	.335	.519	.390	-.012	-.017	-.197	.431	-.550	.956	.907	.867	-.479	-.167	-.208
Area (km^2)	.929	**1.000**	.437	.535	.421	.281	.261	.100	.436	-.383	.812	.972	.935	-.547	-.383	-.216
Rb	.335	.437	**1.000**	.283	.278	.224	.191	.068	.231	-.052	.228	.436	.435	-.834	-.202	-.267
Fu	.519	.535	.283	**1.000**	.952	.073	.101	-.014	-.178	-.527	.500	.678	.737	-.430	-.148	-.323
Dd	.390	.421	.278	.952	**1.000**	.096	.124	.018	-.374	-.540	.373	.573	.626	-.491	-.144	-.325
Re	-.012	.281	.224	.073	.096	**1.000**	.992	.868	.206	.476	-.268	.259	.241	-.086	-.863	.290
Rf	-.017	.261	.191	.101	.124	.992	**1.000**	.857	.171	.436	-.264	.241	.223	-.064	-.826	.328
Rc	-.197	.100	.068	-.014	.018	.868	.857	**1.000**	.101	.424	-.367	.078	.068	.004	-.754	.293
R	.431	.436	.231	-.178	-.374	.206	.171	.101	**1.000**	.342	.332	.331	.287	.067	-.274	.103
Rr	-.550	-.383	-.052	-.527	-.540	.476	.436	.424	.342	**1.000**	-.680	-.433	-.425	.468	-.355	.360
Lb	.956	.812	.228	.500	.373	-.268	-.264	-.367	.332	-.680	**1.000**	.800	.766	-.427	.051	-.229
SLu	.907	.972	.436	.678	.573	.259	.241	.078	.331	-.433	.800	**1.000**	.990	-.571	-.383	-.305
Nu	.867	.935	.435	.737	.626	.241	.223	.068	.287	-.425	.766	.990	**1.000**	-.562	-.364	-.357
HI	-.479	-.547	-.834	-.430	-.491	-.086	-.064	.004	.067	.468	-.427	-.571	-.562	**1.000**	.093	.438
Bs	-.167	-.383	-.202	-.148	-.144	-.863	-.826	-.754	-.274	-.355	.051	-.383	-.364	.093	**1.000**	-.281
AF	-.208	-.216	-.267	-.323	-.325	.290	.328	.293	.103	.360	-.229	-.305	-.357	.438	-.281	**1.000**

Table 4.11: Correlation coefficient matrix of the drainage basins geomorphometric indices, as extracted in GIS environment (those closer to 1 are the most correlated).

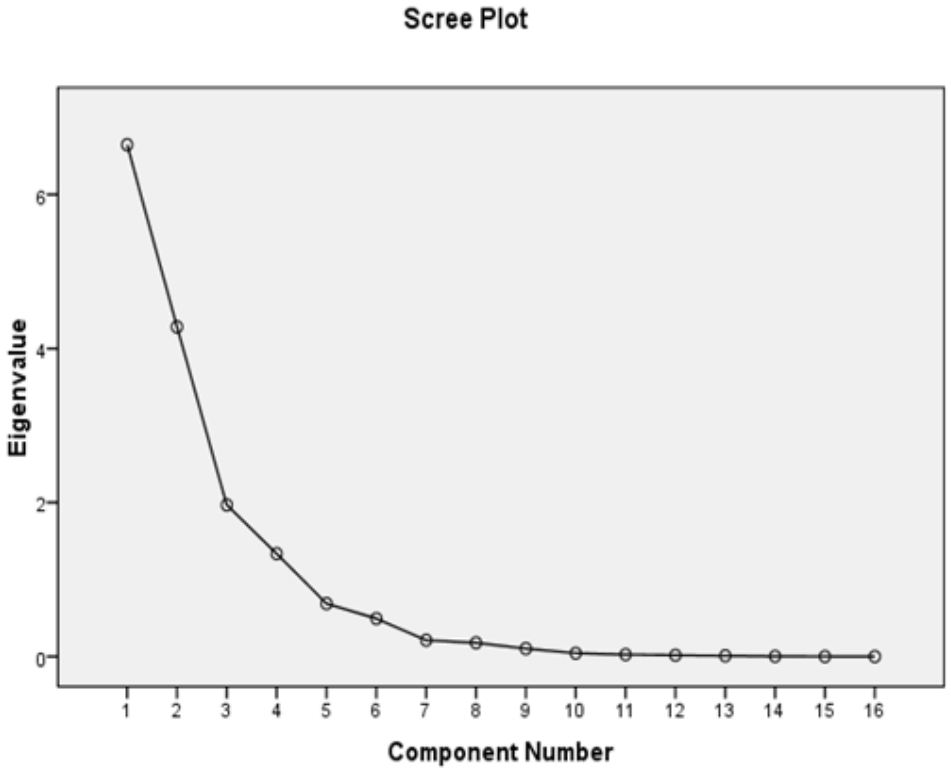

Component	Initial Eigenvalues	
	Total	% of Variance
1	6.648	41.548
2	4.281	26.756
3	1.968	12.301
4	1.335	8.344
5	.687	4.294
6	.492	3.076
7	.212	1.323
8	.178	1.114
9	.102	.640
10	.043	.268
11	.026	.160
12	.016	.102
13	.009	.056
14	.003	.017
15	.000	.003
16	.000	.001

Fig. 4.10: The scree plot shows that the first four components are those containing most of the information (regarding percentage of variance) and those are expected to be retained in final stage of factor analysis.

Rotated Component Matrix

	Component															
	1	2	3	4	5	6	7	8	9	10	11	12	13	14	15	16
P (km)	.975													-.043		
Area (km²)	.924											.089		.030		
Rb				.900												
Fu			.759										.086			
Dd			.865										-.085			
Re		.982													-.016	
Rf		.971													.016	
Rc		.909							.345							
R			-.749		.847											
Rr			-.574				.559									
Lb	.924											-.099				
SLu	.902															.011
Nu	.867										.146					
Hl				-.851						.164						
Bs		-.891						.432								
AF				-.562		.916										

Table 4.12: Factor analysis of the geomorphic indices (regional scale), discriminated and grouped the indices in four main components. Each component refers to particular information that can be acquired by the associated indices. The discrimination and identification of the four components can be associated with the following information:

Component 1: Basin size/extent

Component 2: Basin shape/geometry

Component 3: Basin relief

Component 4: Hillslope or fluvial processes and tilting

ID basin	Component 3				Component 2				Component 4		
	ID Rr	ID R	ID_Fu	ID_Dd	ID Bs	ID_Re	ID_Rf	ID_Rc	ID HI	ID_Rb	ID AF
1	7	20	19	18	10	14	13	11	18	20	4
2	1	18	12	8	15	18	18	14	4	11	6
3	6	17	7	5	16	16	16	20	8	12	15
4	14	19	13	13	7	8	8	15	13	8	2
5	16	14	10	9	8	4	4	8	10	6	18
6	17	21	9	7	1	3	3	5	16	15	7
7	19	13	8	10	13	10	11	10	14	13	8
8	21	15	16	14	2	1	1	1	11	7	17
9	20	10	1	1	17	13	14	9	17	16	1
10	13	6	6	12	11	15	15	12	20	19	14
11	12	7	3	2	6	5	5	4	21	21	20
12	11	3	5	6	19	17	17	19	19	17	10
13	9	11	15	15	21	21	21	21	9	5	5
14	8	12	14	17	9	9	9	13	6	4	16
15	18	16	2	4	3	2	2	3	3	2	13
16	15	9	11	11	14	11	12	6	15	9	21
17	10	8	4	3	20	20	20	18	12	18	11
18	4	5	17	16	18	19	19	17	5	10	12
19	3	1	18	19	4	7	7	7	1	1	9
20	2	2	21	20	12	12	10	16	7	14	3
21	5	4	20	21	5	6	6	2	2	3	19

Table 4.13: Ranking of indices within each factor analysis component**.**

In the AHP method the level of importance of the preference values, among the indices, was based on the geological and permeability conditions of each basin (see Fig. 2.7 and Appendix II Fig. 2). For instance, high rock resistance and permeable bedrock will result in relief being the dominant factor of basin development. A range of values from 1 to 9, describing the intensity of importance, will be used for completing the pair-wise preference matrix (see Table 4.5).

For example, the Arapi basin, (Figure 4.14, basin 8) has formed over weak Neogene bedrock with low permeability. Its drainage density (Dd) and drainage frequency (Fu) indices will be of ñhigher importanceò in the pairwise preference matrix relevant to relief indices (such as Rr and R), as they will be dominant in basin development. For that reason Dd and Fu have a ñstrong importanceò (value 5 in pairwise preference matrix) over relief. As Dd and Fu are important factors in this basin, ñequal importanceò (value 1 in the pairwise preference matrix) was selected for indices such as Re, Rf, Rc and Bs, as the basin shape will be dependant in Dd and Fu. The index of Rb is also dependent on the drainage network, so because Dd and Fu are important factors, then ñequal importanceò (value 1) will be the appropriate selection within the preference matrix. The Rb index, as the factor analysis showed, is associated with the HI and AF indices, as information regarding the degree of neotectonic activity can be determined. As these indices are within the same component as provided by the factor analysis then ñequal importanceò (value 1) is predominant in the preference matrix. The HI is an index associated with relief and degree of incision by the drainage network, but that basin, due to its characteristics in geology and permeability, will have a ñmoderate importanceò relative to relief indices (Rr, R) (value 3 in pairwise preference matrix). The AF index can reveal whether migration of drainage is dependent in tectonic activity, as the drainage network pattern develops basin shape. The AF index - apart from the relief indices (Rr and R), which are not dominant in this basin (and so are of ñmoderate importanceò with value 5 in pairwise preference matrix) - has almost ñequal importanceò with the rest of the indices (value 1 in pairwise preference matrix). Indices Rb, AF and HI are significant in the Arapi basin as the geological conditions are suitable for neotectonic deformation to be determined. The AHP results for Arapi basin are presented in figure 4.11.

[Preference Matrix]

	Rb	HI	AF	Re	Rf	Rc	Bs	Dd	Fu	Rr	R
Rb	1	1	1	1	1	1	1	1	1	5	5
HI	1	1	1	1	1	1	1	1	1	3	3
AF	1	1	1	1	1	1	1	1	1	5	5
Re	1	1	1	1	1	1	1	1	1	5	5
Rf	1	1	1	1	1	1	1	1	1	5	5
Rc	1	1	1	1	1	1	1	1	1	5	5
Bs	1	1	1	1	1	1	1	1	1	5	5
Dd	1	1	1	1	1	1	1	1	1	5	5
Fu	1	1	1	1	1	1	1	1	1	5	5
Rr	0.2	0.3333	0.2	0.2	0.2	0.2	0.2	0.2	0.2	1	1
R	0.2	0.3333	0.2	0.2	0.2	0.2	0.2	0.2	0.2	1	1

Eigenvalues	**Eigenvector of largest Eigenvalue**	**Criteria weights**	**Consistency ratio Cr (revision of preference values if Cr> 0.1)**
11.035	0.3344	0.107 (Rb)	0.0023
-0.0175	0.3088	0.0988 (HI)	
-0.0175	0.3344	0.107 (AF)	
0	0.3344	0.107 (Re)	
0	0.3344	0.107 (Rf)	
0	0.3344	0.107 (Rc)	
0	0.3344	0.107 (Bs)	
0	0.3344	0.107 (Dd)	
0	0.3344	0.107 (Fu)	
0	0.0706	0.0226 (Rr)	
0	0.0706	0.0226 (R)	

Fig. 4.11: The AHP results for Arapi basin.

Similarly, by examining geological and permeability conditions in the Pelekaniotis basin (Figure 4.14, basin 14), it is observed that the drainage network developed over Phyllite-Quartzite bedrock (moderate hardness and low permeability). So the Dd and Fu indices will be of high importance with relevance to relief indices, as they will dominate the basin development. For that reason Dd

and Fu are of ñstrong importanceò over relief indices (value 5 in the pairwise preference matrix). As Dd and Fu are important factors in this basin, of ñequal to moderate importanceò is selected with indices such as Re, Rf, Rc and Bs (value 2 in the pairwise preference matrix). This is due to the basinôs shape being dependant on Dd and Fu, but the moderate bedrock hardness prevents the ñequal importanceò option from being selected. The index of Rb is dependent on the drainage network, so as long as Dd and Fu are important factors then ñequal to moderate importanceò will be the appropriate selected option in the preference matrix. As mentioned earlier, factor analysis revealed that the Rb index is associated with the HI and AF indices, because information can be determined regarding the degree of neotectonic deformation. For that reason ñequal importanceò is selected for these indices in the preference matrix. The HI is an index associated with relief and degree of incision by the drainage network. In the Pelekaniotis basin, due to its geology and permeability, will have an ñequal to moderate importanceò to ñmoderate importanceò in the preference matrix relative to other indices. The AF index has ñequal to moderate importanceòwith the rest of the indices (value 2 in the pairwise preference matrix). As the drainage network pattern develops basin shape, the AF index can reveal whether migration of drainage is dependent in neotectonic activity. Indices Rb, AF, and HI are significant as the geological conditions are suitable for tectonic processes to be determined. The AHP results for Pelekaniotis basin are presented in figure 4.12.

[Preference Matrix]

	Rb	Hi	Af	Re	Rf	Rc	Bs	Dd	Fu	Rr	R
Rb	1	2	2	3	3	3	3	2	2	5	5
Hi	0.5	1	2	3	3	3	3	2	2	3	3
Af	0.5	0.5	1	2	2	2	2	2	2	5	5
Re	0.3333	0.3333	0.5	1	1	1	1	2	2	5	5
Rf	0.3333	0.3333	0.5	1	1	1	1	2	2	5	5
Rc	0.3333	0.3333	0.5	1	1	1	1	2	2	5	5
Bs	0.3333	0.3333	0.5	1	1	1	1	2	2	5	5
Dd	0.5	0.5	0.5	0.5	0.5	0.5	0.5	1	1	5	5
Fu	0.5	0.5	0.5	0.5	0.5	0.5	0.5	1	1	5	5
Rr	0.2	0.3333	0.2	0.2	0.2	0.2	0.2	0.2	0.2	1	1
R	0.2	0.3333	0.2	0.2	0.2	0.2	0.2	0.2	0.2	1	1

Eigenvalues	Eigenvector of largest Eigenvalue	Criteria weights	Consistency ratio Cr (revision of preference values if Cr> 0.1)
11.7292	0.5629	0.1943 (Rb)	0.0486
-0.0237	0.4766	0.1645 (HI)	
-0.0237	0.3625	0.1252 (AF)	
-0.107	0.2478	0.0855 (Re)	
-0.2874	0.2478	0.0855 (Rf)	
-0.2874	0.2478	0.0855 (Rc)	
0	0.2478	0.0855 (Bs)	
0	0.1882	0.065 (Dd)	
0	0.1882	0.065 (Fu)	
0	0.0635	0.0219 (Rr)	
0	0.0635	0.0219 (R)	

Fig. 4.12: The AHP results for Pelekaniotis basin.

In the case of the Samaria Gorge basin (Figure 4.14, basin 18), the drainage network overlies in moderately hard bedrock with high permeability. The relief indices are thus of high importance for the basin development. The drainage network will be very limited in this basin and as it is not dominant in the development of the basin. The indices Dd and Fu, will be of ñstrong importanceò (value 5 in the pairwise preference matrix) relative to relief indices. Similarly, the indices revealing information about the basin geometry, which are dependant on the drainage network, will have a ñstrong importanceò (value 5 in the pairwise preference matrix), with regard to relief indices. The indices of Rb, AF and HI will have ñequal importanceò to each other and ñmoderate importanceò with regard to relief indices. ñModerate to strong importanceò and ñstrong importanceò are selected in the pairwise preference matrix for the less important factors concerning drainage network aspects (such as Dd, Fu and shape/geometry indices). The AHP results for Samaria basin are presented in figure 4.13.

[Preference Matrix]

	Rb	HI	AF	Re	Rf	Rc	Bs	Dd	Fu	Rr	R
Rb	1	1	1	4	4	4	4	5	5	3	3
HI	1	1	1	4	4	4	4	5	5	3	3
AF	1	1	1	4	4	4	4	5	5	3	3
Re	0.25	0.25	0.25	1	1	1	1	2	2	5	5
Rf	0.25	0.25	0.25	1	1	1	1	2	2	5	5
Rc	0.25	0.25	0.25	1	1	1	1	2	2	5	5
Bs	0.25	0.25	0.25	1	1	1	1	2	2	5	5
Dd	0.2	0.2	0.2	0.5	0.5	0.5	0.5	1	1	5	5
Fu	0.2	0.2	0.2	0.5	0.5	0.5	0.5	1	1	5	5
Rr	0.3333	0.3333	0.3333	0.2	0.2	0.2	0.2	0.2	0.2	1	1
R	0.3333	0.3333	0.3333	0.2	0.2	0.2	0.2	0.2	0.2	1	1

Eigenvalues	**Eigenvector of largest Eigenvalue**	**Criteria weights**	**Consistency ratio Cr (revision of preference values if Cr> 0.1)**
12.3914	0.5177	0.1892 (Rb)	0.0928
-0.4805	0.5177	0.1892 (HI)	
-0.4805	0.5177	0.1892 (AF)	
-0.4304	0.1936	0.0708 (Re)	
0	0.1936	0.0708 (Rf)	
0	0.1936	0.0708 (Rc)	
0	0.1936	0.0708 (Bs)	
0	0.1344	0.0491 (Dd)	
0	0.1344	0.0491 (Fu)	
0	0.0699	0.0255 (Rr)	
0	0.0699	0.0255 (R)	

Fig. 4.13: The AHP results for Samaria Gorge basin.

The final outcomes of AHP analysis are presented in figure 4.14. The basins with reddish colour (e.g. Arapi, Pelekaniotis) owe their development in high tectonic activity and can be detected in the western part of the study region. Bluish basins observed in the north-east part of the study area are characterized by minimal tectonic activity. Yellowish basins, indicating moderate tectonic activity, are observed nearby the reddish basins (i.e. high tectonic activity). The AHP

procedure applied in this research regarding the determination of regional tectonic control showed that the basins in: i) reddish owe their development in high tectonic activity; ii) yellowish in moderate tectonic activity and; iii) bluish in minimal tectonic activity. The region with the basins showing the higher regional tectonic activity is revealed in the western part of the study area and that region is examined as a new case study in the subsequent chapters (Fig. 4.14).

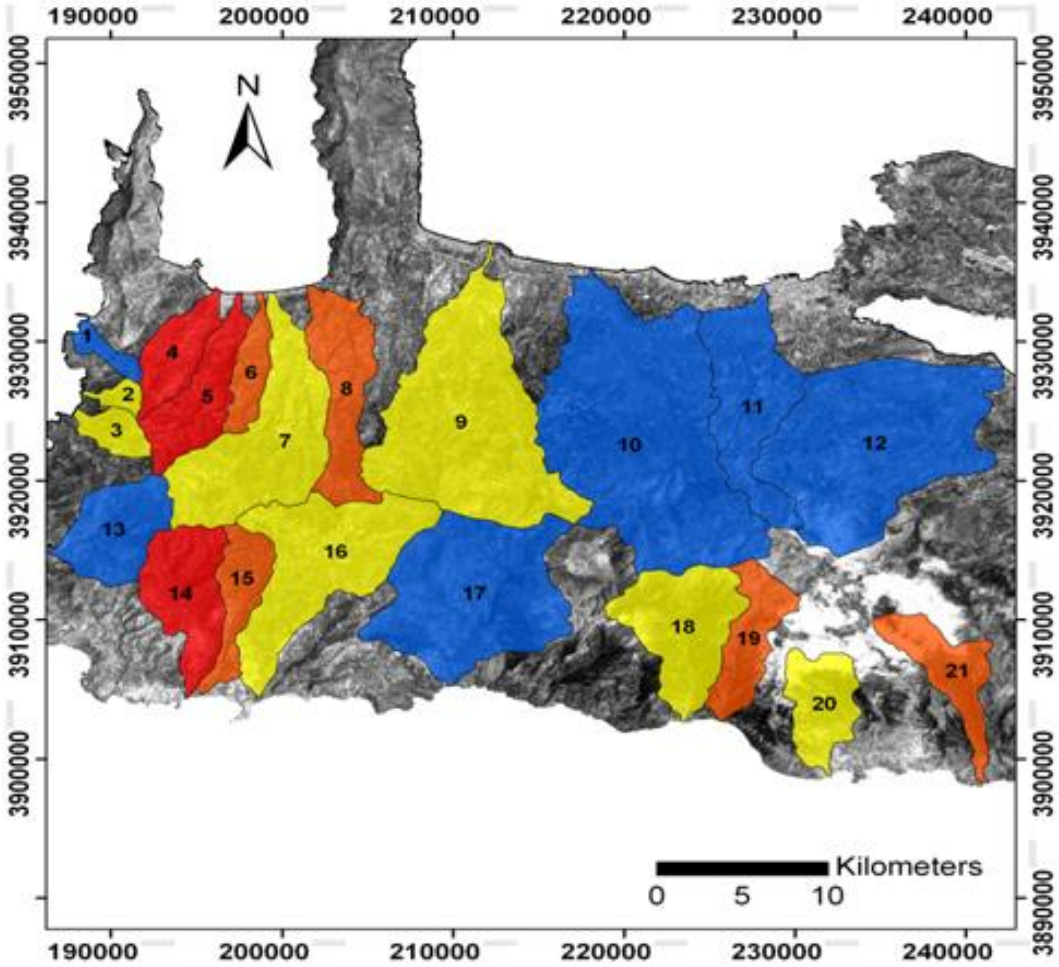

Fig. 4.14: The AHP procedure applied in this research regarding the determination of regional tectonic control showed that the basins in: i) reddish owe their development in high tectonic activity; ii) yellowish in moderate tectonic activity and; iii) bluish in minimal tectonic activity.

4.7 Discussion

This chapter examined the potential response of drainage basin development to regional tectonic control. Various geomorphic indices were calculated: these provided insights into the processes taking place within the study basins. The indices used in this chapter allow assessments of the relationships between the geomorphology, structure and lithology, via factors such as basin relief, basin geometry/shape, dominant processes (i.e. hillslope/tectonic or fluvial) and tilting of basins.

A key feature of this chapter was the selection of particular indices for drainage basin morphometry evaluation. The selected indices were useful for evaluating regional tectonic activity. This evaluation is discussed below, regarding the information provided by each index respectively. Index values that were not in accordance with the findings of published studies were examined in detail. Further examination of geomorphic characteristics, by examining their interrelationships, can be useful to the determination of regional tectonic controlled areas. Assemblages of geomorphic indices can offer valuable information on regional tectonic control processes occurring within a basin. In order to make the interrelationships of the indices more explanatory and clear to understand, a multivariate factor analysis was applied, in order to group the indices and rank them. Those interrelationships are discussed later in this section to clarify the individually indices outcomes. Some interesting observations regarding the relations among the indices, can also be reviewed in the section 4.5.2.(v). Analysis of these ñnot in accordanceò relationships indicated that exogenous factors, such as tectonics, were influencing the range of geomorphic indices values.

The first stage of this chapter was the calculation of the geomorphic indices. A first look at the calculated indices allows a review of each index attribute information, by evaluating the high or low values of each index respectively. The calculation of the relief ratio (Rr) revealed that high values apply to hilly regions and resistant rocks. Such characteristic basins are Aradaina Gorge and Potamos basins, which overly in moderate resistant rock formation but the presence of high permeability reinforces the validity of the high values of relief ratio (Rr) index. There are basins in western part of study region that are characterized by

moderately resistant impermeable rock types (e.g. the Phyllites-Quartzites of the Balsamakia and Pelekaniotis basin). In such impermeable regions fluvial processes were expected to provide lower values of the relief ratio (Rr) index, but instead high values are predominant. That reinforces the implication that their high relief is a result of ongoing uplift and not due to lithological control, by high resistant rock types.

The lowest drainage density (Dd) values are expected to characterize regions with highly resistant material, low relief and not a consistent fine drainage network development (i.e. dendritic drainage). Basins 19, 20 and 21 do not fulfill the expected observations as they are characterized by significantly high relief. That might be because those basins have evolved can in moderately permeable resistant material, preventing uniform drainage network development and as a result the relative relief remains close to 2000m. Comparison with drainage frequency (Fu) index values reinforces that interpretation, as those basins have lower Fu values, indicating a low frequency of stream segments. Considering the relative highly relief and the fact of not quite resistant presence of rocks within these basins, an explanation that can be given for their development is due to ongoing uplift in those basins, it has lead to a lack of a uniform drainage network development, with the drainage dominated by long length stream segments.

In general, the majority of the basins in this study have a high Fu values range (>5) which is associated with impermeable subsurface material, high relief and low infiltration capacity. These characteristics supposedly provide a more fine drainage pattern (e.g. dendritic). This is not in accordance with the nature of quite few drainage basins in the study area, as although the drainage network is flowing over impermeable Phyllite-Quartzites and Neogene deposits, justifying the indexes values, instead of an expected dendritic pattern, there are trellis and long linear length stream patterns. In addition, the bifurcation ratio (Rb) index has values less than 3 for all the basins, indicating that geological structures are disturbing the drainage pattern within all the basins. This issue is in accordance with Mekel (1970) who first showed that abnormal values of Rb less than 3 are indicative of dominant geological control. The range of values being less that 3 is in accordance also with Kouli et al (2007) study, who calculated Rb for two of the basins within the study area revealing similar low Rb values. The highest degree

of drainage network disturbance is observed in basins such as 5, 8, 14, 15, 19 and 21 where significant low values of Rb are observed (1.49<Rb<1.65). Considering the above characteristics of the indices calculations a first sight of the basins being under the influence of tectonic factors is preserved.

Based on Bhatt et al (2007) study about the ranges of elongation ratio (Re) values, table 4.10 shows that the basins 13 and 17 are inactive regions, with basins 4, 7, 14 and 16 being characterised as moderately active regions as Re values range between 0.5 to 0.75, while basins 5, 6, 8 and 15 imply to Re values lower than 0.5 indicating drainage basins that are influenced by tectonically active settings. Basin circularity (Rc) indicates that only basins 3, 12, 13 and 17 have not elongation tendency, with the basins having the most elongated shape being 6, 8, 15 and 21. This is reinforced additionally by the highest values of drainage basin shape index (Bs) index as it reveals that the basins 6, 8, 15 and 19 are indicative of high elongation shape. Form factor (Rf) reveals that lower values for basins 5, 6, 8 and 15 indicates that less side flow for shorter duration and high main flow for longer duration takes place in those basins, resulting in more elongated basins with low peak flows for longer duration. That can be associated with lack of circularity and prevention of a uniform drainage network (e.g. dendritic), which in comparison with Rc and Bs indices justifies the elongated nature of those basins, in particular basins 6, 8 and 15. The latter basins are all characterized by low elongation ratio (R_e) values and have lower infiltration, high run off capacity and significantly elongated basin circularity (R_c). These characteristics are typical of basins that erode rapidly and owe their elongated shape to neotectonic factors, associated with enhanced fluvial downcutting (Bull & McFadden, 1977; Ramirez-Herrera, 1998; Pedrera et al., 2007; Hamdouni et al., 2008).

The asymmetry factor (AF) is a powerful index in order to determine basins characterized by high degree of tilting. Such tilting implies to tectonic control being responsible for stream migration and development of an asymmetry within the basin. The basins with the higher degree of tilting were basins 1, 4, 9, 20, 13, 6 and 7. There are other basins with moderate asymmetry which in relation with other indices (such as HI) can also be associated with potential tectonic activity.

The basins that have undergone well defined deep incision and slight erosion are characterized by high hypsometric integral (HI) values and sub-parallel drainage, indicating deformation control by tectonic processes (such as the

Pelekaniotis and Sarakiniotis basins). As observed by Willgoose and Hancock (1998) and Hurtrez et al. (1999), small basins generally have high HI percentage (dominance of hillshope processes), whilst larger basins have low HI percentage (dominance of fluvial processes). The drainage basins of Metoxi-Platanos and Milias are not in accordance with that theory as they are quite small in scale but characterised by low HI percentage and low drainage density (Dd) (see Fig. 4.5 and Table 4.10). This indicates that their severe erosion is not a result of fluvial processes, but can be associated with the different tilting observed in the region by the AF index (see 4.5.2. iv section).

After calculating the indices, analysis of their interrelations formed the next stage of this study. A large number of indices relations were examined: particularly interesting was the issue of understanding the indices relationships that were not in accordance with the published literature. Despite the information acquired by the indices interrelationships for particular basins, it was necessary to group and rank the indices for easier determination of basins for further analysis in Chapter 5.

The application of factor analysis in this study grouped the calculated indices into four different components. One component provided a group of indices relevant with the basins extent/ area, which was not as interesting as the following three components are the ones, which can be associated and aid the interpretation of regional tectonic activity. Indices such as HI, Rb and AF were able to identify drainage basins that were more susceptible to hillslope/tectonic processes. These indices were linked with geological processes being dominant to basins development and in association with the following component comprised the prior ones to determine tectonic activity. The next component was consisting of Re, Rf and Rc indices associated with the geometry/shape of the drainage basin and determining the degree of basins elongation. Higher elongation indicated higher impact of regional tectonics within the basin. The final component consisted of Fu, Dd, R and Rr, indices being associated with the relief and the nature of the physiographic structure. These components extracted by factor analysis were particular useful as apart from the ranking of the indices, there are useful in the AHP procedure regarding the criteria of weights to be extracted. As a result the AHP stage was more coherent due to knowledge of the related indices, by factor analysis, provided more representative criteria weights for the final discrimination

of the drainage basins, regarding their regional tectonic activity. This issue in relation with the geological conditions considered for each basin during the determination of the criteria of weights, revealed which basins are characterized by high degree of regional tectonic activity. The western basins of the study area (e.g. 4, 5, 6, 8, 14, and 15) owe their development in high degree of tectonic control and provide the basins to be considered in Chapter 5 for further investigation of detecting the local tectonic activity within each basin.

CHAPTER 5 DRAINAGE BASIN ANALYSIS AT LOCAL SCALE

5.1 Introduction

Surface drainage characteristics can provide useful indicators about the recent tectonic regime of a region and the development of geomorphic indices has led to the identification of areas formed by rapid and recent tectonic deformation processes (Bull & McFadden, 1977; Keller, 1986; Keller & Pinter, 2002; Silva et al., 2003; Pedrera, 2009). These indices provide a useful tool to determine tectonically active regions that are being deformed by active faults, affected by erosional processes or influenced by vertical and horizontal movements of crustal blocks (Burbank & Anderson, 2001; Kobor & Roering, 2004; Tsodoulos, 2008; Pedrera, 2009). The extraction of these indices was usually obtained from aerial photographs and topographic maps. In recent decades, the usefulness of geomorphic indices has become even greater due to: i) faster computer processing; ii) greater use of Digital Elevation Models (DEMs) and iii) improved functionality of GIS. All these benefits led to rapid evaluations of tectonically active areas. The use of GIS was an additional tool, aiding with the processing of data and the speeding up of the decision making process (Troiani & Della Seta, 2008). The geomorphic indices are characterized by indices that can determine the tectonic activity of mountain fronts, the positional migration of streams due to tectonic forces, slopes with uplift or tilting and generally identify the most tectonically active areas, at a local scale. Because of the fact that a large amount of extracted information by such indices needs to be thoroughly evaluated, a multi-criteria decision analysis (MCDA) performance is considered in this research in a subsequent chapter (Chapter 8). Selective amount of geomorphic indices from this chapter will be considered in Chapter 8 to determine a GIS-based MCDA model that will provide a neotectonic activity map.

5.2 Background

In Chapter 4 specific geomorphometric indices descriptions were provided, in order to easily and quickly recognize potential zones of near tectonic activity in regional scale areas. According to these indices, particular areas proved to be influenced by geomorphological and lithological causes (e.g. tilting, relief and rock permeability). These specified regions, consisting of drainage basins, are suitable for the most powerful indices to be applied. Those powerful indices are referring to

local tectonic activity identification within the basin and include: i) the transverse topographic symmetry factor (T); ii) mountain front sinuosity (Smf); iii) the stream-length gradient index (S_L); iv) the valley floor width to valley height ratio (Vf) and; v) the hypsometric curve (HC). All these indices are meant to evaluate the types of stream characteristics, as proposed by Summerfield (2001), being associated with active tectonics identification (e.g. change of channel and valley gradient; change of channel width and depth etc.) (see Chapter 1, *"How can active tectonics be determined*ò section). These indices have an additional benefit, in comparison with the indices used in Chapter 4, that they can be used to classify the degree of tectonic activity taking place. Their application focuses on the study of morphotectonic anomalies, in order to detect and characterize the active tectonic structures (Bull and McFadden, 1977; Ramirez-Herrera, 1998; Keller and Pinter, 2002; Silva et.al, 2003; Verrios, 2004; Zovoili, 2004; Molin et.al, 2004; Malik, 2006; Toudeshki & Arian, 2011). The calculation of those indices has played a key role in the determination of local tectonic activity, particularly in the development of fault generated mountain fronts and migration of streams or slopes in uplifted regions (Keller, 1986; Silva et.al, 2003).

Previous studies applying these indices revealed valuable information about tectonically active areas, for example, the SW USA (Bull and McFadden, 1977; Rockwell et al., 1984; Keller 1986) Acambay graben in Mexico (Ramirez-Herrera, 1998) the Pacific coast of Costa Rica (Wells et al., 1988) the SE coast of Spain (Silva et al., 2003) the northern Apennines (Troiani & Della Seta, 2008) and central Greece (Zovoili, 2004; Tsodoulos, 2008). The analysis of these particular indices has the potential to reveal a more detailed evaluation of erosional processes, as well as, the degree of active tectonics in an area (Keller & Pinter, 1996; Silva et al., 2003; Verrios, 2004; Zovoili, 2004; García-Tortosa, 2008).

Comparisons of the Smf and Vf indices provide insights into the evaluation of fault-bounded mountain fronts, especially in the analysis and depiction of active faults, revealing three tectonic activity classes; namely, active fronts, moderate active fronts and inactive fronts (Bull and McFadden, 1977; Rockwell et al., 1984; Silva et al., 2003; Verrios, 2004; Zovoili, 2004). These classes analyze the degree of mountain front sinuosity, with regard to the incision that the valley floor has undergone, in order to indicate the level of tectonic activity. In SE Spain, a

semiarid tectonically active zone, fault generated mountain fronts provide a characteristic developed landform. In this region Smf and Vf indices indicated the various tectonic activity classes regarding the landscape characteristics (Silva et al., 2003). A similar study for the tectonically active Baza fault in southern Spain refered to the importance of Smf and Vf indices to classify this fault as one of the most tectonically active ones within Betic Cordillera (García-Tortosa, 2008). In Acambay graben, Mexico, the geomorphic study of fault-generated mountain fronts and þuvial systems examined the intensity of active tectonics. The Vf and Smf indices are particular useful in this study for the assessment of active tectonics as they provide information regarding the relative rates of tectonic uplift. The combined geomorphic and morphometric data provide evidence for relative variations in tectonic activity among the Acambay graben faults (Ramirez-Herrera, 1998).

The index of T was applied in large drainage systems and areas of sustained uplift, providing interesting tilting results (Hare & Gardner, 1985; Garrote et.al, 2006; Alastair, 2008; Toudeshki & Arian, 2011). The T index proved unreliable in areas with subtle topography and young anticlines (~0.5 Ma in age), making tilting trends imperceptible (Alastair, 2008). This indicates that a region should be undergoing tectonic tilting for a long time, to be recognised by the drainage basin asymmetry indices. Such a region is our study area in western Crete which consists, as previously mentioned, one of the most continuously tectonically active regions in the world (McKenzie, 1978; Papazachos & Comninakis, 1978; Le Pichon et.al, 1982; Pirazzoli et al., 1992; Kellletat, 1996; Pirazzoli, 2005; Shaw et.al, 2008). The T index was useful for recognising the tilting during Holocene and Quaternary of the Guadiamar river, with the Tertiary bedrock showing a uniform trend of the index results and the Palaezoic bedrock a variable one (Salvany, 2004).

The S_L index provided valid results in discriminating tectonic influence from lithological factors and detecting local uplift, even in small drainage basins (Troiani, 2008), such as some basins in this study. The S_L index anomalous values were supposed to highlight lithological control along the streams in the Appalachians (Hack, 1973). Different assumptions were raised when changes in S_L index values proved to be linked with tectonic factors and not relevant with

lithological control, in the drainage network development of Himalaya in the southern Asia (Brookfield, 1988). To test these differences a study of Chen (2003) proposed that for high order rivers, changes in S_L index correspond to tectonic activity and no lithological variations. On the other hand, for lower order rivers, due to less stream power, S_L index anomalous values reflected primarily to lithological control and secondarily to tectonic control (Chen et al., 2003). In general, the S_L index is useful in the analysis of drainage network characteristics. Like in the case of the NE spur of the Bohemian Massif, central Europe, where S_L index was considered thoroughly in the analysis of drainage network characteristics for determination of the neotectonic development of the region (Stepancikova et al., 2008). A normalised S_L index (SLk) was performed by Pena (2008) for spatial distribution analysis of tectonic regions: this is better than a simple spatial S_L map because it involves normalisation, with a constant value spacing within the rivers (see α_1 in equation, Table 5.1). The SLk index was applied by Pena (2008) in southern Spain revealing main tectonic and lithological features in a more coherent representation than the S_L map, which has deficiencies due to lack of value normalization.

Another useful index for the characterization of tectonic control is the hypsometric curves determined by the hypsometric analysis. The high percentage values of hypsometric integral indicate landscapes undergoing tectonic control (Keller & Pinter, 2002). These high percentage values can be characterized by a convex curve (impact by recent active tectonics) while lower values by a concave shape (eroded landscapes) (Keller & Pinter, 2002; Hamdouni et al., 2008). Hamdouni (2008) considered the hypsometric curves in association with aforementioned indices for the assessment of relative active tectonics in southern Spain. This study made the assumption that in the case that the hypsometric curves reveal a convex shape in the lower portion, this can be related to uplift along a fault or perhaps an uplift associated with recent folding. The application of hypsometric analysis in two drainage basins, Perachora and Pissia in Greece, revealed an anomalous evolution (Maroukian et al., 2008). Instead of exhibiting a normal concave shape, a convex discontinuous form is observed with the curve being useful in the identification of depositional surfaces or uplifted regions (Maroukian et al., 2008). Hypsometric curve (HC) and topographic distribution was

considered in the study of Giamboni (2005) to evaluate the geomorphic response of alluvial rivers to active tectonics in southern Rhinegraben, central Europe. In this study, the evaluation of hypsometric curves revealed that in few drainage basin cases the findings are compatible with the Ohmori (1993) study. The Ohmori (1993) study referred to the possibility that young landscapes result from concurrent tectonics and denudation that do not necessarily produce convex hypsometric curves but concave and/or s-shaped curves.

This research considers geomorphological and morphotectonic spatial distribution maps as their interpretation and interrelationship can be associated with the determination of tectonic control. Such spatial distributions maps, as the ones described in detail below, are: i) amplitude relief (Ar); ii) drainage density (Dd); iii) drainage frequency (F) and; iv) slope gradient.

The spatial distribution of the amplitude relief (Ar) can provide useful information about active or recent vertical displacements (Ciccacci et al., 1988; Centamore et al., 1996; Currado and Fredi, 2000; Della Seta et al., 2004). Quantitative morphotectonic analysis of the southern Marches area, Italy, improved the knowledge of morphotectonic setting in the region as the amplitude relief (Ar) was useful to the determination of the observed asymmetry and of the differential regional uplift (Della Seta et al., 2004). Another study in northern Sicily, Italy, made use of the amplitude relief to highlight zones characterised by more or less deep fluvial erosion, caused by differential uplift or subsidence phenomena (Arisco et al., 2006). Similarly results were initially determined by Centamore et al. (1996), where existence of various differentially uplifted and subsiding blocks were revealed by the amplitude of relief (Ar) in central Italy. The spatial distribution of the amplitude relief (Ar) was also helpful to determine that the eastern Monti Vulsini volcanic area, Italy, is controlled by different tectonic alignments (Ciotoli et al., 2003).

The relationship between drainage density, drainage frequency and slope gradient can indicate some particular aspects, regarding the dominant processes that take place in a region. It is generally accepted that an increase in the slope gradient leads to a drainage density decrease (Lin & Oguchi, 2004; Paraschou, 2005). The high values of drainage density are associated with very gentle slopes (Kouli et al., 2007). Howard (1997) observed that drainage density and slope

gradient correlate negatively in quickly eroding areas but positively in slowly eroding areas, where hillslope processes are dominant. Comparison between spatially analyzed drainage density (Dd) and drainage frequency (Fu) maps can characterize the type of permeability in a region. High drainage density and high stream frequency regions seem to associate with impervious rocks, enhancing severe erosion. On the other hand, low values of drainage density and drainage frequency are implying to permeable formations and steep rugged surfaces (Reddy et al., 2004; Kouli et al., 2007). A study of two drainage basins in western Crete, Greece, revealed that high stream frequency values were represented in almost linear patterns, parallel or sub-parallel to major tectonic lineaments indicating the drainage network being developed under tectonic influence (Kouli et al., 2007).

The quantification of the control of local topography on hydrological processes and determination of the spatial distribution of soil moisture and surface saturation can be examined by the topographic wetness index (TWI) (Quinn et al., 1991). Topography controls the movement of water in slopes terrain and as a result the water has a tendency to accumulate at the foot of slopes, where high values of the TWI index can be observed (Rodhe and Seibert, 1999). In areas with very low value of slope gradient, the TWI value is expected to be highly large, while high slope gradient implies low values for the TWI (Rodhe and Seibert, 1999). The types of TWI distribution were examined by Paraschou (2005) in the geomorphological evolution of the drainage basin of Inachou, central Greece. In this study an attempt to discriminate regions regarding the TWI values took place with low values being indicative of: i) highly incised V shaped valleys; ii) high relief surfaces with low moisture accumulation and; iii) longitudinal ridges. On the other hand, higher values were indicative of: i) gradient surface with high moisture accumulation and; ii) alluvial deposits. Recently the TWI index was associated with landslide susceptibility studies where high values of the index revealed favourable conditions for landslide formation (Conoscenti et al., 2008; Gorum et al., 2008; Nefeslioglu et al., 2008).

5.3 Methodology

The response of the drainage network to faulting, folding or tilting aids the investigation of various geomorphic features and their interaction with tectonic processes. This is because a drainage network develops its geometry and pattern in a distinct way wherever active tectonic deformation exists (Maroukian et al., 2008). The most common indices that can detect the local tectonic activity are the stream-length gradient (Sl), the mountain front sinuosity (Smf), the ratio of the width of valley floor to valley height (Vf), the transverse symmetry topographic factor (T) and the hypsometric curve (HC) (Table 5.1). These indices are used to detect anomalies that indicate tectonic activity and their classification indicates the most tectonically active regions in a local scale. In order to better comprehend their significance, the capability of GIS is considered in this research to extract some spatial distribution maps that can be associated with the aforementioned indices in order to make easier and more meaningful decisions. Such maps are: i) drainage density; ii) drainage frequency; iii) slope gradient; iv) amplitude relief and; v) terrain wetness index. These maps are straightforward linked with geomorphological and relief aspects of the study area. In addition they can be particular useful in the interpretation of the indices outcomes and their interactions with active tectonics.

5.3.1 Morphotectonic indices

The morphotectonic indices to be used in this research and their relation to active tectonics determination are discussed below.

The *transverse topographic symmetry factor **(T),*** is the ratio of the distance from the midline of the drainage basin to the active meander belt midline (Da) to the distance from the midline to the basin divide (Dd) ($T = D_a/D_d$) (Fig. 5.1) (Cox, 1994; Cuong & Zuchiewicz, 2001; Fountoulis, 2001; Salvany, 2004; Virdi, 2005; Toudeshki & Arian, 2011). The index of the Transverse topographic symmetry factor can characterize the ground tilting and the asymmetry of the drainage network; when the ground is not stable then deformation conditions prevail in the drainage basins. This index can be used in order to provide important asymmetry information in large drainage systems (Garrote, 2006) and regions of rapid uplift (Cox, 2001). Furthermore, this index examines the active meander belt and the

basin midline; it indicates lateral tilting and the level of asymmetry or symmetry of a river within the drainage basin (Cox, 1994; Salvany, 2004; Virdi, 2005). It also indicates the migration of the drainage segments perpendicular to the main axis of the basin (as a result of either internal fluvial processes or external forces) (Keller & Pinter, 2002; Salvany, 2004; Verrios, 2004). The dendritic drainage networks respond better with that index as a larger range of T is achieved. The values close to 0 indicate an absolute symmetric basin, while values close to 1 an asymmetric basin. The scale of the drainage basins in this research extends to an average of 15km in length, so smaller mass movements (such as landslides) do not have a significant impact on these indices.

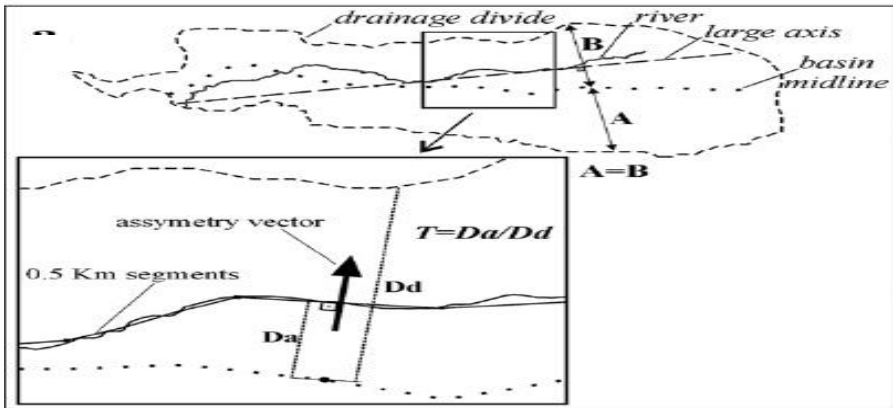

Fig. 5.1: The transverse topographic symmetry method proposed by Cox (1994) (modified from Salvany, 2004; in Tsodoulos, 2008)

The *stream length gradient index* ***(Sl),*** is the ratio of the change in elevation of the reach to the length of the reach, multiplied by the total length of the channel from the point where the index is being calculated ($S_l = (\Delta H/\Delta L)*L$) (Hack, 1973; Keller, 1986; Zovoili, 2004; Stepancikova, 2008; Troiani, 2008; Toudeshki & Arian, 2011). Stream power can be related to this index, as the stream has the tendency to erode its bed and transfer sediment from the highest part of its drainage basin to the basin mouth (Keller & Pinter, 2002). In this study the majority of stream channels are not ephemeral and not more than 10 meters across. The extracted flow accumulation (threshold 400m^2) revealed that only high ordered (4^{th}-5^{th}-6^{th}) streams exhibit a continuous flow, with widths of up to 30 m; This means that stream channels are quite small, so local within-channel processes (such as bank erosion) are not going to have an impact on the index calculation. The

relationships between tectonic activity, rock resistance and topography can be investigated with S_L index due to the influence of sudden changes in channel slope. Large differences (either anomalously high or low) in the values of this index indicate zones of tectonic activity (Keller, 1986). Any changes occurring along the longitudinal profile of a stream reflect possible tectonic influences (Hack, 1973; Keller & Pinter, 1996; Garcia-Tortosa et.al, 2008). For this reason, stream longitudinal profiles were also extracted from DEM, as they were able to examine changes in the slope along the stream, which might reflect active tectonic structures when compared with Sl index (Maroukian et al., 2008; Pedrera, 2009). The values of stream longitudinal profiles were extracted for each pixel of the DEM. Because channel width does not exceed the 30m pixel size, existing slope changes will reflect active structures and not local bank erosion.

This study considered the methodology proposed by Perez-Pena (2008) to calculate the updated normalized stream-length gradient (SLk) in the main stream segments. In order to achieve better results in comparison with Kellerôs proposed method (1986), the use of constant point spacing was considered in the interpolation of values in a horizontal plane (Perez-Pena, 2008). The calculated SLk values were used to create an anomaly map by using a kringing statistical method based on a variogram model (Perez-Pena, 2008; Pedrera, 2009). The anomalous values were detected by following a cross-validation analysis so that the tectonic controlled areas could be recognized (Goovaerts, 1997; Perez-Pena, 2008). The geostatistical analyst application of ArcGIS was used for the final calculation of the index.

The *ratio of valley floor width to valley height* ***(V_f),*** uses the width of the valley floor (V_{fw}), the left and right elevations of the valley divide (Eld and Erd) and the elevation of the valley floor (Esc): $V_f = 2V_{fw} / [(E_{ld}-E_{sc})+(E_{rd}-E_{sc})]$ (Fig. 5.2) (Bull & McFadden, 1977; Keller, 1986; Ramirez-Herrera, 1998; Cuong & Zuchiewicz, 2001; Silva et al., 2003; Zovoili, 2004; Malik, 2006; Pedrera, 2009; Toudeshki & Arian, 2011). Transverse channel profiles of the streams that cross the fault-bounded fronts were extracted from the DEMs. Fault-bounded fronts were determined by 10m contours intervals on 1:50,000 topographical maps. The calculation of the index takes place at a set distance upstream from the mountain front (Keller, 1986; Ramirez-Herrera, 1998; Cuong & Zuchiewicz, 2001; Silva et.al,

2003). The reason for this is the tendency of valley floors to become narrower upstream from the mountain front (Ramirez-Herrera, 1998). Transverse valley profiles were created 250 m upstream from the mountain front and continued for about 1 km away from the mountain front for small drainage basins and 2 km for larger drainage basins. After that, distance valley floors become wider due to erosional processes. The values of Vf were calculated along streams with similar geological and morphological characteristics (Bull, 1978; Wells et al., 1988), as differential underlying bedrock lithology provide variations in the index values. This index reveals information about the level of incision and erosion development of the valleys (Verrios, 2004; Malik, 2006; Garcia-Tortosa et.al, 2008). High values are due to broad floor valleys (ñUò shaped, associated with low uplift rates), that have been carved by erosional processes. On the other hand, lower Vf values are due to narrow and actively incised valleys (ñVò shaped), formed by fluvial incision in response to tectonic uplift. The most difficult value to be calculated in the index was the parameter of the width of the valley floor. In order to increase the accuracy of the index calculation, aerial photos with 1m spatial resolution were used for the measurement of that parameter.

$$V_f = 2V_{fw} / [(E_{ld} - E_{sc}) + (E_{rd} - E_{sc})]$$

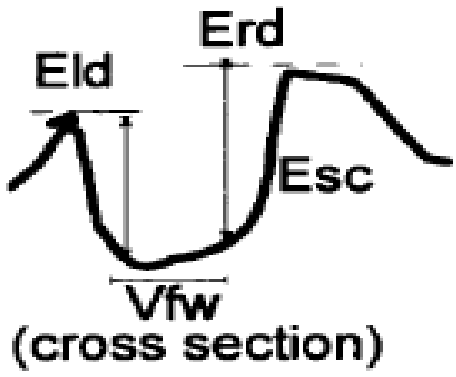

Fig. 5.2: The ratio of valley floor width to valley height developed by Bull & McFadden (1977) (modified by Ramirez, 1998).

The *mountain front sinuosity* ***(S_{mf}),*** is the ratio of the length of the mountain front along the foot of the mountain to the straight-line length of the mountain front ($S_{mf} = L_{mf} / L_s$) (Fig. 5.3) (Bull & McFadden, 1977; Keller, 1986; Ramirez-Herrera, 1998; Keller & Pinter, 2002; Cuong & Zuchiewicz, 2001; Zovoili, 2004; Malik, 2006; Troiani & Della Seta, 2011; Toudeshki & Arian, 2011). Fault generated escarpments reflect tectonic activity through the relation that exists between stream power and slope processes (Keller, 1986). The variables of the index were measured on 1:50,000 topographic maps with 10 m contour intervals. The Smf index aims to estimate the rectilinearity or irregularity of a mountain front in order to determine the degree of tectonic activity and the erosion status that affects the mountain front (Mayer, 1986; Verrios, 2004). Tectonic processes create rectilinear mountain fronts representing active fault-bounded regions, while erosional processes have the tendency to cut embayments into a mountain front (Keller & Pinter, 2002). The resulting values separate the fronts into *active* and *less active* or *inactive classes*, depending on how straight (due to tectonic forces) or irregular (due to erosion processes) a mountain front becomes (Wells et al., 1988; Malik, 2006). Thus, depending on the values extracted, the mountain fronts can be classified as *active* fronts for low values (Smf $\leq$1,4), *moderate active* fronts (3$\geq$Smf $\geq$1,4) and *inactive* fronts for high values (Smf $\geq$3) (Silva et al., 2003).

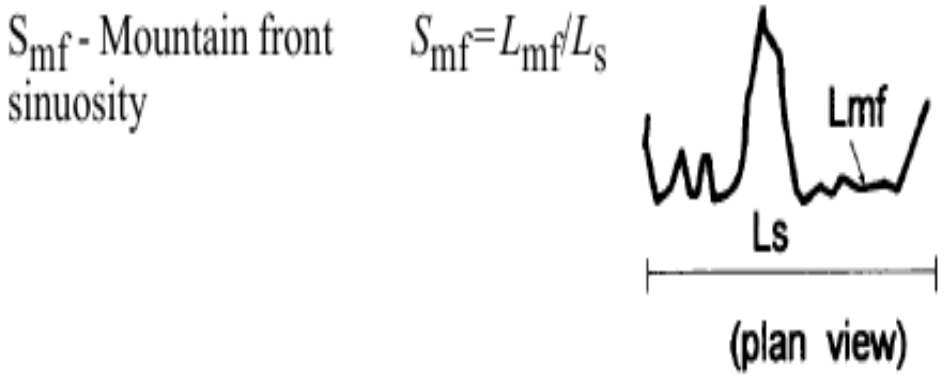

Fig. 5.3: The mountain front sinuosity calculated parameters (modified by Ramirez, 1998).

Hypsometric curves ***(HC),*** is a powerful technique that reveals the degree of disequilibrium in the balance of erosive and tectonic forces (Strahler, 1952, 1958; Weissel and Pratson, 1994; Luo, 1998; Keller & Pinter, 2002). By employing this technique, useful information about the relationship that exists between the drainage basin area and the distribution of elevations are obtained (Strahler, 1952; Miller, 1953; Schumm, 1956; Weissel and Pratson, 1994; Dowling et al., 1998). Small basins generally have convex hypsometry curves (dominance of hillshope processes), whilst larger basins have concave curves (dominance of fluvial processes) (Willgoose & Hancock, 1998; Hurtrez et al., 1999; Segura et al., 2007). The values depend on various factors, such as rock resistance, and cannot be related directly to active tectonics (Hamdouni et.al, 2008).

The hypsometric curve is created by plotting the ratio of total basin height (h/H=relative height) to the ratio of total basin area (a/A=relative area), where (H) is the relief within the basin (maximum elevation minus the minimum elevation), (A) is the total area of basin and (a) is the area of the basin above a specific elevation (h) (Keller & Pinter, 2002). It is worth noting that hypsometric curve results are not affected by drainage basin size and relief. This is due to the fact that they are characterized by the total area and total elevation (Dowling et al., 1998; Keller & Pinter, 2002). As described in *Chapter 4,* the use of HI can reveal the three stages of erosional status of a drainage basin. The first stage has a convex hypsometric curve (HC) and shows areas representing basins with deep incision and slight erosion. The second stage tends to have a straighter HC, revealing approximate equilibrium and an intermediate stage of incision and erosion. The third stage is characterized by concave HC with basins characterized by low relief and severe erosion (Keller & Pinter, 2002; Hamdouni et.al, 2008). Apart from the aforementioned hypsometric curve types there is also a discontinuous convex/concave form which indicates the influence of either depositional surfaces (alluvial fans) or knickpoints (uplift) at specific elevations of the drainage basins along the curve (Hamdouni et.al, 2008).

Mountain front sinuosity, S_{mf}	$S_{mf} = L_{mf} / L_s$	The ratio of the length of the mountain front along the foot of the mountain to the straight-line length of the mountain front.
Ratio of the width of valley floor to valley height, V_f	$V_f = \frac{2Vfw}{[(Eld - Esc) + (Erd - Esc)]}$	The ratio between the V_{fw}, the width of valley floor, the Eld and Erd the left and right elevations of the valley divide and the Esc, elevation of valley floor.
Stream length gradient index, S_l	$S_l = (\Delta h / \Delta L) * L$	The ratio of the change in elevation of the reach to the length of the reach multiplied with the total length of the channel from the point of interest where the index is being calculated.
Transverse topographic symmetry factor, T	$T = D_a / D_d$	The ratio of the distance from the midline of the drainage basin to the midline of the active meander belt to the distance from the midline to the basin divide.
Hypsometric Curve, HC	HC= graph plot of relative height to relative area	Plotting the ratio of total basin height (h/H=relative height) to the ratio of total basin area (a/A=relative area)

Table 5.1: The morphotectonic indices used to characterize the tectonic activity of the study area.

5.3.2 Geomorphometric data and derivatives extracted from DEMs

Some additional spatial distribution maps can be extracted by using GIS and the DEM (see Table 5.2). These spatial distribution maps can then be associated with the aforementioned calculated indices. With that way the comprehension of their implications can be determined and make the aforementioned indices outcomes more meaningful:

Stream frequency ***(F_u),*** was described earlier in chapter 4 as the ratio of the total number of the stream segments to the area of the basin (Al-Sulaimi, 1997; Jamieson et al., 2003). The capability of GIS usage is crucial for the creation of distribution maps of stream frequency to be accomplished using Spatial analyst application in ArcGis software, with the basins being divided into a grid of 20 m x 20 m squares (an area of 400 m^2) and the parameters of the segments being calculated in an area of 2000 m radius around each square (Fourniadis, 2002). The stream frequency maps can reveal regions were lower number of stream segments exist due to tectonic forces presence, uplifted regions, and prevent the proper development of the drainage pattern. When high stream frequency values are prevailed following linear patterns, parallel or sub-parallel to the faults, this fact indicates the development of the stream segments under tectonic influence (Kouli et al., 2007).

Drainage density ***(D_d),*** was described earlier in chapter 4 as the ratio of the total stream length to the area of the basin (Al-Sulaimi, 1997; Awasthi, 2002; Jamieson et al., 2003). Again the usage of GIS is useful for the creation of distribution maps of drainage density to be carried out in the same way as the stream frequency extracted maps. High D_d values imply to the presence of dissected terrains where the drainage network can be properly developed. Low D_d values indicate the existence of long hill slopes where stream segments (mainly of low order) are prevented to provide a fine pattern (Berger and Entekhabi, 2001; Awasthi et al., 2002).

Slope gradient*,* is an algorithm that shows maximum slope steepness therefore indicating the change in elevation between each cell and its neighbors (ESRI, 2003). Low values imply a flat surface while an increasing value implies an increase in slope steepness. The angle of the slope can be expressed either in degrees or as a percentage.

The *Amplitude Relief* ***(A_r)*****,** is a parameter that can be used for the statistically orographic configuration of the study area in order to determine fluvial erosion (Della Seta, 2004). The spatial distribution of A_r can indicate active or recent vertical displacements (Ciccacci et al.,1988; Currado & Fredi, 2000; Troiani & Della Seta, 2008). Especially, the geostatistical approach of A_r (the maximum difference in elevation within unit areas of 1 km^2) is powerful for active tectonics assessment (Ciotoli et al., 2003). The geostatistical approach of Ar was calculated using ArcGis spatial analyst application and selecting Kriging method as an interpolation method, to obtain a spatial distribution map of the parameter (Della Seta et al., 2004).

The *Topographic Wetness Index* ***(TWI),*** determines the spatial distribution of soil moisture and surface saturation with regard to the influence of topography, based on digital elevation models (DEMs) (Beven & Kirkby, 1979; Sorensen, 2005) (see Appendix I, Theory formulas (iii)). This index has a relationship with slopes, as water has a tendency to accumulate at the foot of slopes. The type of distribution being depicted with this index can identify regions with low values indicating: i) highly incised V shaped valleys; ii) high relief surfaces with low moisture accumulation and; iii) longitudinal ridges. Higher values indicate: i) gradient surface with high moisture accumulation and; ii) alluvial deposits (Paraschou, 2005). Topography is an important control of hydrological processes, so TWI can represent water distribution regarding topography influence (Anderson & Kneale, 1982; Hjerdt et al., 2004). The requirements of this index are that: i) a spatially uniform channel velocity exists; ii) the degree of subsurface recharge is steady; iii) there are no lateral flows; iv) subsurface flow rates are proportional to a hydraulic gradient approximately equal to the surface slope and; v) only one exponential transmissivity function is used throughout the basin (Beven & Kirkby, 1979; Quinn & Beven, 1991). This study does not utilise the Topographic Wetness Index for explaining hydrological processes and soil moisture differences in the drainage basins. Therefore neither quantitative evaluation nor further depth investigation of its parameters is considered. However, the TWI is applied solely to provide ancillary data for the characterisation and identification (with regard to the topography) of possible regions that may be influenced by structural control.

Stream frequency (F_u)	Spatial distribution of stream frequency, with the basins being divided into a grid of 20 m x 20 m squares (an area of 400 m^2) and the parameters of the segments being calculated in an area of 2000 m radius around each square
Drainage density (D_d)	Spatial distribution of drainage density, with the basins being divided into a grid of 20 m x 20 m squares (an area of 400 m^2) and the parameters of the segments being calculated in an area of 2000 m radius around each square
Slope gradient	Shows maximum slope steepness therefore indicating the change in elevation between each cell and its neighbors
Amplitude Relief (A_r)	Spatial distribution of the maximum difference in elevation within unit areas of 1 km^2 can indicate active or recent vertical displacements
Topographic Wetness Index (TWI)	Spatial distribution of soil moisture and surface saturation with regard to the influence of topography based on digital elevation models (DEMs)

Table 5.2: Geomorphic indices used to analyze spatially the study area. Spatial distribution maps provide geomorphological and tectonic information.

5.4 Results

In this section we present the results of the methodological indices described above and we determine regions of active tectonics within the drainage basins. Due to a large amount of datasets, part of the outcomes, mainly those covering the spatial distribution aspects, will be selected in Chapter 8 for multi-criteria decision analysis (MCDA) modeling, regarding assessment of neotectonic activity.

5.4.1 Morphotectonic indices

This section presents the morphotectonic indices described in methodology and their implication to active tectonics is examined. High values of the transverse topographic symmetry factor (T>±0.50) indicate uniform migration of the main drainage basin river, with values close to 1 indicating the highest degree of stream migration and basin tilting towards that direction (Fig. 5.4). There is no relationship between bedrock trends and stream migration directions, therefore tectonic deformation is a more likely explanation.

The results extracted from the stream-gradient index (S_L) along the main streams of the drainage basins were calculated using 100m contour intervals. Fluctuations in S_L values along the measured profile may correspond to areas with higher tectonic activity. The most anomalous high values of S_L index indicate that these areas are being deformed by tectonic processes (Fig. 5.5). The values of S_L >300 imply to tectonic deformation with higher values indicating higher degree of tectonic processes. Moreover, the spatial distribution of SLk map can highlight such tectonically controlled areas. Tectonically controlled areas are identified/spotted every time the calculated index assumes a high value (darker colour) (Fig. 5.6). The main anomalies are highlighted and pointed out by the black arrows, representing the regions where the change of stream gradient is probable a result of active tectonics occurrence (see Fig. 5.6).

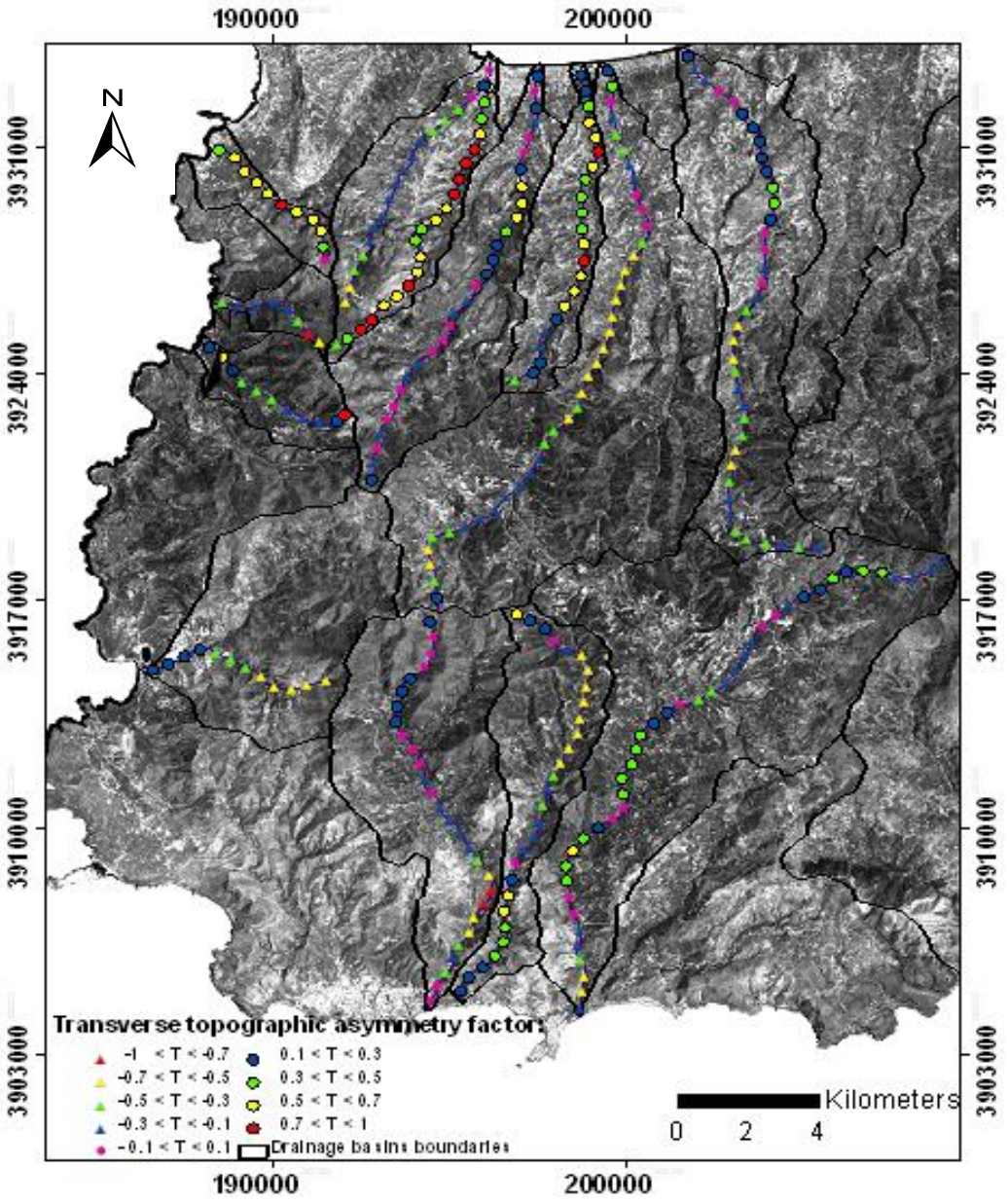

Fig. 5.4: The basin asymmetry vectors of the Transverse Topographic Symmetry factor (T) along the main streams of the study area. The vectors highlight the degree of tilting with regard to the basin midline (to left downstream with triangle or to right downstream with circle). Small circles (-0.1<T<0.1) indicate symmetric drainage networks.

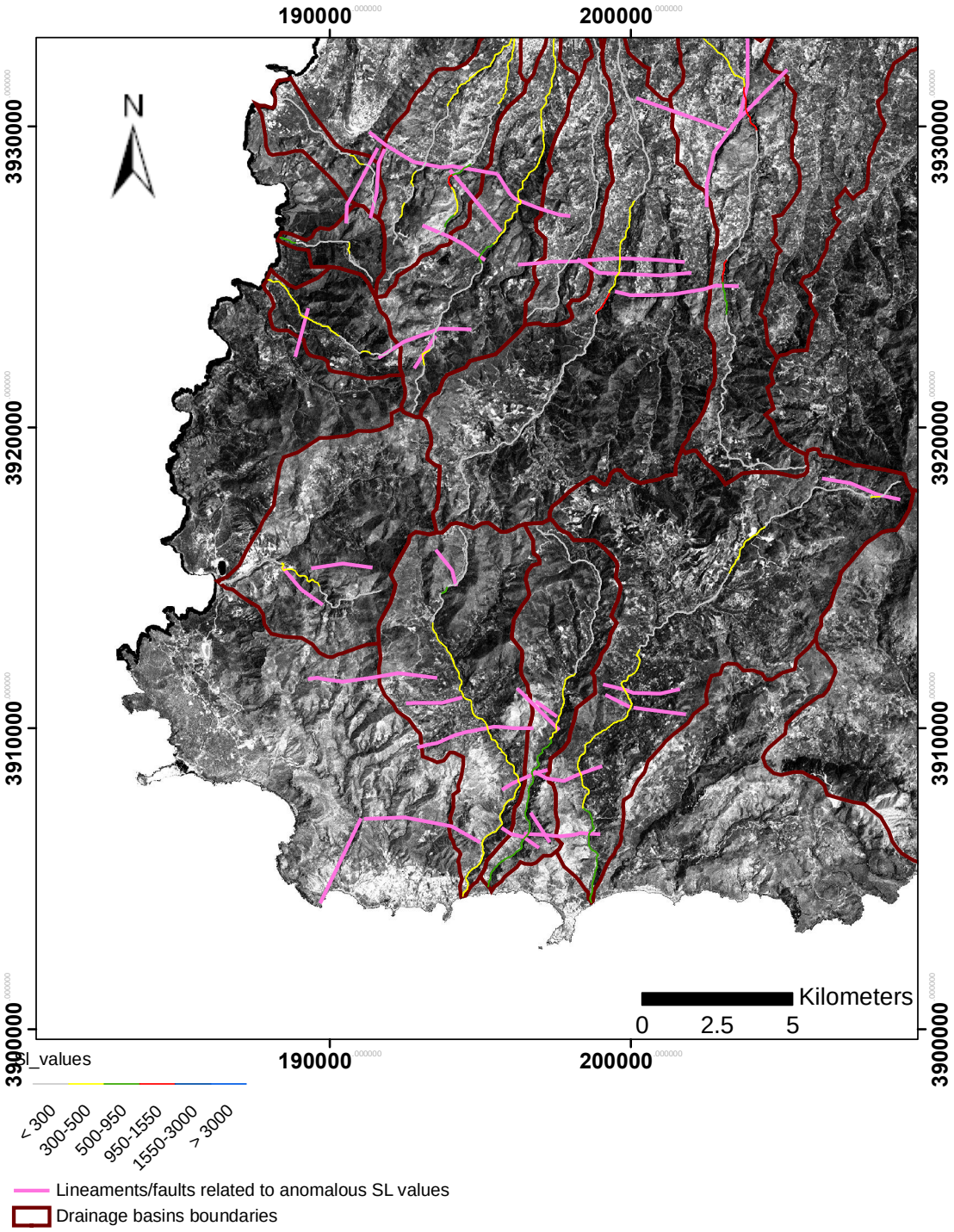

Fig. 5.5: S_L index values along the main streams of the drainage basins. The S_L index clearly varies, with anomalous changes in values, indicating regions with higher tectonic activity.

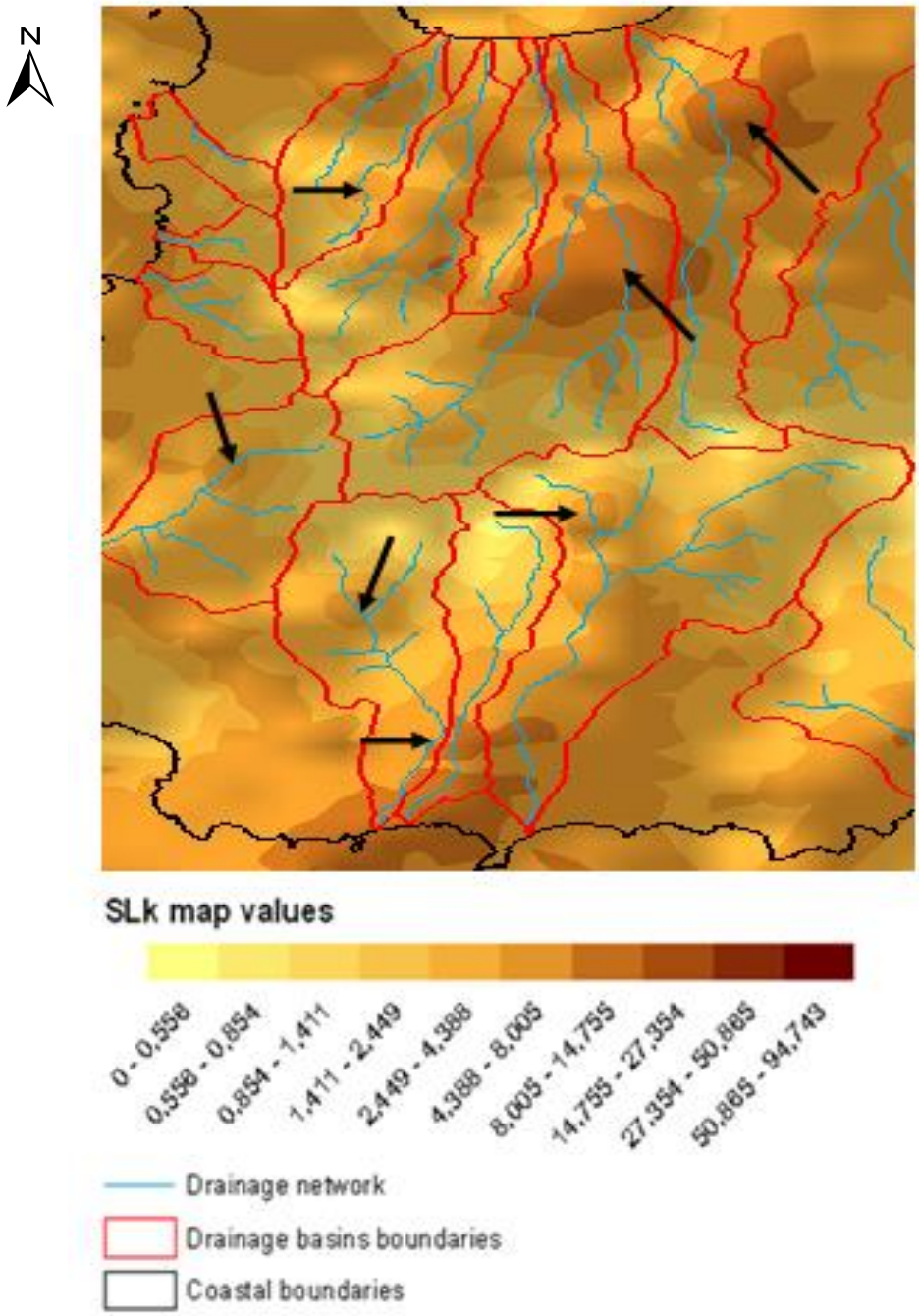

Fig. 5.6: The SLk anomaly map with a ýxed dl of 200 m. The black arrows indicate the higher tectonically active zones, where the index has major fluctuation anomalies.

The valley floor width to valley height ratio (Vf index) indicates the degree of valley incision and the degree of mountain front uplift. The values were obtained upstream of various fault-bounded mountain fronts across the study area. Fault-bounded fronts were determined by the topographical maps. The majority of the results show tectonically active mountain fronts with a range of values that spans below 1. Most of the measurements in the study area correspond to low values indicating tectonically active mountain fronts (red points in Fig. 5.7 & Table 5.3). The lower values (Vf<1) indicate deeply incised valleys with V-shaped valleys; this is in contrast with the broad U-shaped valleys, characterized by higher values of the index (Vf>1), that indicate less tectonically active mountain fronts (green points) (Fig. 5.7 & Appendix II, Fig. 5). Three classes were determined with index values lower than 1: (Class 1) indicating high tectonic activity, values ranging between 1 to 1.5 (Class 2) indicating moderate tectonic activity and values higher than 1.5 (Class 3) implying to low tectonic activity. In valleys with higher stream power or changes in lithology the Vf index was also calculated downstream from the mountain front. This showed that higher values of the Vf index occur regardless of the lithology or the stream power. The Vf index was not applied in the SE drainage basins of the study area, due to high relative relief and many gorges, as well as minimal development of mountain fronts.

The mountain front sinuosity (Smf) is an index that reveals the sinuosity of the fault-bounded escarpment with regard to the piedmont (Fig. 5.8). It indicates the degree of tectonic activity along a mountain front (Table 5.4), and in combination with the Vf index values, the classification of the mountain front could be determined with regard to its tectonic activity.

The relationship of the Vf and Smf indices indicates the most affected tectonically affected mountain fronts (Fig. 5.9 a, b). To compare these two values, the Vf indices calculated for each segment profile (across the river and perpendicular to the Smf profiles) were simplified by calculating their standard deviation values. The classification was based on the values range defined in Figure 5.10 a. Class 1 consists of values with VfÒ1.2 and SmfÒ1.6, indicating high active tectonics; class 2 of values with VfÒ1.5 and 1.6<SmfÒ2.5, indicating moderate active tectonics; and class 3 of Vf values associated with Smf>2.5, indicating low active tectonics. Most of the recorded values indicate high to

moderate tectonic activity of the study region (Class 1-2) (values in red circle in Fig. 5.9 b). An extra region was investigated by both Vf and Smf index as it constitutes the closest area to the highest observed co-seismic uplift of the 365 A.D. earthquake (see red rectangle in SW region in Fig. 5.7).

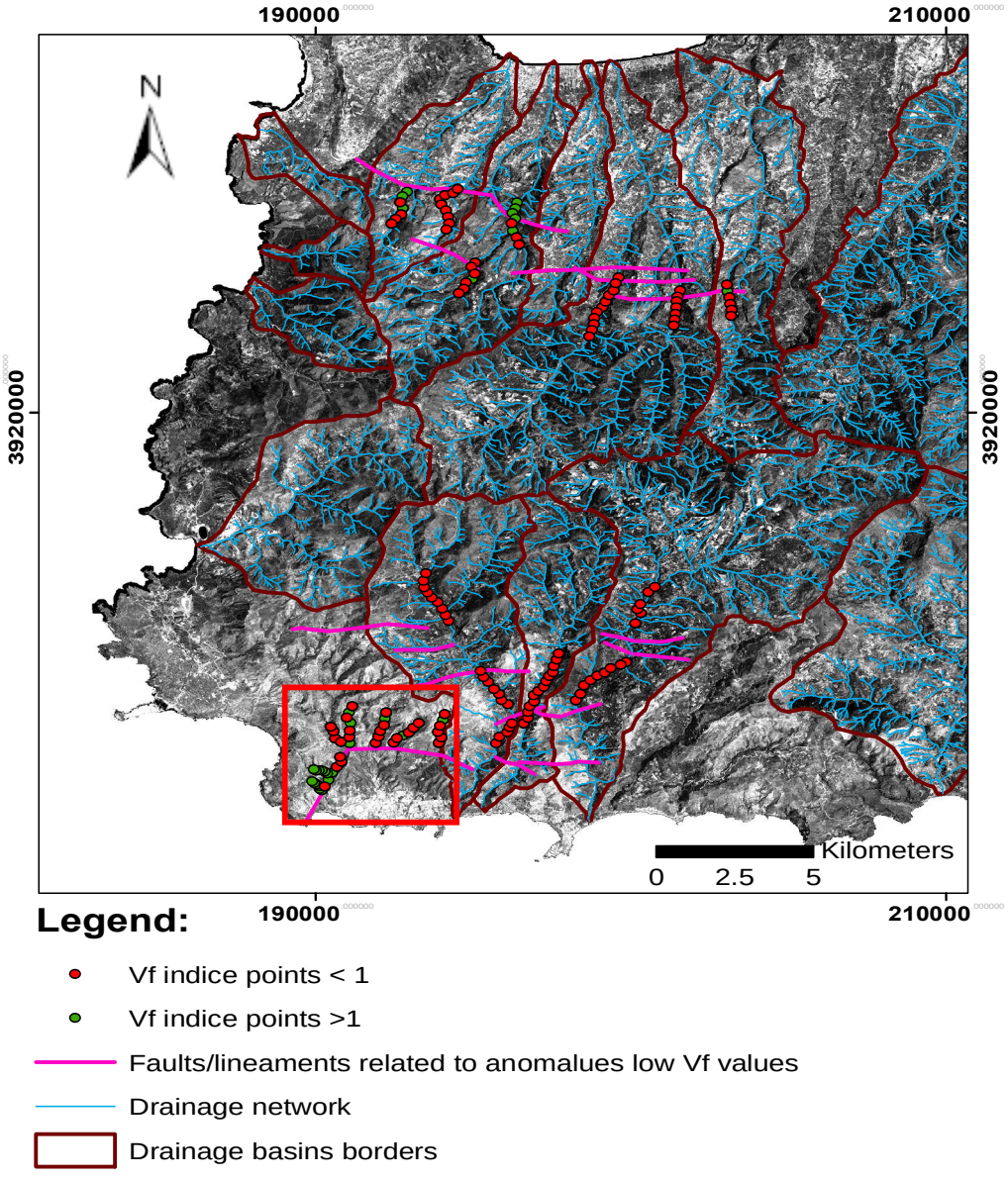

Fig. 5.7: The calculated Vf index with values lower than one (red points), indicate high tectonic activity of the mountain fronts, particularly in the western basins where high incised valleys are present. Values larger than 1 (green points) indicate mountain fronts with less tectonic activity (even inactive).

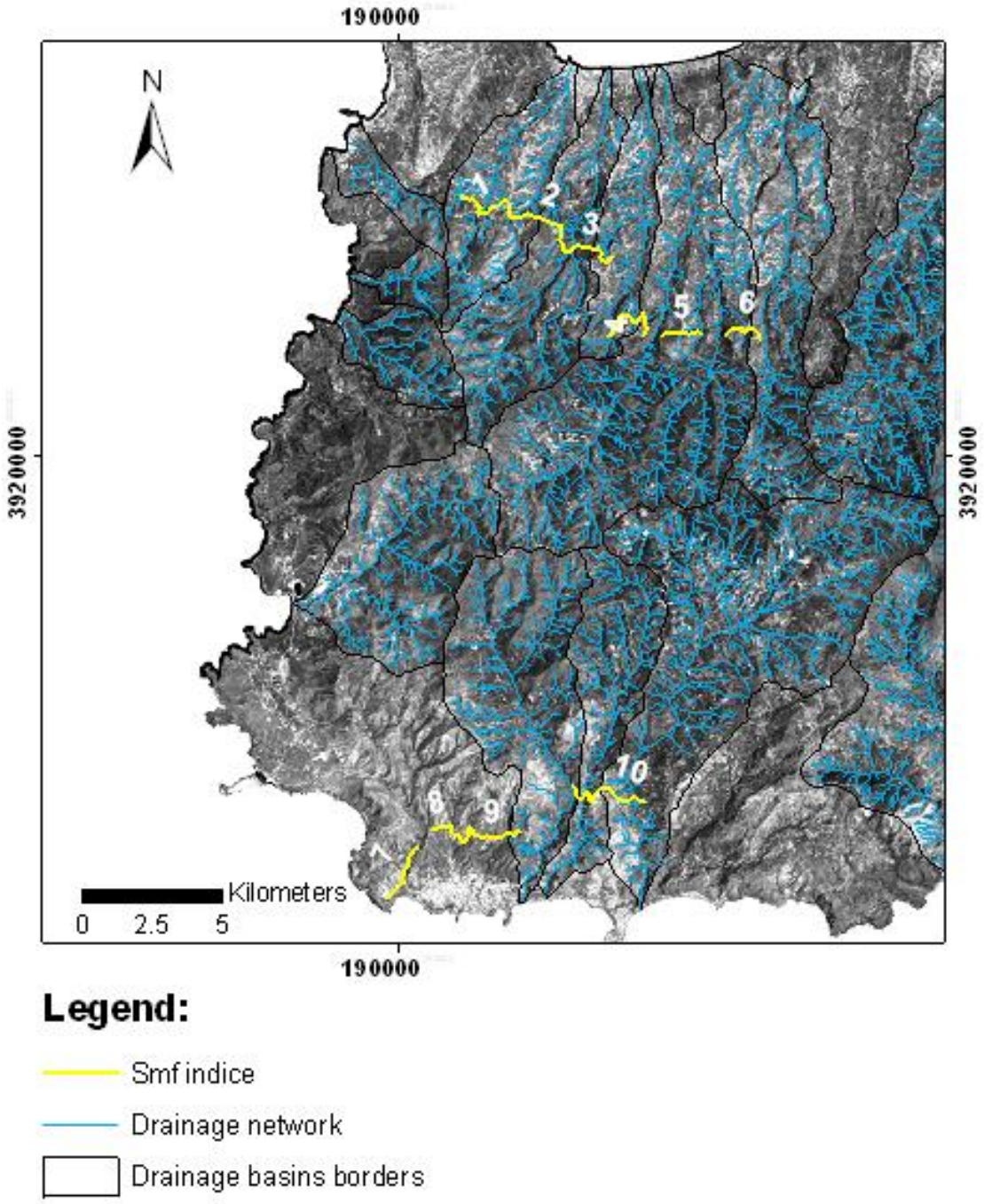

Fig. 5.8: The mountain fronts for which the Smf index was estimated and the Vf index points calculated upstream of the front. The fault- bounded fronts indicate the sinuosity and the degree of mountain front tectonic activity.

Basins ID	Mountain front ID	Lithology of the valley floor	Vf index			Class
			n	Vf	stdev	
4	1	Phyllites & Quartzites	5	0.895	0.309	**1**
4	2	Carbonate Tripolis nappe	8	0.737	0.172	**1**
5	3	Carbonate Tripolis nappe	5	1.009	0.488	**1**
7	4	Neogene	9	0.471	0.25	**1**
7	5	Neogene	7	0.769	0.124	**1**
8	6	Quaternary	4	0.342	0.097	**1**
-	7	Carbonate Pindos nappe	6	4.09	2.376	**3**
-	7	Flysch Pindos nappe	6	10.74	6.313	**3**
-	8	Phyllites & Quartzites	17	0.934	0.357	**1**
-	9	Carbonate Tripolis nappe	12	1.05	0.556	**1**
16	10	Phyllites & Quartzites	9	0.252	0.055	**1**
15	10	Phyllites & Quartzites	14	0.456	0.152	**1**

Table 5.3: The Vf values calculated in the drainage basins of the study area. The Vf column shows the number of Vf calculations (n), the mean values (Vf) and the standard deviations (stdev) of the Vf index.

Mountain front Id	Length_Lmf	Length_Ls	Smf	Class
1	2344.616	1574.512	1.489	**2**
2	2627.723	2166.579	1.213	**1**
3	3285.072	2141.283	1.534	**2**
4	3033.775	1318.037	2.302	**3**
5	1484.671	1370.259	1.083	**1**
6	1834.032	1207.084	1.519	**2**
7	2271.667	2055.569	1.105	**1**
8	2117.033	1260.039	1.6	**2**
9	2129.249	1817.180	1.171	**1**
10	3818.254	2602.052	1.467	**2**

Table 5.4: Values of the Smf index along the mountain fronts.

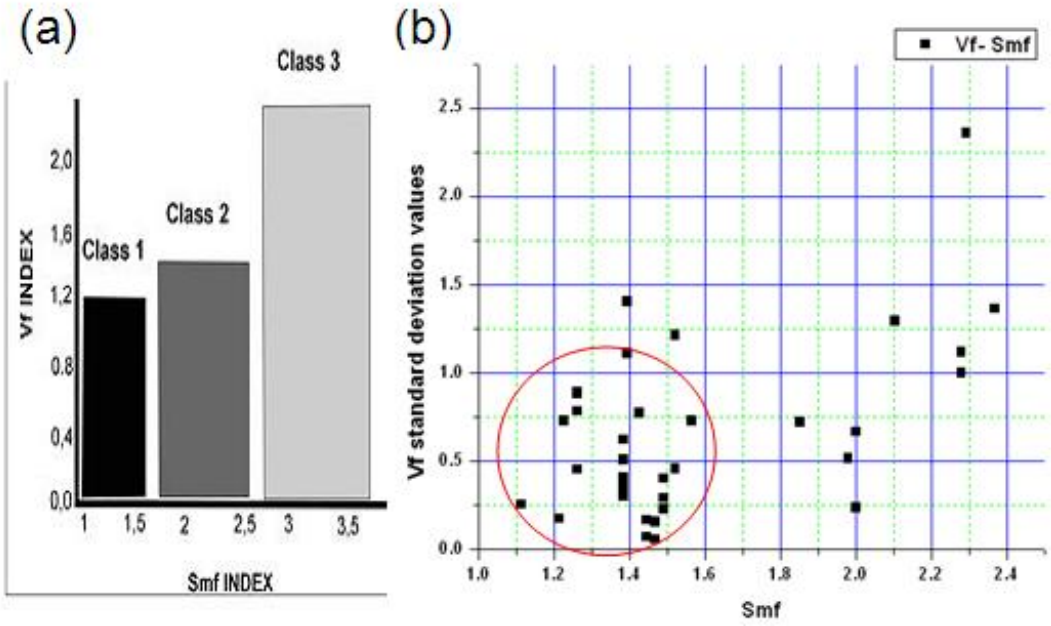

Fig. 5.9: a) The Vf-Smf index classification of the mountain front in three classes of tectonic activity (after Verrios, 2004); **b)** The classes represent the relative degree of tectonic activity (with the values in class 1 being most active). Values in the red circle show that the Vf-Smf indices calculated for the study region correspond to class 1, indicating high tectonic activity.

As described earlier, small basins generally have convex hypsometry curves (dominance of hillshope processes), whilst larger basins have concave curves (dominance of fluvial processes) (Willgoose & Hancock, 1998; Hurtrez et al., 1999; Segura et al., 2007). The hypsometric curves (HC) of the drainage basins that have convex forms indicate potential tectonic influence. However, there are some interesting variations. A discontinuous convex/concave form indicates the influence of either depositional surfaces (alluvial fans) or knickpoints (uplift) at specific elevations of the drainage basins (Fig. 5.11, Table 5.5 & Appendix II, Fig. 6). Fluctuations of the hypsometric curves at these specific elevations are also observed, whereby the calculated indices indicate the possible tectonic activity of each region (Fig. 5.11). The calculation of hypsometric curves for the drainage basins of the study area is presented in figure 5.10.

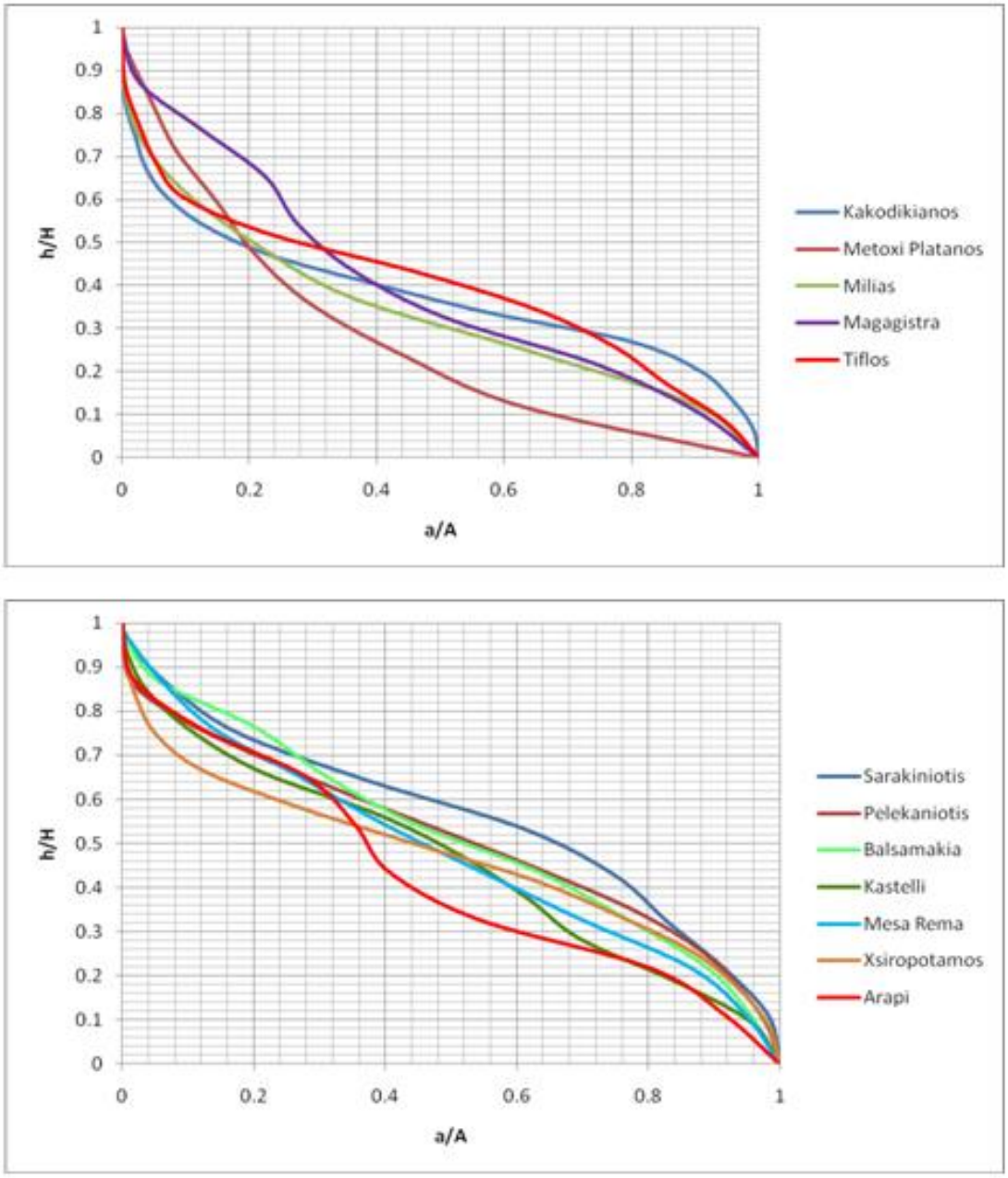

Fig. 5.10: The hypsometric curves extracted for each drainage basin. The upper graph (concave) contains the drainage basins that are transitional from intermediate incision and erosion to severe erosion and low relief. The lower graph (convex) represents the drainage basins that are transitional from deep incision and slight erosion to an intermediate stage of incision and erosion.

Drainage basins	Convex form	Concave form	Elevation of depositional surfaces (alluvial fans)	Elevation of knickpoints (uplift)
Arapi	X		100m	200 m, 600 m
Balsamakia	X		400 m, 700 m	200 m
			(Elevation of slight depositional surfaces)	
Sarakiniotis	X		500 m	200m, 400 m
Kakodikianos		X	400 m	300 m
Magagistra		X	200 m	600 m

Table 5.5: Sample of drainage basins with their hypsometric curves type revealing the presence of depositional surfaces (alluvial fans) and knickpoints (uplift) along the curve.

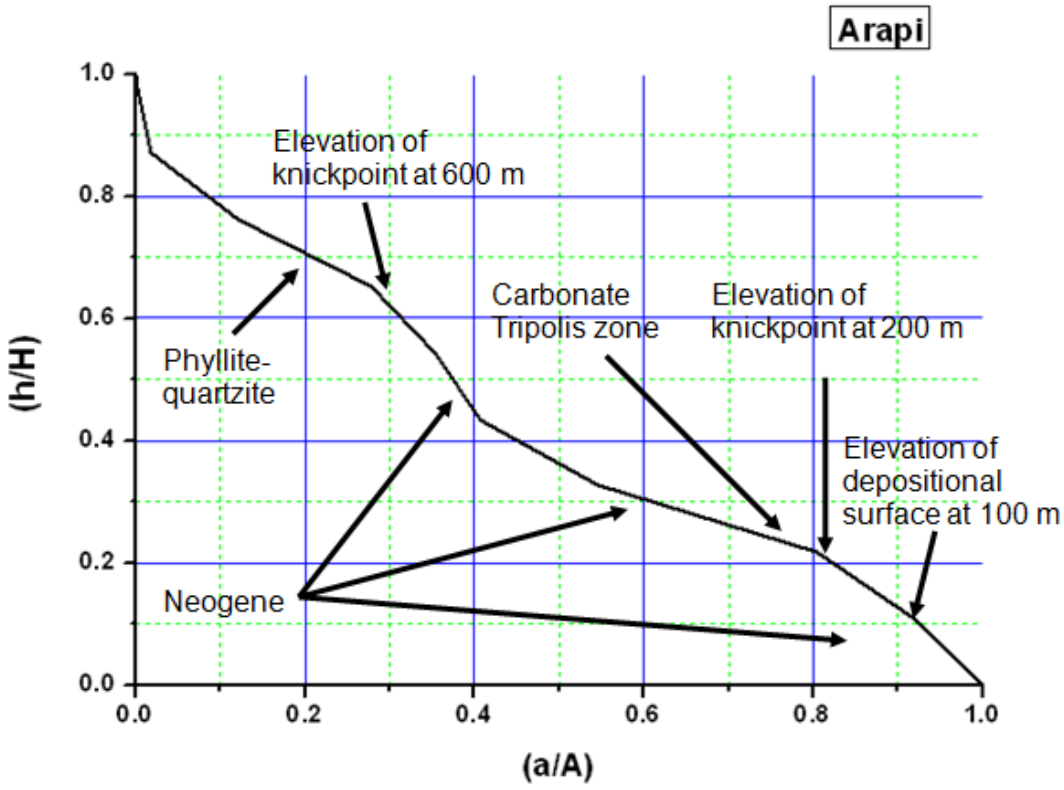

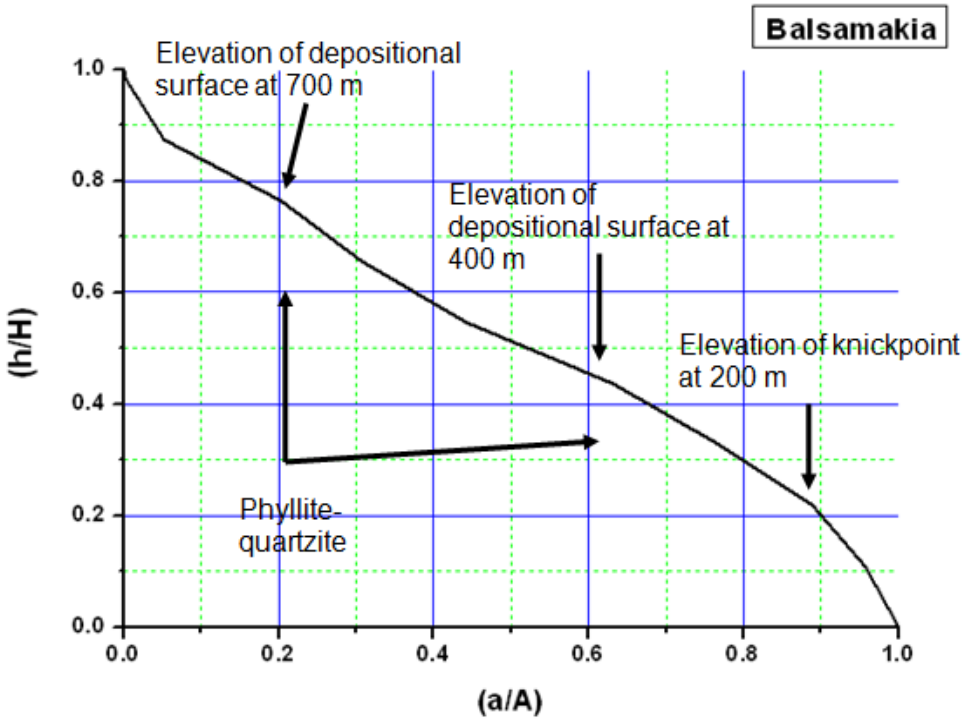
Balsamakia
Elevation of depositional surface at 700 m
Elevation of depositional surface at 400 m
Elevation of knickpoint at 200 m
Phyllite-quartzite
(h/H)
(a/A)
0.0
0.2
0.4
0.6
0.8
1.0

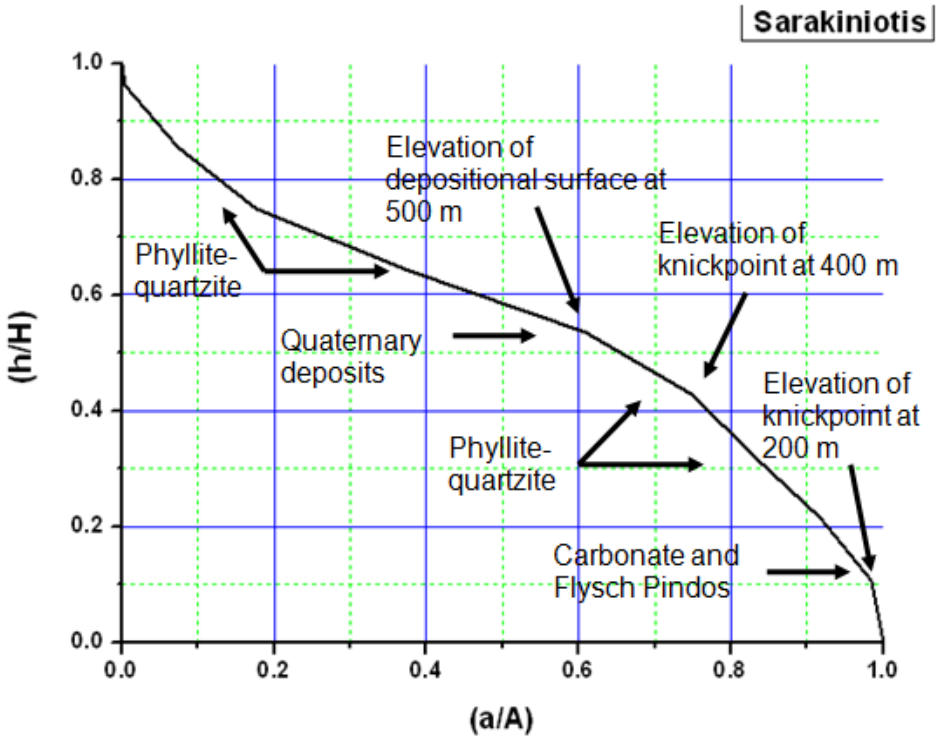
Sarakiniotis
Elevation of depositional surface at 500 m
Elevation of knickpoint at 400 m
Phyllite-quartzite
Quaternary deposits
Elevation of knickpoint at 200 m
Phyllite-quartzite
Carbonate and Flysch Pindos
(h/H)
(a/A)
0.0
0.2
0.4
0.6
0.8
1.0

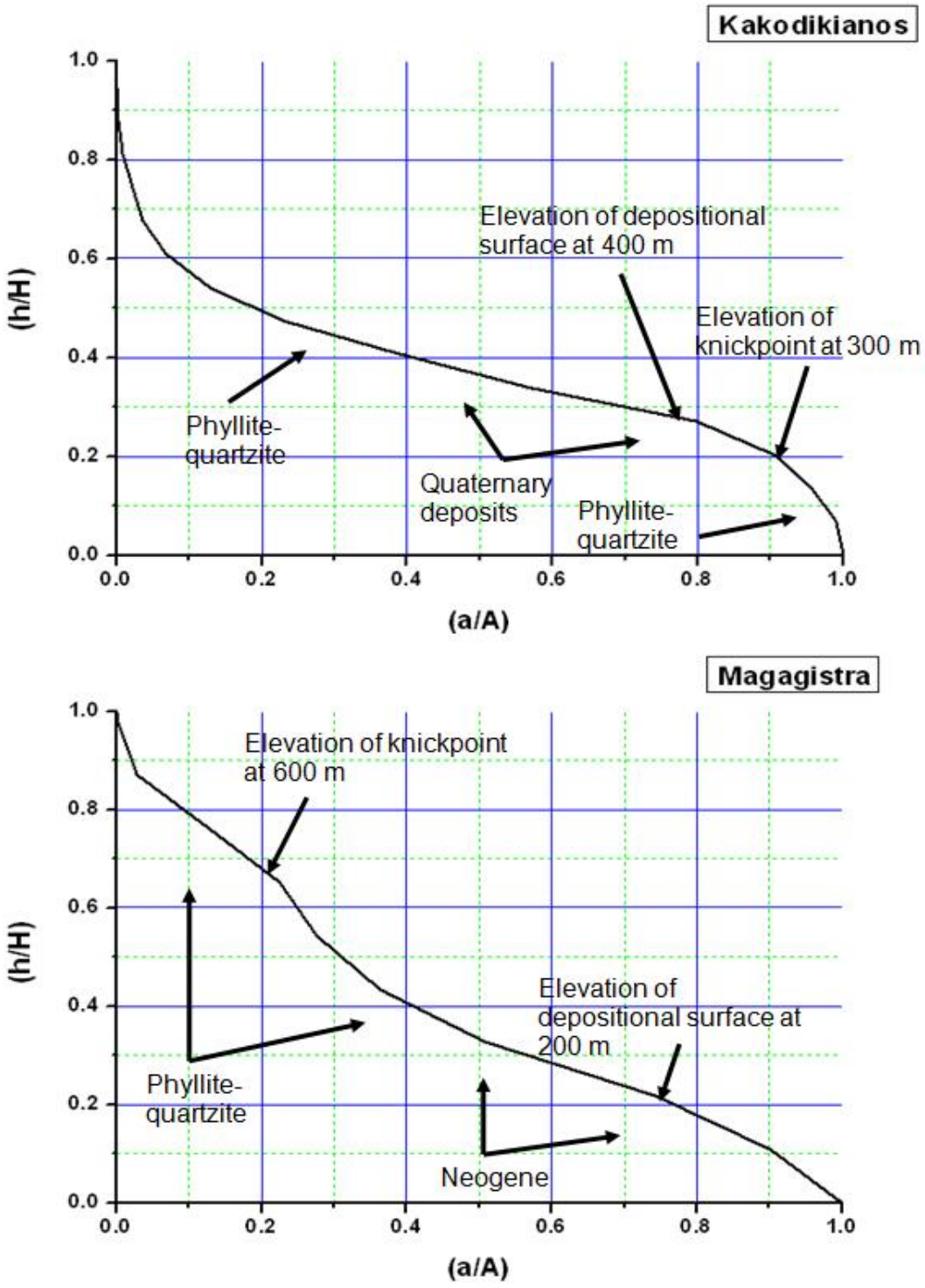

Fig. 5.11: Sample of the hypsometric curves (HC) of drainage basins with the fluctuations along the curve, indicating depositional surfaces (alluvial fans) or knickpoints (uplift). Lithology across the basins is depicted to make more meaningful these observed fluctuations.

5.4.2 Geomorphometric data and derivatives extracted from DEMs

The spatial distribution maps that were extracted using GIS were useful as their interpretation can indicate potential zones of tectonic uplift and/or tilting which determine: i) the presence of tectonic activity spatial distribution within the entire study area and; ii) identification of zones of still of higher susceptibility to active tectonics. The data derived from the DEMs was particularly useful for the calculation of geomorphic indices and extraction of geomorphometric information associated with tectonic activity (such as slope, amplitude relief, topographic wetness index, drainage density and drainage frequency).

The slope gradient algorithm shows maximum slope steepness, indicating the change in elevation between each cell and its neighbors (ESRI, 2003), thus allowing relationships in basin morphometry to be determined (Fig. 5.12). Areas under nearly level to level slopes ($0\text{-}2^0$) are observed in the northernmost parts of the basins. Foot slopes of upland areas with very gentle slopes ($2\text{-}5^0$) are observed in the north basins. Gentle slopes ($5\text{-}15^0$) are observed in undulating terrain and intermittent valley zones in the south-west and central basins. Moderate slopes ($15\text{-}35^0$) characterised by rolling plains can be found in western and south-eastern basins. Steep ($35\text{-}55^0$) and very steep slopes ($>55^0$) associated with escarpments and dissected ridges are found in the southern basins.

Information associated with recent vertical displacements of uplifted or subsidence blocks can be identified by the spatial distribution of the amplitude relief (A_r) (Fig. 5.13). In the study area the A_r values range between 0-640 m. Values higher than 400m can be found mainly in the southern drainage basins. Relatively high values of A_r, form an alignment with an E-W, NW-SE and NE-SW extension zones, about 5-7km (Region A). Highly anomalous increased values, with regard the surrounding neighborhood region, can be found across the entire study area indicating tectonically active regions (Region B). The lowest values occur along the northern part of the study area where the Neogene and Quaternary formations are lying down. The asymmetry of the basins and differential tilting can also be determined every time increasing A_r values (uplift) are bounded by relatively low values of the index (subsidence) (Fig. 5.13).

The topographic wetness index (TWI) provides ancillary information about factors controlling slope drainage (Fig. 5.14). In region A, high values of TWI

indicate a flat receiving area where moisture could accumulate. Region B generally has lower TWI values than region A, suggesting lower stream ordering and lower water discharge. The linearity occurring between high and low values of the TWI indicates tectonic influence in the region (black arrows). The areas with intermediate TWI values in C region indicate major ridges and steep slopes. Region C is characterized by low permeability Phyllites-Quartzites, but small amounts of soil moisture are observed in areas of steep slope that may coincide with faults. Region D has steep slopes and V-shaped valleys with deeply incised, extensively eroded valley floors and very low values of TWI.

Drainage density and drainage frequency maps are presented in figure 5.15. The interrelationship of those maps can discriminate zones of potential tectonic influence deformation. Both the drainage density and drainage frequency distribution maps reveal lower values in western and southeastern basins (Region A). This implies structural controlled regions where the drainage network cannot be adequately developed. This is reinforced by the fact that these regions (mainly the western basins) are covered by low permeability Phyllite-Quartzites; an unusual aspect, as high values of drainage density and frequency are the ones that correspond to impervious rocks (see Fig. 5.15 & Appendix II Fig. 2).

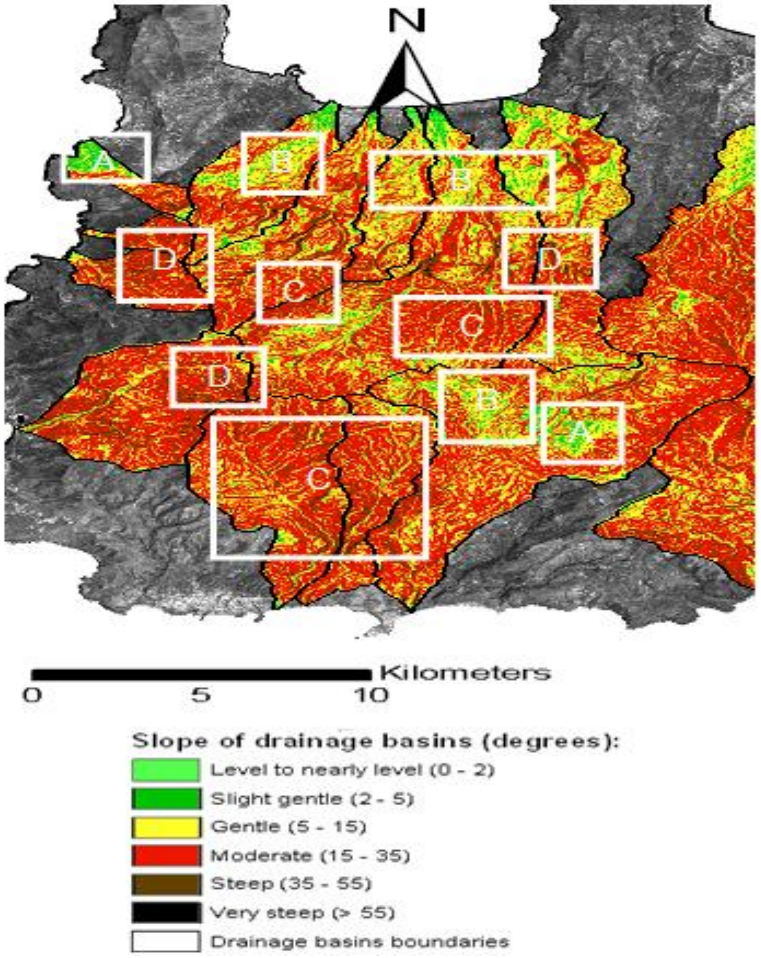

Fig. 5.12: Slope map of drainage basins. (Region A), flat surfaces to slight gentle slopes, occupying 6.8% of the study region; (Region B), gentle slopes, covering 32.27% of total area; (Region C), moderate slopes covering 55% of the study region and; (Region D), steep to very steep slopes covering 5.8% of the total area.

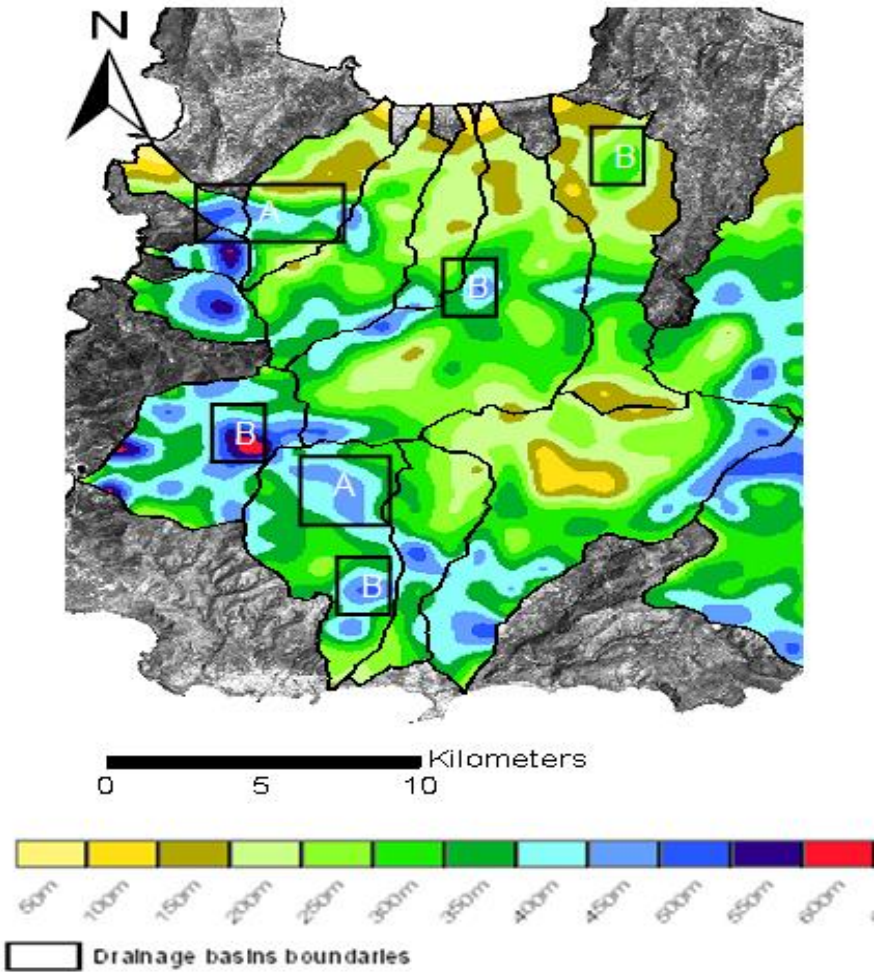

Fig. 5.13: Amplitude relief. The black rectangles indicate tectonically active zones, with high relative relief observed. Alignment formation zones and high variations in relative relief, with regard the surrounding neighborhood regions, are the highly active zones.

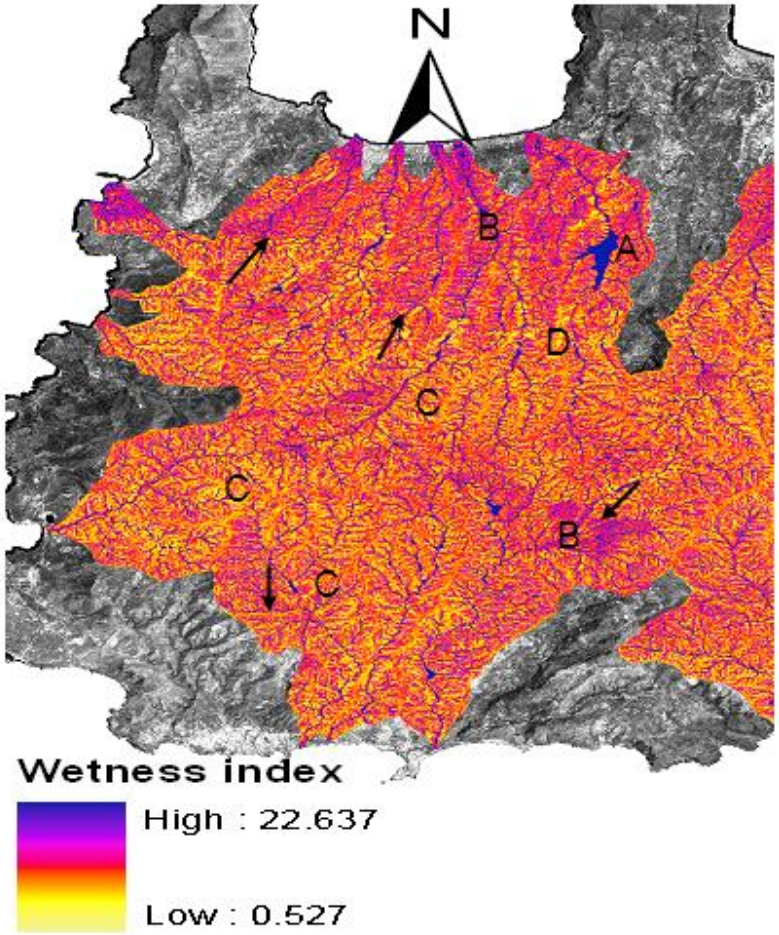

Fig. 5.14: The TWI regions cited in the text. Region A shows high values of TWI; Region B has high values (but lower that region A due to lower stream ordering and water discharge); Region C has intermediate values, revealing steep slopes and major ridges; Region D indicates lower values of TWI characterized by incised V-shaped valleys. The black arrows indicate sample regions of tectonic influence due to the linearity observed between the high and low values of the index.

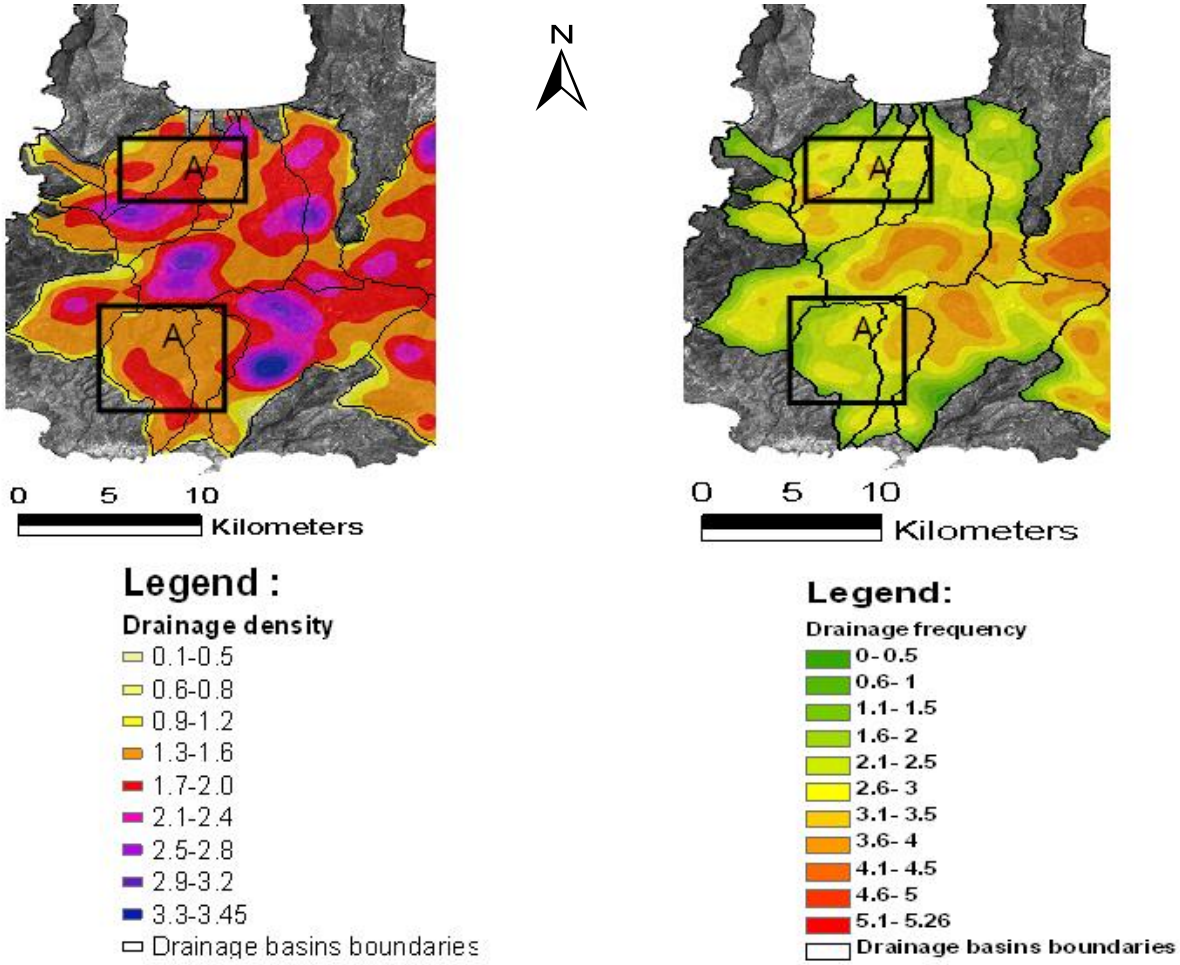

Fig. 5.15: Left: The drainage density distribution map of the drainage basins, with higher values depicted in blue. Right: The drainage frequency distribution map of the drainage basins, with higher values depicted in red. Lower values of drainage density and frequency mainly to impervious rocks indicate tectonically structural zones (Region A).

5.5 Discussion

In Chapter 4, geomorphometric indices revealed potential neotectonic zones (based on drainage basin analysis) close to areas with high rates of uplift in the western part of study area. In this chapter the morphotectonic indices provided additional information regarding the degree of mountain front tectonic activity, stream migration, as well as uplifting within the drainage basins. Such information was useful to help aiding the identification of potential local neotectonic ground deformation within tectonically controlled drainage basins. As will be discussed below some sites are selected as case studies. Also some datasets such as lineaments/faults are considered to make the morphotectonic indices outcomes more meaningful. However, a more detailed presentation of lineament maps is given in chapter 6.

As mentioned in the õ5.4 Resultsò section, high values of the transverse topographic symmetry factor (T>±0.50) indicate uniform migration of the main drainage basin river, with values close to 1 indicating the highest degree of stream migration and basin tilting towards that direction (Fig. 5.4). There is no relationship between bedrock trends and stream migration directions, therefore tectonic deformation is the more likely explanation. In addition, faults with NWSE and EW strikes seem to be downcutting and crossing those regions that exhibit higher T index values. The interpretation of T index is easier if the calculated index of asymmetry factor (AF) in chapter 4 is also considered. This is in line with the Alastair (2008) study in which the comparison of the two indices was used for identifying lateral stream migrations and detecting neotectonic tilting. Except for the Tiflos and Arapi basins, which have a westwards tilt as a result of N-S azimuth Keras fault (Fig. 5.16) all other northern drainage basins have an eastwards tilting direction. This is further reinforced by the asymmetry factor (AF) index, which supports the basins tilting. This region is an interesting case as the basinsô development seems to be affected by two major faults: the N-S Keras Fault and the E-W Platanos Fault (Fig. 5.16). The Keras fault is a tectonically active normal fault with NE-SW strike and three co-seismic displacements during the Pleistocene

and Holocene (Mouslopoulou, 2001). Prior to this study, neotectonic features along the Platanos fault had not been investigated: morphotectonic indices can be a rapid and cost-effective method of assessing tectonic activity. The Tiflos and Arapi basins ï with their main river flowing in a N-S direction ï tilt to the west. This is probably due to local neotectonic movement, with the left-lateral strike-slip Keras fault (located on the east side of these basins) being the source of the deformation and stream migration as T index indicates. This is an anomalous direction of tilting and stream migration, relative to the surrounding basins, which tilt towards the east. The shaded relief maps highlight the tilting status of these basins: the gentler slopes tilt westwards, while surrounding basins have an eastern inclination (Fig. 5.17). Turning to the western basins with an E-W mainstream flowing and influence of Platanos fault, a southerly tilting is observed in the Balsamakia, Mesa Rema and Xsiropotamos basins. In contrast, the Metoxi-Platanos basin is northerly tilting, probably due to neotectonic deformation along the Platanos fault (Fig. 5.16). In all aforementioned cases an apparent transition of the T values is observed (from close to zero to greater than 0.7 values). This indicates an evidence of significant tilting and stream migration which coincides with the Alastair (2008) study observations.

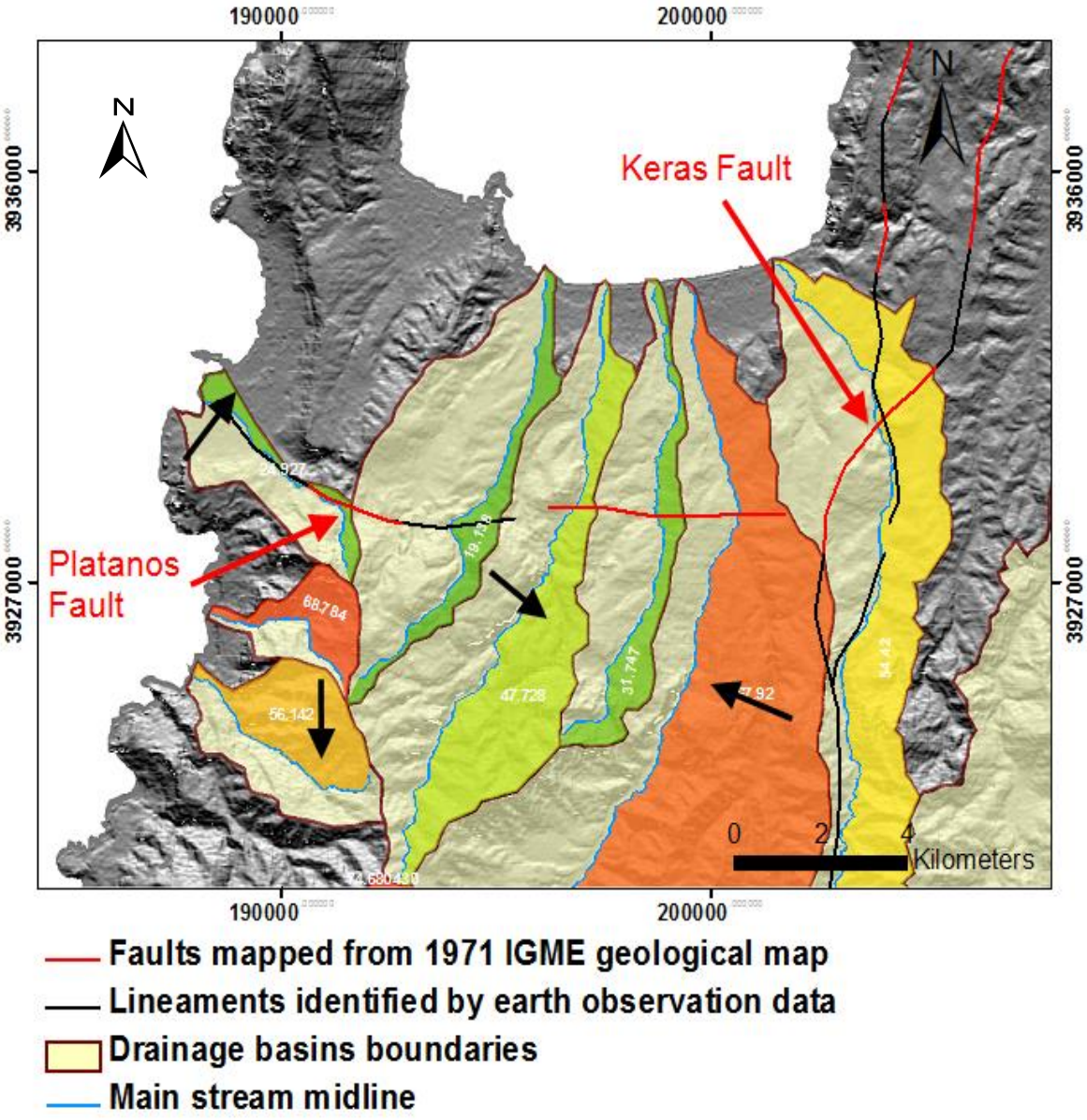

Fig. 5.16: Tilting of drainage basins affected by major faults in E-W (Platanos fault) and N-S (Keras Fault) directions. For the broadly N-S aligned basins, green tones indicate eastward tilting while red/yellow tones indicate westward tilting (see black arrows). For the western coastal basins, green tone indicates northward tilting while red/yellow tones show southward tilting (see black arrows).

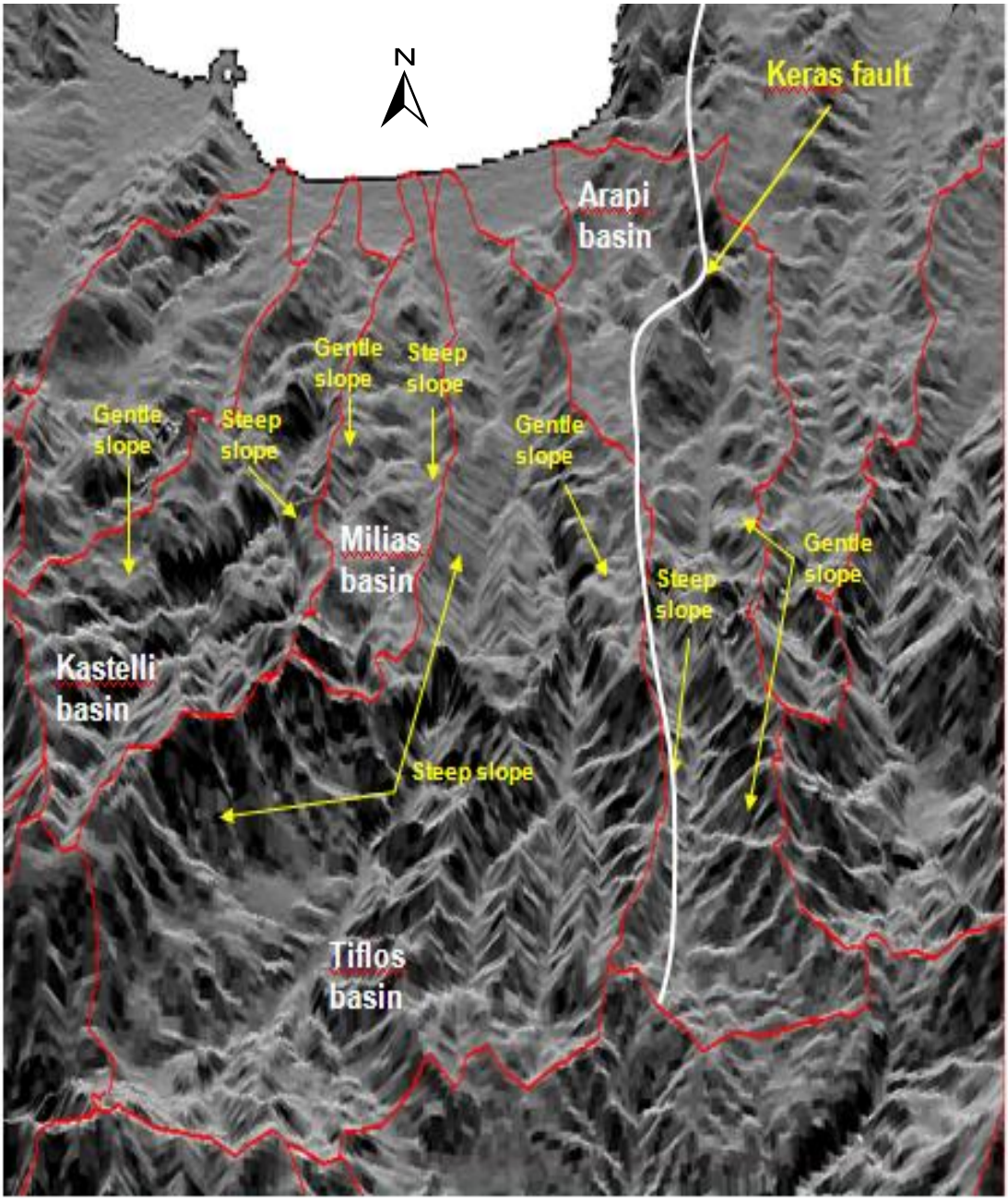

Fig. 5.17: The shaded relief map reveals the difference of the tilting observed in the south-west basins, due to the tectonically active Keras fault presence.

Zones of potential vertical neotectonic movement along faults result in escarpments with high S_L index fluctuations. High-value fluctuations of the S_L index (S_L>300) in the particular areas are associated with faults shown on the 1971 geological map or with lineaments derived from the lineament analysis (see Chapter 6). Moreover, stream longitudinal profiles extracted from DEM, revealed changes in the slope along the stream within the areas where S_L high-value fluctuations were observed. This comparison is in accordance with studies of Maroukian et al. (2008) and Pedrera (2009) as such regions seem to reflect active tectonic structures. The SLk map is a powerful spatial distribution representation of S_L index, highlighting stream anomalies as a result of disruption by tectonic structures. Those high anomalous values of the normalized stream length-gradient SLk index, indicated areas where the stream was potentially tectonically controlled (Fig. 5.6). The observations of SLk anomalies by Perez (2008) and Pedrera (2009) indicated that a high percentage (81%) of the anomalies was correlated with tectonic contacts. Fault activity seemed to be responsible for the changes in river gradients, as the higher values were not related to lithological changes or river piracy (Perez, 2008). The SLk anomalous values in this research seem to be in accordance with the aforementioned studies. Moreover, the study area in this research is mainly characterized by poorly organized drainage patterns. In terms of investigating the correlations among rivers, the SLk analysis is more appropriate when drainage networks are not well organised (Perez, 2008). The high anomalous values of SLk reinforce the aforementioned asymmetry indications by T index, for those particular basins referred earlier. These basins based on SLk and T index outcomes are undergoing potentially high degree of active tectonics due to the major Keras and Platanos faults presence (see Fig. 5.4, 5.6 & 5.16).

The relationship between the Vf and Smf indices shows the relative degree of tectonic activity. The majority of the measurements extracted for the Vf and Smf indices were assigned to class 1, where active tectonic deformation is taking place. Such measurements are similar with those provided by Silva et al. (2003), Verrios (2004) or Pedrera (2009). Some examples of Vf and Smf values behavior

in sites where neotectonic activity dominates over lithological variations are presented in figure 5.20.

Two specific test areas were selected to check Vf-Smf morphotectonic indices interaction. In the case of the Kastelli landscape (site 1) (Fig. 5.18), the mountain front is developed on the boundary of soft unconsolidated Cenozoic sediments (Fig. 5.18) making it more susceptible to erosion. A similar situation occurs with the Baza fault in SE Spain (Garcia-Tortosa et al., 2008): this indicates the importance of the Vf-Smf results as providing evidence of neotectonic activity, as opposed to erosion. The mountain front is divided into three segments and although the Smf index indicates that each segment undergoes different tectonic deformation, all of them are assigned to class 1, indicative of neotectonic activity.

The S_L index also shows higher values for segments of the mountain front with low Smf values. This is in line with the Garcia-Tortosaûs (2008) study of the Baza fault, which is developed upon soft sediments and is characterized as tectonically active by geomorphic indices. Similar features to the Baza fault are illustrated by the fluctuating values in figure 5.18 of the study area (site 1), which emphasize specific variances between the western, the central and the eastern part of the mountain front. In the central section of site 1, the Tripolis carbonate nappe has a less sinuous mountain front and shows a decrease in slope erosion processes. This explains the variance between the S_L values described earlier and indicates that the central part is more tectonically active.

The Vf index values increase in the upstream direction of the mountain front, supporting the presence of tectonic activity, as Verrios (2004) observed at the Eliki fault in Greece. The results of this studied mountain front reveal increased Vf values, followed by abrupt decreases of the index values. Such situation indicates regional uplift with smaller en-echelon active faults parallel to the major mountain front.

Furthermore, as it will be presented in subsequent chapter (see chapter 6) field work along the mountain front indicated the presence of slicken-lines, fault breccias and fault-offset recent deposits (Fig. 7.11 to 7.14), indicating the active status of the mountain front. The fault plane examined during fieldwork was

characterized by left oblique slip indicators (see Chapter 6 for details). This fault plane is part of Platanos fault and responsible for the extension of the Magagistra drainage basin in an E-W direction, as is revealed by its shape in the middle part of the basin.

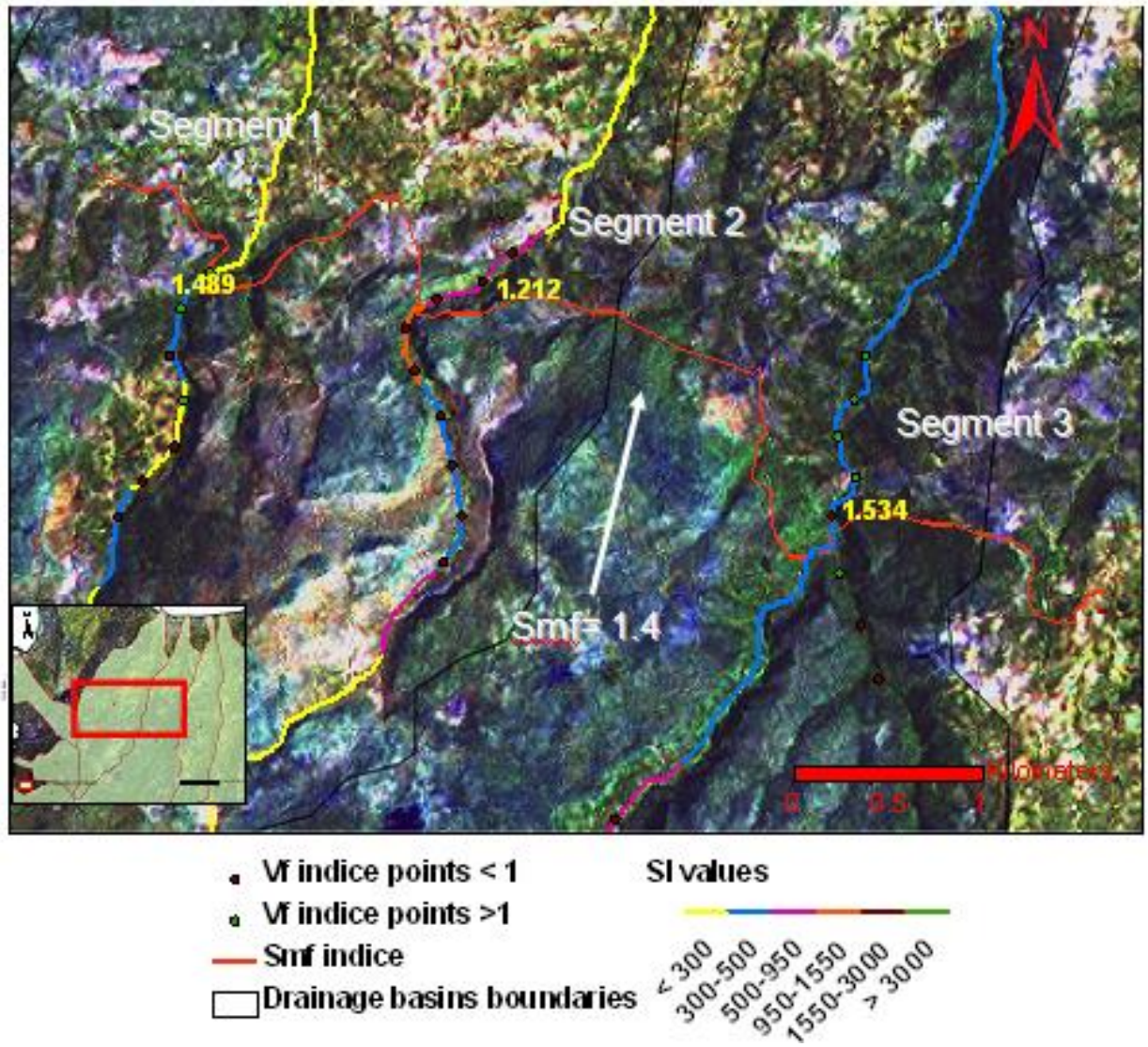

Fig. 5.18: Site 1: The three individual segments of mountain front sinuosity (with values 1.489; 1.212 and; 1.534) with the central being the most tectonically active (Smf =1.212). The total Smf value of the mountain front is 1.4

The second case study (Site 2) of neotectonic deformation is located southwest of the study region (Fig. 5.19), where the highest regional uplift is observed. The region is characterized by complex geology, with numerous distinct rock types (Phyllite-quartzite series, Tripolis and Pindos carbonate nappes, the Flysch Pindos nappe and unconsolidated Cenozoic sediments (see Fig. 2.7).

The mountain front eroded escarpment #1 (Fig. 5.19) has a sinuosity that indicates neotectonic activity. The low sinuosity value is also influenced by the presence of the strong rocks of the Pindos Carbonate nappe, which reduces mountain front erosion. In addition, fieldwork revealed the presence of slickenlines on exposed fault planes along the front (Fig. 2.2). The Vf index values suggests limited tectonic activity despite the very clear field evidence of tectonically active uplift, including about 9 m of co-seismic uplift (Fig. 2.2). However, the fact that the Vf index values increase upstream indicates a tectonically active mountain front (Verrios, 2004). It may be that these contrasting indications of neotectonic activity might be due to very recent faulting not yet impacting on the headwater drainage (ie. there is a lag time). Another factor that would add to the lag time effect in this case is the relative hardness of the bedrock in the headwater zone.

Mountain front #2 (Fig. 5.19) is located between the boundaries of different rock types and can be divided into two segments. The western zone is over the boundary of unconsolidated Cenozoic sediments with Phyllite-quartzite rocks, while the eastern zone is between the boundaries of unconsolidated Cenozoic sediments and the Carbonate Tripolis nappe. The mountain fronts are apparently more susceptible to erosion due to their soft unconsolidated Cenozoic sediments, as in the case of the Kastelli region. Again, both segments are characterized as tectonically active to moderately active, with regard to the mountain front sinuosity results (Fig. 5.19). The eastern segment is tectonically more active than the western. This could be because in the eastern segment the contact is between the Tripolis Carbonate nappe and unconsolidated Cenozoic sediments, with the first formation being a strong rock type and therefore minimizing the erosion of the mountain front. In contrast, on the western segment the presence of the relatively

weak Phyllite-Quartzite rocks with unconsolidated Cenozoic sediments is a zone of enhanced erosion and increased sinuosity. The difference in rock type indicates why different mountain front sinuosity values are observed in the two segments of the region. Field work along the mountain front revealed breccias and slickenlines indicative of tectonic activity (see chapter 6 for details).

Mountain front #3 (Fig. 5.19) has moderate tectonic activity according to the mountain front sinuosity value, while deep incision is preserved in the valleys, which have low Vf index values. The Vf indices increase upstream but then abruptly decrease and then abruptly increase, implying a zone of regional uplift with a set of small en-echelon active faults. The transverse topographic symmetry factor indicates the deviation of the mainstream in the drainage basins, as well as the presence of tectonic deformation (Fig. 5.4). The hypsometric curve calculation highlights the limited erosion in the basin as a whole, for the mountain front (eroded escarpment #3; Fig. 5.11). This implies that the basins have experienced rapid tectonic uplift while the background erosion has remained minimal. The geomorphic indices indicated neotectonic activity, regardless of the lithology.

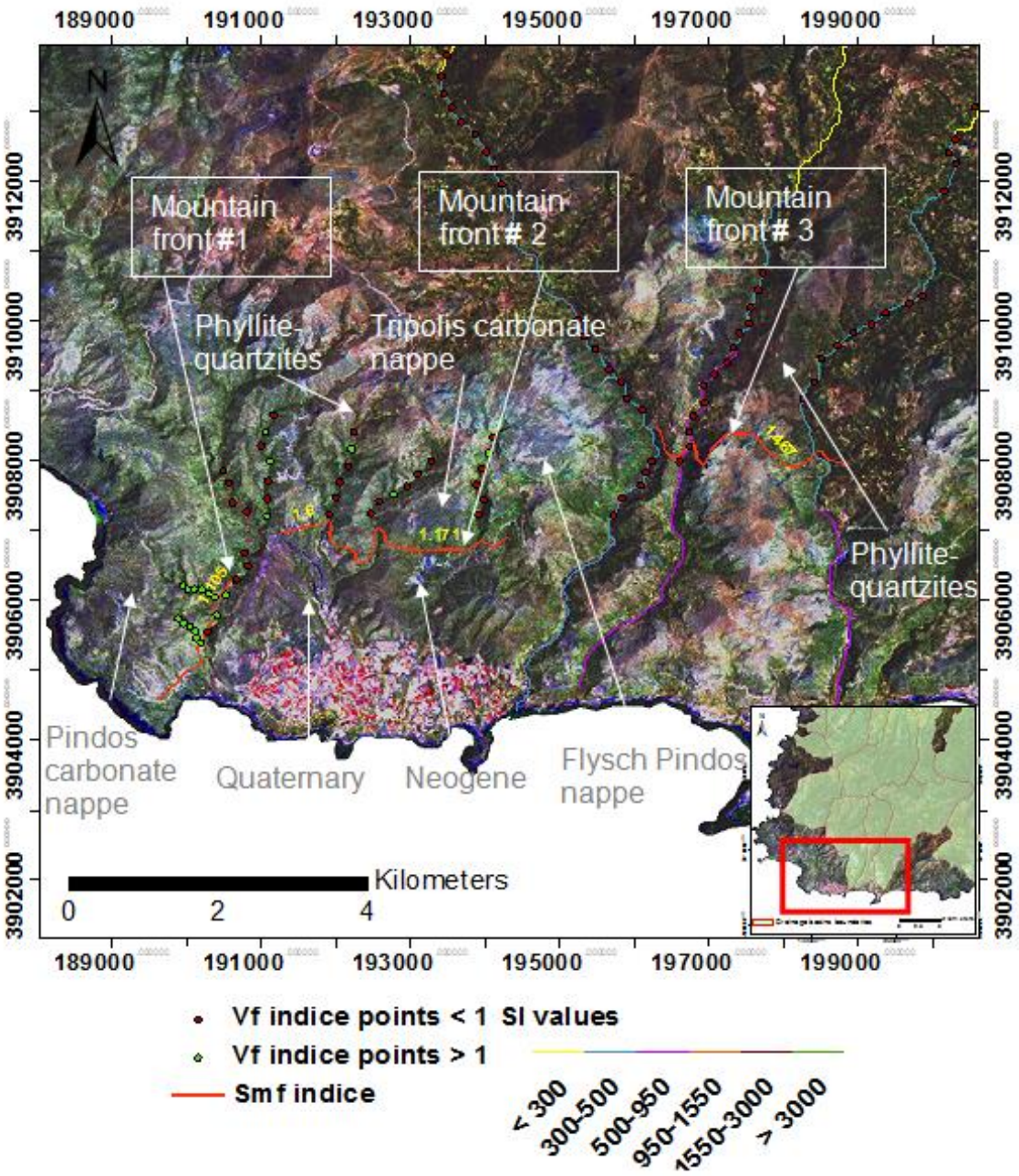

Fig. 5.19: Site 2: Map of Smf, Vf and SL indices with mountain front locations referred to in the text.

Plan view of mountain front	*Transverse valley section*	*Neotectonics or geological setting*
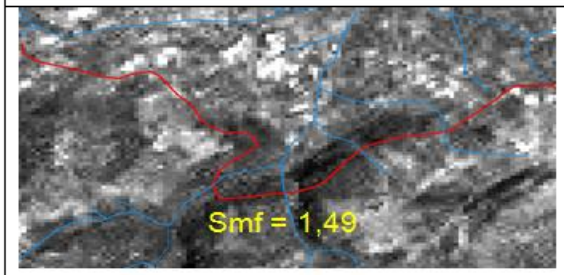	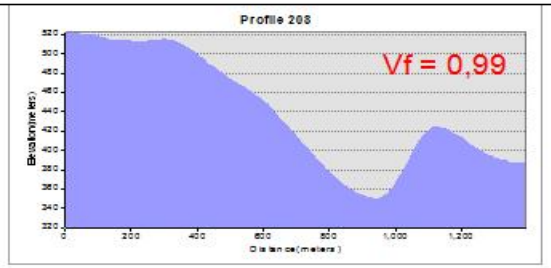	Quartzites with phyllites (strong rock strength) bounded by Neogene deposits (weak rock resistance) and crossed be 3rd order stream. Class 1->Class2 of relative degree of tectonic activity.
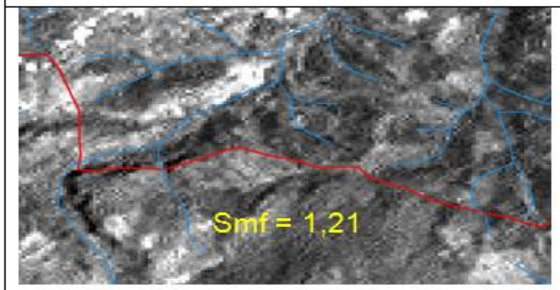	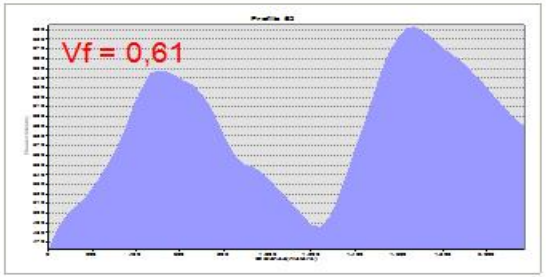	Carbonate nappe (very strong rock strength) bounded by Neogene deposits (weak rock resistance) and crossed by 3rd order stream. Class 1 of relative degree of tectonic activity.
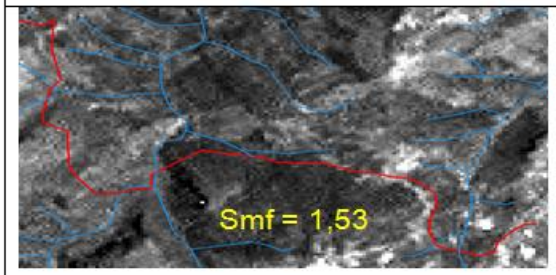	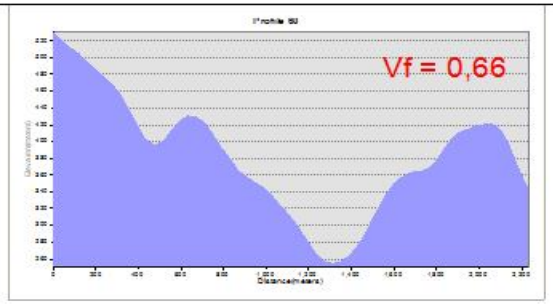	Carbonate nappe (very strong rock strength) bounded by Flysch nappe (strong rock resistance) and crossed by 5th order stream. Class 1->Class2 of relative degree of tectonic activity.

Fig. 5.20: Sites where neotectonic activity dominates over lithological variations. First column: plan view of mountain front sinuosity and drainage lines. Second column: valley profiles of sample points where the Vf index was calculated. Third column: lithology of each segment of the mountain front, the stream order at the mountain front and the relative degree of tectonic activity with regard to V_f-S_{mf}.

Small basins generally have convex hypsometry curves (dominance of hillshope processes), whereas larger basins have concave curves (dominance of fluvial processes) (Willgoose & Hancock, 1998; Hurtrez et al., 1999; Segura et al., 2007). The drainage basins of Metoxi-Platanos and Milias are not in accordance with the aforementioned theory as they are characterised by concave curves. This indicates that their severe erosion can be associated with the different tilting observed in the region (see AF and T indices indications), perharps reinforcing the influence of the Platanos and Keras faults in surface deformation. Additionally, the hypsometric curves (HC) for the Kakodikianos and Magagistra basins have a concave form, which implies a transition from intermediate incision and erosion to severe erosion and low relief, and thus, no significant tectonic influence. Hamdouni et.al (2008) and Maroukian et al. (2008) report a convex discontinuous form, with the curve being useful in the identification of depositional surfaces or uplifted regions. A convex formation in the lower part of the curve was considered to be related to recent uplift along a fault or fold.

Maps showing the spatial distribution of geomorphometric values D_d, F_u, slope, A_r and TWI were created (section 5.4.1). The maps of drainage density and stream frequency when draped over the hydrolithological map, indicate that areas with high drainage density and high stream frequency correspond to impermeable rocks. The study areas with high surface permeability have low drainage density and low stream frequency values. However, some regions did not accord with this general observation, particularly western and southern basins of the study area, which are dominated by low permeability rocks (Phyllite-Quartzites). Lower values of D_d and F_u occur in those regions, indicating that structural factors control those areas, with limited drainage network development. High stream frequency values are characterized by linear patterns that are parallel or sub-parallel to major tectonic lineaments, further indicating that the drainage network is being developed under neotectonic influences (e.g. Appendix II, Fig. 7). Similar were made by Kouli et al. (2007) for two particular drainage basins of western Crete.

An increase in the slope gradient generally leads to a drainage density decrease, indicating a negative correlation (Lin & Oguchi, 2004). This study includes several study areas for which this observation holds true, and this increase is usually related to channelization as erosion progresses. However, in some of the study areas this is not the case as positive correlation is observed

between the slope gradient and the drainage density. This may be the result of long linear stream segments with trellis or parallel patterns which are controlled by tectonic structures rather than lithological boundaries, as those basins have homogenous bedrock (see southwestern basins in Fig. 5.12 & 5.15).

The spatial distribution of the amplitude relief (A_r) is associated with recent vertical displacements of uplifted or subsidence blocks (Fig. 5.14). High values bounded by low values of the index are observed in the Magagistra basin (see northwest region in Fig. 5.13), indicating uplifted regions (high values) relevant to observed subsidence (low values). These regions are within the area where the Platanos fault is located. Highly anomalous increased values, with regard to surrounding areas, can be found across the study region indicating tectonically active zones (Region B). The Keras fault is located in such a zone as it has anomalous increased values of amplitude relief (Ar), relative to adjacent areas. The Ar map detected relatively high values, forming an alignment with an E-W and NW-SE extension zones (Region A), revealing potential blocks bounded by faults linearity (see Fig. 5.13). The aforementioned observations are in accordance with the asymmetry and the differential regional uplift or subsidence phenomena detected by Centamore et al. (1996), Della Seta et al. (2004) and Arisco et al. (2006) in various regions of Italy.

The topographic wetness index (TWI) provides ancillary information relating to factors that control slope drainage. As mentioned in the studies of Anderson & Kneale (1982) and Hjerdt (2004) topography is an important control of hydrological processes and TWI can represent water distribution regarding topography influence. Very low values of TWI can be observed in particular zones of the study region (see regions C and D in Fig. 5.14). This indicates major ridges, steep slopes and V-shaped valleys with deeply incised, extensively eroded valley floors. These areas appear to be related to neotectonic zones, as identified by the amplitude relief index (A_r), with high values, indicating neotectonic landscape deformation (Fig. 5.13). A comparison with recent vertical displacements can then be made: slope gradients in these regions range from moderate (5-10%), to very steep (>30) (see Fig. 5.12).

The spatial distribution maps and the evaluation of the morphotectonic indices shows that the influence of the main factors controlling morphometric expression, neotectonics (recent faulting), geomorphology (steeps slopes) and

lithology (rock permeability) is marked within the examined drainage basins (see Fig. 2.7 for drainage basins location). The dominant signal in these basins is that of neotectonic deformation. To reinforce these aspects the multi-criteria decision analysis (MCDA) approach is considered in Chapter 8, in association with lineament and lithological discrimination information provided by the subsequent Chapter 6, to assess the neotectonic acticity on a spatial analyzed basis.

CHAPTER 6 MAPPING LITHOLOGIES AND LINEAMENTS

6.1 Introduction

As presented in Chapter 2 the geological and tectonic setting plays a significant role in the landscape development of the study area in this research. The mapping of lithologies and lineaments can offer an overview of lithological and structural factors that influence the development of Crete's landscape. These mapping features can reveal the actual association of lithological/structural control with tectonically active regions.

In Chapters 4 and 5 the evaluation of various geomorphological and morphotectonic characteristics led to the determination of the tectonic activity in both regional and local scale, respectively. This evaluation corresponded to the actual reflection of drainage network and drainage basin development to tectonic control, regarding examination of geomorphological factors. An interesting point was to examine these geomorphological factors versus certain lithological and structural factors (such as lineaments/faults). The lithological aspects were considered in earlier chapters (see Chapter 4 and 5) and thus, the identification of lineaments corresponding to faults was of higher priority at that stage of research. This correspondence is investigated in this chapter with the view to determining and comparing the lineament/fault aspects with the drainage network aspects, with the aim of recognising tectonic control. Apart from this, the determination of lithological boundaries was also essential at that stage of research as isolation between lineaments corresponding to lithological contacts and those corresponding to tectonic features (e.g. faults) needs to be discriminated. The existence of geological maps created in 1971 (IGME geological map) is the only available dataset for the study region to gather lithological information. This fact reinforces the need to determine in more detail the lithologies in the study region by making use of other datasets (such as Earth observational data).

The nature of the study region is so complicated that the tectonically active regions which were identified in earlier chapters need to be further investigated. The geological perspectives of the last decades can be examined by the use of remote sensing and image processing of freely available satellite images (e.g. Landsat ETM+). This is particular useful in regions (such as African, Asian or

Caribbean countries) where no digital formats of geological maps might exist and a first sight view of the existing lithologies and lineaments/faults is needed. In this study, as mentioned above, there are available geological maps (IGME, 1971) that were produced in the 1970s. This fact gives emphasis to the value of using the freely available digital image data, in order to examine the geological factors in a study region. This approach can provide an update of the existing geological maps (IGME, 1971) that are based on conventional methods of aerial photo interpretation. Further investigation of the need to evaluate the lithologies and lineaments identified within tectonically active zones, determined in Chapters 4 and 5, is examined in the subsequent Chapter 8 (on the basis of multi-criteria decision analysis (MCDA)).

The mapping of lithologies and lineaments in this research is based on utilization of earth observational image data (e.g. Landsat ETM+ and DEMs) and outcome comparison with digitised published geological maps (IGME, 1971). These datasets are used to create products that: i) discriminate lithological units and; ii) identify tectonic lineaments in the study area. Moreover, this research describes an approach that allows satellite imagery processing to combine both lithological and lineament information in a single satellite image. The aim is to enable the isolation of lineaments corresponding to lithological contacts from those corresponding to fault zones. The data sources that are used in this section are summarized in Table 3.1.

6.2 Background on satellite image data in geological mapping

6.2.1 Lithological discrimination

The image processing operations described in subsequent sections were selected to discriminate lithological units and highlight tectonic features. These methods are commonly based on the use of simple RGB band combinations (see Table 6.1) (e.g. Abrams, 1985; Drury, 1987; Crosta, 1989; Kenea, 1997; Won-In and Charusiri, 2003; Junek, 2004; Teeuw et al., 2005; Pena & Abdelsalam, 2006; Solomon & Ghebreab, 2006) and on RGB band ratio combinations (see Table 6.1) (e.g Kaufmann, 1988; Crippen, 1989; Ramadan et al., 2001; Rowan, 2003; Al

Rawashdeh, 2006; Fu, 2007; Gad, 2007). For example, Pena & Abdelsalam (2006) considered in their study the RGB combinations 742 and (5/7)(4/5)(3/1) of Landsat ETM+ sensor as an effective approach for lithological mapping in arid regions. The benefit of those images is their capacity to preserve morphological features while displaying different lithological units. Another study revealed that RGB band combination 754 (Landsat TM) seems to display a good contrast for analyses of lineaments and regional geology (Won-In & Charusiri, 2003). The RGB combination (3/1)(5/7)(3/5) (Landsat ETM+) was applied in a geological investigation of El Azraq, Jordan, and revealed more geological information with higher contrast between the lithologies than the conventional color RGB images (Rawashdeh et al., 2006). In general, the arithmetic operations between bands (such as band ratio, multiplication, subtraction or addition) can be used either individually or in combination with other bands. This enables the creation of new RGB combinations that can emphasize the spectral differences of geology or vegetation (see Table 6.1) (e.g. Adbeen et al., 2001; Teeuw et al., 2005 Wolter et al., 2005; Qari, 2008).

In many cases lithological mapping through satellite imagery should be considered on a site-by-site basis, as outcrop lithologies can often be very variable. Some geological information that cannot be depicted by individual bands in RGB combinations needs to be indicated by other procedures. Principal component analysis (PCA) determines the statistical dimensionality of the image by representing most of the original image information into a smaller dataset, enhancing the multispectral data (Ready & Wintz, 1973; Green et al., 1988; Chen, 2000). PCA is particularly useful as information from all bands is utilized. The PCA outcome images could be displayed either individually or in combination with other bands, like RGB combinations, in order to highlight spectral differences (Novak & Soulakellis, 2000). This can be particularly useful for the identification of features and relations that are not clear in the original data (Jensen, 1996). Such an approach is used effectively in cases of geological mapping (e.g. Novak & Soulakellis, 2000; Gomez, 2005). Novak & Soulakellis (2000) study revealed that RGB combinations PC1-PC2-PC3 and TM7-PC2-PC3 of Landsat TM sensor were

effective in identifying geomorphic, lithological and lineament features in Lesvos, Greece.

Apart from the PCA approach, a less commonly used approach in literature is the MNF transformation. This approach is similar to the PCA but it can also gradually decrease the image quality with regard to the increasing component number (Chen, 2000). This characteristic cannot be accomplished easily by other techniques, such as PCA and factor analysis (Chen et al., 2003). The MNF transformation is a better image enhancement approach than the PCA if the image quality is a prior concern (Green et al., 1998). This is due to the separation of signal and noise components that can be achieved (Chen, 2000). A strong colour contrast among characteristic features (e.g. urban areas, woodland and grass) was revealed by the use of RGB combination MNF2-MNF1-MNF3 (AVIRIS data) in a region of Utah, US (Chen et al., 2003).

The discrimination of lithologies can be achieved in cases where the bands have the highest spectral information and the lowest correlation (Loughlin, 1991; Yongjun, 2003; Wenbo, 2008). Such circumstances can be specified by the use of the optimum index factor (OIF) approach. Band combinations with highest OIF contain more spectral information, by having the highest variance and the lowest duplication for the image (Kamal, 2004; Nield, 2007). Nield's (2007) study applied the OIF analysis to extract the best Landsat ETM+ RGB combination and to examine nitric and gypsic soil areas in Colorado, USA. The main conclusion of this study was that the investigation of a Landsat ETM+ scene by using the highest OIF band combinations can provide the analyst with the most suitable spectral bands, which may be diagnostic for particular land surface features within a study area. Knowledge of the degree to which each band combination contributes to the spectral information is important as it allows the user to select the appropriate combinations that can be advantageous for further processing. The OIF analysis has been applied to multispectral satellite imagery in studies that needed enhanced image visualization to distinguish various rock types and produce geological maps (e.g. Oza, 1989; Beauchemin, 2001; Al-Juaidi, 2003; Ren and Abdelsalam, 2004; Gad, 2007; Nield, 2007; Qari, 2008; Dehnavi, 2010). The OIF

analysis was considered in the study of Dehnavi (2010) to create band colour composite images for examining lithological and geological aspects to map alteration zones, by using Landsat ETM+ in eastern Kurdistan. Using the optimum index factor (OIF), Al-Juaidi (2003) determined RGB band combination 751 of Landsat TM sensor to be the optimum colour composite image for the investigation of the geomorphological features in central Saudi Arabia. Moreover, calculation of the OIF analysis can be useful as a process of validation, for drawing comparisons between analysts who examined RGB combinations against other studies of the satellite imagery (Gad, 2007).

RGB		Highlighted features	Band ratio	
Landsat ETM+	ASTER		Landsat ETM+	ASTER
321		"True colour" image		
432	321	Vegetation chlorophyll highlighted in red	4/3, (4-3) / (4+3)	3/2, (3-2) / (3+2)
453 456 457 741 (*Kenea, 1997*) 754 (Won-In 2003) 721 (Leech, 2003) 742 (Pena, 2006)	468 631 731 (Pena, 2006) 468 (Moloney, 2007) 631 (Junek, 2004)	Soil and rock types	5/7, 4/5 (Abrams et al., 1983), 3/1 (Sabins, 1997), (5/7) (4/5) (3/1) (Ramadan , 2001), (3/1) (5/7) (3/5) (Al Rawashdeh, 2006), (4/5) (5/7) (7/5) (Won-In, 2003)	(4/1) (3/1) (12/14), (4/7) (3/4) (2/1) (Adbeen et al., 2001), (7/6) (6/5) (6/5) (Wolter et al., 2005), (4/7) (4/6) (4/10) (Gad, 2007), (4/8) (3/4) (2/1) (Pena, 2006), (6/8) (4/8) (11/ 14) (Qari, 2008)
541 741	456	Hydrothermal alteration of volcanic rocks		(4+6) / (5*2), (5/6) (7/6) (7/5), (2/1) 3 (4/8) (Fu, 2007)
751		Discrimination between Fe-rich soil and rock	3/1, 4/5	2/1, (5/3) + (1/2), 5/4, 7/4, 4/3, (14/12) (1/2+5/3) (MNF band 1)
531 672 234 654 742 (*Pena, 2006*)		Useful with various vegetation and rock types		

Table 6.1: Useful RGB combinations and band ratios for ASTER, Landsat TM and ETM+ (modified after Teeuw et al., 2005).

6.2.2 Lineament analysis

As soon as the aforementioned image enhancement stage is accomplished, the satellite image products can be used for the identification of lineaments, since the discrimination of lineaments corresponding to lithological boundaries can be determined. In order to have more than one source for the identification of lineaments, other datasets such as geological maps and DEM are used as reference datasets for the final lineament mapping. The term ñlineamentò is defined by O'Leary (1976) as "a mappable, simple or composite linear feature of a surface, whose parts are aligned in a rectangular or slightly curvilinear relationship and which differs distinctly from the patterns of adjacent features and presumably reflects a subsurface phenomenon". Other definitions of lineaments exist in the literature, such as ña linear topographic feature of regional extent that is believed to reflect crustal structureò (Hobbs, 1976 in Bates & Jackson (1980)) or ñlong, often subtle linear arrangements of various topographic, tonal and geological featuresñ (Drury, 1987). Tectonic features can be indicated by anomalies in vegetation without any influence of topographic factors (Gustafsson, 1993). In this study the definition of Lattmans (in Gold, 1990) is considered as the most appropriate, identifying the lineament as ña natural linear feature consisting of topographic (including straight stream segments), vegetation or soil tonal alignments, that can be visible on aerial photos and expressed continuously or discontinuously over a certain distanceò. Many lineaments are fracture zones where brittle deformation in the uppermost crust has taken place (Fig. 6.1) (Gustafsson, 1993). The surface expressions of lineaments can be either geomorphic features (due to relief) or tonal features (due to contrast difference) (Cortes et al., 1998). Lineaments are revealed in satellite images as linear topographic features caused by faults, fracture patterns, lithological boundaries or breaks within a uniform terrain (O'Leary et al., 1976; Ollier, 1981; Panizza et al., 1987; Remo, 1999). Linear features between areas of contrasting tone or differences in moisture, vegetation, soil and rock characteristics consist mostly of tonal contrasts, indicating their possible structural origin (Sabins, 1978; Campbell, 1987).

The identification and analysis of lineaments would be difficult if it was limited only to fieldwork data. The steep mountainous regions of the study area are difficult to investigate by fieldwork. The synoptic coverage of the satellite imagery overcomes access problems and offers a regional structural overview. The large synoptic coverage of Landsat ETM+ satellite imagery, as well as their multispectral capability and digital format, allows rapid digital image enhancement and immediate import into GIS software. This makes satellite remote sensing datasets particularly useful for lineament detection (Rowen and Wetlaufer, 1974; Walsh, 1986; Suzen and Toprak, 1998; Cortes, 1998). The spatial resolution and low acquisition costs of Landsat ETM+ are considered optimum for this study. This is because higher spatial resolution satellite imagery (such as Quickbird) is not always the best option for lineament analysis, due to the high data costs for a large region, as well as the limited spectral information that such images provide. High spatial resolution images can lead to a poor interpretation of lineaments as their regional extent cannot be revealed (Sander, 2007). Furthermore, higher noise can sometimes be an unwanted feature of lineament analysis techniques (such as in spatial filtering), because shadows cast by tall objects (Sawaya et al, 2003) or vegetation from anthropogenic factors (Bruning, 2009) lead to lineaments that are not the result of tectonic processes. Lineaments could be generated by natural morphological factors or anthropogenic features (roads, crops). Generally, lineaments could be expressed by the drainage network, truncated relief and vegetation patterns. Lineament research studies using satellite image data and DEMs have been carried out by many researchers, examining tectonics (e.g. Koopmans, 1986; Walsh, 1986; Tibaldi & Ferrari, 1991, Marple & Schweig, 1992; Suzen & Toprak, 1998; Oguchi, 2003; Cengiz, 2006; Walker, 2006; Songmuang, 2007) or geomorphology (e.g. Sabins, 1978; Hooper, 2003; Kervyn, 2006; Fu, 2007b; Ribolini, 2008). The identiýcation of lineaments from the RGB combinations 541 and PC1-PC2-PC3 of Landsat TM images was performed in the highlands of Erithrea (Solomon & Ghebreab, 2006). The determination of lineament extraction in this study was based on colour differences at the boundaries of contrasting lithological units and visible faults. A remote sensing

study of active folding and faulting in southern Kerman province, Iran, was accomplished by Walker (2006), where the availability of remote sensing data such as the SRTM DEM and ASTER satellite imagery, is considered to make reconnaissance studies of active faulting feasible. The use of Landsat TM and ASTER data was applied effectively to evaluate the neotectonics of Western Mongolia, by identifying in the images geomorphic features such as triangular facets, recent fault scarps, shutter ridges, beheaded streams and abrupt changes in slope angles along faults (Woldai & Dorjsuren, 2008). Similar morphotectonic characteristics (e.g. triangular facets, fault scarps, offset streams etc) indicative of active faulting were also recognized from remotely sensed data in the Sri Sawat Area, Western Thailand (Songmuang, et al., 2007). Abdallah et al. (2005) study detected, effectively, through visual interpretation of remotely sensed data (Spot 4 and DEM), terrain parameters (e.g slope, aspect, land use, proximity to fault zone etc) associated with mass movementsô in the mountainous area of Lebanon. Based on the analysis of radar satellite and DEM imagery, Backe et al. (2006) considered these datasets thoroughly to investigate and represent a new understanding of the tectonic evolution of the Venezuelan Andes. In general, remote sensing is valuable in neotectonic studies to the point where reliable morphologic measurements can be obtained (Hooper et al., 2003). An interdisciplinary study applying band rationing, principal component analysis (PCA) and lineament analysis based on Landsat TM satellite imagery determined the palaeotectonic and neotectonic features in western Turkey (Kavak, 2005).

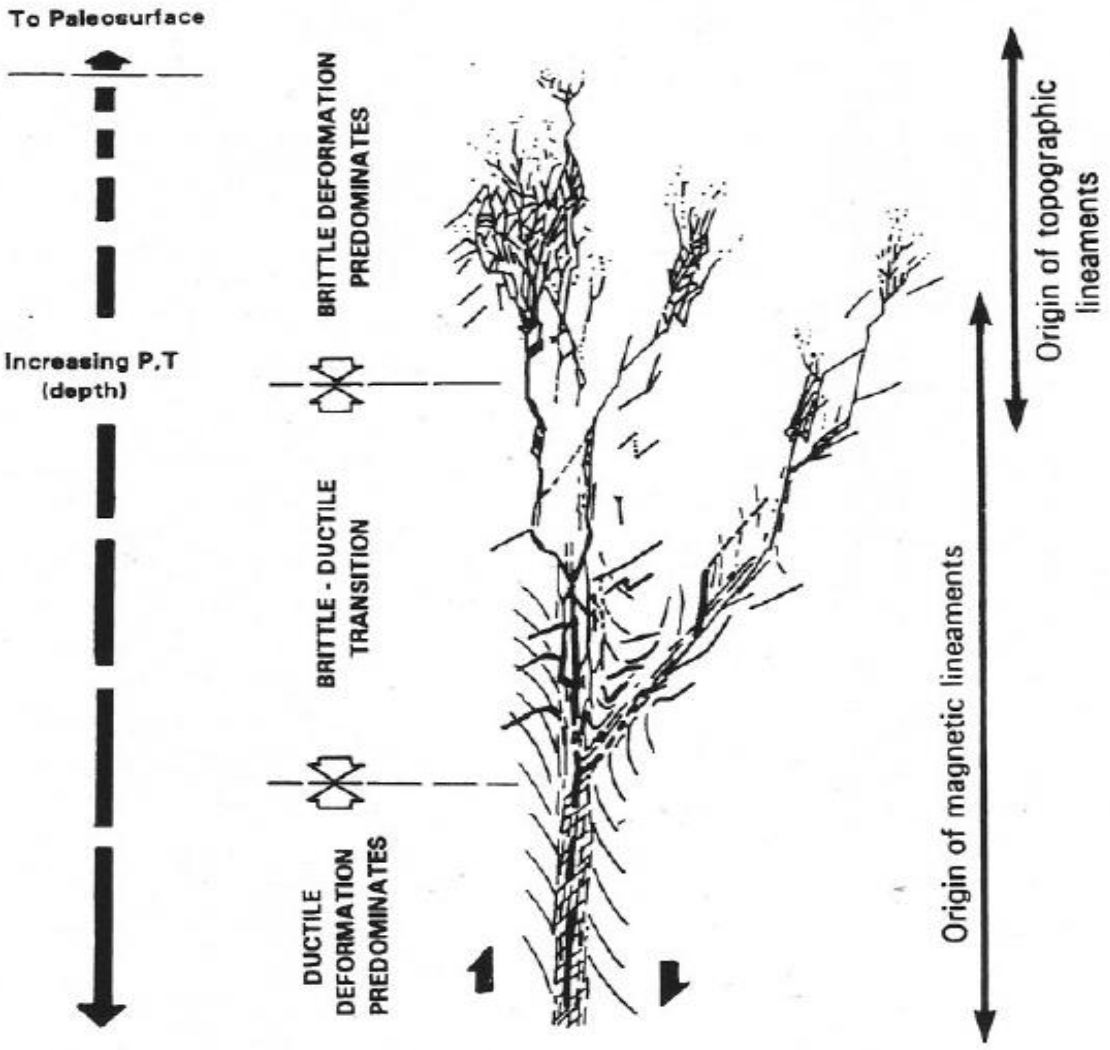

Fig. 6.1: Cross-section of lineaments representation in the Earth's crust (modified by Gustafsson, 1993) (after Colvine et al., 1988).

6.3 Digital image analysis

The digital image analysis contains some standard enhancement techniques such as contrast stretching, pan-sharpening, filtering and spectral arithmetic operations to improve the discrimination of lithological units and identification of lineament features in the semi-arid study area. Initially, image processing of satellite imagery consisted of a few pre-processing stages, which are described in Chapter 3. For instance, the spatial resolution of the Landsat ETM+ imagery was improved by pan-sharpening techniques. As presented in

Chapter 3, various techniques for pan-sharpening were tested (e.g. Goforth, 1998; Vijayaraj, 2004; Song et.al, 2007; Wenbo, 2008; Klonus, 2008). These approaches were evaluated in order to find the most appropriate bands to be used for this research in the multispectral imagery. The selected pan-sharpened bands, as well as providing improved spatial resolution, also keep the spectral information of the original multispectral images (see Chapter 3). This is particularly useful for the image processing procedure, described below, as the essential elements of spectral information quality are preserved for the discriminated lithologies to be determined. The necessary pre-processing procedure of datasets, regarding satellite imagery were documented in Chapter 3.

The next stage is to examine the image enhancement of the satellite imagery. The image enhancement uses various processes with the view to emphasize the particular features of an image. The objective is to enhance the information provided by the satellite images for the better visual perception and interpretation results for the ñviewerò. The Landsat ETM+ sensors utilised in this study record digital grey-level values that range from 0-255. For lithological discrimination two principles had to be considered during the image enhancement: i) the acquisition of best spectral info and; ii) spatial information extracted by the use of available satellite image data. Several studies, as described earlier use various methods that provide the bands and RGB combinations needed for the discrimination of lithologies and lineaments. Despite that, no study attempted to discriminate the lithologies and to highlight the lineament features at a single satellite image. In this research, an approach, as described below in the methodology, evaluates which bands and RGB combinations can enhance tectonic features while providing lithological information. That issue is beneficial to the isolation of linear features corresponding to either tectonic or lithological contacts.

6.3.1 Image enhancement evaluation for geological mapping

The discrimination of lithologies and identification of lineaments in a satellite image data can be significant when the satellite image processing procedure uses the selection of appropriate bands and RGB combinations. So it is necessary to examine which aspects are representative to lithological mapping by using satellite image data. Previous studies have predominantly been interested in the use of satellite imagery for mapping lithologies in low-relief arid regions, where easier discrimination is accomplished due to the lack of vegetation cover (e.g. Rowan, 2003; Al Rawashdeh, 2006; Pena, 2006; Qari, 2008). This study focuses on a semi-arid mountainous region, such as Crete, where vegetation cover will not be totally absent. That characteristic aspect should be considered by aiming to vegetation suppression. Hence, the evaluation of image enhancement is expected to derive RGB combinations (see table 6.1), to discriminate lithologies in semi-arid regions. Some criteria for selecting the best bands and the RGB combinations (with regard to lithological and lineament information) have to be determined. The criteria for focusing on the bands or RGB combinations that highlight lithological information and suppress vegetation discrimination are summarized below:

i) The lithology can be discriminated by the use of Landsat ETM+ bands 4, 5 and 7, as can be observed in Table 6.1. These bands highlight and emphasise the rock types, as well as linear features. Studies by Kenea (1997), Suzen (1998), Pamadan (2001), Won-In & Charusiri (2003) and Pena (2006) utilized these bands in RGB combinations or band ratios for lithological mapping or lineament extraction.

ii) The Chlorophyll due to photosynthesis absorbs the blue and red regions of the spectrum. This results in low-reflectance of vegetation in the satellite imagery. In the green region however, vegetation reflects more green light than any other visible color. The purpose of this study is to suppress vegetation, rather than eliminate its presence. This is for avoiding the loss of spectral information, and will be achieved by using Landsat ETM+ bands 1 and 3 in the band multiplication procedure (described below), to minimize the signal of the vegetation impact.

iii) A comparative evaluation of pan-sharpening techniques was carried out (see Chapter 3). Appropriate bands for further processing were then selected to create a new enhanced Landsat ETM+ multispectral image. This ñewò multispectral image contains bands that keep most of the spectral information of the original multispectral image.

As it will be described below, the mapping of lithologies is based upon: i) the appropriate band selection highlighting such features and; ii) the usage of essential bands or RGB combinations to be used for the band arithmetic operations in order to extract single satellite images revealing both lithological and lineament information.

a) Band selection for mapping of lithologies and lineaments

The utilization of proper band combinations is important for the enhancement of multispectral images. As mentioned earlier, the bands that have the highest spectral information and the lowest correlation need to be specified (Loughlin, 1991; Yongjun, 2003; Wenbo, 2008). This can be achieved by the Optimum Index Factor (OIF) analysis, combined with correlation coefficients extracted by the Principal Component Analysis (PCA) (Chavez, 1982; Oza, 1989; Beauchemin 2001; Gad, 2007).

The OIF analysis ranks all possible RGB colour combinations of multispectral remote sensing data on the basis of: i) the total variance within bands and; ii) the coefficient correlation between bands (Chavez, et al., 1982; Chavez, et al., 1984; Oza, 1989; Ren and Abdelsalam, 2004) (see Appendix I, Theory formulas (i)). The greatest variance bands, with the least correlation and lowest redundant information, indicate the best RGB combination bands (Jensen, 1996; Gad, 2007).

In this study, the OIF analysis is used for preliminary evaluation of the RGB combinations that can be provided by multispectral imagery. The objective is to identify those RGB combinations that provide most of the spectral information, while their bands are related by lithological discrimination and by enhancement of linear features. After the OIF analysis, the results are combined with the

correlation coefficient matrix table extracted by PCA. The uncorrelated bands of the original multispectral images are determined by the PCA correlation coefficient. Knowledge of the least related bands and the RGB combinations that provide high spectral information (by OIF analysis) is useful in this stage of research. Such information enables the selection of those RGB combinations that include bands containing valuable information about lithological types or sharp edge features, such as lineaments (Sabins, 1986; Kenea & Haenisch, 1996; Carranza, 2002; Abera, 2005). For example, Abera (2005) considers in his study the least correlated bands extracted by PCA to determine RGB combinations fused with DEMs to highlight mineral presence in western Ethiopia. Further processing (e.g. spectral band arithmetic operations) of the RGB combinations, regarding the aforementioned, can be considered with those bands or RGB combinations that are more useful for geological mapping being selected.

Other studies in the past referred to lineament extraction, based on the colour differences at the boundaries of contrasting lithological units by using components of PCA in RGB combinations (e.g. Novak & Soulakelis, 2000; Solomon & Ghebreab, 2006). In this research these assumptions are evaluated as an alternative approach to discriminating lithologies, while the use of the Minimum Noise Fraction (MNF) technique is also considered as comparative approach to the PCA. As described earlier, the Minimum Noise Fraction (MNF) technique is more reliable than the PCA when the target is of a better image quality (Lee et.al, 1990; Green et.al, 1998; Chen, 2000). The MNF emphasizes the differences, rather than the similarities, between the bands, and also identifies the noise in the image. This provides better functionality as more coherent information is extracted from the separation of the noise through the MNF transformation (Jensen, 2005). The combination of the PCA and the MNF products can be particularly useful in this research for enhancing and identifying the features that cannot be discriminated with typical RGB band combinations. Such approach can be useful, as mentioned above, when lithological discrimination is examined on a site-by-site basis, as outcrop lithologies can often be very variable. Any features that cannot be recognized by such a combination approach (such as lineaments) can

potentially be enhanced and discriminated by the use of spectral band arithmetic operations described below.

b) Spectral band arithmetic operations for mapping of lithologies and lineaments

Simple band RGB combinations can discriminate lithology when the least correlated bands are combined (such as RGB 751 for Landsat ETM+) (Beauchemin, 2001; Carranza, 2002; Al-Juaidi, 2003; Gad, 2007). Band ratio is achieved by the division of the DNs (Digital Numbers) of one band with the DNs of another band. Band ratio images differentiate rock types better than traditional RGB band combinations by minimizing the effect of shadows and different slope orientations (Okada and Ishii, 1993; Jensen, 1996; Rowan et al., 2003).

The disadvantage of the band ratio approach is that it does not enhance tectonic features through tonal contrast difference. To overcome this difficulty, band multiplication was applied. The multiplication of bands improves the performance of higher spectral information (Papadaki, 2005). It also provides better edge enhancement under certain circumstances, such as utilization of bands highlighting tectonic information (e.g TM 4 or TM 7). This can enhance tectonic features by making use of the total spectral information provided by each band. The Landsat ETM+ bands often used in geological studies are TM4, TM5 and TM7 (e.g Abrams, 1985; Crosta, 1989; Louglin, 1990; Charusiri et al., 1993; Suzen, 1998). Those studies effectively identified lineaments and lithological boundaries. On the other hand, TM1, TM 2 and TM3 are usually used in vegetation studies identifying superficial features, such as soil and vegetation (e.g. Rouse et al., 1973; Tucker, 1979; Gao, 1996; Vonders and Clevers, 1998; Ceccato, 2002; Won-In, 2003; Jackson et al., 2004).

The section 6.3.1 (a) described above, in particular the OIF analysis, can indicate which bands and RGB combinations are best for band multiplication. The reason is that multiplication of bands or RGB combinations giving emphasis to geological information can enhance and amplify tectonic features by reinforcing contrast differences. The final multiplication products extracted, on the basis of the

6.3.1 (a) section, can be used for RGB combinations. If uncorrelated band-multiplied products are selected, then improved discrimination of lithological and tectonic features will be possible. This can be achieved because the uncorrelated bands discriminate lithology better (Beauchemin, 2001; Nield 2007), while the band multiplication technique, pioneered in this study, enhances the signal of contrast difference in tectonic features. This approach has rarely been used before as most practitioners tend to use normalised difference ratios. This band-multiplication approach was tested in this study and an effective set of RGB combination images was created. Depiction of detailed lithological and tectonic features, which cannot be visualized with the ósstandardôRGB band combinations or band ratios of Table 6.1, was achieved (see ñ*6.5 Results*ò section). After the multiplication between bands, a rescaling is needed to transform the DN values back to a 0-255 range since multiplication will increase this range. The final images were overlaid on the 1971 geological map and the matching lithologies were clearly revealed. The accuracy assessment between the satellite image which discriminated the lithologies and the geological map (IGME, 1971), as presented in Chapter 3, was evaluated by the calculation of kappa coefficient statistics**.** The overall accuracy was 87.76%, which is more than the suggested target of 85% accuracy (Foody, 2002). That percentage of accuracy reinforces the efficiency of the processing stages for lithological discrimination in this study, without being based only on the visual depiction of lithologies, as provided in the figures below. The discrimination of lithologies and lineaments enhancement is better than any other existing RGB combination or band ratio in the literature that was tested in this study.

The positional accuracy provided by the satellite images has a straightforward connection with their spatial resolution. As a consequence, the better spatial resolution led to the improvement of the accuracy of the lineament identification. Pixel size was improved through the pan-sharpening of the images (see Chapter 3), providing a more detailed discrimination of lineaments or feature boundaries (tonal contrast), while at the same time, making spectral band arithmetic operations more effective.

6.4 Lineament analysis

For the purpose of this research, lineament mapping is the extraction of tectonic features identified on satellite image data (Landsat ETM+) and DEM (SRTM-ASTER DEM). The importance of lineament analysis for the study region is reinforced by two aspects: i) the existence of geological maps created in 1971 (IGME geological map) and; ii) previous studies of onshore continental seismicity (Delibasis, 1999; Meier et al., 2004; Becker et al., 2009). These two aspects are the most commonly considered until today, in characterising tectonics in Crete.

The digital lineament analysis of image data was carried out by: i) digitising of geological maps; ii) directional filtering techniques applied either on the fused SRTM-ASTER DEM (see Chapter 3) or the satellite imagery (Landsat ETM+); iii) manual interpretation based on the processed satellite images and; iv) gathering of geophysical measurements considered in the subsequent chapter (see Chapter 7). Each method utilized in this research aims to fill any gaps generated by other processing techniques. The identification of lineaments by more than one Earth observational dataset provides the opportunity to perform a comparative analysis and a multidisciplinary lineament detection approach. The lineament mapping stages of this study are presented as a flow diagram in figure 6.2

a) Digitizing geological maps

Digitizing of faults was conducted via ArcGIS software. The geological maps of the study region are imported into ArcGis (along with their georectification). The creation of a shapefile with digitised faults is also provided, indicating their digital depiction on the satellite images.

b) Data fusion of DEM and directional filtering

Relief is a spatial interpolation of elevation data, which until recently was extracted by topographic maps by tracing the contour lines. Geometric inaccuracies involved in the final interpolated DEM result in imprecise measurements. Recent developments in computer software allowed direct measurements of elevation from satellite images and digital photographs (Al-

Rusan, 1998; Gooch, 2001; Toutin, 2002). Lineaments, for instance, with a range from 300 m to 12 km can now easily be identified by the ASTER DEM (see earlier section, 3.4 in Chapter 3). Fusion of ASTER and SRTM DEM is described in Chapter 3 to overcome gaps caused by cloud cover and combine the higher spatial resolution of ASTER DEM with the better absolute vertical height accuracy (~16 m) of SRTM DEM (Koch & Lohmann, 2000; Muller, 2005; Austin, 2007).

After the generation of a more reliable fused DEM, edge enhancement filters and directional filters were used to enhance the surface expression of the lineaments. The lineaments that were identified by using the DEM in this study, based on its spatial resolution, had dimensions of at least 300 m in length and more than 30 m width to be recognisable (Cortes, 1998). Those dimensions are the optimum with regard to the spatial resolution of the DEM used in this research (Mei et al., 2004). Furthermore, smaller lineaments are of limited value in studies of tectonic activity. This is due to their relation with smaller earthquakes, landslide features and lithological controls rather than tectonic activity.

Shaded relief images with various sun angles and azimuths were produced from the DEMs, aiding the recognition of regional lineaments and tectonic structures (Deffontaines et.al., 1997; Chorowicz et al., 1999; Guiraud et al., 2000; Dewez, 2003). Erdas Imagine was used to create various illumination and shadow effects from various azimuths (0^0, 45^0, 90^0, 135^0, 180^0, 225^0, 270^0 and 315^0) with a sun elevation at 45^0. The extracted lineaments were digitised on screen using ArcGis 9.1, with lengths ranging from a few hundred meters (~300m) to a few kilometres (~12km).

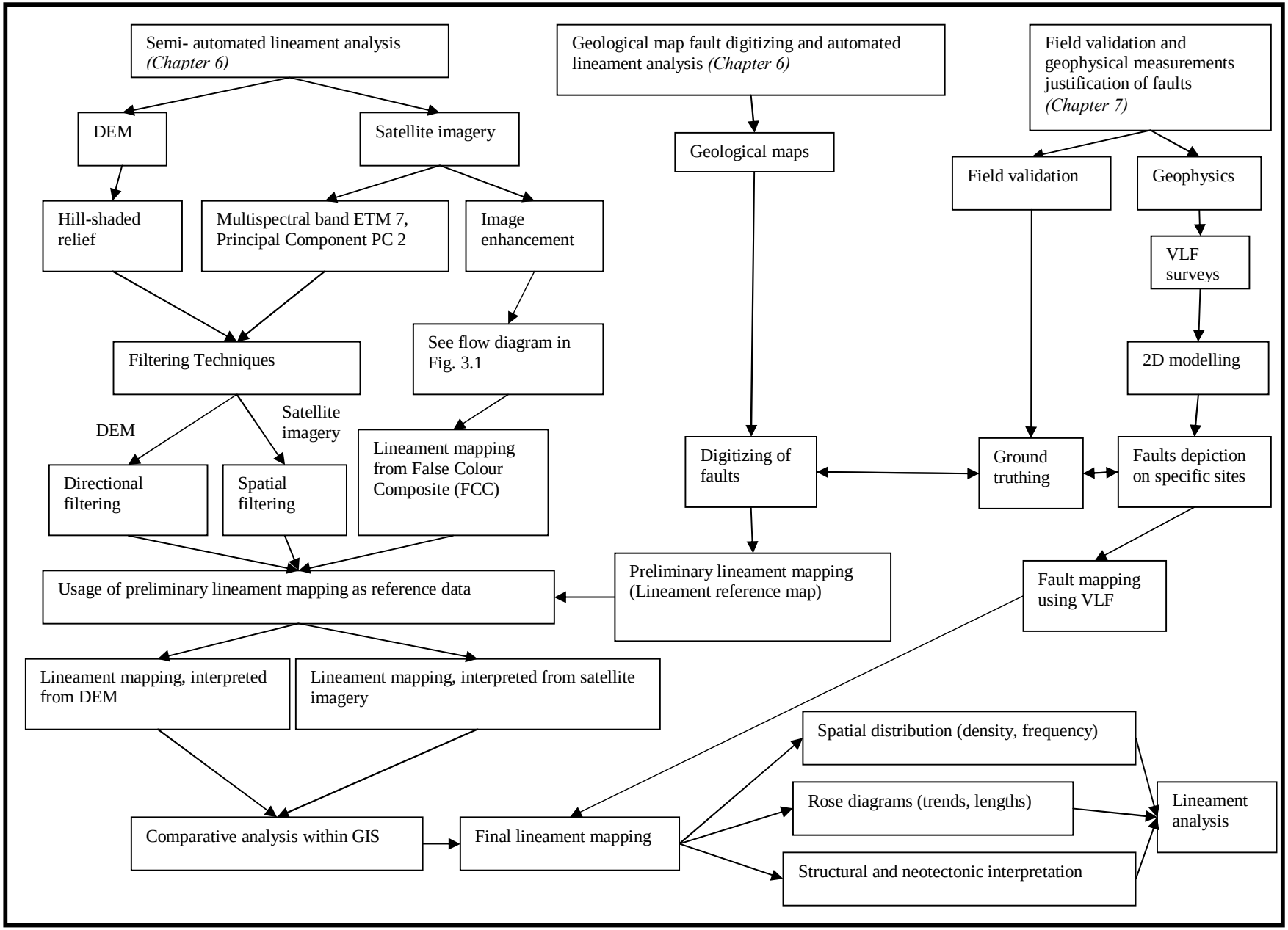

Fig 6.2: Flow diagram of lineament analysis.

(Acronyms: ETM: Thematic Mapper; FCC:False Colour Composite; PC:Principal Component)

c) Satellite image filtering

Spatial convolution filtering was used to enhance or subdue the spatial frequency of the satellite imagery. This improved the spatial interpretation of the image by sharpening the edges and enhancing linear features, such as lithological boundaries or fracture zones (Reames, 2002). Edge enhancement was used to exaggerate local contrast and to recognize common linear landscape features (Lillesand and Kiefer, 1999; Jensen, 2005). This is particularly effective for geological mapping as the boundaries of lithologies and lineaments are enhanced and better discriminated.

One of the main linear edge enhancement methods is the use of compass gradient masks. With these masks, images filtered to the major directions (N, NE, E, SE, S, SW, W and NW) (see Appendix I) were created, to perform two dimensional, discrete differentiation directional edge enhancement (Jain, 1989; Pratt, 2001; Jensen, 2005).

Common directional filtering was applied for the recognition of features with particular orientations. This edge-enhancement filter superimposes lineaments by using the range of azimuths and sun elevations. Shaded relief images are widely used in studies of active tectonic zones as changes in slope gradient and direction can easily be visualised (Worthington & Hancock 2001). Features associated with neotectonic activity (such as fault scarps, linear river valleys and shutter ridges) are more easily discriminated (Deffontaines et.al., 1997; Jordan, 2004; Abarca, 2006)

Another method of performing edge enhancement is the use of various Laplacian filters (Jahne, 2001; Pratt, 2001; Jensen, 2005) (see Appendix I). Points, lines and edges are enhanced by decreasing the smoothness of the image. Mask 3 (see Appendix I) can be used for the restoration of overall greyscale variation by subtracting the filtered image from the original one. Due to the difficulty of interpreting the filtered images on their own, they can be added back to the original image by utilising Mask 4 (see Appendix I) (Jensen, 2005). Other edge detection filters are achieved by Prewitt filtering and non-directional

Sobel filtering. Prewitt and Sobel filters detect the edges that appear in the image after the application of horizontal and vertical filters (see Appendix I).

The edge enhancement methods provided a reasonable identification of the edges, but this research aims to select the most reliable and rapid approaches. Laplacian edge enhancement was the most easily interpreted (Jensen, 2005), providing the greater ñnaturalò image for the rapid discrimination of geological structures.

d) Satellite imagery manual interpretation

Manual interpretation was performed on the satellite images that had been processed to highlight lithological and lineament information. The on-screen digitization of lineaments was accomplished by using a zoom window to approximately 1:20000 scale. Lineaments were identified on these satellite images on the basis of meeting a set of criteria for topographic expression and recognition of active faulting. These criteria involve (see Fig. 6.3 (a) to (h)): (a) lines of variable length, linearity and continuity, which can be revealed by tonal contrasts in the image; (b) tonal discontinuities in the image; (c) alignments of topographic forms, like alluvial fans or marine terraces; (d) alignments of drainage patterns, beheaded drainages, deflected and offset streams; (e) heavy vegetation cover patterns along which linear trends exist; (f) superficial deposits with the presence of clear breaks and low bluffs, truncated or faceted spurs, shutter ridges; (g) triangular facets and graben and; (h) geological formations where the underlying structural and surrounding topographic control imply tectonic contacts (Walsh, 1986; Drury, 1993). This stage of the methodology took into account these issues in order to manually identify lineaments in the new constructed multispectral satellite images.

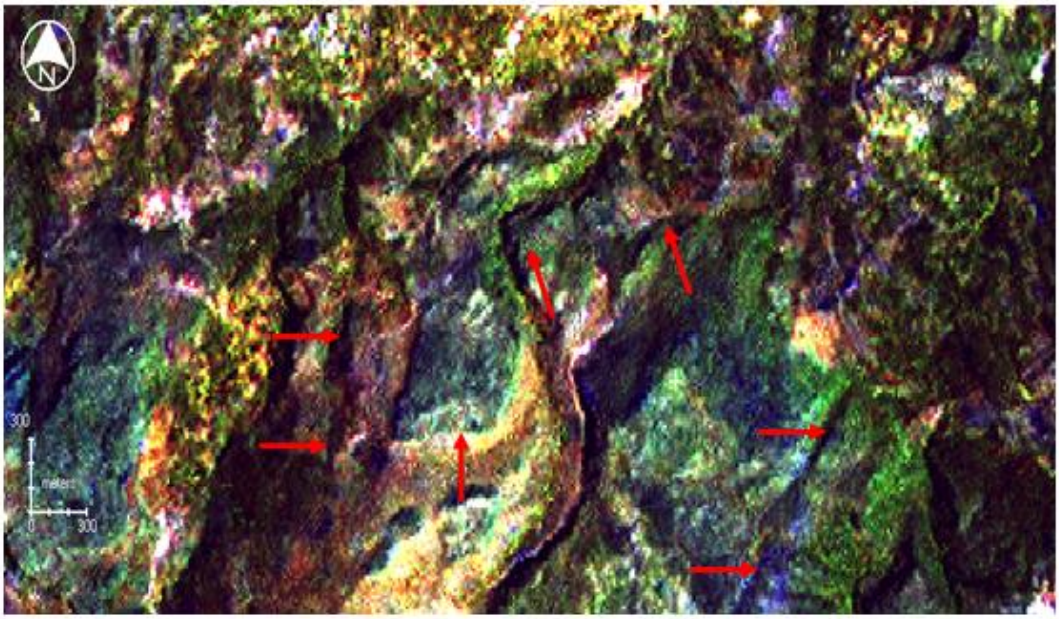

(a) Red arrows indicate lines of variable length, linearity and continuity, which can be revealed by tonal contrasts in the image

(b) Red arrows indicate alignments of drainage patterns and deflected streams.

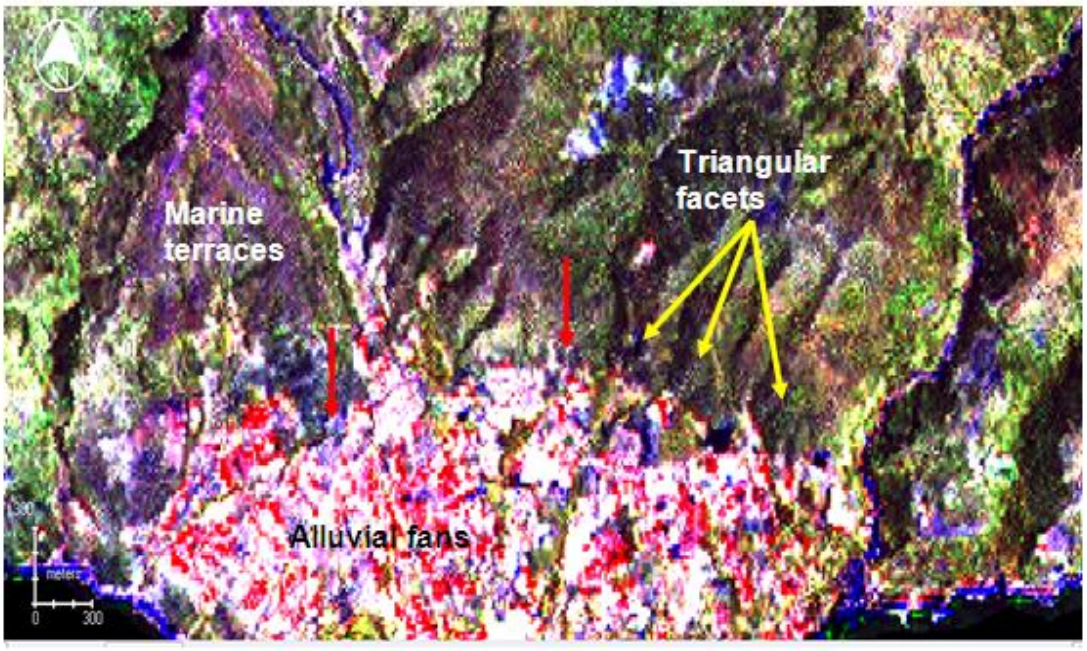

(c) Red arrows indicate alignments of topographic forms, such as alluvial fans or marine terraces. Yellow arrows indicate the triangular facets developed across the mountain front.

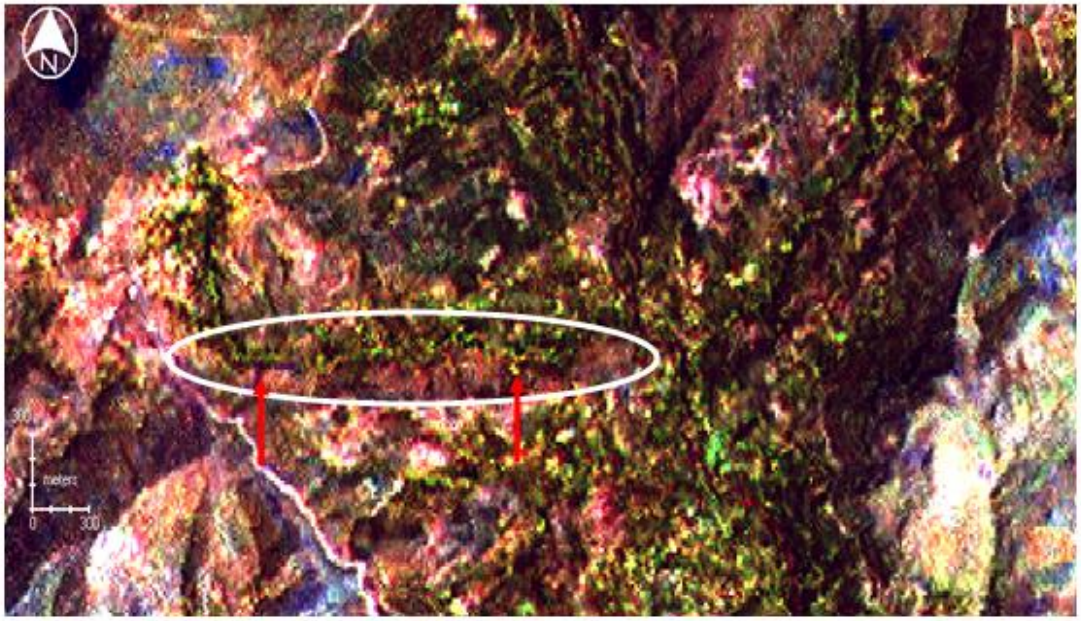

(d) White circle indicates the area with the dense vegetation along which linear trends exist (red arrows).

Fig. 6.3 a to d: Few of the criteria characteristics, at a scale of 1:20000, which can be determined by the use of satellite images.

6.4.1 Lineament map evaluation

This section evaluates all gathered lineament maps via buffer zones in order to produce one final tectonic lineament map. The final lineament map can be useful to the extraction of valuable information concerning lineament geometry (length, azimuth, density). For that reason, rose diagrams or spatial correlation plots will be performed (see below), as they provide common lineament distribution analysis methods that illustrate the differences between azimuth and lineament lengths (Sanders, 1996). Such information can be associated with potential zones of tectonic activity, determined in earlier chapters, to characterize the degree of active tectonics hazard (see Chapter 8).

i) Confidence in lineament locations

The use of GIS application can be used to create buffer zones (100m) that allow the identification of coinciding lineaments. The coinciding lineaments (more than one) can then be represented as singular lineaments. Therefore, a more comprehensive and simplified final lineament map of the study region can be created. This final tectonic lineament map will be used in the further lineament map evaluation stages described below.

ii) Lineaments/faults versus Earth observational datasets and geological maps

The lineaments that constitute the final lineament map can be categorised into three groups that consist of: i) lineaments that were present on the 1971 geological map as faults, but which were not identified on either the satellite imagery or the DEM; ii) lineaments that were interpreted by the satellite imagery and the DEM and correspond to previously mapped faults by geological maps and; iii) lineaments that were previously unmapped on the 1971 geological map but were interpreted by both satellite imagery and the DEM.

iii) Spatial distribution of lineaments

The density and frequency maps of the detected lineaments in the final lineament map can indicate zones where higher tectonic control occurs. The density map quantified the total length of lineaments per km^2 while the frequency map quantified the total number of lineaments per km^2 that are present in the study region. Such maps will be used in following chapter to evaluate through the multi-criteria decision analysis (MCDA), whether the higher values of drainage density and frequency lineament maps coincide within tectonically active zones (see Chapter 8).

iv) Rose diagrams of fault azimuths

The identified lineaments in the final lineament map can be evaluated with regard to their strike. Rose diagrams of lineaments can be created and their comparison with drainage network rose diagrams can illuminate whether the stream azimuths are being controlled by fault structures. In addition, these particular lineaments/faults can indicate whether their association with stream segments imply linkage to current tectonic regime described in Chapter 2 (Fig. 6.25 & Appendix II, Fig. 8 a, b).

6.5 Results

6.5.1 Image pre-processing

The satellite imagery used was subject to initial pre-processing stages before the application of further processing and analysis. One of the first steps was the creation of masks to isolate the sea (digital number range DN=0-5) from the land (Fig. 3.2). In addition, the satellite images acquired for this research were georeferenced and transformed to the Greek geodetic reference system (GGRSô 87). The stretching of the DNs to the full range of 256 (intensity levels of grey), reveals the difference between the two images; it can be observed that the stretched image has considerably more detailed information (Fig. 3.3). This step was to ensure that the layer stack included sufficient information (via the bandôs histogram) in order to produce a multispectral image.

6.5.2 Image enhancement

The image enhancement of the satellite imagery was essential in order to produce better-quality images for visual interpretation. The application of pan-sharpening, as described in Chapter 3, improved the spatial resolution of the Landsat ETM+ satellite imagery, however, the image enhancement procedure improves and highlights better the visual interpretation of any characteristic features. Such enhanced images can be then used to extract information regarding the lithology, tectonics and geomorphology of the study area. The results of the image enhancement methods described in the methodology are presented below.

6.5.2.1 Image enhancement to lithological mapping

i) Principal Component Analysis (PCA)

With regard to the principal component analysis (PCA) application for the Landsat ETM+ satellite multispectral imagery, the following were calculated:

1. Covariance matrix
2. Correlation matrix
3. The factors of linear transformation (eigenvectors and eigenvalues)

The detailed results of all the calculations are presented in Appendix II.

The covariance matrix is symmetrical. The values of the main diagonal express the dissemination per spectrum channel while their sum expresses the total dissemination that exists in the initial data (Appendix II, Table 1). In our case, the total calculated dissemination is 14382,643. The values of the correlation matrix (Appendix II, Table 2) imply a qualitative and quantitative correlation between the spectrum channels of visible (VIS) (bands 2, 3) and Short-wave IR (SWIR) (band 7) where values close to 1 are observed. The highest correlation (0.976) is observed in visible (VIS) bands 2 and 3, while the near-infrared (NIR) band 4 is differentiated from VIS bands, as well as from SWIR bands, with correlation values close to 0. The least correlated bands can highlight their differences and discriminate the lithology. The eigenvectors (Appendix II, Table 3) determine the new rectangle coordinate system of transformation. This suggests that the degree of correspondence between the principal components and the initial bands are as follows (Fig. 6.4):

For example, PC1: $DN_{PC1} = 0.4665 \times DN_{Band1} + 0.4546 \times DN_{Band2} + 0.4534 \times DN_{Band3} + 0.1680 \times DN_{Band\ 4} + 0.3998 \times DN_{Band\ 5} + 0.4265 \times DN_{Band\ 7}$

The level of dissemination for each new component is determined from the eigenvalues (Table 6.3). For instance, the first principal component (PC1) has a dissemination value of 11868.834 while the total dissemination was (SUM) = 14382.643. It becomes clear that the higher percentage of the variance information is included mainly in the first two principal components (PC1 and PC2) (~94%).

Although the images obtained from the principal component analysis have a linear relationship with the initial data, their components are statistically uncorrelated. For example, the percentage of covariance (Table 6.3) is decreased progressively for higher principal components.

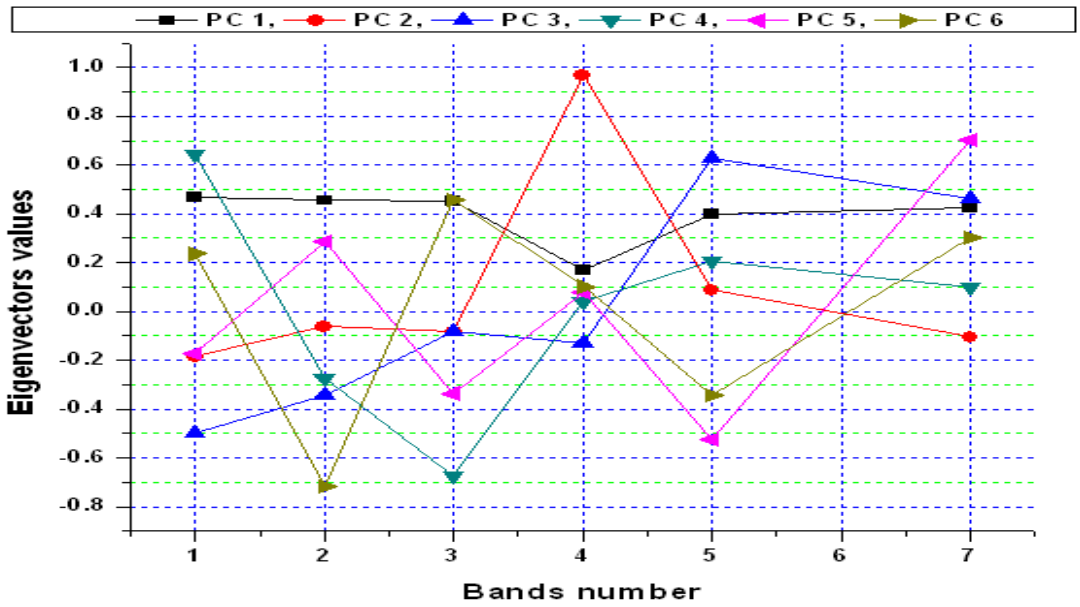

Fig. 6.4: Plot of eigenvectors values against ETM+ band number.

The factor loadings with which the individual spectral bands (k = 1, 2,é ,7) contribute to the configuration of every new component (s = PC1, PC2,é ., PC6) is evaluated with the following mathematic equation (Oppenheimer et al., 2000; Papadaki, 2005):

- **P(k, σ)** = eigenvectors(k, ů) × sqrt covariance(k)/ sqrt eigenvalues(ů)

The results of the factor loadings are presented in Table 6.2, where the horizontal columns indicate the spectrum bands that occur in the transformation while the vertical columns indicate the resulting principal components. The values oscillate inside the range of [- 1, 1]. Providing the divergence increases away from zero, the contribution of the band in the configuration of the corresponding principal component is considerably higher (Papadaki, 2005). An interesting point is the high contribution of TM 4 (used for geological studies) to PC 2, which could also be observed in the eigenvector values-band numbers plot (Fig. 6.4). Thus, PC 2 becomes a representative image to be used for geological and geomorphological purposes (as opposed to PC 1 which is generally considered to contain more information). A particular site was selected as an example, revealing (aided by red arrows) the structural features in PC 2 that are not present in PC 1

(Fig. 6.5). The Principal Component Analysis (PCA) images of the entire study region are presented in Appendix II (Fig. 9).

Factor loadings	PC 1	PC 2	PC 3	PC 4	PC 5	PC 6
Band 1	0.9507	-0.1408	-0.2422	0.1290	-0.0219	0.0223
Band 2	0.9779	-0.0497	-0.1768	-0.0578	0.0382	-0.0716
Band 3	0.9841	-0.0667	-0.0434	-0.1445	-0.0450	0.0462
Band 4	0.4206	0.9036	-0.0778	0.0099	0.0123	0.0118
Band 5	0.9291	0.0748	0.3490	0.0472	-0.0753	-0.0372
Band 7	0.9589	-0.0886	0.2482	0.0215	0.0975	0.0315

Table 6.2: The factor loadings calculated for the Landsat ETM+ multispectral imagery.

The aforementioned PCA outcomes of Landsat ETM+ sensors determine: i) which bands are least correlated when used in an RGB combination to highlight their differences and discriminate lithology and; ii) that an ideal RGB combination of principal components might include PC 1 and PC 2 from the Landsat ETM+ sensor, in order to keep most of the spectral information. The correlation matrixes revealed as uncorrelated bands 7, 4, 1 and 3 for Landsat ETM+ imagery (see Appendix II, Table 2).

	Eigenvalues	% of covariance
PC 1	11868.834	82.521
PC 2	1651.210	11.480
PC 3	676.559	4.704
PC 4	115.062	0.800
PC 5	45.334	0.315
PC 6	25.641	0.178
Sum	14382.643	100

Table 6.3: The eigenvalues for the Landsat ETM+ multispectral bands and the percentage of covariance.

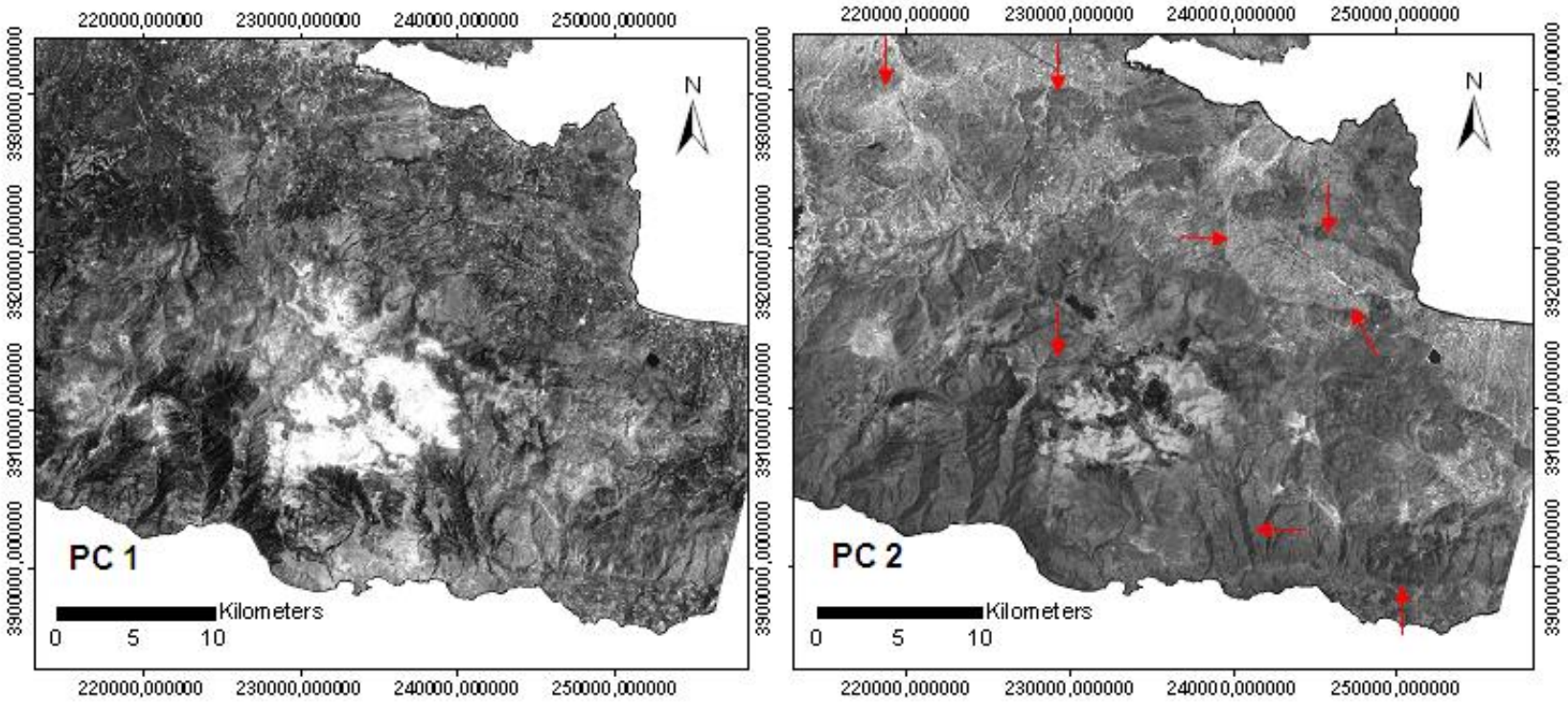

Fig. 6.5: The comparison of the first and second principal components. Red arrows highlight linear features indicating tectonic structures.

ii) Minimum Noise Fraction transformation (MNF)

The MNF transformation was implemented using ENVI 4.2 software on the bands of Landsat ETM+ satellite imagery. As this study focuses on the better enhancement and visualization of multispectral images, no thermal band was included, as its spatial resolution was larger than the rest of the bands. The image pixels were represented by eigenvalues. For the purposes of further spectral processing, the dimensionality of the data was determined by examination of these values (Fig. 6.6). By examining the eigenvalues, it can be seen that the first and second MNF band had the highest values and contain most of the information, while the remaining bands had consistently low values. The remaining low value bands (for example, 3 and under) were seen as noise. The redundancy of the data was eliminated and noise was also removed.

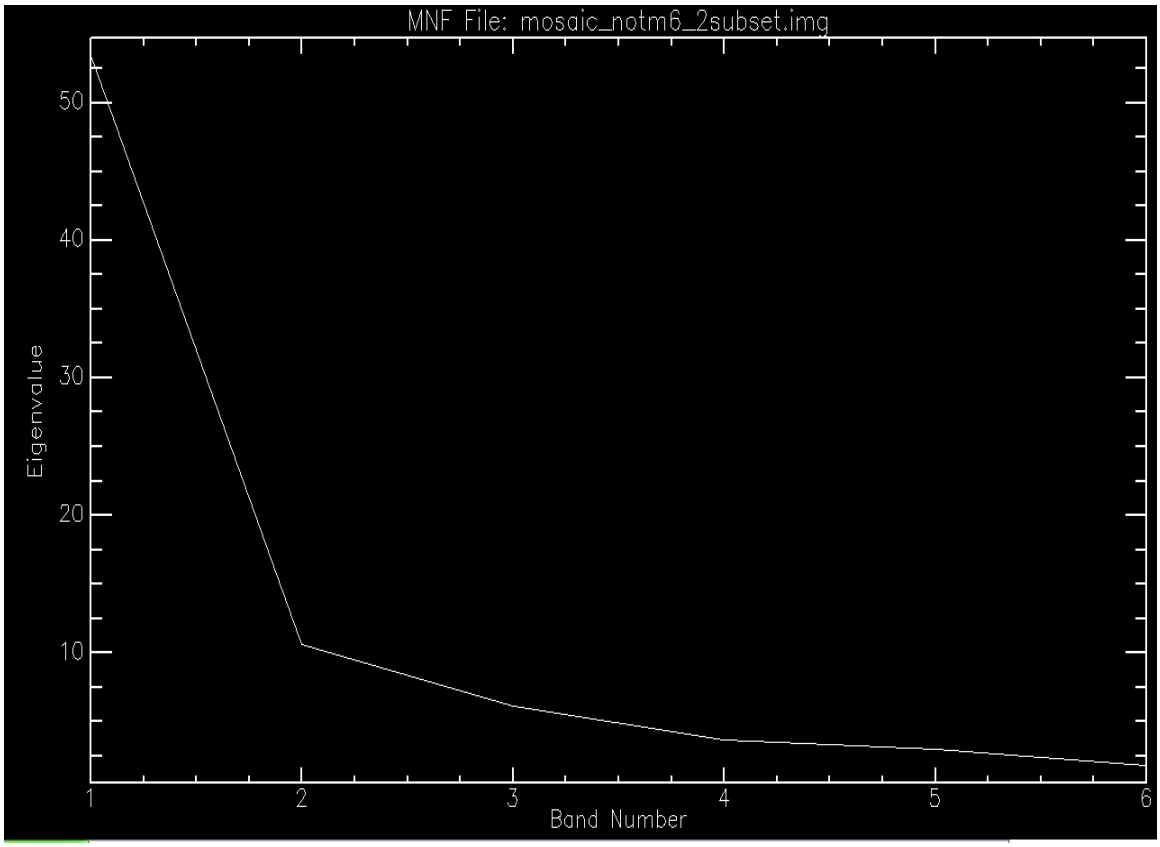

Fig. 6.6: The MNF eigenvalues plot for Landsat ETM+ imagery scene.

The level of dissemination for each new maximum noise fraction image was determined from the eigenvalues (Table 6.4). For example, the first maximum noise fraction (MNF1) for Landsat ETM+ images had a dissemination value of 53.41 and the total dissemination (SUM) = 78.6. In comparison with the PCA analysis results, where the first two principal components of the variance information percentage was close to ~94%, the MNF percentage of total covariance was steadily decreasing the image quality for higher MNF transformed images (Appendix II, Fig. 10). The first two principal components contained less variance information than the PCA analysis (~80%) (Table 6.4).

The aforementioned outcomes of MNF transformation for Landsat ETM+ revealed that MNF components decrease more steadily the image quality. It was observed that there is significantly lower percentage of information contained in the first two components for MNF transformation (~80%) than in PCA analysis (~94%). The latter implies that much more information was provided by the higher MNF components. As a result, comparison of covariance between MNF and PCA, reveals that MNF 2 component contains by 3% more information than the PC 2 component, while MNF 1 has significantly less information than PC 1 by 15% (see Table 6.3 & 6.4).

	Eigenvalues	% of covariance
MNF 1	**53.4083**	**67.9470**
MNF 2	**10.5747**	**13.4533**
MNF 3	**6.1152**	**7.7798**
MNF 4	**3.6564**	**4.6517**
MNF 5	**3.012**	**3.8329**
MNF 6	**1.835**	**2.3350**
Sum	**78.602**	**100**

Table 6.4: The percentage of information % of covariance for the MNF transformation and the eigenvalues for Landsat ETM+ satellite imagery.

6.5.2.2 PCA analysis and MNF transformation for lithological mapping

In order to present the differences of PCA analysis and MNF transformation with regard to the aforementioned outcomes, the drainage basin of Tiflos was selected as a sample site. The combination of PCA and MNF approaches can potentially offer better lithological discrimination as it will be examined below. It can be observed at figure 6.7 that PC1 contained more information of covariance than MNF1, while higher components of PCA contained less information of covariance than respectively MNF components. The Landsat ETM+ RGB combinations of PC1-PC2-PC3 and MNF1-MNF2-MNF3 are presented in figure 6.8. The better lithological discrimination (see inset boxes in Fig. 6.8), was succeeded through combining the PCA and the MNF components that contained the most multispectral information. PC1 contains more information than MNF1, so if PC1 replaces MNF1 in RGB combination MNF1-MNF2-MNF3 then the feature boundaries are even more enhanced. Following Novak & Soulakellis (2000) study, the RGB TM7-PC1-PC2 combination was created for lithological discrimination; compared with RGB TM7-MNF1-MNF2 combination, the latter produced better discrimination of lithology (Fig. 6.9).

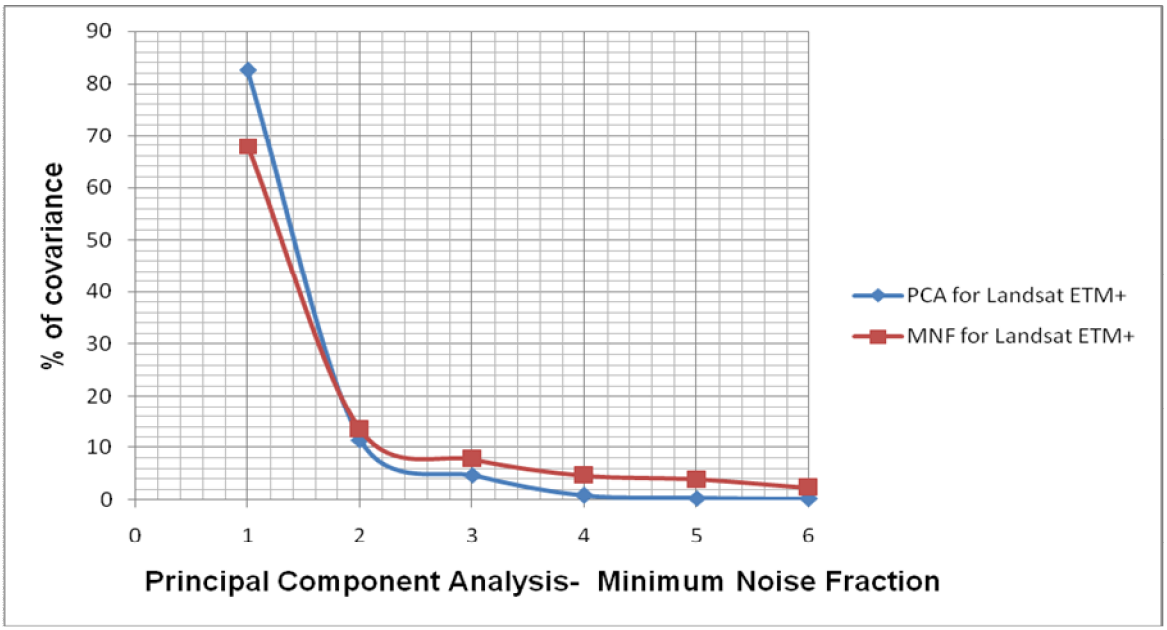

Fig. 6.7: The magnitude of eigenvalues percentage of covariance for PCA and MNF transformation in the Landsat ETM+ satellite imagery.

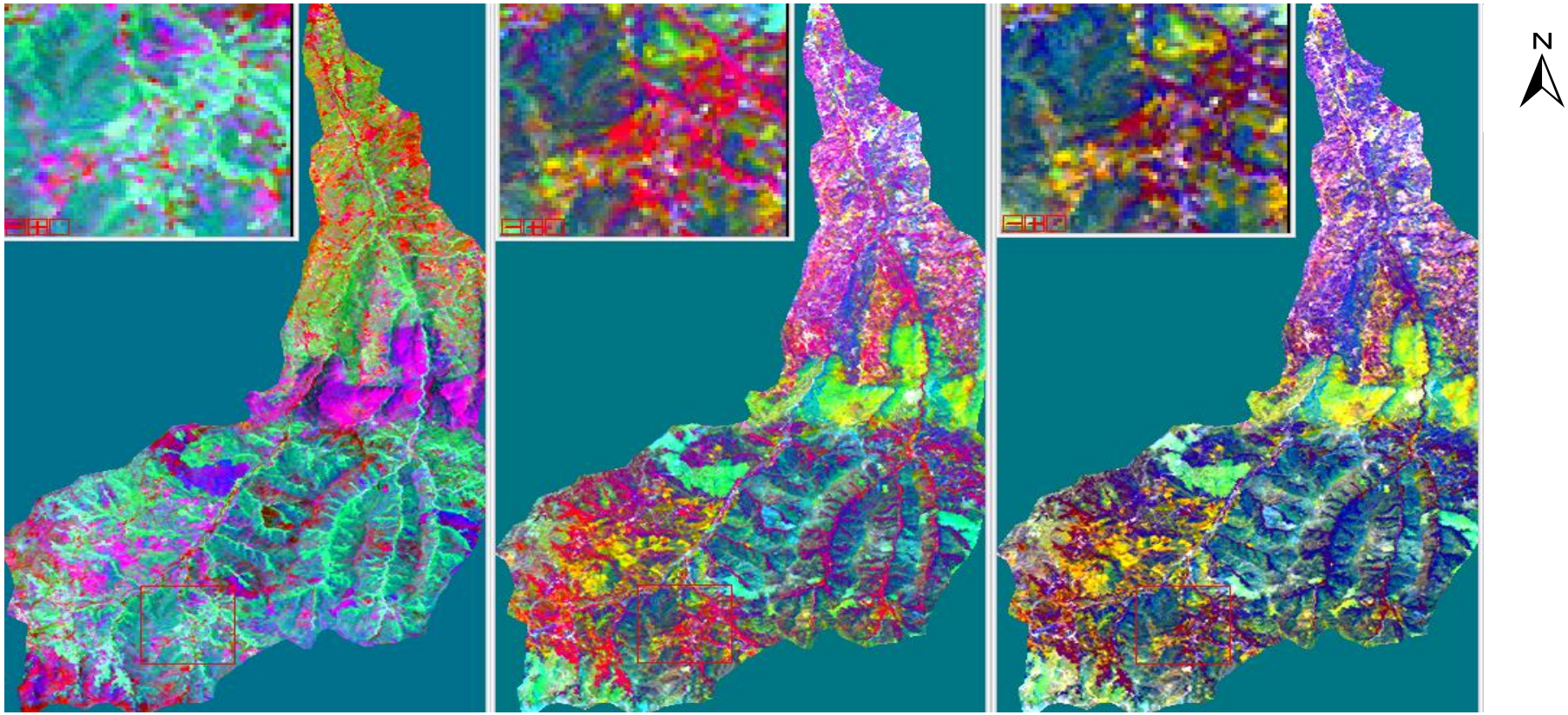

Fig. 6.8: The RGB combinations of PC1-PC2-PC3 (left image), MNF1-MNF2-MNF3 (middle image) and PC1-MNF2-MNF3 (right image). The RGB combination consisting of MNF components provides better interpretation and discrimination of features (see zoom in of red rectangle). Replacement of component MNF1 by PC1 results in better discrimination of lithological boundaries as vegetation is suppressed.

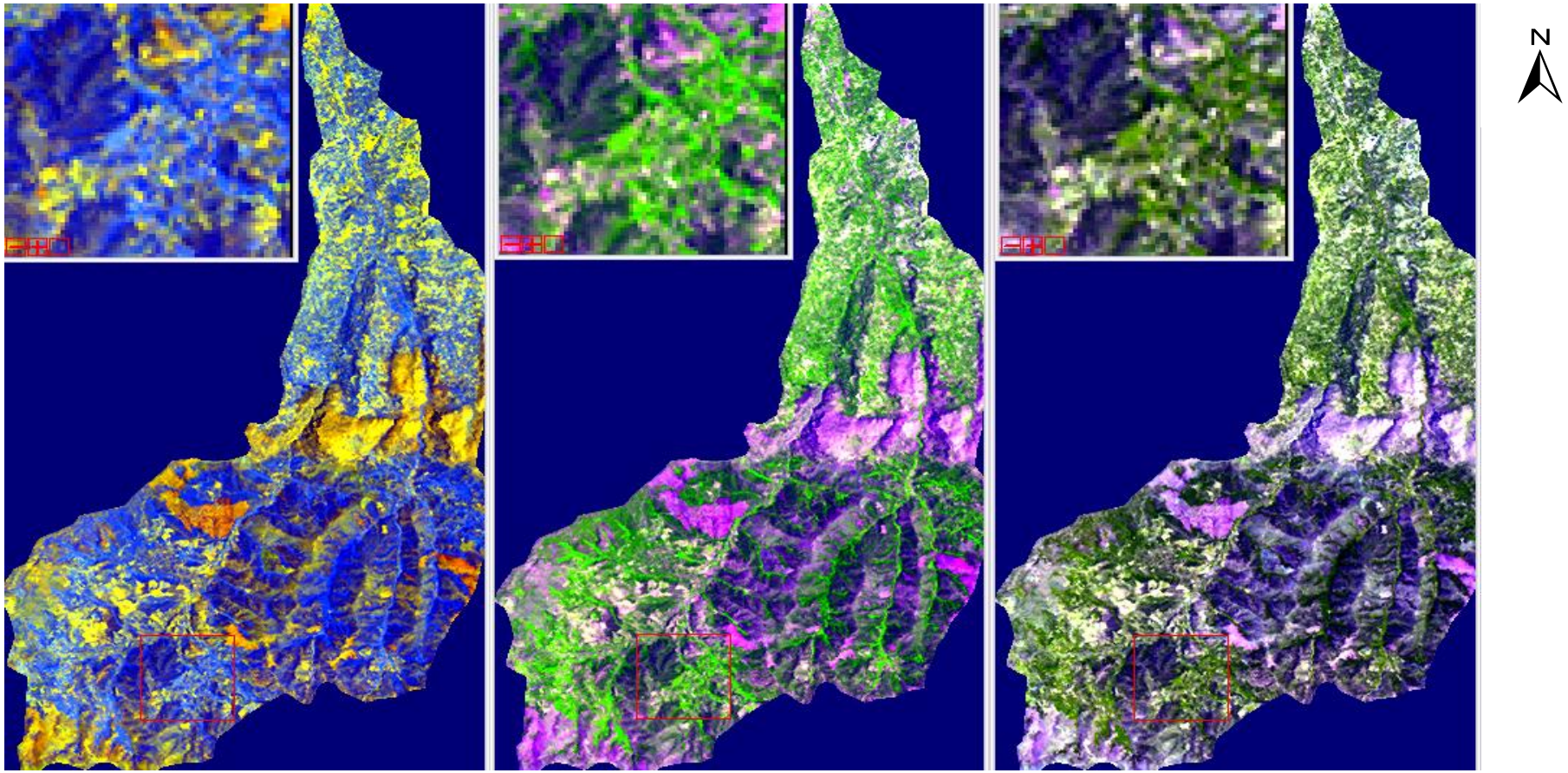

Fig. 6.9: The RGB combinations of TM7-PC1-PC2 (left image), TM7-MNF1-MNF2 (middle image) and TM7-PC1-MNF2 (right image). It can be seen that MNF components offer more detailed discrimination of lithologies and when PC1 replaces the MNF1 more enhancement is achieved.

6.5.3 Image enhancement for both lithological and lineament mapping

The preliminary evaluation of PCA and MNF for lithological discrimination, on a site-by-site basis, as was expected given by other published observations, reveals a good lithological discrimination. Nevertheless, this approach cannot enhance the lineaments effectively. Because lineament analysis is the next stage of this research and satellite images that will highlight the lineament information need to be created, the following approach is considered. The approach of OIF analysis in combination with spectral band arithmetic operations is thoroughly taken into account as it is expected to provide the most suitable RGB combinations to enhance the tonal contrast for any linear features to be detected.

i) Optimum Index Factor analysis (OIF)

The OIF analysis was performed for the original Landsat ETM+ multispectral imagery (no thermal bands were included). The results of the analysis are presented in the following tables (Appendix II, Table 4) with the best RGB combination for the Landsat ETM+ images being extracted. The Landsat ETM+ provides 20 FCCs, with 741 having the highest OIF value and as a consequence a larger amount of spectral information (Appendix II, Table 4).

ii) Spectral band arithmetic operations

Spectral band arithmetic operations utilize the spectral information of each band, therefore providing enhanced RGB combinations with valuable information for the human eye (as far as linear feature detection is concerned).

The lithological discrimination was achieved through multiplication of Landsat ETM+ bands. The selection of this arithmetic operator is due to the fact that multiplication enhances edges and contrasts differences that can then be linked with the identification of linear features. The RGB combination (4*3*2)(7*4*1)(7*5*3) was selected as the most appropriate (Fig. 6.10) (see geological map in Fig. 2.6 for overview comparison). Such false colour composite: i) combines bands highlighting geology (e.g. band 4 & 7) and; ii) uses multiplied products of uncorrelated RGB combinations provided by OIF analysis (based on

threshold OIF values observations). The accuracy assessment of that final RGB combination with the digital geological map, as described by Kappa statistics in Chapter 3, revealed a percentage of 87.76%. This percentage is higher than the suggested target of 85% accuracy (Foody, 2002), indicating the acceptable reliability of the RGB combination outcomes.

The combination of those three components was able to provide a robust depiction of the study region, by isolating the lithological information of each band component. As mentioned, the choice of RGB combination depended on the OIF analysis and selection of uncorrelated false colour composites was beneficial in lithological discrimination (Appendix II, Table 4). A closer view to site 1 shows a better overview of the aforementioned RGB combination outcome, with the geologic map and simple RGB combination 741 provided for comparison (Fig. 6.11).

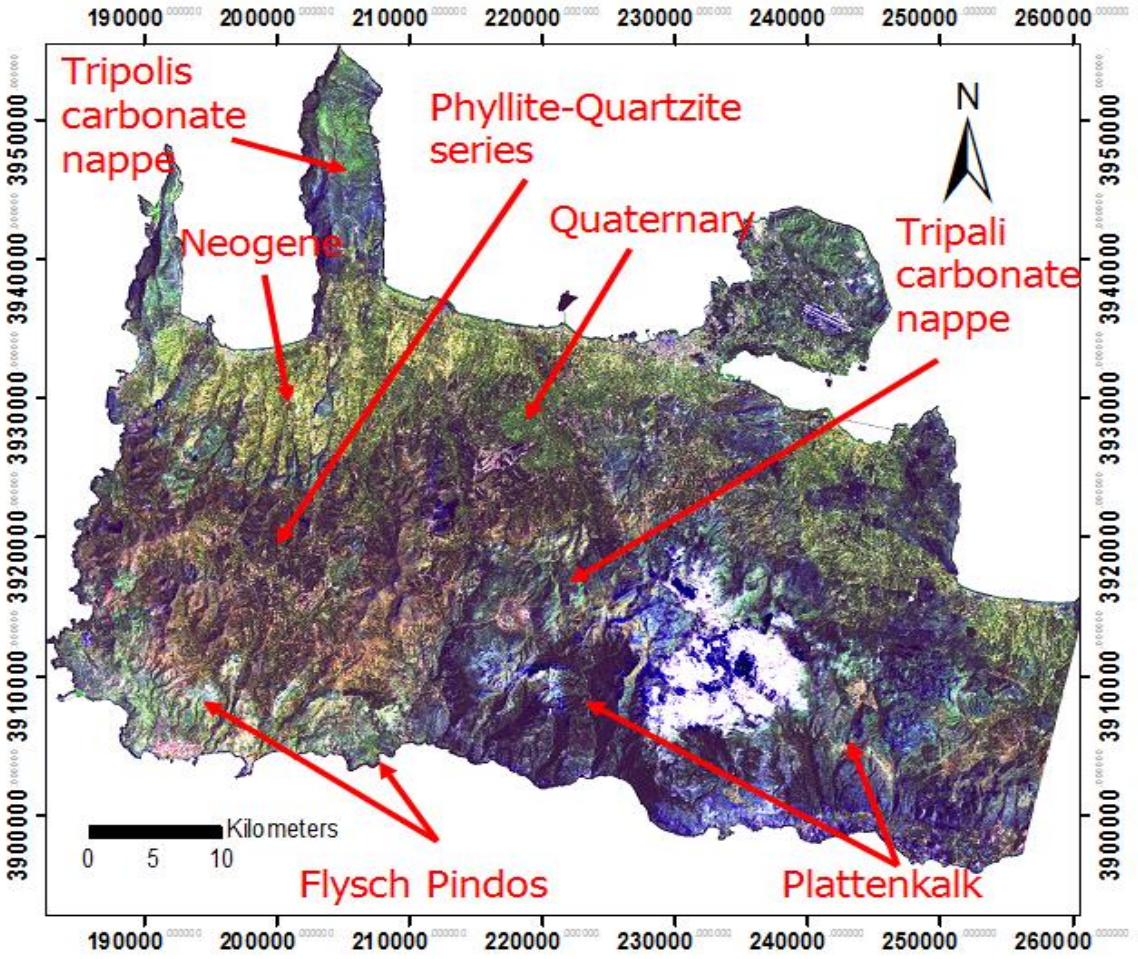

Fig. 6.10: The RGB combination (4*3*2)(7*4*1)(7*5*3) of Landsat ETM+ data depending on OIF results.

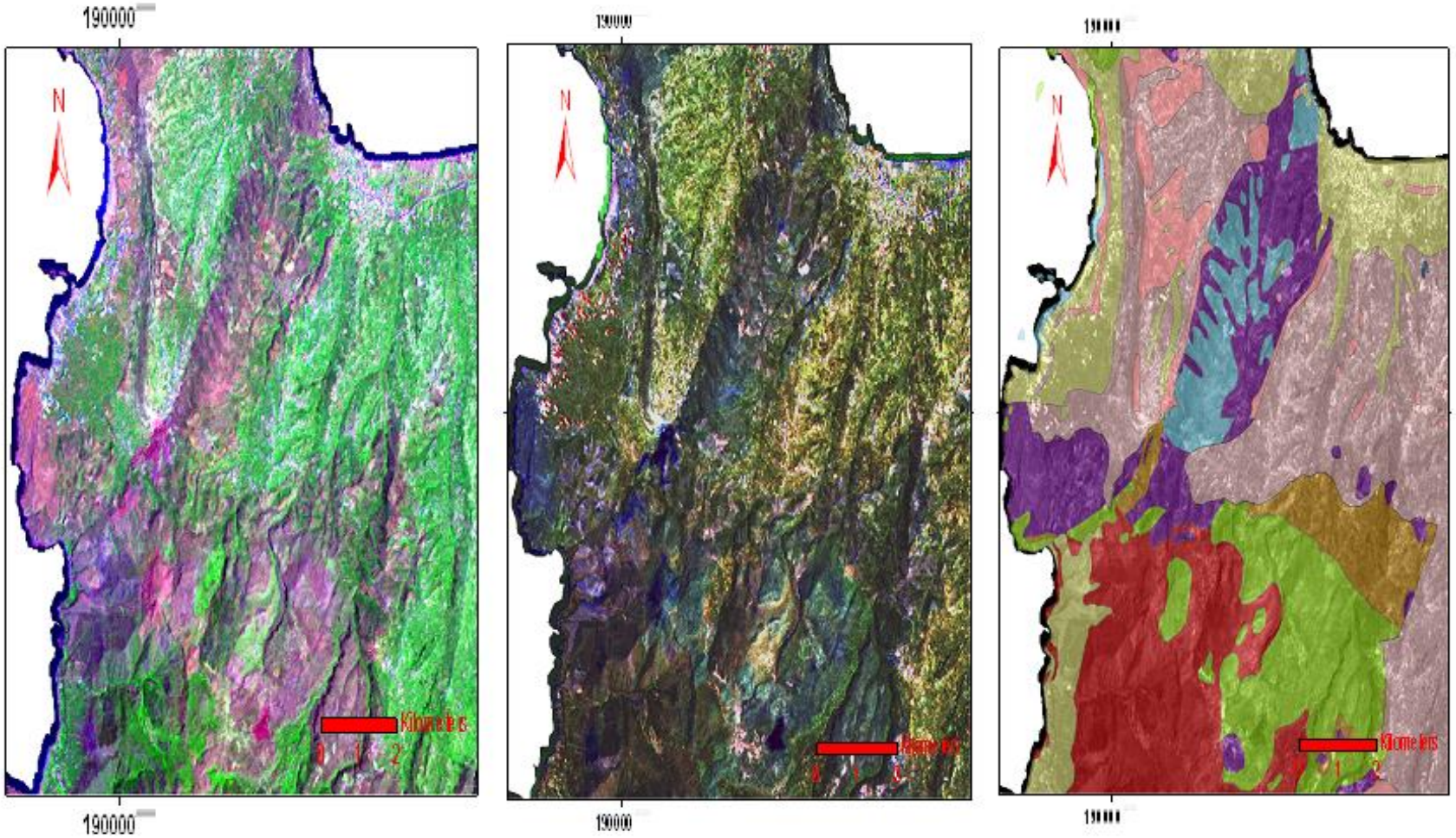

Fig. 6.11: Detail of site 1. Left: RGB 741; Centre: RGB (4*3*2)(7*4*1)(7*5*3); Right: Geological map (IGME, 1971).

The accuracy assessment of the RGB combination (4*3*2)(7*3*2)(7*3*1) against the digital geological map was described earlier. As in this stage of research there are two aforementioned approaches examined to discriminate lithologies, their accuracy assessment is now considered. The percentage being revealed, by Kappa statistics, among the RGB combination (4*3*2)(7*3*2)(7*3*1) and the PC1-MNF2-MNF3 was 90.91%, indicating the acceptable reliability of both RGB combination outcomes. The coverage of the Tiflos basin is selected as a sample region, presented in figure 6.12, to show the outcomes of the two RGB combinations and the geological map.

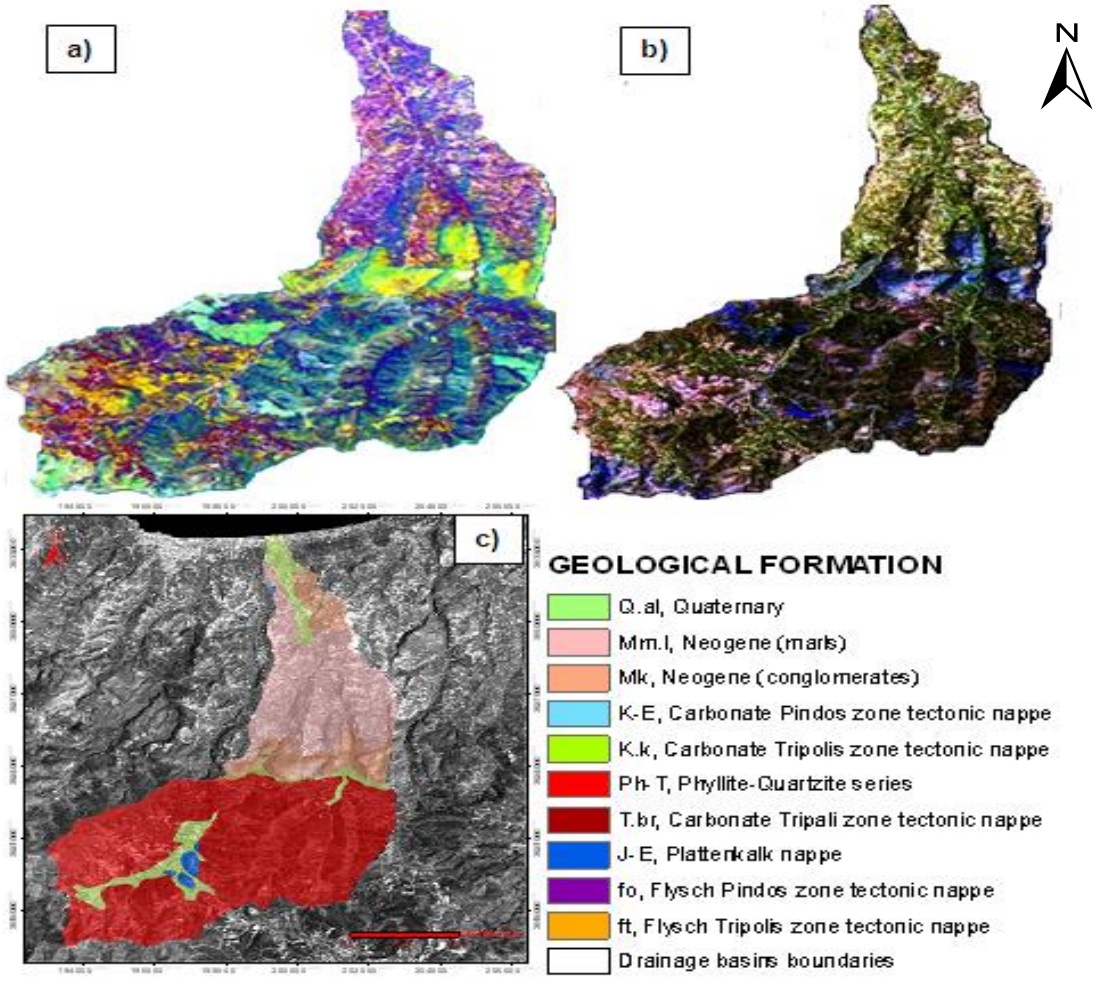

Fig. 6.12: a) A Landsat ETM+ RGB combination, involving both PCA and MNF components (PC1-MNF2-MNF3) covering the Tiflos basin; **b)** Landsat ETM+ RGB combination (4*3*2)(7*3*2)(7*3*1), after application of the band multiplication image processing procedure: this discriminates lithology and suppresses vegetation; **c)** overlay of the 1971 geological map on panchromatic Landsat ETM+ imagery of the Tiflos basin.

6.6 Lineament analysis

6.6.1 Lineaments/faults based on digital geological maps

The geologic maps (IGME, 1971) were utilised so as to digitise the faults of the study region (Fig. 6.13). The lineament analysis stages performed identified lineaments which can correspond to faults, and not all of them are shown on the 1971 geological map of the area. Since the 1971 map was based mainly on field work surveys and the interpretation of aerial photos, the usage of satellite imagery provides an updated version of the 1971 map.

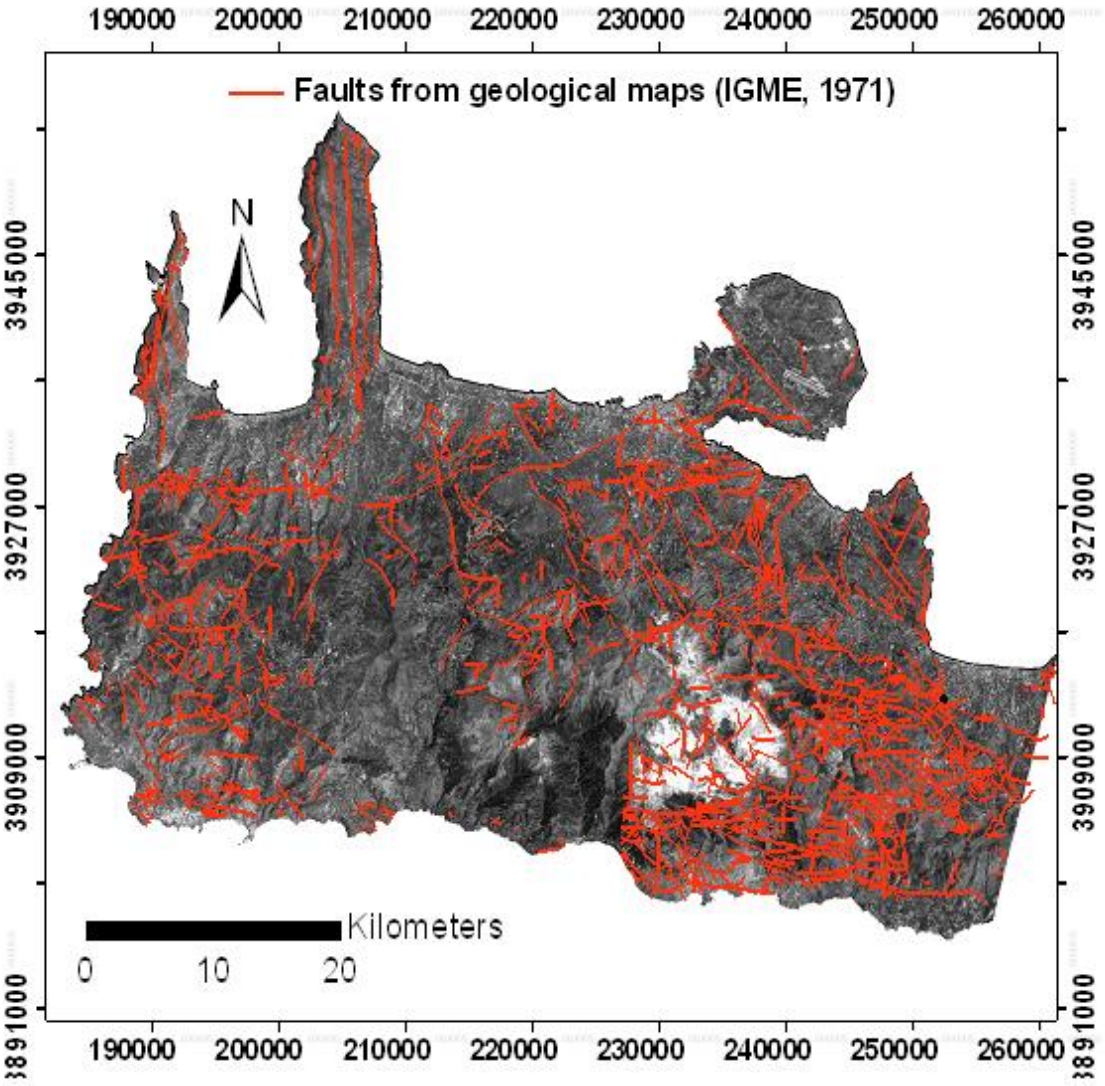

Fig. 6.13: The digitised faults of the geologic maps.

6.6.2 Lineament interpretation by Earth observational image data

i) Interpretation of multispectral images

The Landsat ETM+ image of RGB combination (4*3*2)(7*4*1)(7*5*3) in figure 6.10 were used to extract lineaments by manual interpretation (using the geomorphological and geological criteria described in Chapter 3). The manually digitised lineament map interpretation is presented in figure 6.14.

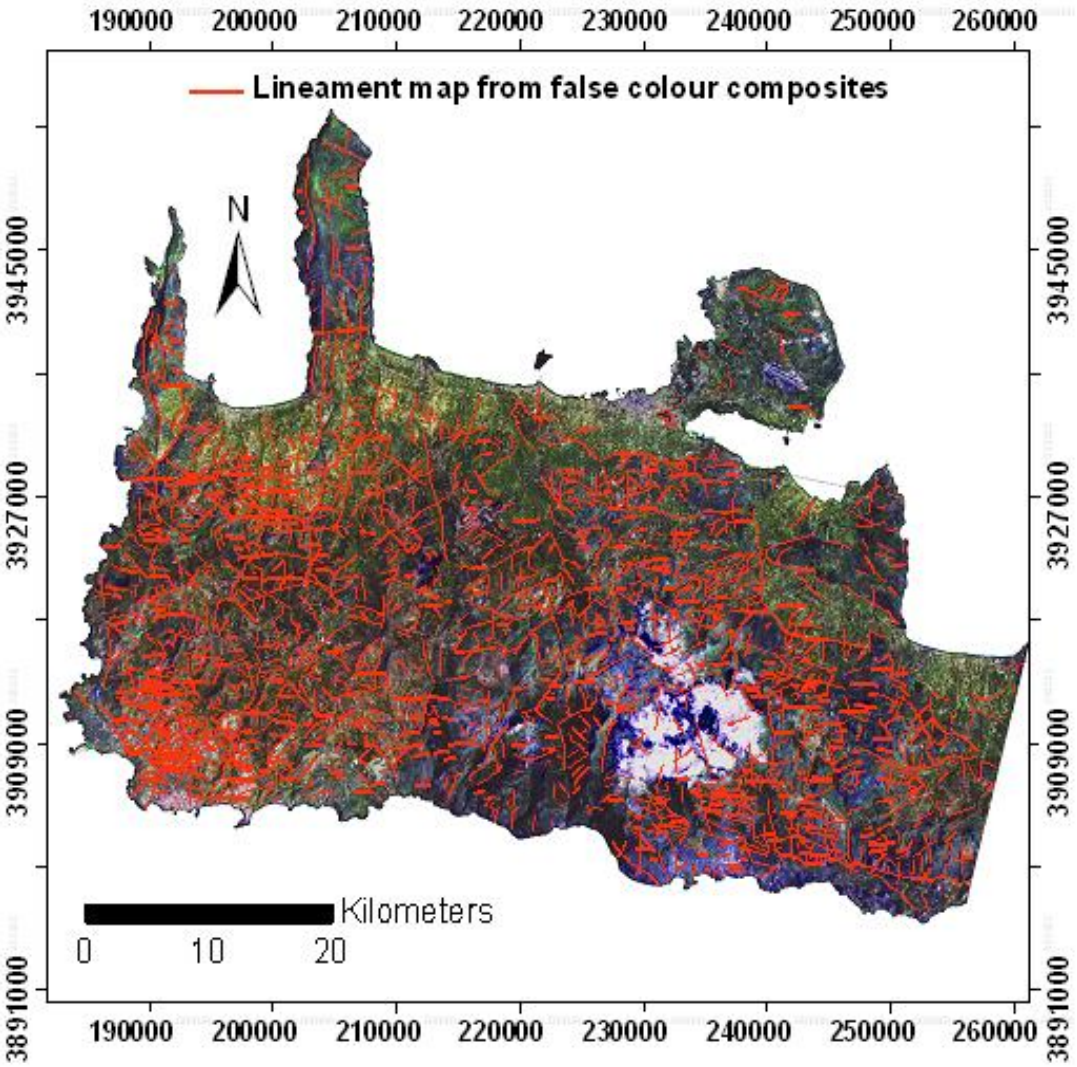

Fig 6.14: The lineament extraction based on the multispectral image analysis of RGB colour combination (4*3*2)(7*4*1)(7*5*3) Landsat ETM+ images.

ii) Spatial filtering of multispectral satellite imagery

Compass gradient masks in various azimuths were applied to pansharpened TM7 of Landsat ETM+ as well as the second principal components of Landsat ETM+ imagery. The filtered images were then added to the original images. The Landsat ETM+ band 7 is principally used for identifying geological features and lineaments (Sabins, 1996). The second principal components were selected for two reasons: i) the high information contribution of Landsat ETM+ band TM 4 and; ii) to produce a fainter drainage network (due to the information from the other bands being contained). Lineaments in figure 6.15 were identified by using spatial filtering techniques, including non directional edge filters (Sobel and Prewitt filters) and Laplacian filter (see Appendix II, Fig. 11). The complete set of spatial filtering images (including compass gradient masks, Laplacian and non-directional edge filters) can be found in Appendix II by selecting the red circle in figure 6.15 as a sample area (Appendix II, Fig. 11). All edge enhancement methods provided reasonable identification of edges that contained clear similarities with one another. Laplacian edge enhancement was the most easily interpreted, thus providing a rapid discrimination of lineaments and the one selected as final spatial filtering lineament map to be considered in following section 6.6.3 Lineament map evaluation**.**

.

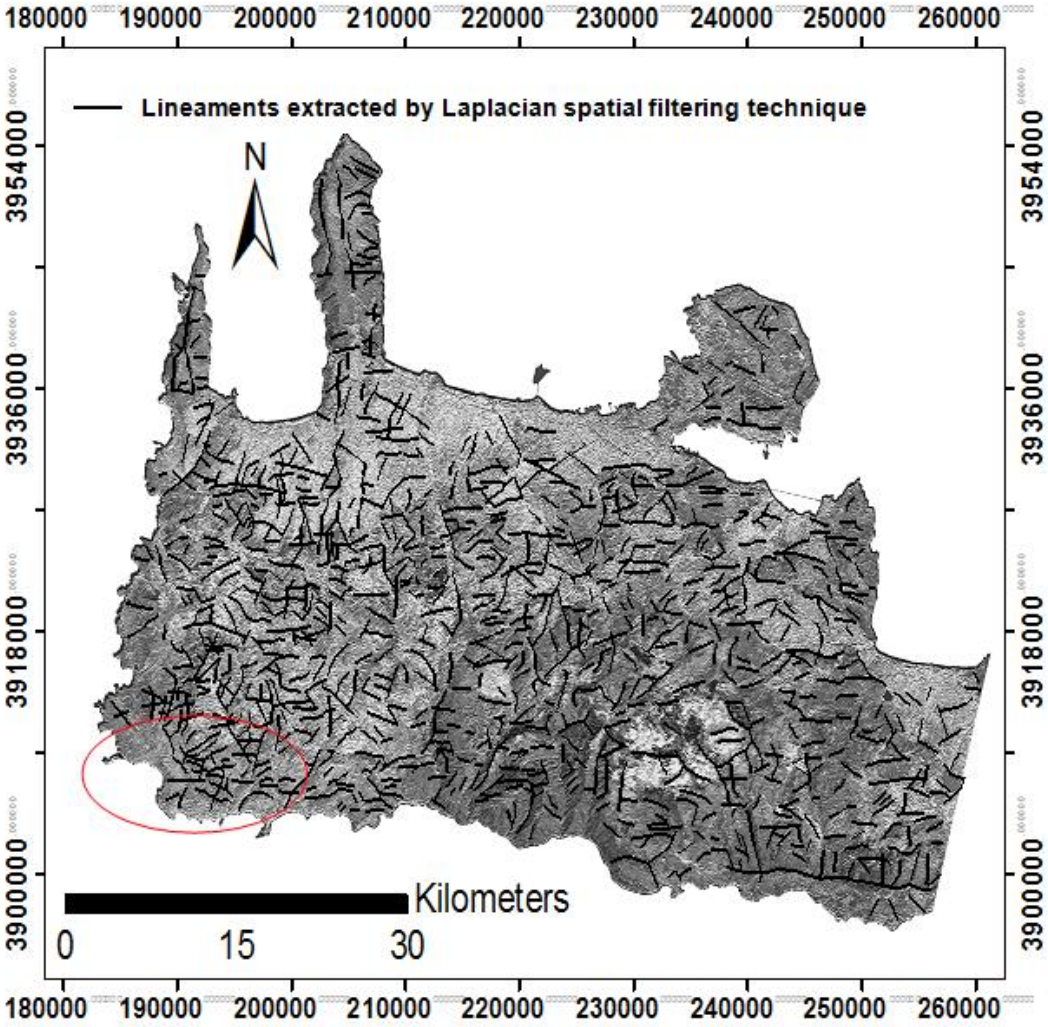

Fig. 6.15: Lineaments extracted by Laplacian spatial filtering technique.

iii) Lineament data extraction from Digital Elevation Models (DEMs)

The DEMs were used to create shaded relief maps. The application of different sun azimuth and elevation angle values to the shaded relief was performed in order to extract manually digitised lineaments observed in various orientations (Fig. 6.16). The value used for sun elevation angle was 45^0, while for azimuths 0^0, 45^0, 90^0, 135^0, 180^0, 225^0, 270^0, 315^0 (Appendix II, Fig. 12).

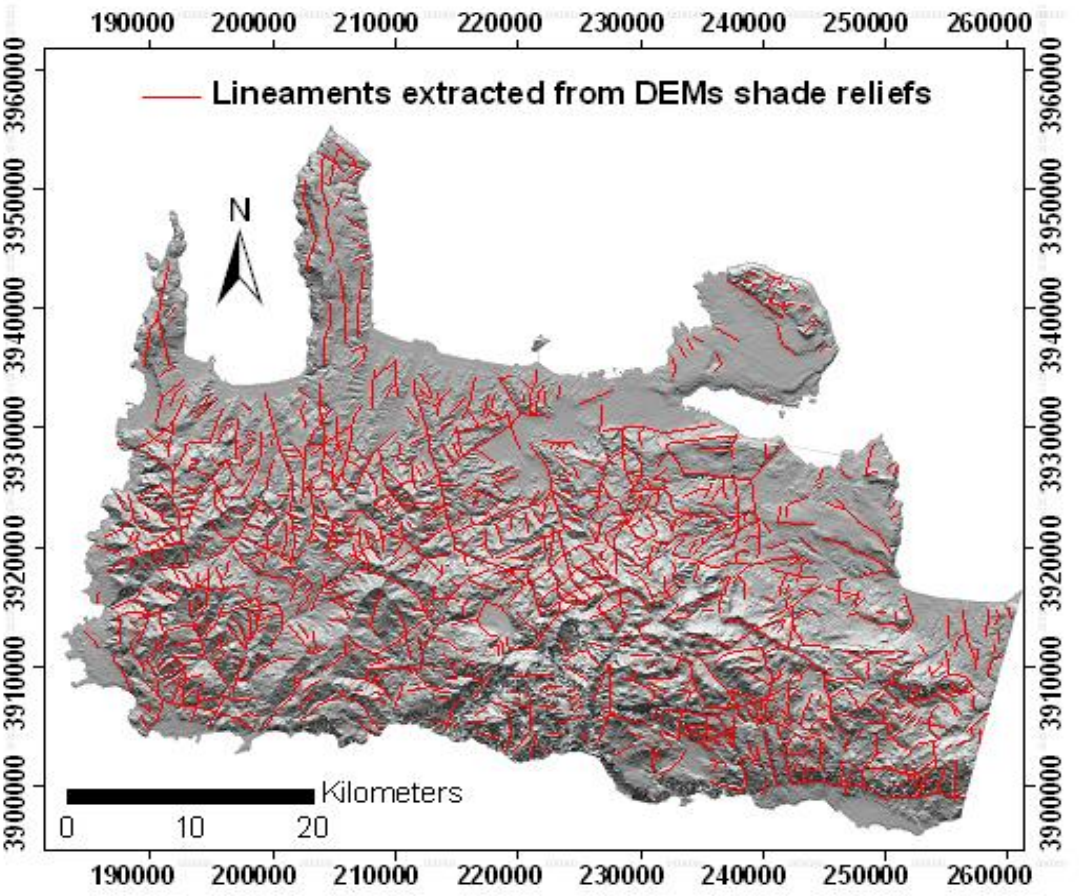

Fig. 6.16: The lineaments identified by the shaded reliefs in different azimuth orientations with sun elevation angle 45^0.

6.6.3 Lineament map evaluation

Each of the techniques applied to manual lineament mapping identified a large number of lineaments, as presented in table 6.5. All the extracted lineament maps indicate lineaments that are better spatially distributed than the less detailed geological maps. The comparison among these lineament maps can extract a final lineament map, with lineaments being indicative of fault structures. The final lineament map that was acquired by the earlier section can then be used to evaluate: i) the identified lineaments/faults with regard to the input datasets that were used; ii) the spatial analysis of the final lineament map (density and frequency of lineaments/faults) and; iii) the comparison of lineaments/faults against the drainage network.

i) Confidence in lineament locations

The interpretation of the Landsat ETM+ FCCs revealed a larger amount of identified lineaments. For that reason this lineament map was used as a reference map in order to create 100m buffer zones used to identify coinciding lineaments. The comparison of all lineament maps was performed to create the final lineament map with regard to the buffer zones.

Dataset	Number of lineaments
Geological map (IGME, 1971)	1232
Landsat ETM+ FCCs	1407
Spatial filtering Landsat ETM+ TM7	850
Spatial filtering Landsat ETM+ PC2	897
DEMs shade reliefs	829

Table 6.5: The number of manually digitised lineaments for each of the applied techniques.

Coinciding lineaments can be a representative characteristic of indicating fault lines, as they are observed in more than one datasets. Buffer zones (100m) allowed the identification of coinciding lineaments (more than one), which were then represented as singular lineaments (Fig. 6.17). As a result, a more comprehensive final lineament map of the study region was produced, including only lineaments indicative of fault lines (Fig. 6.18). Any lineament which was not identified by at least one of the other techniques was omitted from the final tectonic lineament mapping.

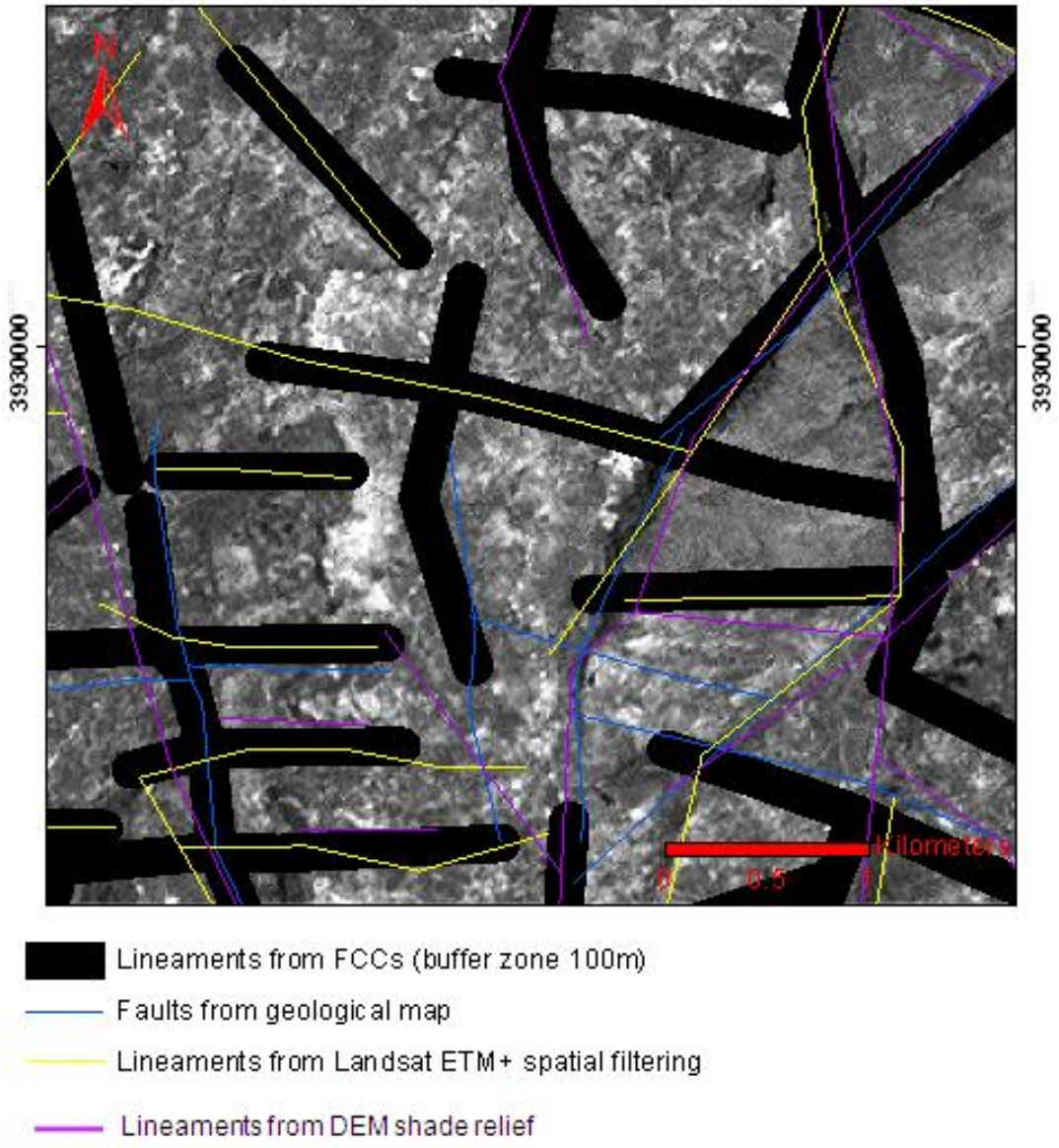

Fig. 6.17: Coinciding lineaments from different lineament mapping techniques were discriminated by buffer zones and were considered as singular lineaments.

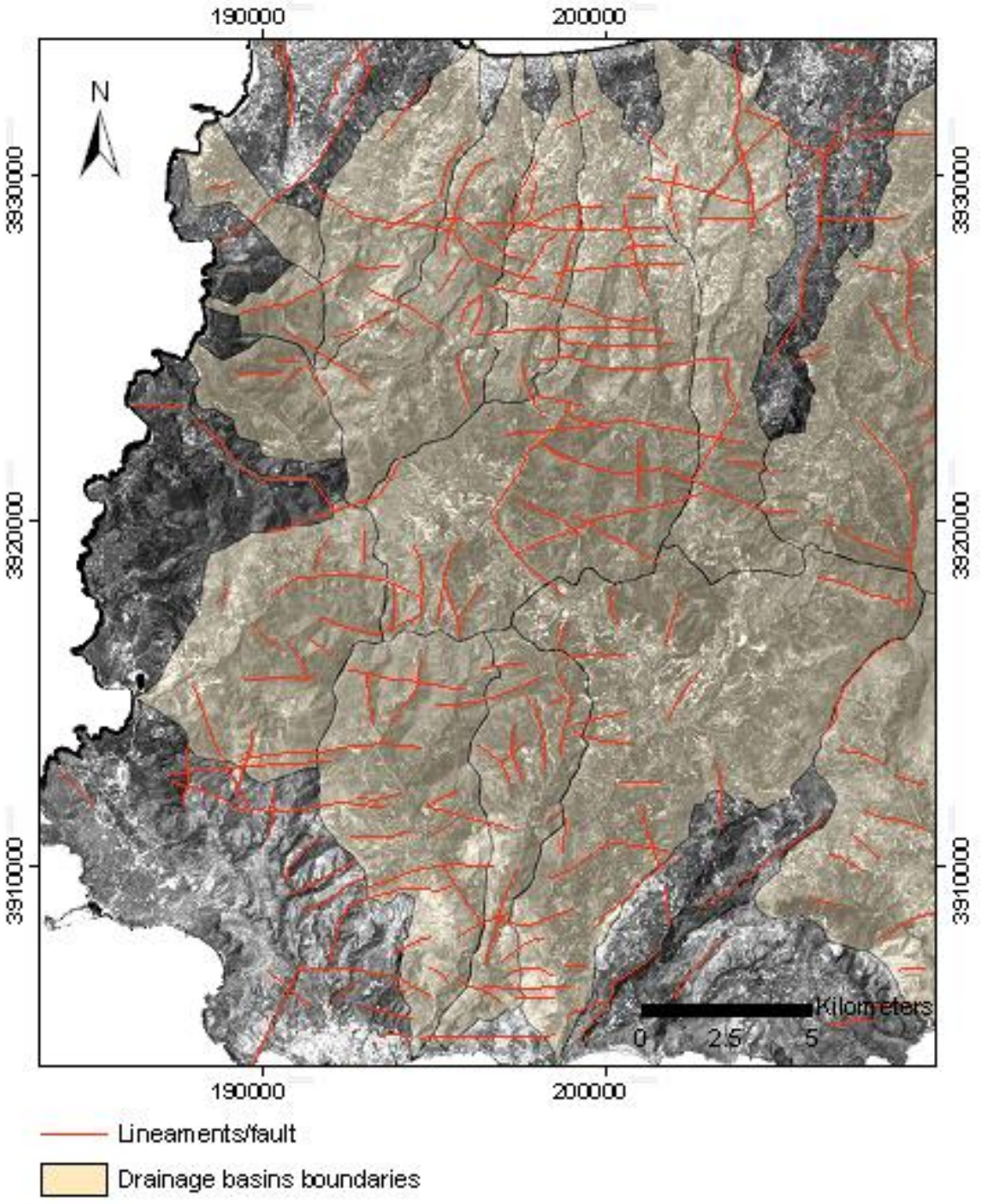

Fig. 6.18: Final tectonic lineament mapping consisting of fault lines, as a product of coinciding lineaments (within 100m buffer zones) from all techniques.

ii) Lineaments/faults versus Earth observational datasets and geological maps

The lineaments that constituted the final tectonic lineament map (Fig. 6.18) were categorised into three groups as following:

i) lineaments that were recorded on the 1971 geological map as faults, but were not identified by satellite imagery and DEM analysis (Fig. 6.19).

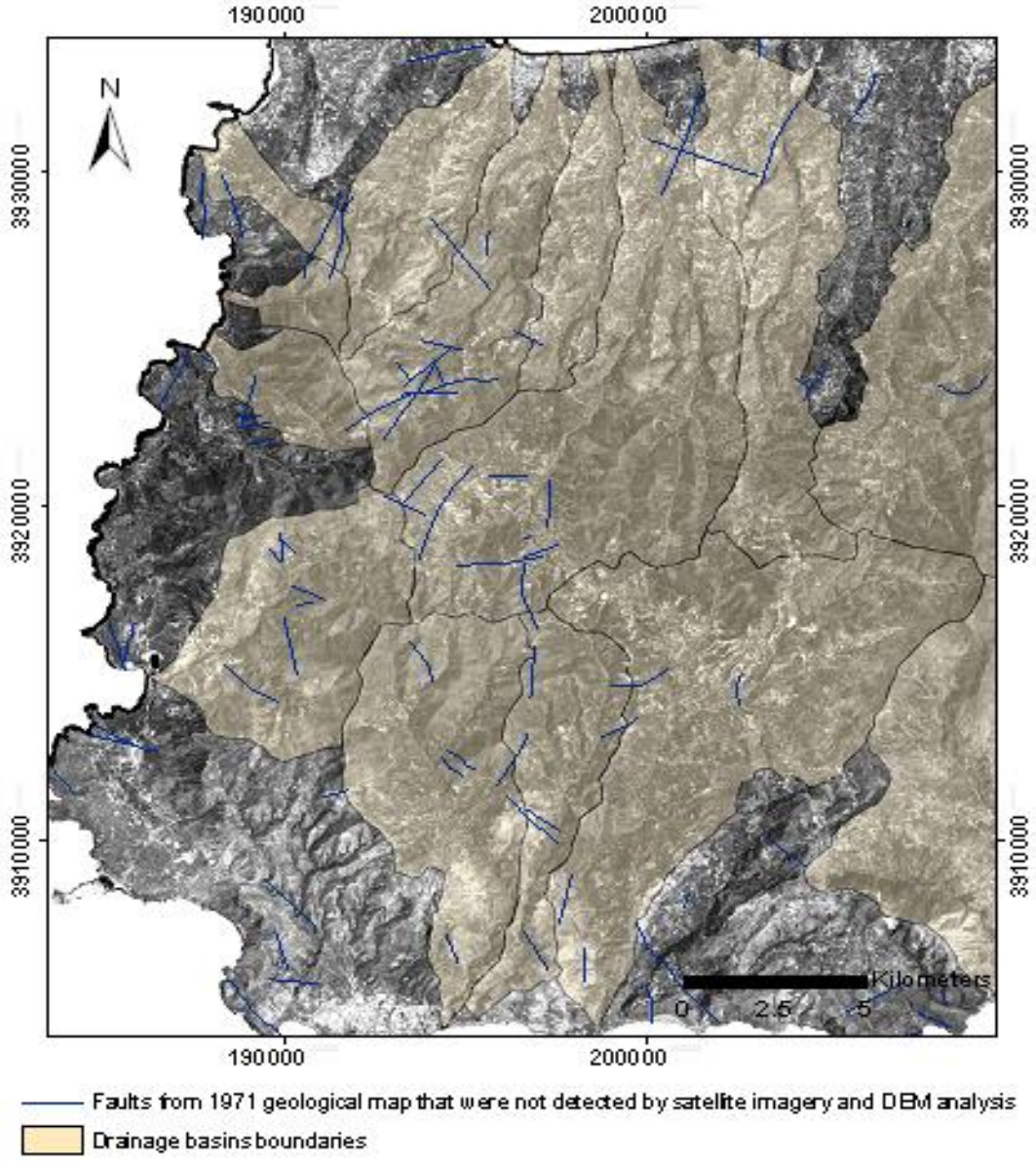

Fig. 6.19: Lineaments that correspond to previously mapped faults from geological maps that were not detected using satellite imagery and DEM analysis.

ii) lineaments that were interpreted through the satellite imagery and the DEM analysis and which correspond to previously recorded faults (Fig. 6.20).

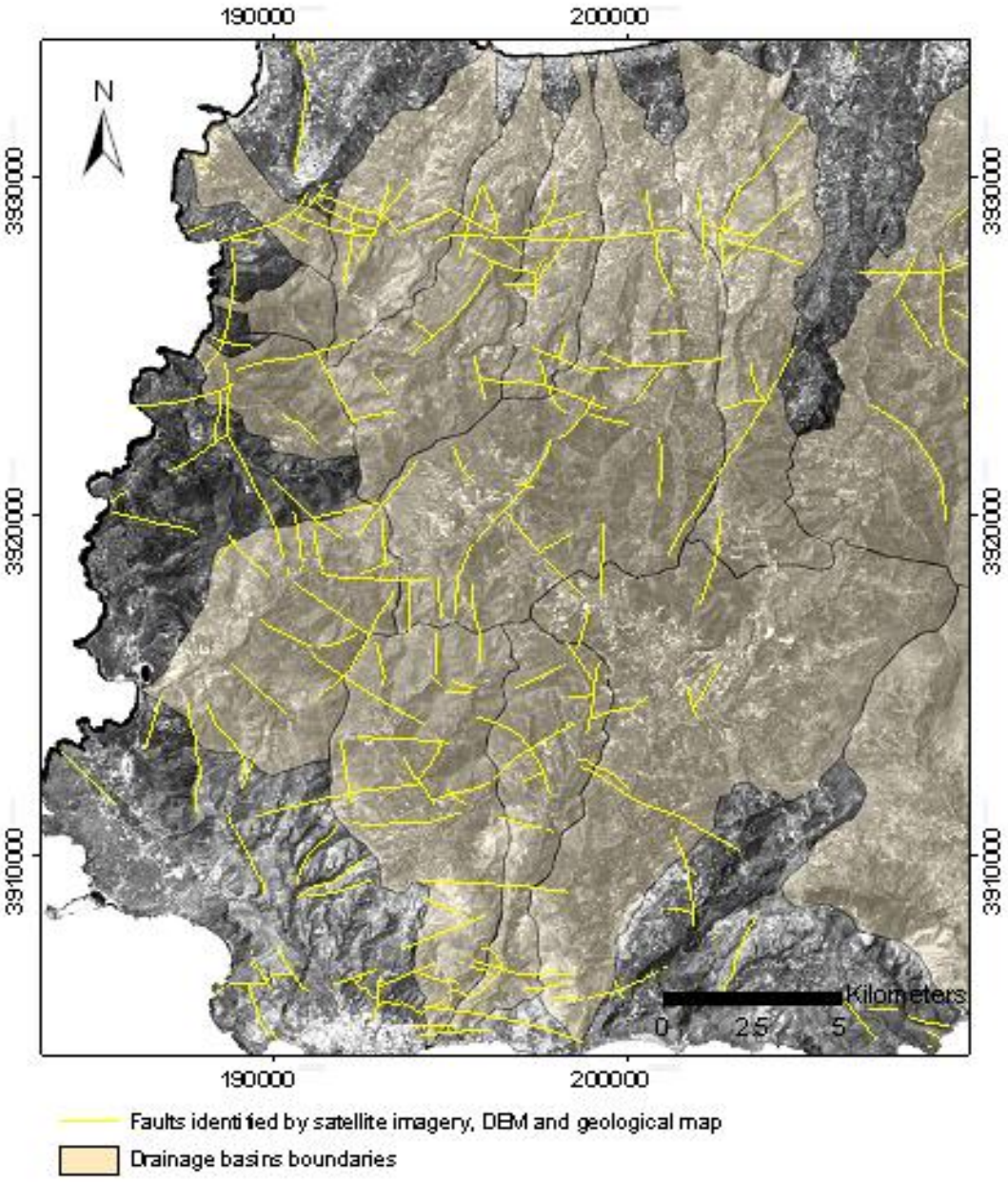

Fig. 6.20: Lineaments extracted by satellite imagery and DEM techniques that fit with previously identified faults in geological maps.

iii) lineaments that were previously unmapped, which were interpreted through satellite imagery and DEM analysis (Fig. 6.21).

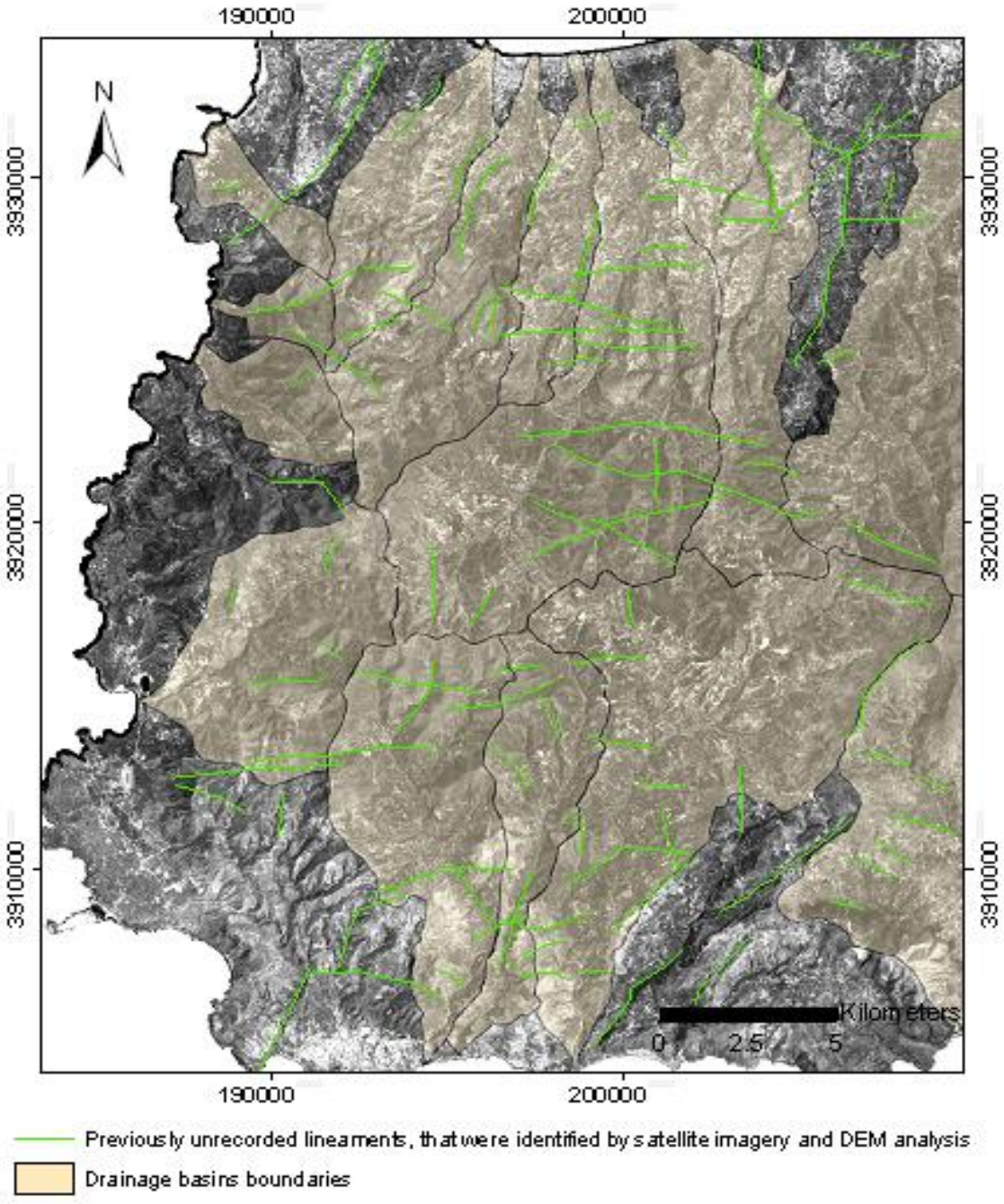

Fig. 6.21: Lineaments extracted by satellite imagery and DEM techniques, previously unrecorded by geological maps.

In addition, lineaments on the final lineament map were classified with regard to their azimuths (6.22). That classification revealed important information about the predominant tectonic status controlling each of the drainage basins, because of higher directional frequency of lineaments (Table. 6.6).

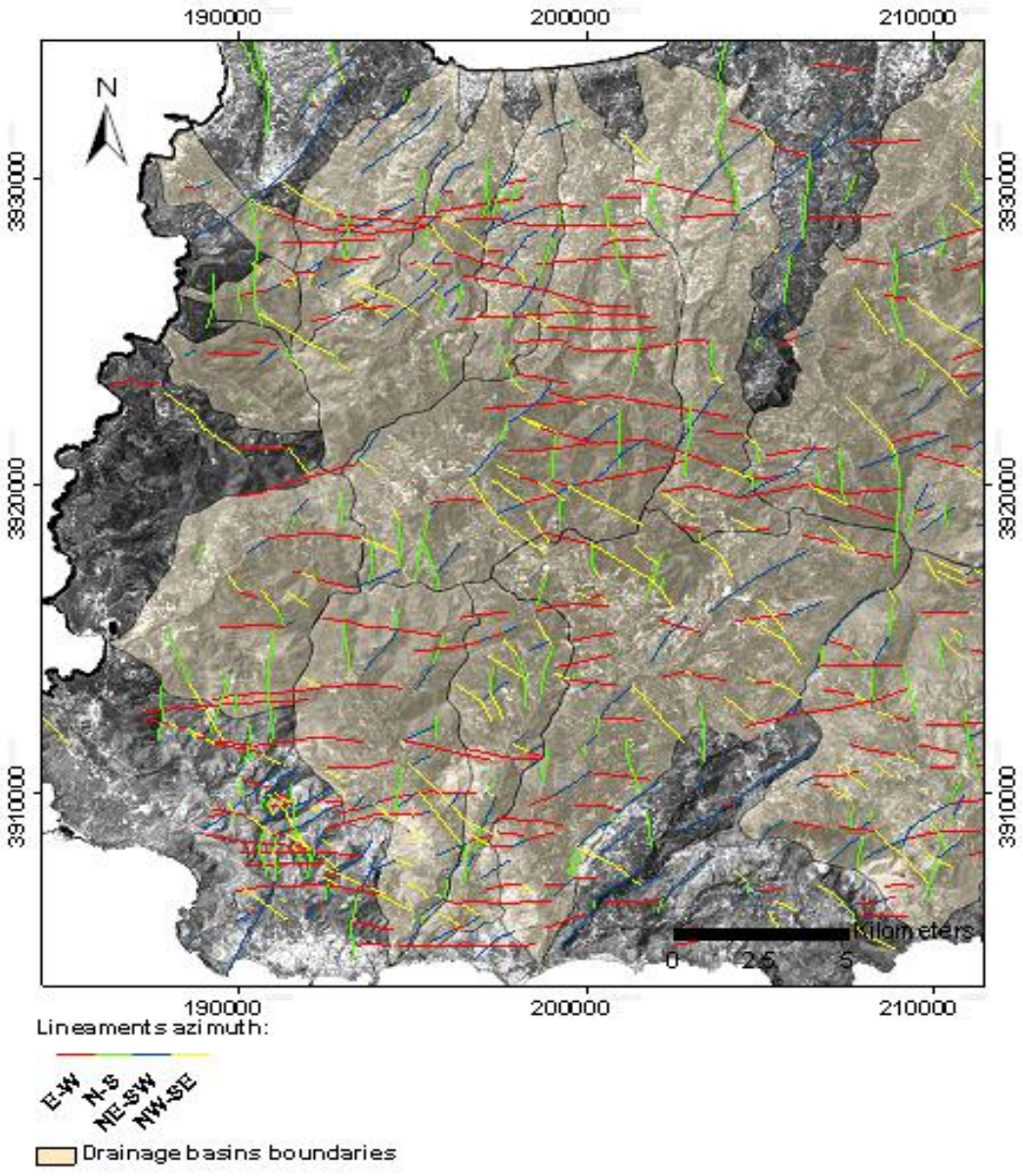

Fig. 6.22: The lineament azimuth classification in four major azimuths. Their statistical analysis indicated which drainage basins are subject to structural control.

Drainage Basins	Lithology	Tectonic
Sarakiniotis	**Phyllite-Quartzite nappe**	**E-W**
Milias	**Neogene deposits**	**E-W**
Arapi	**Neogene deposits and Phyllite- quartzite nappe**	**N-S, E-W**
Kastelli	**Neogene deposits, Tripolis and Pindos nappe**	**NW-SE**
Tiflos	**Neogene deposits and Phyllite- quartzite nappe**	**E-W**
Magagistra	**Neogene deposits, Tripolis and Pindos nappe**	**E-W**
Kakodikianos	**Phyllite-Quartzite nappe**	**E-W**
Mesa Rema	**Phyllite- quartzite nappe**	**E-W**
Metoxi-Platanos	**Phyllite- quartzite nappe**	**NE-SW**
Pelekaniotis	**Phyllite-Quartzite nappe**	**E-W**
Balsamakia	**Phyllite- quartzite nappe**	**N-S, NE-SW**
Xsiropotamos	**Phyllite- quartzite and Plattenkalk nappe**	**E-W**

Table 6.6: The classification of lineament strike revealed the predominant tectonic status controlling the drainage basins in Chapter 5.

iii) Spatial distribution of lineaments

The density and frequency maps of the manually identified lineaments, indicative of faults (see Fig. 6.18), are presented in figures 6.23 and 6.24. The density map quantified the total length of lineaments, per km^2, whereas the frequency map quantified the total number of lineaments present in the study region.

iv) Rose diagrams of fault azimuths

The final lineament map was used to extract the lineaments within each of the drainage basins. Rose diagrams of lineaments were then created for comparison with the drainage network rose diagrams to examine whether stream azimuths are controlled by fault structures (presented below). The rose diagrams show the presence of E-W to NW-SE lineaments, which imply the current tectonic regime (see Chapter 2). In addition, these particular lineaments/faults seem to correspond to stream segments of second and third order, implying to the structural control of these stream segments by the current tectonic regime (Fig. 6.25 and Appendix II, Fig. 8 a, b).

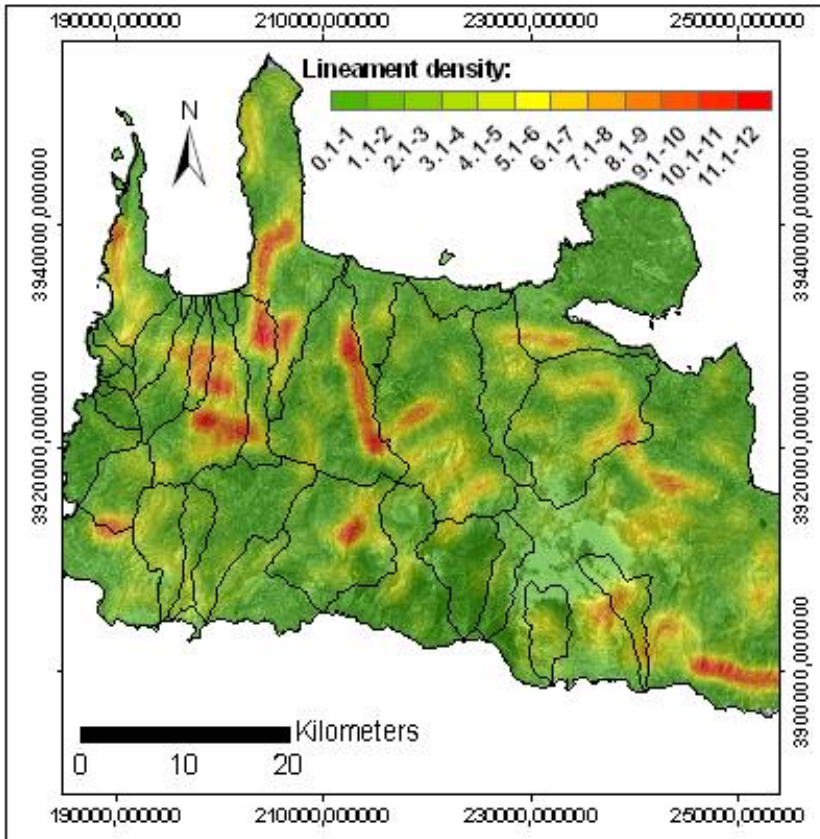

Fig. 6.23: Density map of manually digitised lineaments.

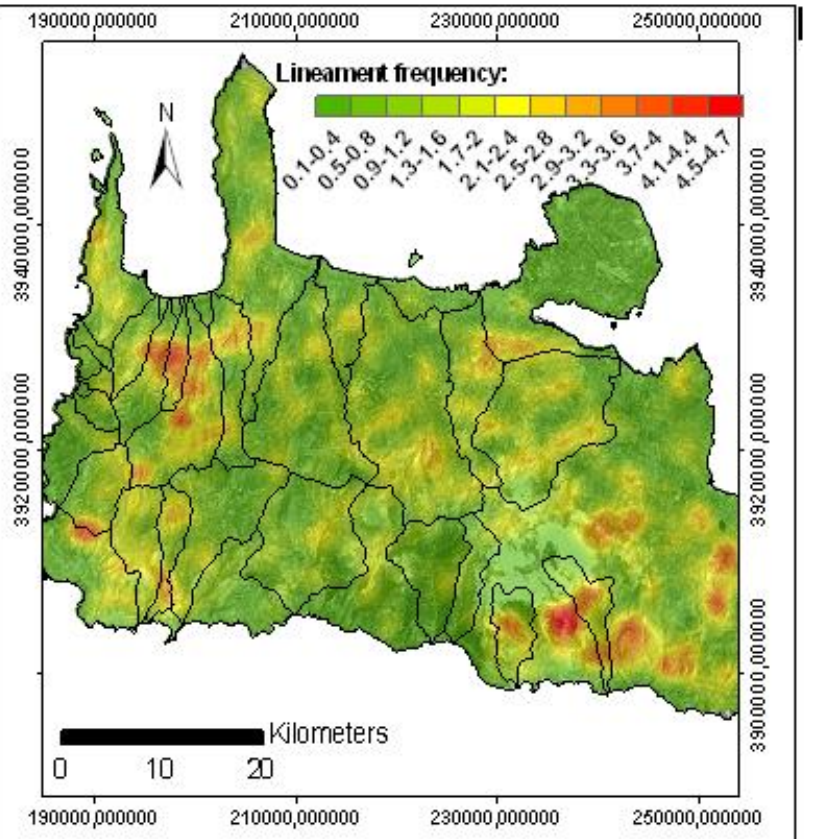

Fig. 6.24: Frequency map of manually digitised lineaments.

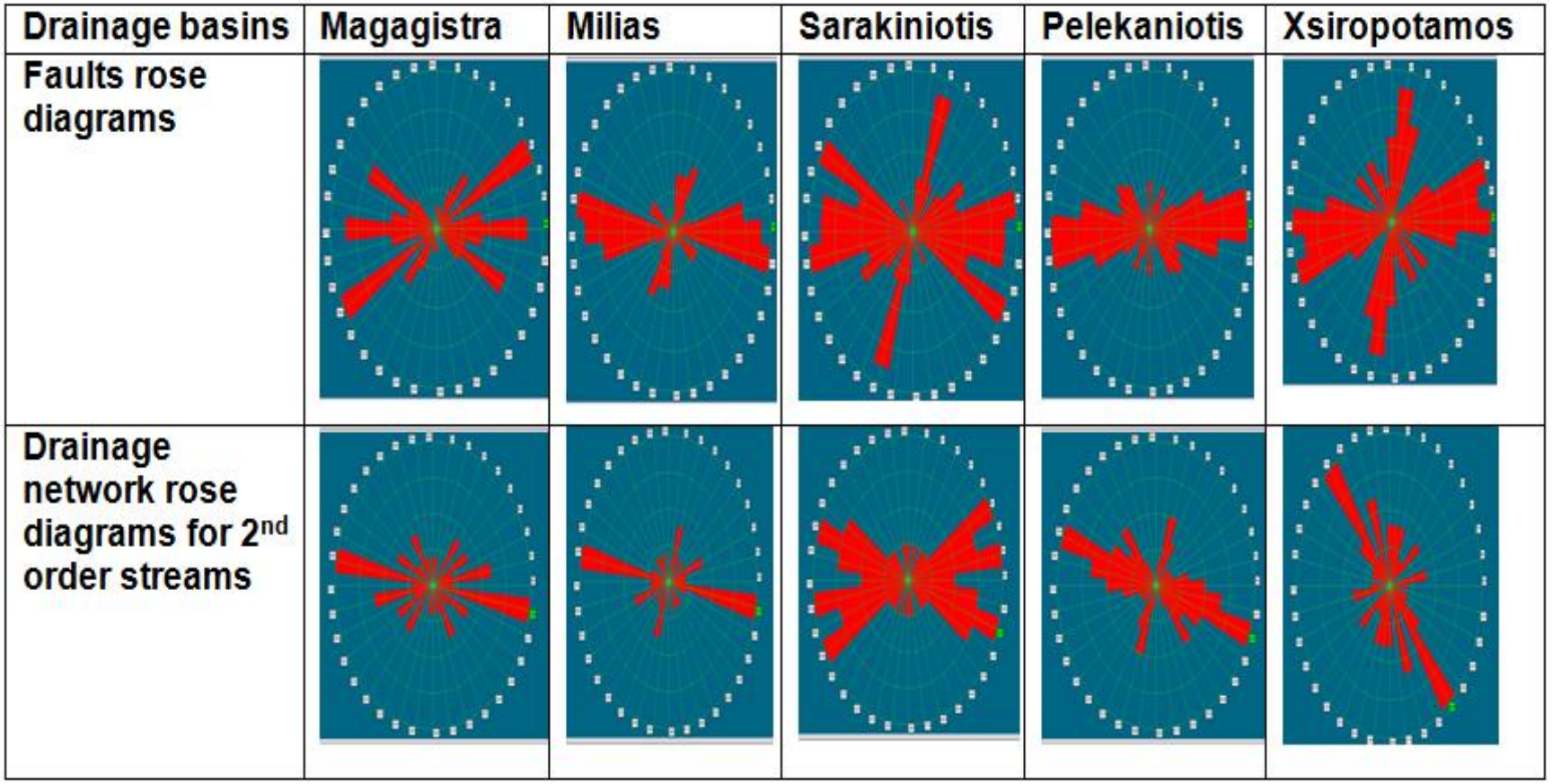

Fig. 6.25: The rose diagrams of faults with regard to drainage network azimuths for particular drainage basins (as a sample) of the study region, indicating mainly their E-W strike.

6.7 Discussion

This chapter presents the stages that are applied in this research in order to discriminate the lithologies and to identify the lineaments of the studied region by using Earth observational datasets. Accomplishment of the described procedure offers valuable information regarding the geological aspects taking place in western Crete. Knowledge of the geological aspects and their interrelationship with information regarding neotectonic aspects can be useful in the overall assessment of active tectonics, as examined later in Chapter 8.

- **Lithological discrimination**

The 1971 IGME geological map is the only available dataset that provides information about the lithologies and faults of the study area. The 1971 map was based on fieldwork and the interpretation of aerial photos, so new technologies such as the multi-spectral satellite Earth observational data are potentially very useful for additional mapping. The Landsat ETM+ image processing provided a semi-automated approach to lithological discrimination, with the outcome images being in addition used for the visual interpretation of lineaments.

Band ratios from multispectral satellite images are commonly used for lithological mapping (e.g. Crippen, 1989; Lawrence, 1994; Ramadan et al., 2001; Teeuw et al., 2005). A feature of band ratios is the suppression of shadow in shaded relief, which can assist lithological discrimination. On the other hand, such procedures result in a poorer depiction of lineaments. The present research goes beyond previous work by enabling the discrimination of the lithological signal and the tectonic signal within a single satellite image. Enhancement of tonal contrast differences, helping to highlight lineaments and to depict lithologies is provided. The procedure is based on criteria that offer isolation of spectral information, using PCA, MNF transformation, OIF analysis and spectral band arithmetic operations via multiplication band products.

Spectral information within each PCA principal component decreases substantially for the components after PC1, with the later components being harder to visually interpret and containing progressively more speckle (e.g. Green

et al., 1988). MNF transformation was found to be more effective than PCA for maintaining image quality for the set of components (e.g. Lee et al., 1990). This observation is in agreement with the Chen (2000) study where MNF proved to decrease more steadily the image quality, with regard to the increasing component number, in comparison to PCA. A major benefit of both PCA and MNF is that some of their components keep most of the spectral information, while suppressing the signal from vegetation cover. As a consequence, combining components of both PCA and MNF in an RGB combination image, such as PC1-MNF2-MNF3, can highlight lithological differences, on a site-by-site basis, more clearly than simple RGB combinations (see *"6.5 Results"* section).

The Optimum Index Factor (OIF) analysis and correlation coefficient matrix (extracted by PCA analysis) were combined here to determine which of the satellite imagery band components kept most of the spectral information, highlighting different lithologies and lineaments at a single satellite image. As a result, bands discriminating lithology and suppressing vegetation were isolated and selected for further processing. That extraction of bands was done via the multiplication procedure, which provided a better visual discrimination of lithologies than the simple RGB combination or band ratio approach (see Fig. 6.11). The RGB combination (4*3*2)(7*3*2)(7*3*1) was selected as the most representative to be used in the next stage of this research which concerns the identification of lineaments. This RGB combination was the most appropriate to determine lineaments corresponding to faults and meet the criteria described in section 6.4 (d) (for example, criteria such as tonal discontinuities in the image, alignment of topographic forms, heavy vegetation cover patterns along with linear trends). An additional benefit of this band multiplication procedure, relative to commonly used band ratios, was the enhancement of tectonic lineaments. This can be a powerful tool for seismic risk assessment studies, with regard to mapping and highlighting soft-rock lithologies and possible fault locations.

- **Lineament analysis**

The techniques used in this study are designed for poorly accessible rugged mountainous terrain. Except for the multi-spectral image processing and the visual interpretation described above, lineament extraction was also carried out via semi-automated mapping through the use of DEM and satellite imagery. Landsat ETM+ band 7 and fused DEM were used to apply specific techniques (such as spatial filtering and visual interpretation) for the identification of lineaments corresponding to mapped faults on the 1971 IGME geological map. The use of DEM shaded relief led to the identification of large and long linear fault scarps, especially in the mountainous terrain. These large-in-extent lineaments are particularly useful for tectonic block identification. Additionally, wherever there was cloud or snow coverage in the multispectral satellite imagery, resulting in no lineament visual interpretation, the DEM allowed lineament extraction.

Lineaments along geological contacts were easier to identify by satellite multispectral data. The digitised faults from the 1971 geological map provided a preliminary level of lineament mapping. Lineament mapping with visual interpretation for: i) DEM and; ii) multispectral satellite imagery (Landsat ETM+), was derived for the semi-automated manual extraction of lineaments. All lineament maps were used as overlaid reference maps to provide better delineation of coinciding lineaments. Comparison of the lineaments produced by each technique, used in this research, enabled the selection of coinciding lineaments (more than one) which are indicative of fault structures. This reduced the overall number of lineaments providing a simplified final tectonic lineament map of the drainage basins (see Fig 6.18). It is clear that all the aforementioned applications of lineament mapping were essential to the final consideration and implementation, as they were complementary to each other for determining the comparative analysis. The stages of the lineament analysis offer a series of overlain lineament maps. Small offsets might be observed due to the large scale of the geological maps (1:50000) and shadow effect in the DEM, with multispectral satellite imagery offering the most accurate lineament positions. Proper correlation between extracted lineaments from all data types exists with little deviation. Despite this,

the use of the GIS for the creation of small buffer zones that included similar lineaments was applied to overcome any deviation issues. The accuracy of lineament locations is influenced by the spatial resolution of the image, as lineament frequency increases with better spatial resolution, while average lineament length decreases (Sanders, 1996): that is in agreement with the findings of this study, as the number of lineaments identified with the Landsat ETM+ satellite imagery was larger than the lineaments identified by DEM (see Table 6.5). Spatial resolution of Landsat ETM+ (15m) was better than the one of DEM (30m), so shorter lineament in length were identified. Also, geophysical measurements (examined in Chapter 7) can provide even greater accuracy in fault location. In the subsequent chapter 7 a number of identified lineaments determined in this chapter, will be validated and justified by the use of geophysical measurements.

.

6.7.1 Comparison of onshore and offshore lineament orientations

Various studies have identified troughs, ridges and lineaments surrounding the island of Crete offshore (Ten Veen and Postma, 1999). These structures are helpful in the comprehension of the regional tectonic framework, through comparing the lineaments identified on the island with those existing offshore. The western part of the island has offshore lineaments with a NW-SE trend, close to Gavdos island (Fig. 6.26 a). The faults south of western Crete are described by Leite & Mascle (1982), as normal faults. As can be seen in fig. 6.26 b (compiled by Ten Veen and Postma, 1999) these NW-SE faults bound asymmetrical horsts (with symbol +) and graben (with symbol -). The western South Cretan Trough continues eastwards across the whole of southern Crete, and is parallel to an offshore horst (the Central Iraklion Ridge). This extensional faulting is responsible for tilted blocks, which create a parallel series of ridges and troughs (Meulenkamp et al., 1994; Ten Veen & Postma, 1999). On Crete there are a few major N-S striking scarps or ridges that indicate major faults, controlling the orientation of the peninsulas in the north-west of the island. In the south-west part of western Crete there are NE-SW faults and NW-SE faults, associated with coseismic uplift up to 9 m (Shaw et al., 2008).The offshore fault directions were compared with the

outcomes of the onshore lineament analysis of this study showing a broad correlation (Fig. 6.27). The more detailed onshore record indicates dominance of E-W fault structures. This implies that the current tectonic regime is governed by generally N-S extension, consistent with the influence of slab rollback at the subducting margin. On this basis, it can be suggested that the current tectonic regime is arranged with ů3 orientated approximately N-S, ů1 vertical and ů2 orientated E-W.

Azimuth rose diagrams were produced to analyze the relationship between the extracted lineaments and the main drainage networks. Comparison between rose diagrams of fault azimuths and drainage network azimuths revealed two sets of geometric relationships, which are similar to the findings of Ribolini (2008). The first lineament set reveals that the drainage network orientation of most of the 2nd order stream segments is the same as lineament structures with NE-SW or E-W to NW-SE azimuths. The second lineament set occurs for low order stream segments that run perpendicular to the highest order stream segments and to the major lineament azimuths. That lineament set only dominates in the Xsiropotamos and Kalami basins, where the dominant lineament direction is along the highest stream order segments (see Fig. 6.22 & 6.27). The rose diagrams also reveal similar correlations between the onshore lineaments determining the main structural features of Crete and the offshore faults investigated by Ten Veen and Postma (1999), as illustrated in figures 6.26 a, b. This implies that the current tectonic regime of the outer forearc of the Hellenic subduction zone has a major impact on the tectonic deformation of the study area.

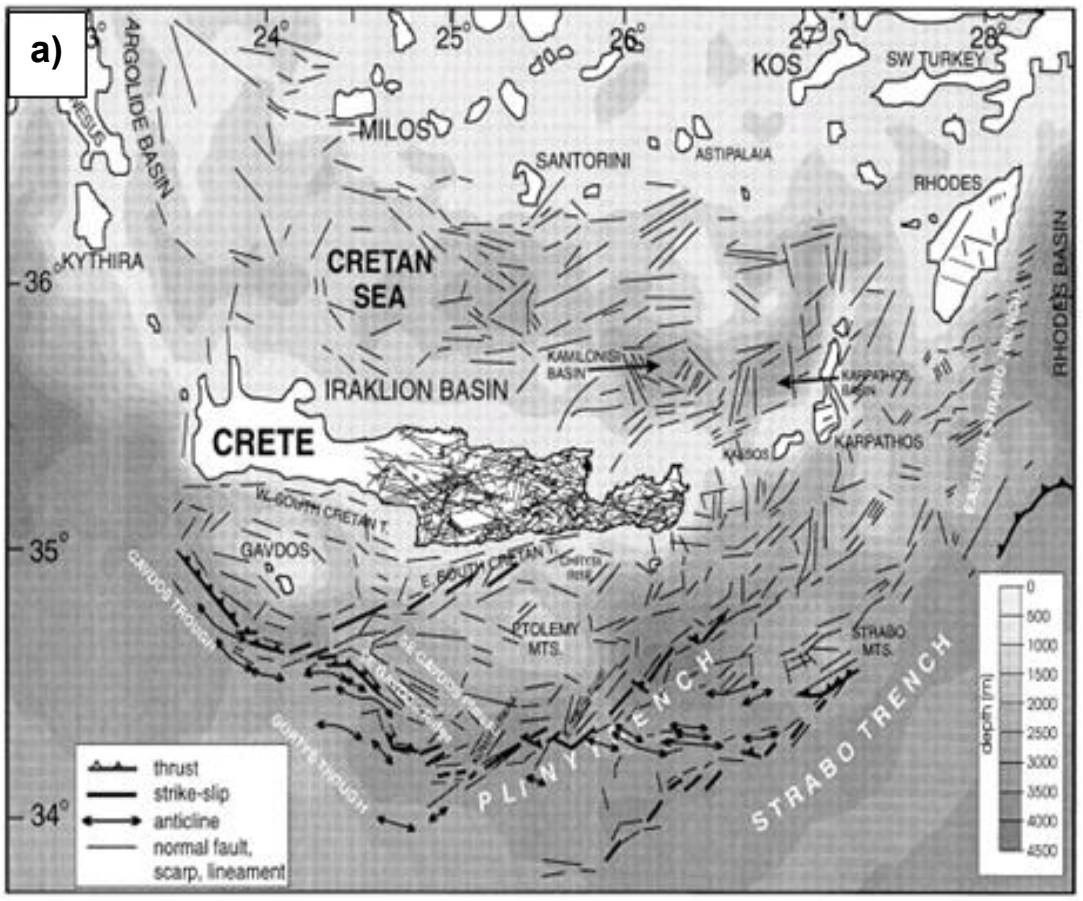

Fig. 6.26 a: Offshore faults from various studies indicate the major trench structures. The map was compiled by Ten Veen & Postma (1999) with offshore data being acquired from Jongsma (1977), Foose (1977), Le Pichon et al. (1979), Angelier et al. (1982), Leite & Mascle (1982), Peters (1985), Peters & Huson (1985), Mascle et al. (1986) and Mascle & Martin (1990).

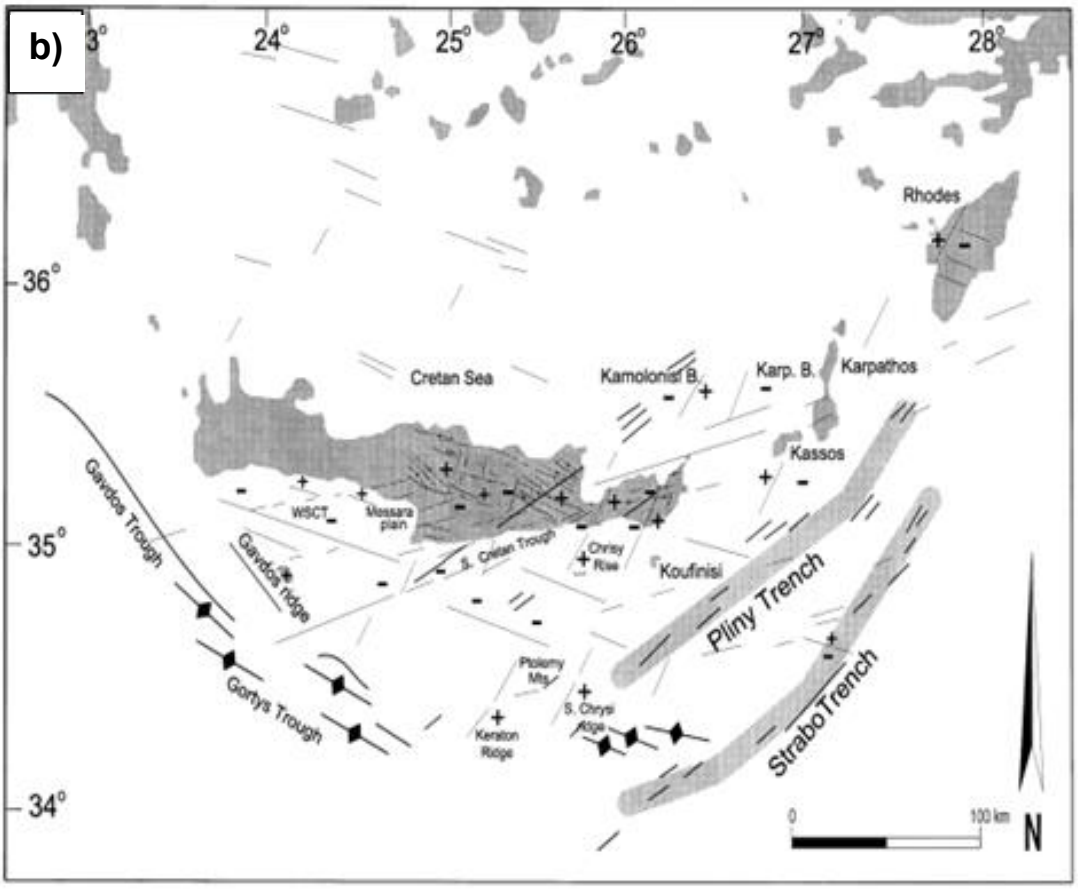

Fig. 6.26 b: Major fault patterns existing in the surrounding of the study region, with (ï) indicating grabens and (+) indicating horsts (modified by Ten Veen & Postma, 1999). Note the lack of data information in the western Crete study region.

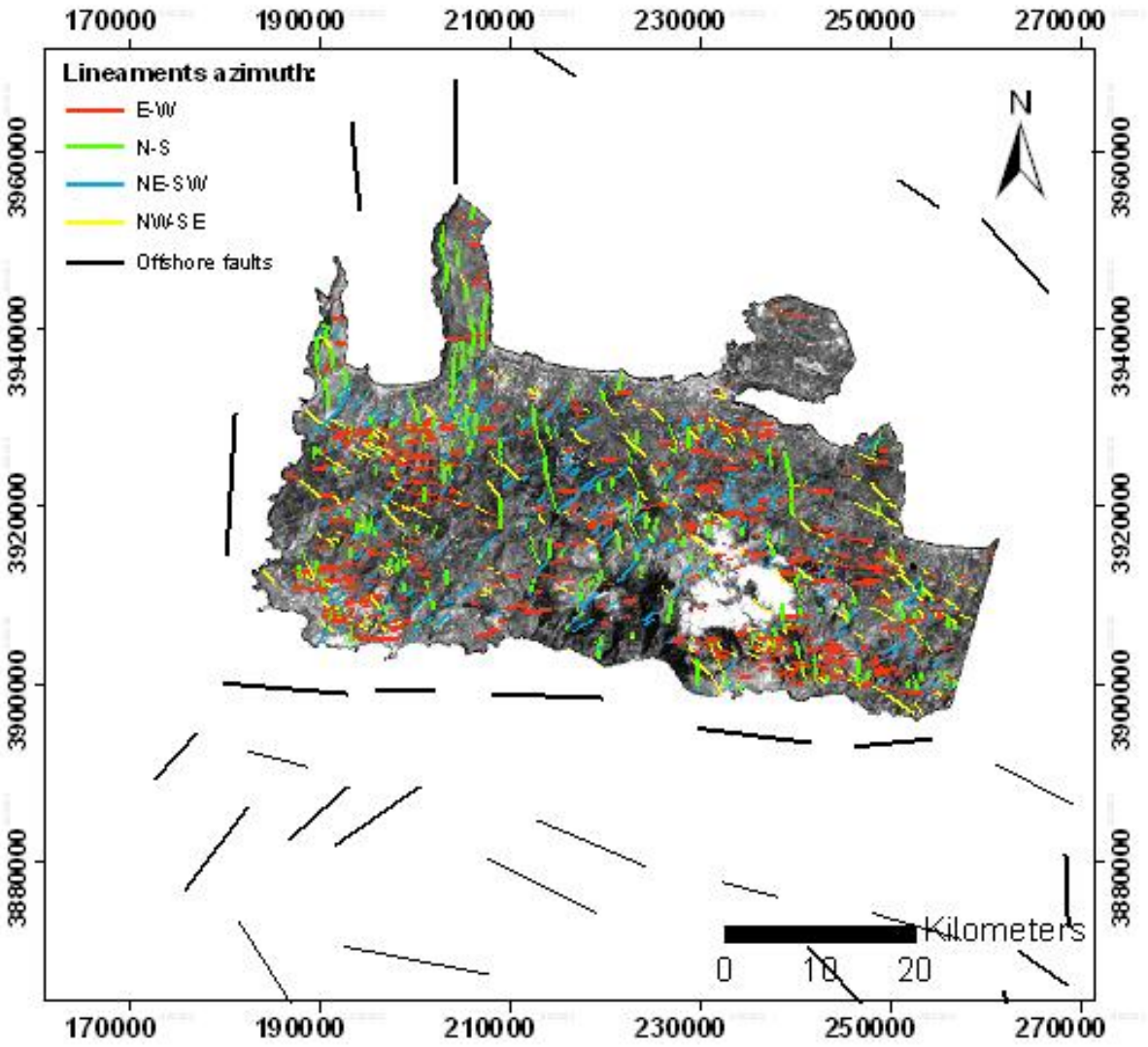

Fig. 6.27: The comparison between the offshore and onshore faults/lineaments indicates their effective association. Offshore N-S striking faults are associated with onshore N-S striking fault lines in the NW of the study area. The offshore NE-SW striking faults on the southern west part of the study area seem to be extended on the mainland by cross-cutting the study region from its southern western part to its north eastern part. Finally, the NW-SE and E-W offshore striking faults seem to play a significant role in the whole study area, particularly in the western and eastern part of study area.